



HYPERMIXER PYLON FUEL INJECTION
FOR SCRAMJET COMBUSTORS

DISSERTATION

Jason Clay Doster, Major, USAF

AFIT/DS/ENY/08-02

DEPARTMENT OF THE AIR FORCE
AIR UNIVERSITY

AIR FORCE INSTITUTE OF TECHNOLOGY

Wright-Patterson Air Force Base, Ohio

APPROVED FOR PUBLIC RELEASE; DISTRIBUTION UNLIMITED

The views expressed in this thesis are those of the author and do not reflect the official policy or position of the United States Air Force, Department of Defense, or the United States Government.

HYPERMIXER PYLON FUEL INJECTION
FOR SCRAMJET COMBUSTORS

DISSERTATION

Presented to the Faculty
Graduate School of Engineering and Management
Air Force Institute of Technology
Air University
Air Education and Training Command
In Partial Fulfillment of the Requirements for the
Degree of Doctor of Philosophy

Jason Clay Doster, B.S., M.S.
Major, USAF

September 2008

APPROVED FOR PUBLIC RELEASE; DISTRIBUTION UNLIMITED

HYPERMIXER PYLON FUEL INJECTION
FOR SCRAMJET COMBUSTORS

Jason Clay Doster, B.S., M.S.

Major, USAF

Approved:

Paul K.
Dr. Paul King (Chairman)

4 Sept 08
date

Mark Gruber
Dr. Mark Gruber (Member)

5 Sep 2008
date

Richard Branam
Maj Richard Branam (Member)

4 Sept 08
date

Larry W. Burggraf
Dr. Larry Burggraf (Member)

5 Sept 2008
date

Accepted:

M. U. Thomas
M. U. THOMAS
Dean, Graduate School of Engineering
and Management

9 Sep 2008
date

Abstract

Fueling the core airflow of a circular or elliptical scramjet combustor cross-section often requires intrusive geometries. Intrusive geometries can distribute the fuel evenly across the combustor cross-section and act as a flameholder for the fuel/air mixture. Compared to conventional transverse or angled wall injection, intrusive geometries allow easier penetration into the core combustor airflow and reduced fuel injection pressures. The design and testing of an intrusive pylon geometry for scramjet combustor fueling is the subject of this research. Three pylon configurations are compared: a basic pylon, a ramp pylon, and an alternating wedge pylon. All three pylon configurations exhibit the same frontal area and inject fuel parallel to the combustor airflow with long, thin rectangular injection ports (thin film fueling). However, the three pylon configurations incorporate different aft shapes to facilitate fuel/air mixing. A cold flow fuel injection study is accomplished to compare mixing capabilities and total pressure losses of the three pylon configurations. Four experimental techniques are used: 1) computational fluid dynamics, 2) aerothermal probing, 3) Raman spectroscopy, and 4) planar laser induced fluorescence. The ramp and alternating wedge pylons show decisive increases in mixing capability compared to the basic pylon. They also exhibit a slight increase in total pressure loss compared to the basic pylon.

Acknowledgements

I would like to thank my advisor, Dr. Paul King, for providing guidance through the PhD process and helping to center my efforts on essential tasks in pursuit of degree completion. Thanks to the Air Force Research Laboratory Propulsion Directorate, Wright Patterson AFB for sponsoring this work and allowing the use of a research wind tunnel. Thanks to Dr. Mark Gruber and Dr. Mark Hsu for overseeing the experiments, to Dr. Cam Carter and Dr. Mike Ryan for your optical experimental techniques expertise, and to Mr. Bill Terry and Mr. Dave Schommer for your tireless efforts in the wind tunnel during setup and testing. I would like to thank Mr. John Hixenbaugh, Mr. Chris Zickafoose, and Mr. Jay Anderson at the AFIT laboratory for their help in manufacturing articles for testing and procurement of construction materials. I wish to thank Dr. Raymond Maple for his computational fluid dynamics expertise.

Thank you to my wonderful wife for your loving support during the learning and research process here at AFIT. I enjoy each day God grants us as husband and wife. I look forward to continuing our mental and spiritual growth together.

Jason Clay Doster

Table of Contents

	Page
Abstract	iv
Acknowledgements	v
List of Figures	viii
List of Tables	xiii
I. Introduction	1
II. Background	5
Parallel and Transverse Fuel Injection	5
Nozzle Shapes	8
Hypermixers	8
Ramps	9
Alternating Wedges	12
Intrusive Fueling Devices	13
Upstream Fuel Injection	14
Current Research	15
III. Injector Design and Fueling	17
Injector Configurations	17
Fuel Flow Requirements	20
Equivalency Parameters	27
IV. Numerical and Experimental Methodology	29
Pylon Effective Areas	29
Computational Fluid Dynamics	30
Numerical Setup	32
Testing	34
Data Reduction	37
Wind Tunnel	42
Aerothermal Probing	44
Experimental Setup	45
Testing	48
Data Reduction	50
Raman Spectroscopy	59
Experimental Setup	61

	Page
Testing	65
Data Reduction	68
Planar Laser Induced Fluorescence	72
Experimental Setup	76
Testing	80
Data Reduction	83
V. Results and Analysis	87
Pylon Wake Region Flowfields	87
Plume Profiles	92
NO-PLIF Signal Intensity Profiles	94
Raman Methane Mass Fraction Profiles	97
Raman and NO-PLIF Profile Comparisons	98
CFD Ethylene Mass Fraction Profiles	103
Aerothermal Probe Profiles	106
Mixing Analysis	109
Streamwise Vortex Magnitudes	110
Plume Dilution	111
Plume Dilution Comparison to Other Work	122
Plume Flammability	125
Total Pressure Loss Analysis	128
Mixing Effectiveness and Total Pressure Loss Tradeoff	131
Energy Analysis	132
VI. Conclusions and Recommendations	136
Conclusions	136
Recommendations	140
Appendix A. Pylon and Wind Tunnel Mounting Plug Designs	142
Appendix B. Fuel Injection and Inlet Calculation Codes	151
Appendix C. Raman Spectroscopy Mass Fraction Profiles	157
Appendix D. NO-PLIF Intensity Profiles	161
Bibliography	168
Vita	173

List of Figures

Figure		Page
1.1.	Scramjet engine.	2
2.1.	Parallel mixing shear layer with vortical structures.	6
2.2.	Compressibility effects on shear layer growth. [1]	6
2.3.	Transverse wall injector. [2]	7
2.4.	Axial vortices generated in a flow.	9
2.5.	Swept and unswept ramp injectors. [3]	10
2.6.	Cross stream shear. [4]	10
2.7.	Compression and expansion swept ramps. [5]	11
2.8.	Combustion efficiencies using swept and unswept ramps. [5] . .	12
2.9.	Alternating wedge hypermixer. [6]	12
3.1.	Basic pylon configuration.	18
3.2.	Ramp pylon configuration.	18
3.3.	Alternating wedge pylon configuration.	19
3.4.	10 <i>in</i> circular scramjet combustor (not to scale). [7]	20
3.5.	Dynamic pressure curve of hypersonic vehicle flight profile. . .	21
3.6.	Two scramjet flight operating conditions.	21
3.7.	Inlet performance curves at Mach number 5.	22
3.8.	Inlet performance curves at Mach number 8.	22
3.9.	Pylon flow isentropic analysis.	25
4.1.	CFD internal grid.	33
4.2.	Mach number at point in wake region over time.	36
4.3.	Mass flow comparison.	37
4.4.	Data reduction planes.	38
4.5.	Fuel plume cartoon.	42
4.6.	Fairchild® model 10264 precision regulator.	43

Figure		Page
4.7.	Aerothermal probes.	45
4.8.	Pitot probe inside test section.	46
4.9.	Probe attached to worm gear traverser.	47
4.10.	Watlow [®] 4.5 kilowatt circulation heater.	47
4.11.	Probing area.	49
4.12.	Array of probing locations.	49
4.13.	Total temperature history (Basic).	58
4.14.	Total temperature history (Ramp).	58
4.15.	Total temperature history (Wedge).	59
4.16.	Ro-vibrational molecular energy levels.	61
4.17.	Raman experiment setup.	62
4.18.	Right side of test section Raman setup.	63
4.19.	Left side of test section Raman setup.	64
4.20.	Air and methane calibration.	65
4.21.	Array of Raman data.	66
4.22.	Horizontal slices from Fig. 4.20	69
4.23.	Calibration curves for air and methane.	70
4.24.	Raman data image.	70
4.25.	Ro-vibronic molecular energy levels.	74
4.26.	NO fluorescence spectrum at $R_1(8.5)$ ro-vibronic transition. . .	74
4.27.	NO-PLIF laser setup.	76
4.28.	NO-PLIF experiment setup.	77
4.29.	Test section with NO-PLIF setup.	78
4.30.	NO-PLIF radiation source setup.	79
4.31.	De-warping of image with grid reference and vertical ruler. . . .	81
4.32.	De-warping of image with horizontal ruler.	82
4.33.	De-warped data image.	84
4.34.	De-warped background image.	84

Figure		Page
4.35.	De-warped flatfield image.	85
4.36.	Cropped image area.	86
5.1.	Basic pylon CFD visualization.	88
5.2.	Ramp pylon CFD visualization.	89
5.3.	Alternating wedge pylon CFD visualization.	90
5.4.	NO-PLIF images at $13.6 d_e$	91
5.5.	NO-PLIF averaged plume profiles at $7.7 d_e$, $10.7 d_e$, and $13.6 d_e$	95
5.6.	NO-PLIF averaged plume profiles at $16.6 d_e$, $19.6 d_e$, and $23.9 d_e$	96
5.7.	Raman plume profiles at $13.6 d_e$ and $23.9 d_e$	98
5.8.	Raman and NO-PLIF plume profile comparison at $13.6 d_e$	99
5.9.	Raman and NO-PLIF plume profile comparison at $23.9 d_e$	100
5.10.	NO-PLIF signal comparison to Raman concentration data.	102
5.11.	NO-PLIF comparison with Raman for pylon configurations (summarized in 5.10)	103
5.12.	CFD plume profiles at $7.7 d_e$, $10.7 d_e$, and $13.6 d_e$	104
5.13.	CFD plume profiles at $16.6 d_e$, $19.6 d_e$, and $23.9 d_e$	105
5.14.	Basic pylon Mach profile at $23.9 d_e$	107
5.15.	Ramp pylon Mach profile at $23.9 d_e$	107
5.16.	Alternating wedge pylon Mach profile at $23.9 d_e$	108
5.17.	Mixing analogy plume profiles at $23.9 d_e$	109
5.18.	Streamwise vortex magnitude comparison.	110
5.19.	Ethylene/air mixing efficiency comparison.	111
5.20.	NO-PLIF averaged versus instantaneous maximum pixel intensities.	114
5.21.	NO-PLIF normalized maximum pixel intensity comparison.	117
5.22.	CFD normalized maximum ethylene mass fraction comparison.	119
5.23.	Raman maximum methane mass fraction comparison.	121
5.24.	Plume dilution comparison between pylons and transverse injection.	124

Figure		Page
5.25.	CFD plume flammability comparison.	126
5.26.	Raman plume flammability comparison.	127
5.27.	CFD total pressure loss comparison.	129
5.28.	Energy summation ratio comparison.	134
A.1.	Front piece of pylon design.	142
A.2.	Back piece of basic pylon design.	143
A.3.	Back piece of ramp pylon design.	143
A.4.	Back piece of alternating wedge pylon design.	144
A.5.	Joining front and back pieces.	145
A.6.	Basic pylon assembled picture.	147
A.7.	Ramp pylon assembled picture.	147
A.8.	Alternating wedge pylon assembled picture.	147
A.9.	Front piece of pylon picture.	148
A.10.	Back pieces of pylon picture.	148
A.11.	All pylon pieces picture.	148
A.12.	Wind tunnel mounting plug isometric view.	149
A.13.	Wind tunnel mounting plug top view.	150
A.14.	Gasket.	150
C.1.	Two alternating wedge plume profile measurements at $13.6 d_e$	157
C.2.	Two alternating wedge plume profile measurements at $23.9 d_e$	157
C.3.	Two ramp plume profile measurements at $23.9 d_e$	157
C.4.	Average alternating wedge plume profile measurement at $13.6 d_e$	158
C.5.	Ramp plume profile measurement at $13.6 d_e$	158
C.6.	Basic plume profile measurement at $13.6 d_e$	159
C.7.	Average alternating wedge plume profile measurement at $23.9 d_e$	159
C.8.	Average ramp plume profile measurement at $23.9 d_e$	160
C.9.	Basic plume profile measurement at $23.9 d_e$	160
D.1.	Basic pylon instantaneous plume images at $13.6 d_e$	161

Figure		Page
D.2.	Basic pylon ensemble averaged plume images.	162
D.3.	Ramp pylon instantaneous plume images at $13.6 d_e$	163
D.4.	Ramp pylon ensemble averaged plume images.	164
D.5.	Alternating wedge pylon instantaneous plume images at $13.6 d_e$	165
D.6.	Alternating wedge pylon ensemble averaged plume images.	166
D.7.	Standard deviation plume images.	167

List of Tables

Table		Page
3.1.	Combustor inlet conditions.	23
3.2.	Fuel injector conditions.	26
3.3.	Wind tunnel and pylon injection gas properties. [8]	28
4.1.	Fuel port effective areas.	30
4.2.	Flow conditions for CFD simulation.	33
4.3.	Nominal flow conditions for aerothermal probe experiments. . .	48
4.4.	Actual flow conditions for aerothermal probe experiments. . . .	50
4.5.	Nominal flow conditions for Raman experiments.	64
4.6.	Actual flow conditions for Raman experiments.	67
4.7.	Nominal flow conditions for NO-PLIF experiments.	80
4.8.	Actual flow conditions for NO-PLIF experiments.	83
5.1.	NO-PLIF averaged versus instantaneous maximum pixel intensity data.	115
5.2.	NO-PLIF averaged versus instantaneous maximum pixel intensity statistical difference.	115
5.3.	NO-PLIF normalized maximum pixel intensity data.	118
5.4.	NO-PLIF normalized maximum pixel intensity statistical difference.	118
5.5.	CFD maximum ethylene mass fraction data.	120
5.6.	CFD maximum ethylene mass fraction statistical difference. . .	120
5.7.	Raman maximum methane mass fraction data.	122
5.8.	Raman maximum methane mass fraction statistical difference. .	122
5.9.	CFD drag comparison.	130
5.10.	Total pressure loss comparison at 23.9 d_e	130

HYPERMIXER PYLON FUEL INJECTION FOR SCRAMJET COMBUSTORS

I. Introduction

Scramjet engines have been investigated since the late 1940s. In the United States both the Air Force and National Aeronautics and Space Administration (NASA) have conducted a large amount of scramjet research. Other countries with extensive scramjet research backgrounds include Russia, Germany, France, Japan, and Australia. Early scramjet investigations from the 1950s - 1970s concluded that a sufficient scramjet thrust to drag ratio existed to sustain a vehicle in hypersonic flight. [9]

Armed with these early investigative results, NASA set out to develop a hypersonic aircraft in the 1980s - 1990s, the National Aerospace Plane (NASP). NASP was a single stage to orbit concept utilizing a hydrogen-fueled scramjet engine. It was canceled in the mid-1990s due to technical risk issues. After the decline of NASP, NASA focused on a scaled down hydrogen-fueled scramjet vehicle called the Hyper-X that could operate at Mach numbers of 7 - 10. This vehicle accomplished its first and second successful flight tests in 2004 at Mach numbers 6.8 and 9.6, respectively. With a hydrogen-fueled scramjet proven possible, development and testing are now underway to show hydrocarbon-fueled scramjets are also capable of flight.

Theoretically, scramjets provide superior specific impulse performance over a large hypersonic Mach number range compared to rockets because they do not carry their oxidizer internally. However, their overall thrust to drag is generally much lower than that of rockets. A scramjet's lower operating range starts around Mach number 4 - 5. The practical upper limit expected for hydrogen-fueled scramjets is around Mach numbers 12 - 16, and the practical upper limit expected for hydrocarbon-fueled scramjets is around Mach numbers 9 - 10. [10]

A scramjet engine consists of a converging inlet, a supersonic combustion section, and a diverging nozzle (Fig. 1.1). The inlet section compresses the hypersonic freestream flow and lowers the Mach number by about 40%. The combustion section injects, mixes, and ignites the fuel in a supersonic flow, and the nozzle section accelerates the flow back to hypersonic speeds. Supersonic combustion is the most challenging part of successful scramjet operation, and fuel injection strategies are a primary field of research in supersonic combustion.

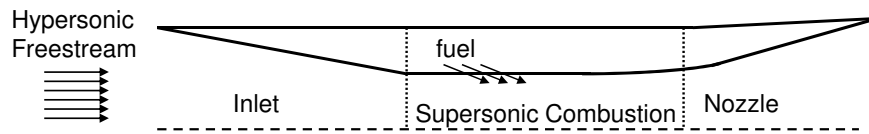


Fig. 1.1 Scramjet engine.

The amount of heat release in a supersonic combustor is largely dependent upon the effectiveness of the fuel injection system. [9] Much of the performance capability of a scramjet relies on efficient and thorough combustor cross-section fueling. The fuel injection system must mix the fuel and air in a reasonable distance within the combustor, accomplishing this with acceptable total pressure losses. The fuel injection system should also distribute fuel throughout the entirety of the combustor cross-section to take advantage of all available oxygen.

In the United States as well as abroad, the plurality of scramjet research has focused on hydrogen fuel combustion, but there has also been a sustained effort on hydrocarbon fuel combustion. In the United States, NASA has primarily pursued hydrogen-fueled scramjets while the Air Force has focused on hydrocarbon-fueled engines. [11] Hydrogen-fueled engines are generally considered for access to space applications and hydrocarbon-fueled engines for air-launched missile or smaller flight vehicle applications. Hydrocarbons reduce logistical complexity and lead to a more space efficient, smaller, and possibly stealthier vehicle. [12] In addition, the flight speed range for hydrocarbon-fueled scramjets results in combustor velocities achievable in existing test facilities, making component verification easier and less costly.

The Air Force Research Laboratory (AFRL) has been studying hydrocarbon scramjet engines in recent years under the Hydrocarbon Scramjet Engine Technology Program. [13,14] AFRL is actively pursuing fuel injector technologies for hydrocarbon scramjet combustors. Some of the technologies involve flush wall injection schemes, in-wall cavities, intrusive geometries like pylons and struts, or a combination thereof. The type of fuel injection strategy largely depends on the geometry of the scramjet combustor cross-section.

The scalability of the combustor cross-section is an important attribute so the same general combustor design can service an array of vehicle sizes. In recent years flush wall injection schemes have led to scramjet combustor geometries that are long and thin. A high aspect ratio combustor allows for core airflow fuel penetration using reasonable fuel injection pressures from flush wall injectors. However, the scalability of high aspect ratio combustors from smaller to larger engines is questionable. A circular or elliptical combustor section is easier to scale.

The objective of current research is to assess the mixing effectiveness and total pressure loss of a new fuel injection pylon for low aspect ratio circular or elliptical combustor cross-sections. The intrusive pylon distributes hydrocarbon fuel into a supersonic airflow, mixing the fuel and air to a sufficient concentration for combustion. The intrusive nature of the pylon allows fueling of the core combustor and injects fuel parallel to the airstream, resulting in a momentum boost to the flow not available with transverse fuel injection. Three geometric variants of the pylon concept are tested and compared. Specific measures of performance to compare the pylon configurations at several downstream planar positions include fuel dilution into the airstream, fuel/air mixture flammability, and total pressure loss.

The background chapter (Chapter 2) describes current scramjet fueling techniques and how current research both fits in and adds to the body of knowledge. The injector design and fueling chapter (Chapter 3) shows the three pylons, describes the fueling requirements for a pylon injector in a scramjet combustor, and estab-

lishes equivalency parameters between operational and cold flow test conditions. The methodology chapter (Chapter 4) details the four numerical and experimental techniques used to study pylon mixing effectiveness and total pressure loss, describing their setups, execution, and data reduction. The results and analysis chapter (Chapter 5) outlines the numerical and experimental findings, comparing the three pylons to one another. The conclusions and recommendations chapter (Chapter 6) summarizes the findings and offers paths for future research.

II. Background

The combustion process inside a scramjet engine begins with the proper mixing of fuel and air (oxidizer). This mixing along with ignition and heat release from combustion process must be accomplished within the residence time available in a scramjet combustor, on the order of a millisecond. Thorough distribution and rapid mixing of the fuel and air is the first step, and the concern of current research.

Parallel and Transverse Fuel Injection

The earliest attempts at fuel/air mixing in a supersonic airflow took the form of parallel injection. Many parallel injection experiments included two parallel velocity flows side by side (in a two dimensional situation) or a co-centric annulus flow (in an axisymmetric situation). The interface between the flows creates a turbulent shear layer. Shear layer growth is the mechanism for mixing the parallel flows. The shear layer grows with time/distance to entrain more of each stream in the mixing process, so quickness of shear layer growth is an important performance parameter.

One example of a shear layer growth experiment with parallel mixing flows involved an upper and lower flow stream meeting at the end of a splitter plate (Fig. 2.1). [1] Just downstream of the splitter plate the shear layer appears two dimensional with the rotational axes of the large structures perpendicular to the two flow streams in the lateral direction. The large structures serve to increase the interface surface area of the two flow streams and promote mixing. Eventually, instability in the primary flow direction (axial direction) generates smaller scale vortices with rotational axes in the axial direction and provides a catalyst for transition to a fully three dimensional turbulent shear layer.

Shear layer growth in parallel mixing flows is hindered by velocity differences between the flow streams due to compressibility. As the velocities of the two flow streams diverge, the shear layer growth is reduced, and hence mixing requires a longer distance. [1, 15–17] A collection of research shown in Fig. 2.2 illustrates the reduction in shear layer growth with increased shear layer compressibility.

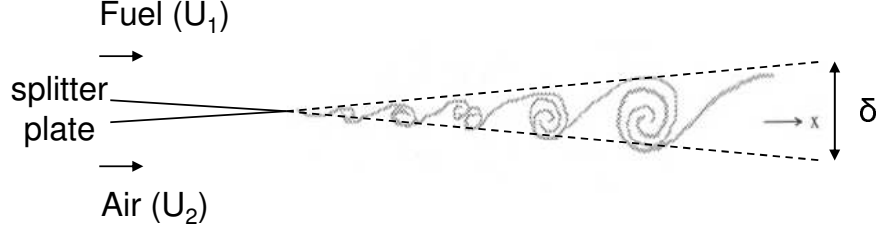


Fig. 2.1 Parallel mixing shear layer with vortical structures.

Examining the data contained in Fig. 2.2, the convective Mach number, M_{c1} , is a measure of the difference in velocities between two merging flow streams. A higher convective Mach number indicates a more compressible shear layer. The vertical axis is a ratio comparison between shear layer growth rate given identical flow stream velocities (an incompressible shear layer), and shear layer growth rate given divergent flow stream velocities. Compressibility reduces the shear layer growth rapidly as it increases and appears to level out around $M_{c1} = 0.80$, where the compressible shear layer growth rate is only about 20% of the incompressible.

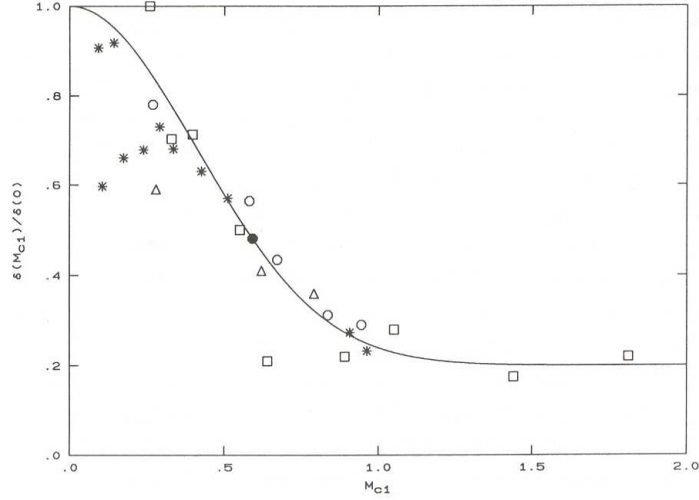


Fig. 2.2 Compressibility effects on shear layer growth. [1]

Large velocity differences between airflow and fuel injection flow is commonplace in a scramjet combustor, increasing the compressibility of mixing shear layers. Airflow velocities in scramjet combustors are generally at Mach number 2 up to high supersonic while fuel stream injection velocities are sonic to low supersonic. Conse-

quently, pure parallel injection leads to very long mixing distances that are not easily tolerated in practical scramjet combustor designs. However, parallel injection is advantageous for the added momentum in the axial direction from the fuel stream. It is incumbent on researchers to find other methods of injection or improve the mixing efficiency of parallel injection techniques in a supersonic airflow.

Once pure parallel fuel injection in scramjet combustors proved challenging to combustor performance, other fuel injection techniques were tried. The number of fuel injection techniques researched is as long as the list of researches studying them. [2,15, 18–22]. They include transverse fuel injection from the combustor sidewall oriented at various angles to the combustor airflow, tandem or yawed sidewall injection, slot injection, injection downstream of a rearward facing step or ramp, in-stream intrusive structures with injection ports, injection from the base of ramps, and many others. Of these listed, transverse injection from the combustor sidewall has been the most extensively researched. Fig. 2.3 depicts a single hole transverse wall injector.

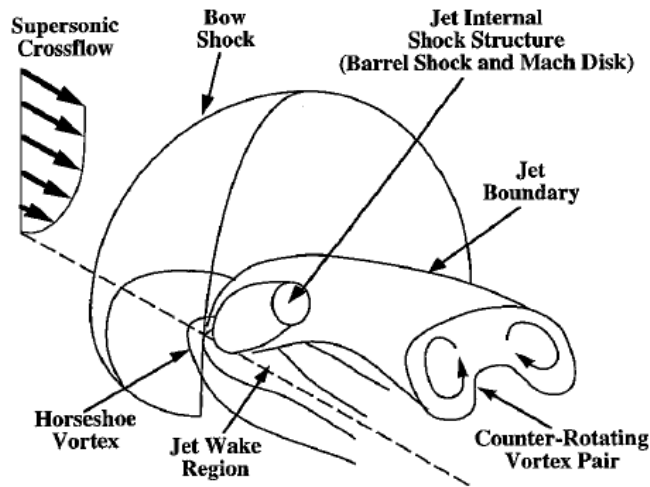


Fig. 2.3 Transverse wall injector. [2]

Transverse injection has been found to be a superior mixing method to pure parallel injection. Combustion efficiency measurements in a scramjet combustor using both injection techniques have verified this (Fig. 2.8). [5] Poor penetration height into the combustor airflow is the drawback of transverse wall injection. In order to

penetrate far into the combustor airflow excessive fuel pressures are required, which translate into excessive total pressure losses. Transverse fuel injection can be made more practical in combination with pylons or struts that place the fuel ports farther into the combustor airflow. Although some transverse injection strategies show promise, improving the mixing effectiveness of parallel injection is the focus of current research.

Nozzle Shapes

Fuel port geometry can affect the mixing characteristics of the fuel and air. Circular fuel ports are the most common geometries. However, elliptical or rectangular ports have exhibited superior mixing characteristics in experiment. In general, fuel port geometries with asymmetric properties and elongated shapes exhibit better mixing characteristics over a circular geometry.

Experimental measurements of injectant/airflow mixing from a variety of fuel port shapes in parallel flows and crossflows have shown the superiority of asymmetric and elongated fuel ports. [5, 21] They increase the interface surface area of injected fluids whereas a circular fuel port geometry minimizes the surface area. Increasing the interface surface area allows for more rapid diffusion and enhances mixing.

Rectangular fuel port geometries have been advocated by numerous researchers to increase mixing potential. [23–25] The perimeter to area ratio of a rectangle is large, allowing a large interface area for the fuel injectant and combustor airflow. Supported by past research, current research utilizes very long, high aspect ratio, rectangular fuel ports on the in-stream fueling pylon configurations.

Hypermixers

Introducing streamwise vortices (vortices in the axial direction of the scramjet combustor) into a fuel/air mixing flow has been studied as a mixing enhancement mechanism (Fig. 2.4). Streamwise vortices increase turbulent fluctuations in the

direction perpendicular to the combustor airflow at the expense of turbulent fluctuations parallel to the airflow. This has been shown theoretically, numerically, and empirically to be advantageous to the mixing process. [5]

By creating fluctuations perpendicular to the flow through the introduction of streamwise vortices, the conversion process of large stable structures into small turbulent structures is accelerated. [15] Turbulent fluctuations perpendicular to the flow break down large 2-D structures into small turbulent vortices essential for diffusion and mixing. In addition, since streamwise vortices are perpendicular to the shear layer, they are less vulnerable to compressibility effects. [26] Devices that introduce streamwise vortices to enhance fuel/air mixing are called hypermixers.

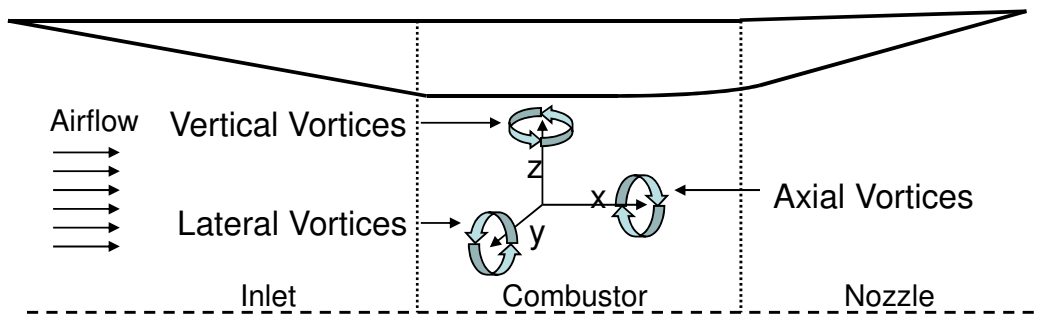


Fig. 2.4 Axial vortices generated in a flow.

Ramps. A compression ramp in the combustor airflow is a type of hypermixer. Ramp hypermixers are normally fueled from the base of the ramp into the wake region of the fuel injection device. Two basic configurations of compression ramp hypermixers, swept and unswept ramps, are prominent in literature. [3–5, 18, 27–34]. Swept compression ramp designs create stronger streamwise vortices than unswept designs, leading to enhanced mixing. [18] Figure 2.5 shows both swept and unswept compression ramps.

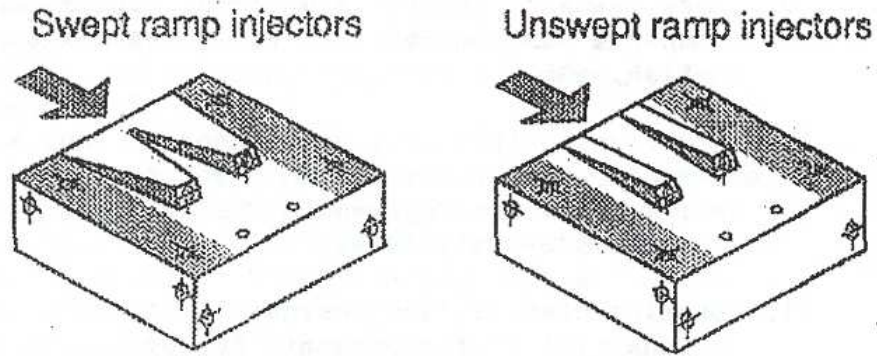


Fig. 2.5 Swept and unswept ramp injectors. [3]

Compression ramps compress the combustor flow and create a high pressure region on the top surface of the ramp. The pressure differential between the top surface of the ramp and the sides causes flow down the sides of the ramp and creates streamwise vortices at the exit plane of the injector. This mechanism is shown in Fig. 2.6. There is a thickness to the ramp injector base wall, and therefore a small distance between the injected fuel and the vortices created along the outside of the ramp sidewalls. Since the vortices are not deposited directly at the fuel/air interface, only a fraction of the vortex energy goes toward mixing the two.

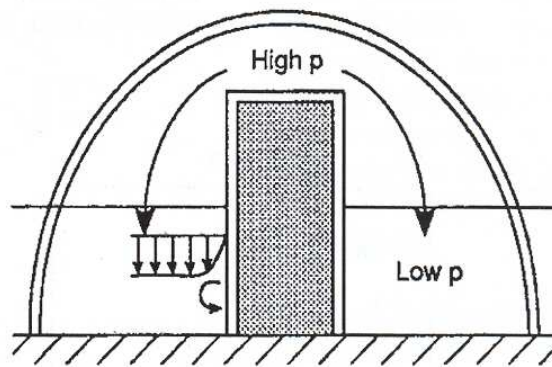


Fig. 2.6 Cross stream shear. [4]

Another type of ramp hypermixer, an expansion ramp (or relieved ramp), expands the combustor flow and generates axial vortices through the same mechanism as compression ramp hypermixers. Figure 2.7 depicts swept compression and swept expansion ramp configurations. Other variations of ramp hypermixer designs have also been studied including aerodynamic ramps, castellated ramps, and cantilevered ramps. [35–41] Aerodynamic ramps are actually a fusion of transverse/angled injection ports and the compression ramp concept.

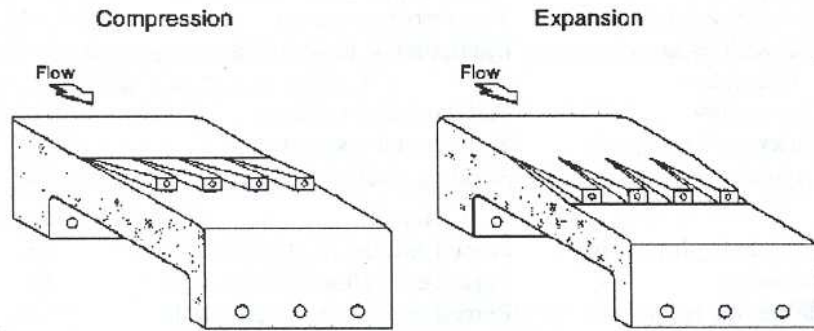


Fig. 2.7 Compression and expansion swept ramps. [5]

Evidence that ramp injectors improve the mixing effectiveness of parallel injection devices has been shown in experimental combustion efficiency measurements (Fig. 2.8). The bottom and top solid lines represent the combustion efficiencies using hydrogen fuel at various equivalency ratios for pure parallel and pure transverse injection respectively. The individual data points show the combustion efficiency using swept and unswept ramp injectors. Combustion efficiencies using ramp injectors are a definite improvement over pure parallel injection, and combustion efficiencies using swept ramp injectors approach the combustion efficiency using transverse injection.

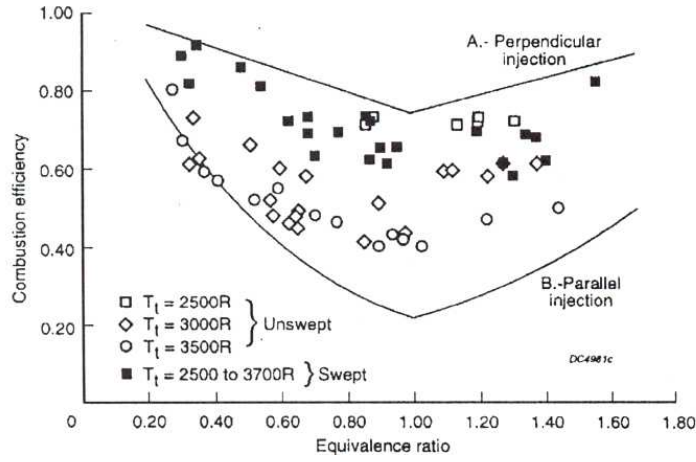


Fig. 2.8 Combustion efficiencies using swept and unswept ramps. [5]

Alternating Wedges. Another type of hypermixer geometry, the alternating wedge, is a series of alternating expansion surfaces. [6,42,43] Like the ramp hypermixers, injection ports are usually placed at the base of the geometry, fueling the wake region of the hypermixer. Figure 2.9 shows a typical alternating wedge hypermixer geometry. The alternating wedge hypermixer studied in current research is slightly different from Fig. 2.9 as it incorporates both compression and expansion surfaces.

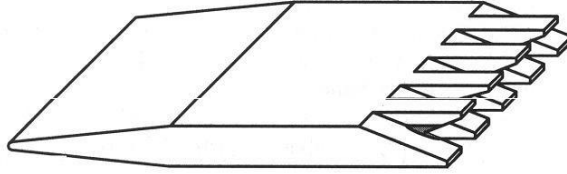


Fig. 2.9 Alternating wedge hypermixer. [6]

The alternating wedge hypermixer operates similarly to the ramp hypermixer, creating localized higher and lower pressure regions to turn the flow and create vortices in the axial direction of the combustor flow. Alternating wedge hypermixers are found less in literature than ramp hypermixers, and the performance of these two hypermixers has never been compared directly. A primary goal of current research is to compare the performance of a ramp and alternating wedge hypermixer.

Intrusive Fueling Devices

The hypermixer geometries can be affixed to combustor walls or placed on intrusive geometries like struts or pylons. Wall injection comes with an inherent combustor airflow penetration challenge as high fuel injection pressure are required. In order to place the fuel into the center of the combustor airflow with lower injection pressures, struts and pylons are used.

A strut is defined here as an in-stream geometric structure that spans the entire width or height of the combustor and attaches to two walls. A pylon is an in-stream geometric structure that spans a portion of the combustor width or height and attaches to only one wall. Using in-stream struts and pylons as fueling devices has been a common practice in scramjet design. Much research continues to be accomplished on strut designs. [6, 31, 35, 36, 42–50] Pylon fueling devices also continue to be studied by many researchers. [29, 30, 48, 51–66] The way pylons are used in a scramjet engine varies. In many instances pylons are used as shields for fuel injector ports located on a combustor wall. In other instances pylons serve as housing structures for fuel injector ports.

Fuel injection from a strut or pylon comes with several advantages. First, they allow fuel injection into the center of the combustor airflow. Second, they allow even distribution of fuel along their extent, the greatest contributor to fuel mixing efficiency according to some research. [59] Third, they have a subsonic wake region that can be used for combustion flame holding. This subsonic wake allows a stable, shielded region for fuel and entrained air from the combustor airflow to mix and ignite, anchoring a flame. [43, 47, 66]

Given the advantages of fuel injection from a strut or pylon, there are also distinct disadvantages. There is an added total pressure loss to the combustor airflow due to the intrusive object. There are also added cooling requirements to sustain the intrusive object in a high enthalpy flow. Understanding these disadvantages, but

looking to maximize the advantages, current research focuses on parallel fuel injection from in-stream pylons.

Upstream Fuel Injection

Fuel injection is traditionally accomplished from the base (aft face) of hypermixer geometries, into their wake region. In this case the streamwise vortex production of the hypermixer geometries are not applied directly where the fuel and air meet. It makes intuitive sense injecting from ahead of the hypermixer geometry would allow the fuel and air to meet and wrap around the hypermixer geometry together, facilitating better mixing. In this scenario the streamwise vortex production of the hypermixer geometry is directly applied to a fuel/air combination. This idea is supported by the small amount of research accomplished so far on upstream fuel injection with a hypermixer geometry. [31, 46, 67]

Kawano [67] compared a standard swept compression ramp with base fuel injection to a new swept compression ramp injector with oblique fuel injection from the top of the ramp. The conjecture was injection from the base of the ramp did not place the injected fluid as close to the streamwise vortices created by the ramp as injection from the top of the ramp. Evaluating volume fraction measurements from wind tunnel schlieren images, he concluded the swept compression ramp with top oblique injection was more effective at mixing than the ramp with base injection. There was no analysis of total pressure losses in the study.

Shreenivasan [46] studied compression ramps with upstream fuel injection from a single circular fuel port. Three different injection locations were tested: far upstream of the ramps, just upstream of the ramps, and from the base of the ramps. Evaluating planar Mie scattering images from several downstream positions, he concluded injection directly in front of the ramps at an oblique angle equal to the ramp angle distributed the injectant into the supersonic flow the best. Injection from the base of the ramps distributed the injectant the worst. There was no analysis of total pressure losses in the study.

Upstream fuel injection for the alternating wedge hypermixer geometry has not previously been studied. In current research, upstream injection is accomplished with both a swept compression ramp and an alternating wedge geometry. A beneficial byproduct of this concept is that the fuel flowing over the hypermixer geometry acts as a cooling mechanism for the hypermixer, advantageous in the high temperature environment of a scramjet combustor. This research will not quantify the cooling benefits of upstream injection on hypermixer geometries. It is left for future study.

Current Research

The concept explored in current research is an in-stream fuel injection pylon. The pylon facilitates gaseous hydrocarbon fuel injection into a supersonic airflow. The pylon studied both houses and shields the fueling ports that inject fluid parallel to the combustor airflow. A mixing enhancement device that introduces streamwise vortices into the airflow is incorporated on the pylon in the form of a hypermixer geometry, and thin rectangular fueling ports are located upstream of the hypermixer geometry.

The novel design concept combines best practices from the past research summarized in this chapter regarding hypermixer geometries, fuel port shapes, and fueling locations. Fueling upstream of a hypermixer geometry has not been studied extensively, and fueling upstream of a hypermixer geometry with a thin fuel sheet from a high aspect ratio fuel port has not been accomplished at all. Ramp and alternating wedge hypermixer geometries are used as mixing enhancement devices. However, the alternating wedge geometry incorporates compression as well as expansion surfaces, a departure from the strictly expansion surfaces of past research. Direct comparison of ramp and alternating wedge hypermixer geometries has not been accomplished before, and will be accomplished here.

The numerical and experimental research conducted compares the mixing effectiveness of each pylon configuration as well as the total pressure loss each create in a cold flow. Total pressure loss correlated with mixing effectiveness from hypermixer fueling geometries is lacking in literature, especially for the alternating

wedge. [6, 31, 42, 43, 46, 67] Mixing effectiveness is evaluated through calculations of streamwise vortex magnitudes, plume dilution, and plume flammability in the pylon wake region. Streamwise vortex magnitudes are calculated using velocity vectors from simulation data. Plume dilution and flammability calculations are calculated using simulation data as well as concentration measurements from un-intrusive, optical wind tunnel experimental techniques. Total pressure loss is gathered using total pressure data from simulation and wind tunnel probe measurements.

III. Injector Design and Fueling

Injector Configurations

The three pylon configurations considered are: the basic pylon (Fig. 3.1), the ramp pylon (Fig. 3.2), and the alternating wedge pylon (Fig. 3.3). [68–70] The construction of each pylon incorporates a two-piece forward and aft area and is shown in detail in Appendix A. The forward area contains a plenum common to all pylons. The aft area forms a constant angled compression ramp on the basic pylon and a hyper-mixer geometry on the others. The mating of the two pieces creates thin rectangular injection slots. The common parameters for all pylons are: height = 75 mm, length = 103 mm, frontal blockage area = 1215 mm², fuel port (slot) geometric area = 57 mm², front wedge half angle = 14.7°, and front wedge nose radius = 1 mm.

The basic pylon embodies two fuel injection strategies of 1) maximizing fuel-air interface area with a rectangular slot, and 2) injecting fuel upstream of the pylon aft area to allow fuel and air mixing prior to leaving the pylon surface. Figure 3.1 shows the basic pylon on a pedestal. The aft region of the basic pylon is a compression ramp at 10.6° (half angle) to the main airflow. The plenum is fed by a fuel tube at the bottom of the pylon and connected to the pedestal. Sonic fuel injection is accomplished from a backward facing step that shields the injectant for a short distance prior to mixing with the main airflow around the pylon.

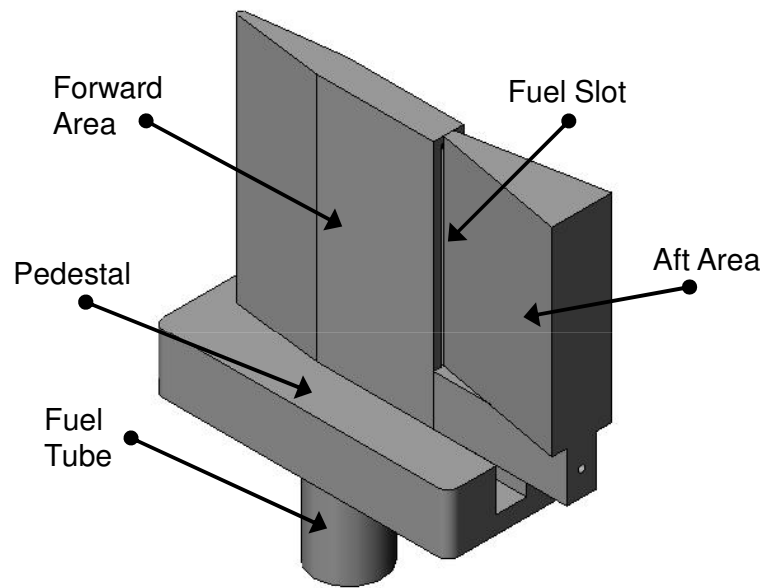


Fig. 3.1 Basic pylon configuration.

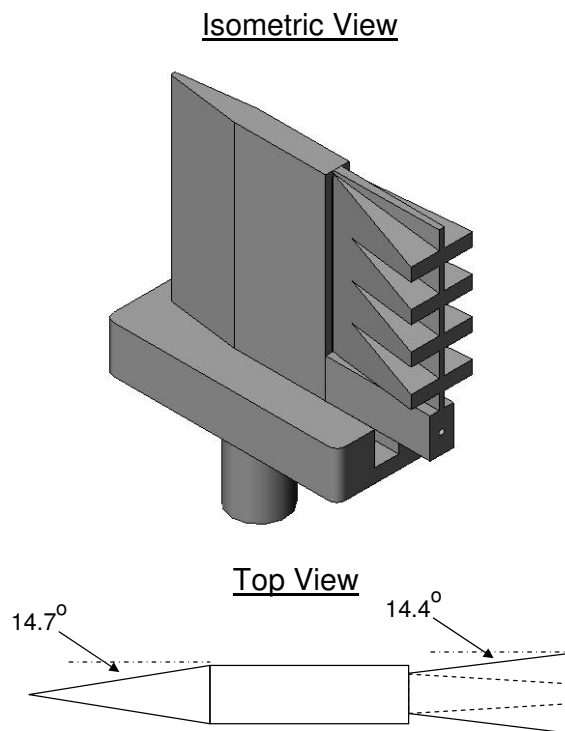


Fig. 3.2 Ramp pylon configuration.

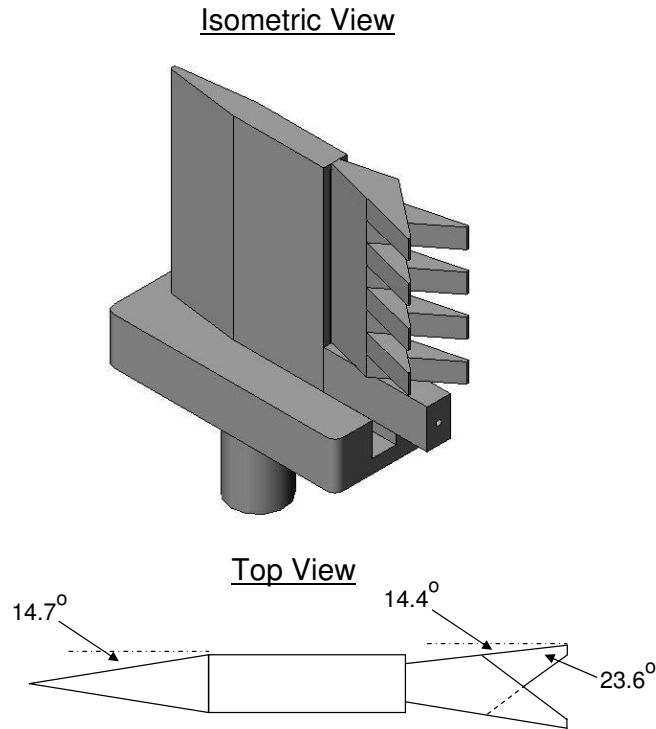


Fig. 3.3 Alternating wedge pylon configuration.

The ramp pylon shown in Fig. 3.2 includes eight compression ramps on the aft area of the pylon. The compression ramps are 14.4° (half angle) to the main airflow with 8.3° (half angle) of ramp taper (sweep). The compression and sweep angles produce the same frontal blockage area as the basic pylon.

The alternating wedge configuration shown in Fig. 3.3 includes eight alternating wedges on the aft area of the pylon. The wedge geometries have a 23.6° angle and attach to the aft area of the pylon, itself having a 14.4° compression angle (half angle) to the main airflow. This configuration produces the same frontal blockage area as the other pylons.

The basic pylon is a baseline. The ramp and alternating wedge pylons are meant to create streamwise vortical motion, entraining both the fuel and main airflow together in the generated vortices. The additional vortex energy should increase the mixing capability of those fuel injection pylons. A major concern of any fuel injection

system is the total pressure loss caused by the structure and mixing action. The total pressure loss of each pylon configuration is studied.

Fuel Flow Requirements

Expected pylon fueling requirements in a combustor section are necessary so an operationally representative flow rate can be studied during cold flow experiments conducted in this research. A nominal 0.254 *m* (10 *in*) circular scramjet combustor section is currently being considered by AFRL as a scalable design strategy (Fig. 3.4). The nominal fuel injection conditions are calculated given an eight pylon configuration.

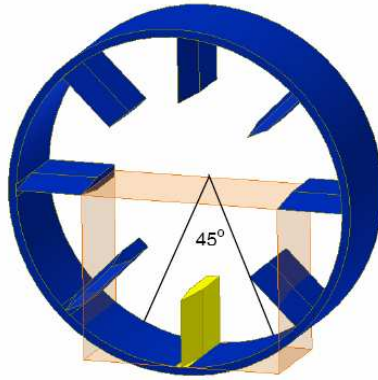


Fig. 3.4 10 *in* circular scramjet combustor (not to scale). [7]

A constant freestream dynamic pressure curve of 47,880 *Pa* (1000 *lb/ft*²) is shown in Fig. 3.5. This dynamic pressure trajectory is in the mid-range expected for a hypersonic vehicle. [15] Two specific points along this curve are chosen as flight condition cases (case 1 and case 2).

Inlet performance in the two flight condition cases is obtained with a 1-D continuity and energy analysis. The code for the analysis is contained in Appendix B. The inlet is assumed to be non-isentropic with a kinetic energy efficiency factor of 0.97. [9] The specific heat of air is varied according to temperature using polynomial curve fits. [71] The polynomial curve fits are valid within the temperature range of 300 *K* - 3500 *K*. Inlet performance curves are depicted in Fig. 3.7 and Fig. 3.8. The

area contraction ratio (CR) of the inlet (freestream capture area divided by combustor area) chosen is approximately 9.5. The two flight cases are displayed in Fig. 3.6. Table 3.1 portrays the combustor inlet conditions for each operating flight condition case.

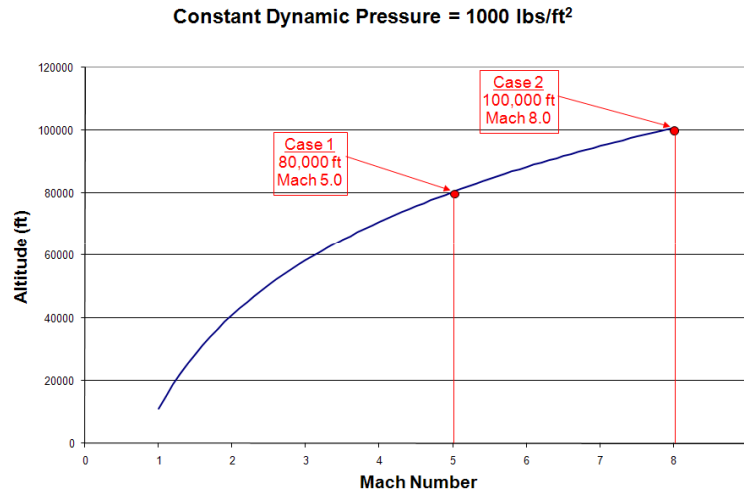


Fig. 3.5 Dynamic pressure curve of hypersonic vehicle flight profile.

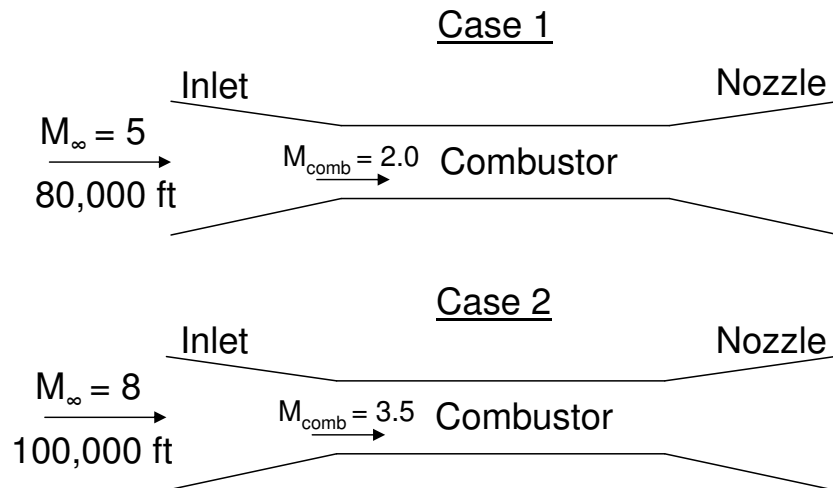


Fig. 3.6 Two scramjet flight operating conditions.

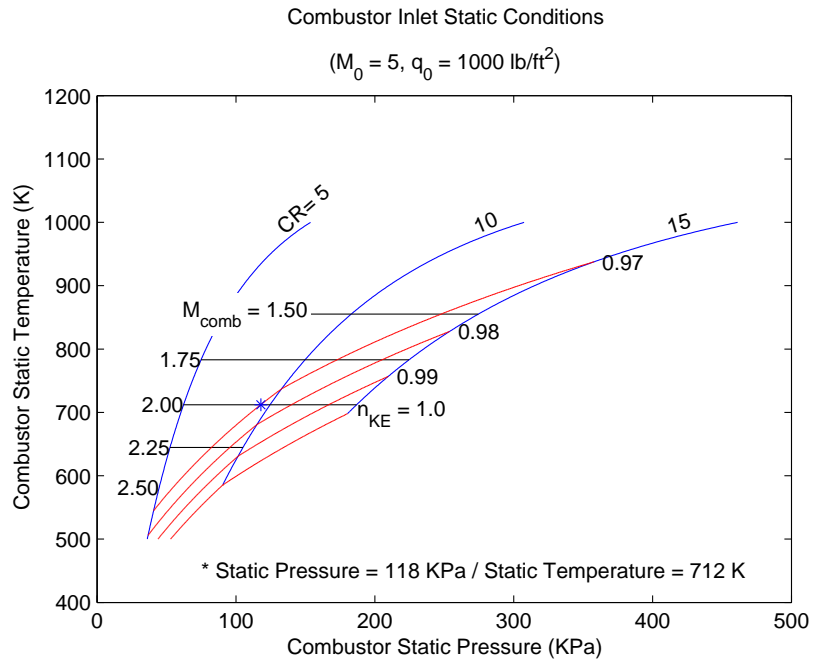


Fig. 3.7 Inlet performance curves at Mach number 5.

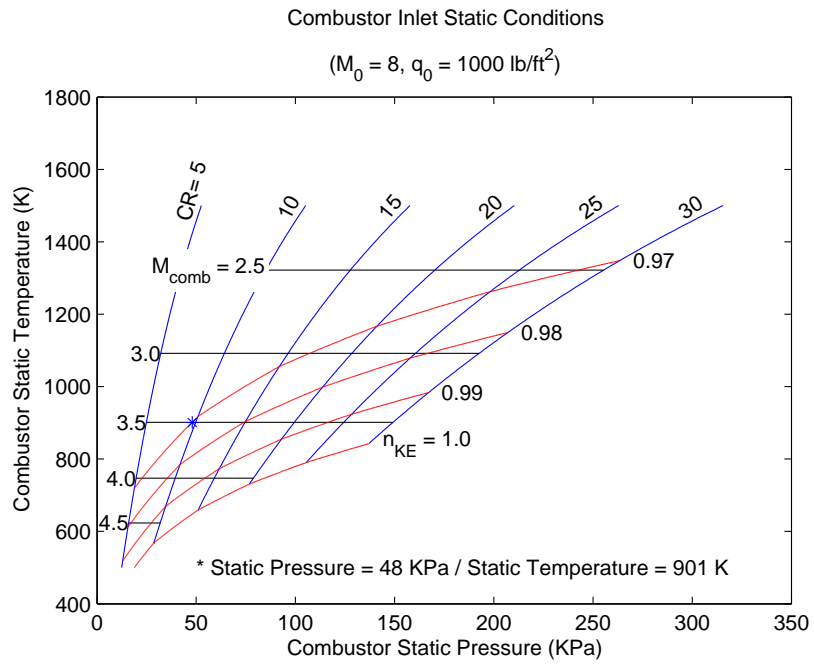


Fig. 3.8 Inlet performance curves at Mach number 8.

Table 3.1 Combustor inlet conditions.

Combustor Inlet Condition	Case 1	Case 2
Mach Number	2.0	3.5
Velocity	1054 <i>m/s</i>	2061 <i>m/s</i>
Mass Flow	30.8 <i>kg/s</i>	19.4 <i>kg/s</i>
Total Temperature	1224 <i>K</i>	2784 <i>K</i>
Static Temperature	712 <i>K</i>	901 <i>K</i>
Total Pressure	0.915 <i>MPa</i>	4.05 <i>MPa</i>
Static Pressure	118 <i>KPa</i>	48 <i>KPa</i>

Fuel injection requirements at the case 1 and case 2 operational flight conditions are calculated to determine the mass flow required from each pylon in the scramjet combustor. Three main assumptions are made. First, the eight pylons supply the combustor with 75% of the necessary fuel to reach a global equivalence ratio of one. Second, each pylon injector has a fueling port area of 57 *mm*². Third, the fuel is vaporized kerosene approximated as $C_{11}H_{22}$, having a molecular weight of 154 *g/mol* and a stoichiometric ratio with air of 1:15 by mass. [72]

The third main assumption for deriving the fueling requirements, a vaporized kerosene fuel, should be expanded upon slightly. It has been found through recent research on kerosene fuel behavior at high temperatures that kerosene goes through a thermal decomposition reaction (cracking) process above 800 *K*. [73, 74] At these higher temperatures kerosene breaks down into lower molecular weight gaseous species such as methane (CH_4), ethylene (C_2H_4), ethane (C_2H_6), propylene (C_3H_6), propane (C_3H_8), and an assortment of other low carbon number species. The volume fraction of each species present in the cracked vapor depends on the temperature. Methane is found to be the dominant product of thermal cracked kerosene, and in general the average molecular weight of cracked products is around 29 *g/mol* depending on temperature.

The low molecular weight of thermally cracked vapor reduces the overall molecular weight of the combined vapor (vaporized kerosene + cracked products) as the cracked vapor volume fraction increases. According to one source [73], at 900 K the volume fraction of cracked vapor is around 52%, and approaches 90% or greater around 1000 K . These temperatures lie in the range of possible fuel temperatures seen in scramjet fuel injection systems since the fuel is used by most engine designers as an endothermic heat sink to cool the combustor walls. Even though cracked kerosene products like methane and ethylene could be present in high temperature fuel, vaporized kerosene alone is assumed for the approximated fuel injection requirements calculated here.

The total temperature, total pressure, and total density of the injected vaporized kerosene are estimated through published charts and data. [11, 75] Charts of approximate endothermic heat sink requirements and total fuel temperatures versus vehicle Mach number are contained in Curran's book. [11] The vaporized kerosene fuel is approximated to have a total temperature of 700 K for the case 1 flight condition and 900 K for the case 2 flight condition. The expected total pressure of the vaporized kerosene fuel from the fuel system is around 1.01 MPa (10 atm). Fuel total density is obtained from property charts contained in a journal article by Fan [75] using a vaporized kerosene simulant. The relationship between total temperature, total pressure, and total density leads to a gas constant, R , of 58 $J/kg K$ for the vaporized kerosene in case 1 and 56 $J/kg K$ in case 2.

Even though the vaporized kerosene is not an ideal gas, the R value calculated using data from Fan's work is very close to that expected for an ideal gas having a molecular weight of 154 g/mol ($R_{ideal} = 54 J/kg K$). For pylon fuel flow calculations, the ideal gas law relationship is used in both case 1 and case 2 with their respective R values (not the ideal gas R value). In addition, the vaporized kerosene is assumed to accelerate to sonic conditions in an isentropic manner inside the pylon plenum.

A specific heat ratio, γ , is required for isentropic flow calculations inside the pylon plenum. Given a typical kerosene specific heat at constant pressure, C_p , of 3000 J/kg K [76], and R values $56 - 58 \text{ J/kg K}$, the specific heat ratio, γ , used for isentropic calculations is 1.02. An isentropic code, contained in Appendix B, is used to accomplish pylon flow calculations. The code models the pylon as a constant area inflow, an ideal pressure vessel (the plenum), and a constant area outflow as seen in Fig. 3.9. It integrates the mass differential in the plenum from inflow and outflow and updates the plenum pressure until steady state is reached.

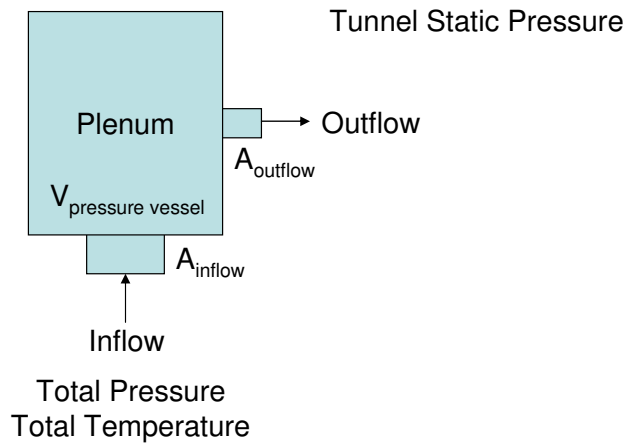


Fig. 3.9 Pylon flow isentropic analysis.

For case 1, 30.8 kg/s of combustor airflow is expected. With a 1:15 stoichiometric fuel/air mass ratio, 75% stoichiometric fueling by the pylons, and eight pylons in the combustor section, each pylon needs to deliver approximately 0.20 kg/s of fuel. For case 2, 19.4 kg/s of combustor airflow is expected, so each pylon needs to deliver approximately 0.13 kg/s of fuel. Table 3.2 portrays the fuel injector conditions.

Table 3.2 Fuel injector conditions.

Fuel Injector Condition	Case 1	Case 2
Inflow Area	130 mm^2	130 mm^2
Inflow Total Pressure	1.15 MPa	0.85 MPa
Inflow Total Temperature	700 K	900 K
Plenum Gauge Pressure	985 KPa	767 KPa
Outflow Area	57 mm^2	57 mm^2
Outflow Mach Number	1.0	1.0
Outflow Velocity	203 m/s	226 m/s
Outflow Mass Flow	0.20 kg/s	0.13 kg/s
Momentum Flux Ratio	1.1	0.64

The total pressure delivered to the pylon to achieve the fuel mass flow required is 1.15 MPa (167 lb/in^2) for case 1, and 0.85 MPa (123 lb/in^2) for case 2. This is the total pressure required from the scramjet's fuel circulation system. The internal plenum gauge pressure of the pylon is 985 KPa (143 lb/in^2) for case 1 and 767 KPa (111 lb/in^2) for case 2. These are the internal wall pressures the pylon must withstand to provide a sufficient mass flow to the combustor.

All the pylon configurations are designed to have the same frontal area blockage to the combustor airflow. The frontal area of each pylon is 1215 mm^2 . Eight pylons span the 0.254 m (50,670 mm^2) circular combustor cross section. This results in an overall combustor area blockage of 19.2%. This is comparable to the area blockage in other scramjet combustor designs. [43]

Only a single pylon in supersonic flow is studied in current research. Current research specifically focuses on cold flow comparisons between the three fuel injector pylon configurations for case 1 operating flight conditions. Equivalency parameters between the operating conditions and cold flow testing conditions are required to give the cold flow experiments some relevancy to expected operating conditions.

Equivalency Parameters

Test condition equivalency parameters are needed to match cold flow simulations and experiments to case 1 operational flight conditions. Equivalency parameters chosen are the wind tunnel and fuel injection Mach numbers and the momentum flux ratio, q . The momentum flux ratio between the wind tunnel airflow and injector flow is defined in Eqns. 3.1 and 3.2.

$$q = \frac{(\rho u^2)_{\text{pylon}}}{(\rho u^2)_{\text{tunnel}}} = \frac{(\gamma P M^2)_{\text{pylon}}}{(\gamma P M^2)_{\text{tunnel}}} = \frac{\left(\frac{\dot{m}}{A} u\right)_{\text{pylon}}}{\left(\frac{\dot{m}}{A} u\right)_{\text{tunnel}}} \quad (3.1)$$

$$q = \frac{\left[\gamma P_t M^2 \left(1 + \frac{\gamma-1}{2} M^2 \right)^{\frac{\gamma}{1-\gamma}} \right]_{\text{pylon}}}{\left[\gamma P_t M^2 \left(1 + \frac{\gamma-1}{2} M^2 \right)^{\frac{\gamma}{1-\gamma}} \right]_{\text{tunnel}}} \quad (3.2)$$

From Tables 3.1 and 3.2, the Mach number is 2.0 and the momentum flux ratio, q , is approximately 1.0 for cold flow testing. The momentum flux ratio depends on total pressure (P_t), Mach number (M), and specific heat ratio (γ). The equations can be simplified slightly in this research. The injected gas is at Mach number 1.0 since the injection pressure is always sufficient to yield sonic conditions through the fuel ports. The pylon total injection pressure is chosen to meet a momentum flux ratio of 1.0, dependent on wind tunnel conditions.

The mass flux ratio, q_m , is another important parameter. It is defined in Eqns. 3.3 and 3.4. The mass flux ratio depends on total temperature (T_t) and gas constant (R) in addition to those parameters the momentum flux is dependent on. It is not possible to equate both the momentum flux ratio and the mass flux ratio between two experiments unless the injectant gas and airflow have the same total temperatures in both experiments. The mass flux ratio is important when considering mass fraction values in the wake region of the pylons.

During an experiment, or between experiments, if the total temperature of the wind tunnel or pylon injection gas changes, the mass flows change. This leads to a mass flux ratio change and hence mass fraction value changes in the pylon wake region.

This is a consideration when reducing wind tunnel experimental data. The injection and wind tunnel total temperatures are kept constant in the CFD simulations.

$$q_m = \frac{(\rho u)_{\text{pylon}}}{(\rho u)_{\text{tunnel}}} = \frac{\left(\frac{P}{\sqrt{T}} \sqrt{\frac{\gamma}{R}} M\right)_{\text{pylon}}}{\left(\frac{P}{\sqrt{T}} \sqrt{\frac{\gamma}{R}} M\right)_{\text{tunnel}}} = \frac{\left(\frac{\dot{m}}{A}\right)_{\text{pylon}}}{\left(\frac{\dot{m}}{A}\right)_{\text{tunnel}}} \quad (3.3)$$

$$q_m = \frac{\left[\frac{P_t}{\sqrt{T_t}} \sqrt{\frac{\gamma}{R}} M \left(1 + \frac{\gamma-1}{2} M^2\right)^{\frac{\gamma+1}{2(1-\gamma)}}\right]_{\text{pylon}}}{\left[\frac{P_t}{\sqrt{T_t}} \sqrt{\frac{\gamma}{R}} M \left(1 + \frac{\gamma-1}{2} M^2\right)^{\frac{\gamma+1}{2(1-\gamma)}}\right]_{\text{tunnel}}} \quad (3.4)$$

Three different wind tunnel and injection gases were used during the course of this research: air, ethylene, and methane. These low molecular weight species, although not as dense as vaporized kerosene, could simulate the molecular weight of the injected fuel more closely than initially thought due to fuel cracking at higher temperatures. Thermal cracking reduces the molecular weight of kerosene down to something closer to these low molecular weight species, although at slightly higher fuel temperatures than approximated here for the case 1 operational condition (700 K).

In cold flow simulations and experiments conducted, air was used for both wind tunnel flow in CFD simulations and experiments, and as a pylon injection gas in experiments. Ethylene was used as a pylon injection gas in CFD simulations, and methane was used as a pylon injection gas in experiments. The general range of temperatures these gases were subjected to during cold flow testing, and the average specific heat ratio used for momentum and mass flux calculations involving each gas is shown in Table 3.3.

Table 3.3 Wind tunnel and pylon injection gas properties. [8]

Gas	Temperature Range (K)	γ	$R \left(\frac{J}{kgK}\right)$
Air	150 - 350	1.40 ± 0.005	287
Ethylene	260 - 300	1.25 ± 0.01	296.4
Methane	200 - 300	1.31 ± 0.02	518.3

IV. Numerical and Experimental Methodology

Computational fluid dynamics (CFD) simulations and cold flow wind tunnel experiments were used to study the mixing effectiveness and total pressure loss of the three pylon fuel injector configurations. FLUENT® was the CFD code employed. Reduced CFD simulation data included flow visualization, calculations of streamwise vortex magnitudes, fuel plume dilution, fuel plume flammability, and total pressure loss.

Experimental measurements were used to corroborate simulation results. A continuous flow supersonic wind tunnel at AFRL was the experimental apparatus. Aerothermal probes, Raman spectroscopy, and planar laser induced fluorescence (PLIF) were the experimental techniques used. Reduced aerothermal probe data included calculations of total pressure loss. Reduced Raman spectroscopy data included calculations of fuel plume dilution and fuel plume flammability. Reduced PLIF data included flow visualization and calculations of fuel plume dilution.

Pylon Effective Areas

The detailed drawings of the three pylon configurations are contained in Appendix A. The drawings call for a geometric fuel port area of $5.7\text{E-}5\text{ m}^2$. The CFD simulations incorporate fuel port boundary surfaces this size. No boundary layer is present in the simulation fuel ports, so the geometric fuel port area is also the effective fuel port area. In experiment however, boundary layers in the fuel port slots cause the effective fuel port area to be slightly smaller than the geometric area. In addition, there is also manufacturing tolerances that could change the geometric fuel port area from that of the drawings.

To quantify the fuel port effective areas, a calibration was accomplished on the three pylons. The primary objective was to ensure the effective fuel port area differences among the three pylon configurations were small. Differences in fuel port effective areas would manifest themselves as mass flow variations between the pylons in experiment although the same total pressure is applied to each pylon during testing.

The three pylon configuration effective areas were attained using a calibrated mass flow system with air as the injection gas. The calibrated mass flow was set to the expected mass flow in experiments, approximately 0.04 kg/s , resulting in sonic conditions ($M = 1$) at the fuel ports. A thermocouple and pressure transducer sampled the total conditions entering the pylon plenum. With total temperature (T_t), total pressure (P_t), mass flow (\dot{m}), and physical properties for air, the effective area, A_e , was determined for each pylon using Eq. 4.1.

$$\dot{m} = \frac{P_t A_e}{\sqrt{T_t}} \sqrt{\frac{\gamma}{R}} M \left(1 + \frac{\gamma - 1}{2} M^2 \right)^{\frac{\gamma+1}{2(1-\gamma)}} \quad (4.1)$$

The results of the calibration, seen in Table 4.1, show the pylon effective fuel port areas are indeed smaller than the geometric drawing area by about 6% on average. The average of the effective fuel port areas is $5.37\text{E-}5 \text{ m}^2$, with less than a 2% deviation between each pylon and the average. This effective area deviation is smaller than the experimental deviation of mass flow in the wind tunnel and pylon injector flow from pressure and temperature variations during testing.

Table 4.1 Fuel port effective areas.

Pylon	Effective Fuel Port Area (m^2)	Normalized to $5.37\text{E-}5 \text{ m}^2$
Basic Pylon	5.30E-5	0.987
Ramp Pylon	5.46E-5	1.017
Alternating Wedge Pylon	5.36E-5	0.998

Computational Fluid Dynamics

CFD simulations are a numerical tool used to predict flowfield behavior in the wake region on the three pylon configurations. All flowfield quantities such as injectant concentration, total pressure, velocities, densities, etc. are available from simulation data throughout the simulated wind tunnel volume. CFD results comparing the mixing effectiveness and total pressure loss of the pylon configurations are validated

with experimental comparison results. FLUENT[®] was the commercial CFD code employed to study ethylene fuel injection from the three pylons.

FLUENT[®] is a three dimensional Navier-Stokes flow solver with multi-species capability. The Reynolds averaged Navier-Stokes (RANS) flow solver used within FLUENT[®] was coupled, solving the continuity, momentum, energy, and species equations simultaneously, followed by the turbulence scalar equations in a single iteration. Since the flow of concern is supersonic and compressible, the recommended practice is to use the coupled solver instead of the segregated solver, which solves the continuity, mass, and energy equations in sequential order in separate iterations. Also, a second-order spatial flux solution for complex flows is appropriate, especially since the flow velocities do not align well with the grid geometry employed. A coupled, second-order solution for sonic ethylene injection into a Mach number 2.0 airflow was obtained for all three pylons.

FLUENT[®] offers a variety of turbulence model options. The the K- ω turbulence model with shear stress transport (SST) is a reasonable selection for free jet flow fields with solid surface boundaries. FLUENT[®] incorporates a materials database, including properties for air and ethylene. The simulations assumed air/ethylene mixtures acted as an ideal gas. Mixture fluid properties such as viscosity and thermal conductivity were averaged within each computational cell, depending on the fractional species makeup of the cell. Species transport with no combustion was modeled.

FLUENT[®] can progress a flow solution in a steady or unsteady manner. When using the steady state solver, a localized time-step is computed for each cell, and each cell progresses at a different rate toward a steady state solution. When using the unsteady solver, a global time-step is computed for the entire flow, and all cells progress at the same time rate for a time accurate solution. Both of these time progression methods were used. The basic pylon, exhibiting a highly unsteady flowfield in its wake, required a time accurate solution. The ramp and alternating wedge pylons, exhibiting a more steady wake region, allowed a steady state solution.

Numerical Setup. There were two main tasks involved in obtaining a CFD solution, grid construction and flow solution. A solid body design for the three pylons was constructed in SOLIDWORKS®. The solid body design was output from SOLIDWORKS® and read into GRIDGEN® as a IGES file, where surface domains were constructed and 2-D triangular meshes placed on the domains. These meshed surface domains were output from GRIDGEN® and read into SOLIDMESH® as a NASTRAN® file, where cells were constructed between the surface domains. The grid cells are an unstructured hybrid of tetrahedral/pentahedral volumes.

The viscous tailoring of the grid near the pylon surfaces was accomplished to the refinement required to utilize the boundary layer wall functions in FLUENT®. The exterior walls of the computational domain are inviscid for all three pylons in order to limit grid size; hence, the grid is not refined with viscous spacing near the wind tunnel walls. The wake region of all three pylons was populated with a dense cell mesh extending 290 mm downstream of the pylon base plane. The cell volumes in the wake region are approximately 1.0 mm³. The grids for the three pylons vary between 5.5 - 6.7 million cells. Figure 4.1 shows a typical grid.

One grid was constructed for each pylon. A grid convergence study was not accomplished to optimize the grids. Any comparison of the flow solutions to experimental data is qualitative due to the inviscid exterior walls. Wind tunnel walls exhibit viscous effects and have a boundary layer not modeled in simulation. The inlet and outlet walls were defined with the freestream condition, Mach number 2.0 airflow. The wind tunnel walls were defined with slip conditions as inviscid boundaries. All pylon surfaces were defined with no-slip conditions as viscous boundaries.

Once the grid was constructed and the boundary conditions defined, the information was output from SOLIDMESH® as a FLUENT® .CAS file and read into FLUENT® to accomplish a flow solution. The cold airflow inlet and ethylene injection conditions are shown in Table 4.2. These conditions result in a momentum flux ratio of one.

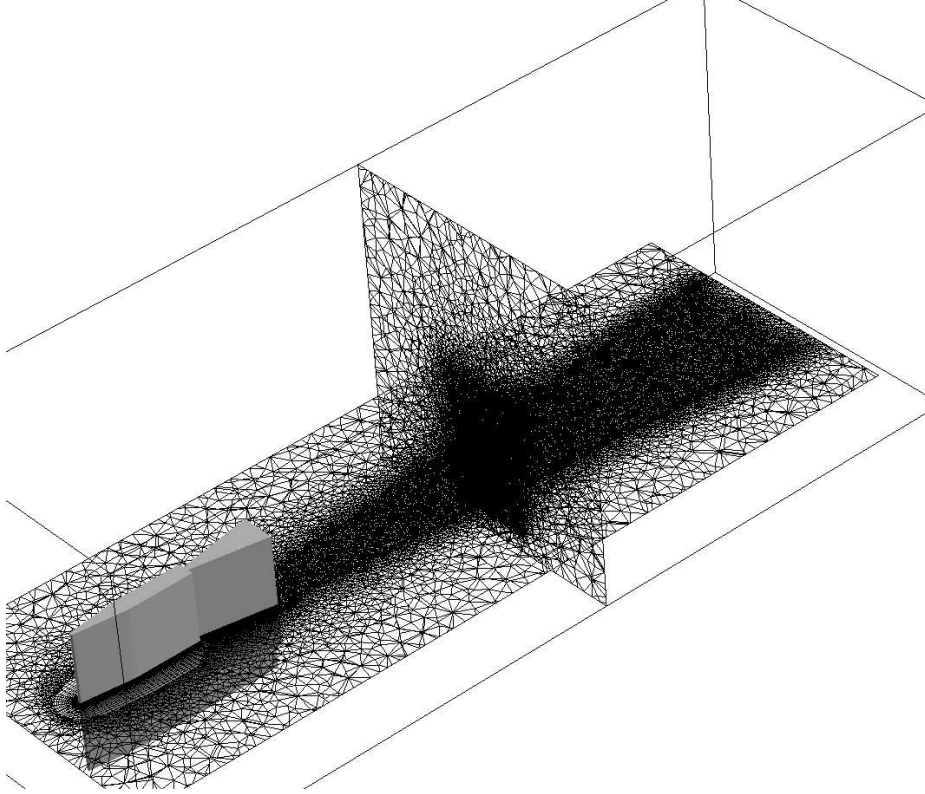


Fig. 4.1 CFD internal grid.

Table 4.2 Flow conditions for CFD simulation.

Property/Condition	Tunnel Airflow	Pylon Inj (Ethylene)
Momentum Flux Ratio	–	1.0
Mass Flux Ratio	–	1.65
Ratio of Specific Heats	1.4	1.25
Molecular Weight	28.97	28.05
Mach Number	2.0	1.0
Velocity	518 m/s	314 m/s
Mass Flow	10.78 kg/s	0.04 kg/s
Total Temperature	300 K	300 K
Static Temperature	167 K	267 K
Total Pressure	310 KPa	320 KPa
Static Pressure	39.7 KPa	178 KPa
Flow Area	25,161 mm^2	57 mm^2

Solution convergence was determined three ways for a steady state solution through 1) stability of the drag on the pylon, 2) reduction of the mass, velocity, and energy residuals at least three orders of magnitude (reasonable for engineering analysis) from the original values, and 3) constant spatially integrated total mass flow and ethylene mass flow downstream of the pylon configurations. The ramp and the alternating wedge pylons have roughly steady wake flowfields and met all three criteria through extended iterations of localized time-stepping. The basic pylon exhibited a highly unsteady flow, and did not meet the mass flow requirement using localized time-stepping, so a time accurate solution was obtained for the basic pylon.

Testing. It was not possible to initialize the entire grid to Mach number 2.0 conditions, with ethylene injection from the pylon at Mach number 1.0, using second-order fluxes, and obtain a convergent solution directly. The simulation very quickly diverged. To achieve reasonable results, a methodical process was necessary. The first step was to accomplish a first-order, single species solution of Mach number 2.0 airflow around the pylon without ethylene injection. To accomplish this the entire interior flow was initialized to a subsonic velocity. An axial flow velocity of 100 m/s was chosen to initialize the flow. A steady state solution was then allowed to progress. The inlet/outlet boundary conditions, defined as the test condition, Mach number 2.0, gradually drove the entire flow to the the correct test condition in a slow/stable manner. Once a first-order solution was obtained (5000 iterations), the spatial fluxes were changed to second-order, and the solution continued (10000 more iterations).

Once a second-order solution was obtained with a single species and no injection, ethylene injection from the pylon was added. The multi-species mixture air/ethylene option in the FLUENT® materials menu was selected, and the fuel port boundary conditions were assigned the proper mass flow values. Adding Mach number 1.0 ethylene injection from the pylon to the second-order Mach number 2.0 wind tunnel airflow solution caused the solution to diverge again. To alleviate the instability in the solution, a pressure boundary condition at the fuel ports was defined with no

ethylene mass flow. This is a non-physical situation, where the static pressure is elevated to the static pressure present if there were mass flow from the fuel ports, but no mass flow actually present. The solution was allowed to progress a couple hundred iterations with the pressure boundary condition on the fuel ports, then the ethylene mass flow was started at the proper flow rate (10000 more iterations). The solution did not diverge. By imposing the pressure boundary condition with no mass flow initially, the solution adjusted to the elevated boundary pressure before ethylene mass flow commenced.

The ramp and alternating wedge pylon solutions converged using steady state time stepping (25000 total iterations). The basic pylon solution did not. The basic pylon exhibited highly unsteady flow in the form of vortex shedding, which was later verified through wind tunnel experiment. Localized time stepping resulted in reduced residuals about three orders of magnitude from original values, and a steady drag on the pylon, but the total mass flow downstream of the pylon was not constant. The total mass flow decreased and the ethylene mass flow increased in magnitude in the downstream direction. This is a violation of mass conservation.

A time accurate solution was thus necessary for the basic pylon. An estimate of the vortex shedding frequency was made in order to calculate a time step required to resolve the unsteadiness in the wake flow. A Strouhal number, St , of 0.25 was assumed as a typical non-dimensional shedding frequency downstream of bluff bodies in high Reynolds number flows. [77] For a flow velocity of 518 m/s and a width of the pylon base of 0.018 m , the estimated vortex shedding frequency was about 7200 Hz (Eq. 4.2).

$$St = \frac{fd}{V} \quad (4.2)$$

A time step of one microsecond was selected to resolve the shedding frequency. This time step results in about 140 iterations per one vortex shedding period. Mon-

itoring the Mach number of three points in the wake region of the pylon, the flow solution was advanced in time until a consistent periodic pattern emerged. Figure 4.2 shows the Mach number over time at one of the three points. The other three points displayed the same behavior. The periodic frequency observed at all three points was approximately 6900 Hz ($St = 0.24$).

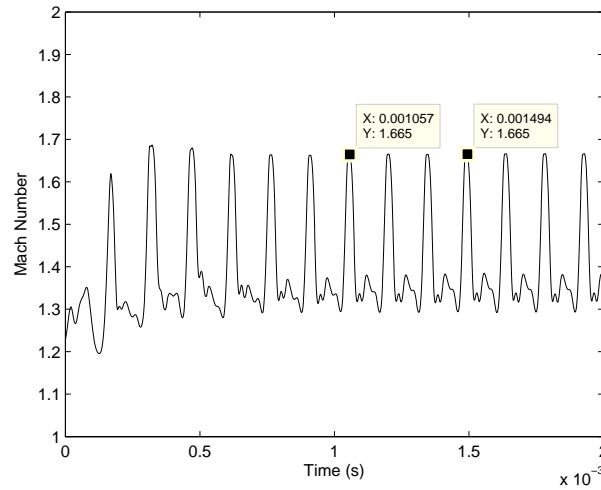


Fig. 4.2 Mach number at point in wake region over time.

The solution snapshot at the final time step was kept as an instantaneous solution. The solution was advanced one half period further, and that solution snapshot also kept as instantaneous solution. Data was collected at fourteen downstream planes in both instantaneous snapshots, one half period separated, and the integrated quantities from each snapshot averaged. As it turns out, all the integrated quantities are virtually identical in the two time snapshots.

The ramp and alternating wedge pylon solutions both exhibited a constant mass flow in their wake region and met the steady drag and residual reductions required for steady state solution convergence using localized time stepping. This is not to say the flow downstream of these pylons is perfectly steady, just steady enough to satisfy the convergence criteria selected for the simulations. It appears the streamwise vortex

production of the ramp and alternating wedge pylons promotes a more steady flow in the wake region since vortex shedding is not present in these CFD solutions. This is supported by experimental wind tunnel data presented later.

The mass flow in the wake region of the three pylons is compared in Fig. 4.3. For the two steady solutions, the total mass flow and ethylene mass flow are constant in the wake region. For the basic pylon time accurate solution, the total mass flow and ethylene mass flow in the wake region vary slightly, but do not, on average, increase or decrease in deviation from the mean with downstream distance. The downstream distribution of basic pylon mass flows oscillate around the correct values of 10.82 kg/s and 0.04 kg/s respectively.

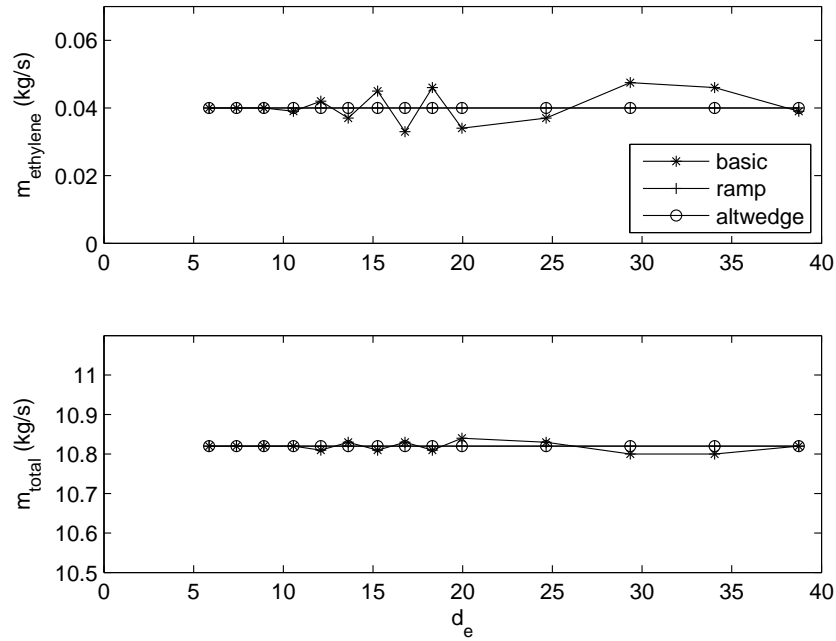


Fig. 4.3 Mass flow comparison.

Data Reduction. The axial distance downstream of the injection slots is normalized by the equivalent diameter, d_e , the diameter of a circle of equivalent geometric slot area (57 mm^2), 8.52 mm . The dense cell wake region extends $34 d_e$ downstream of the pylon base plane (aft rear face). The base plane of each pylon

is 40 mm ($4.7 d_e$) aft of the injection slots. Figure 4.4 shows fourteen downstream positions selected for reduction of four parameters: streamwise vortex magnitude, total pressure loss, mixing effectiveness (plume dilution), and flammable plume extent. These fourteen positions correspond to $5.9 d_e$, $7.4 d_e$, $8.9 d_e$, $10.6 d_e$, $12.1 d_e$, $13.6 d_e$, $15.3 d_e$, $16.8 d_e$, $18.3 d_e$, $20 d_e$, $24.7 d_e$, $29.4 d_e$, $34 d_e$, and $38.7 d_e$ aft of the injection slots.

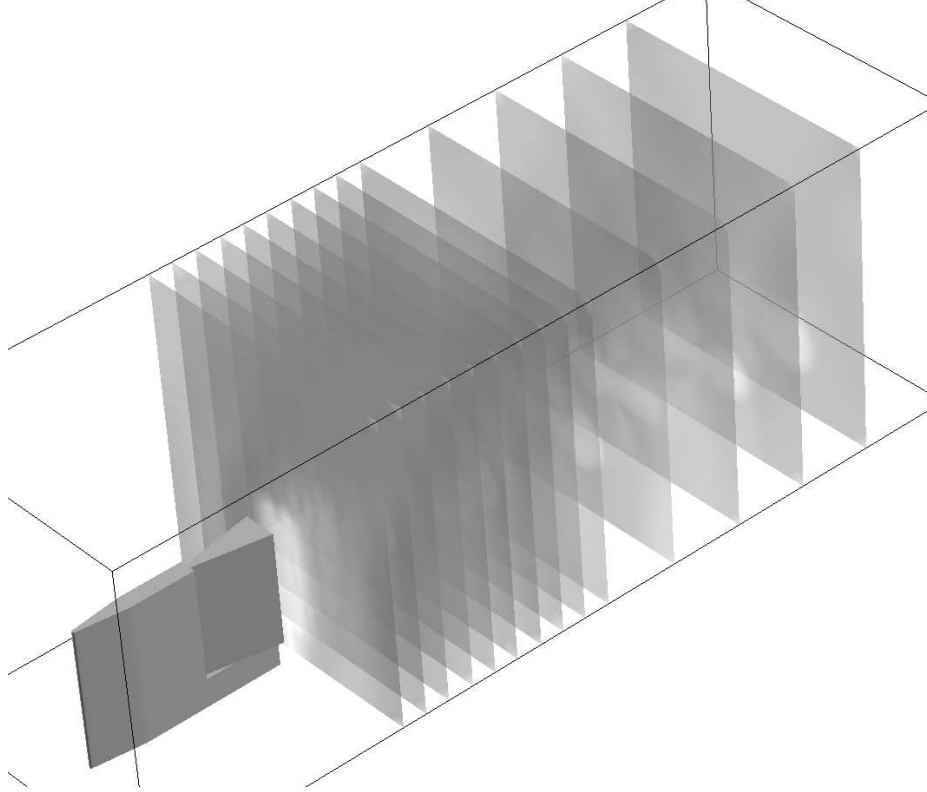


Fig. 4.4 Data reduction planes.

Streamwise vortex magnitude, ω_x (Eq. 4.3), is defined as the axial, or x-component, of the curl of the velocity vector. The mass averaged integral of the absolute value of axial vortex component is the measure of streamwise vortex magnitude, Ω_x (Eq. 4.4). Relative magnitudes were computed, normalized by the maximum vortex magnitude value present in the data globally at any planar position.

$$|\omega_x| = \left| \left(\nabla \times \vec{V} \right)_x \right| \quad (4.3)$$

$$\Omega_x = \frac{\int |\omega_x| \rho u dA}{\int \rho u dA} \quad (4.4)$$

Total pressure loss, Λ (Eq. 4.6), was calculated from the mass averaged integral of total pressure (Eq. 4.5). The mass averaged integral, divided by the wind tunnel total pressure and subtracted from unity, is the measure total pressure loss (Eq. 4.6).

$$\bar{P}_T = \frac{\int P_T \rho u dA}{\int \rho u dA} \quad (4.5)$$

$$\Lambda = 1 - \frac{\bar{P}_T}{P_{T_{\text{tunnel}}}} \quad (4.6)$$

Mixing efficiency, η_m (Eq. 4.7), is a measure of fuel dilution into the airstream at a planar position previously defined in other research. [40, 78] The local (point) mass fractions, α (Eq. 4.9), are obtained directly from simulation results. The stoichiometric mass fraction for a fuel/air mixture is calculated from Eq. 4.10 (f_s is the stoichiometric fuel/air mass ratio and ϕ is the equivalence ratio). For ethylene ($f_s = 0.068$), the mass fraction in air at stoichiometric conditions ($\phi = 1$) is $\alpha_s = 0.064$. The mixing efficiency calculation assumes the least available reactant, fuel or air, is the reactant considered for mixing. The other reactant is considered completely mixed already. For instance, in a globally fuel-lean situation (which is the case here), the fuel is the mixing concern, so the air is considered completely mixed.

$$\eta_m = \frac{\dot{m}_{\text{fuel,mixed}}}{\dot{m}_{\text{fuel,total}}} = \frac{\int_{A_{\alpha=0}} \alpha_R \rho u dA}{\int_{A_{\alpha=0}} \alpha \rho u dA} \quad (4.7)$$

$$\alpha_R = \begin{cases} \alpha, & \alpha \leq \alpha_s \\ \alpha_s(1 - \alpha)/(1 - \alpha_s), & \alpha > \alpha_s \end{cases} \quad (4.8)$$

$$\alpha = \frac{\text{mass of fuel}}{\text{mass of fuel} + \text{mass of air}} = \frac{f}{f + 1} \quad (4.9)$$

$$\alpha = \frac{\phi f_s}{\phi f_s + 1} \quad (4.10)$$

A local mixing quantity, α_R , defined by Eq. 4.8, is evaluated at a point location from the local fuel mass fraction. At each point location, if the local fuel mass fraction is less than or equal to the mass fraction required for stoichiometric combustion, the fuel is fully mixed there ($\alpha_R = \alpha$). If the local fuel mass fraction is greater than the stoichiometric mass fraction, the fuel is unmixed to some degree at that location, and α_R is reduced by a weighting function ($\alpha_R < \alpha$). The local mixing quantities are multiplied by the density and velocity at the point locations and integrated over the fuel plume area in Eq. 4.7 to determine the mixing efficiency at a planar position, η_m . The area of integration extends to the edges of the fuel plume where the fuel mass fraction drops to zero, or to some minimum detectable mass fraction, say $\alpha \geq 0.001$. If the fuel plume is completely mixed at a planar location, the integrated mixing efficiency is one ($\eta_m = 1.0$). If the fuel plume is completely unmixed at a planar location, the integrated mixing efficiency is zero ($\eta_m = 0$).

The maximum fuel mass fraction is another measure of fuel dilution into the airstream. The amount of fuel mixing occurring at a planar position downstream is represented by the maximum fuel mass fraction in the plume at a planar position. In other experimental data where density and velocity information are not available, the maximum fuel mass fraction measure is an alternative measure to the complex mixing efficiency calculation. The maximum fuel mass fraction decreases in the downstream direction as the fuel is diluted into the airstream. A smaller maximum fuel mass fraction indicates a more mixed (more diluted) fuel plume. The maximum fuel mass fraction is calculated by averaging the top 1% of local fuel mass fraction values at a planar position. Averaging the top 1% of values rather than just taking the top value is to guard against a single data outlier.

Fuel dilution into the airstream does not complete the fuel/air mixing picture, however. Mass fractions below stoichiometric, considered perfectly mixed, include those below the threshold for combustion. In addition, flammable mixtures exist above stoichiometric. The mixing efficiency and maximum fuel mass fraction measures do not take either of these flammability limits into account. The combustion potential of the mixture is not represented well by either measure. For a combustible mixture measure, one must evaluate the flammable plume extent.

Figure 4.5 shows a generic fuel plume cartoon. The shape (circular) is notional, and not realistic. The flammable plume extent is observed in two quantities (Eqs. 4.11 and 4.12). First, FP_a , is the fuel plume area, A_p , with fuel mass fractions falling within the flammable limits, A_f . This quantity is normalized by the effective fuel injector area, A_e . Second, FP_f , is the fraction of the fuel plume, A_p , falling within the flammable limits, A_f . The first quantity compares the overall flammable plume area among pylons. The second quantity determines the planar position where the fuel plume exhibits the largest fraction of flammable area.

The flammability equivalence ratio limits for ethylene are $0.41 \leq \phi \leq 5.5$. [72] Consequently, from Eq. 4.10, the range of flammable mass fractions of ethylene fuel in air is $0.027 \leq \alpha \leq 0.272$. The effective fuel injector area, A_e , is $5.7E-5 \text{ m}^2$ for CFD simulations, and the fuel plume area, A_p , is the area of plume with fuel mass fractions greater than 0.001.

$$FP_a = \frac{A_f}{A_e} \quad (4.11)$$

$$FP_f = \frac{A_f}{A_p} \quad (4.12)$$

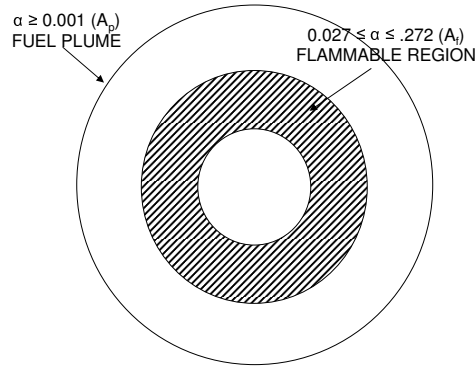


Fig. 4.5 Fuel plume cartoon.

Both the FLUENT[®] post-processing package and another post-processing package called FIELDVIEW[®] were used. FLUENT[®] has an option to output the entire flow solution into an unstructured data file that is read into FIELDVIEW[®]. During data reduction, the vortex magnitude and pressure loss calculations were accomplished within FLUENT[®]; and the mixing efficiency, maximum fuel mass fraction, and flammable plume calculations were accomplished in FIELDVIEW[®]. Three dimensional flow visualization pictures were also generated in FIELDVIEW[®].

Wind Tunnel

The AFRL supersonic wind tunnel in test cell 19 was used for aerothermal probing, Raman spectroscopy, and NO-PLIF imaging. [79] The wind tunnel is continuous running and produced the following stable conditions for these experiments: Mach number 1.95 and 241 *KPa* (35 *lb/in*²) total pressure. The total temperature of the wind tunnel varied from 260 *K* - 290 *K* throughout testing. The total temperature variation during a single test run was no more than 5° *C*. The test section of the tunnel measures 132.1 *mm* (5.2 *in*) high and 152.4 *mm* (6 *in*) wide. The length of the test section is approximately 1.0 *m*. Static pressure taps are embedded in the walls at the upstream end of test section. Total pressure and total temperature of the wind tunnel flow are obtained from the stagnation tank upstream of the test section.

Optical windows (fused silica) were available for the test section walls during laser experiments, and metal walls were available for probe experiments. Below the test section is a three axis movable table. The design of the manufactured pylons for wind tunnel testing is shown in Appendix A along with the mounting plug for the wind tunnel floor.



Fig. 4.6 Fairchild® model 10264 precision regulator.

Figure 4.6 shows the precision regulator with attached pressure transducer and thermocouple connected to the bottom of the alternating wedge pylon pedestal. Injection gas for the pylon was supplied by high pressure bottles stored outside the facility. The high pressure gas was fed into a dome regulator that maintained the pressure entering the wind tunnel room at approximately 1.4 MPa (200 lb/in^2). A Fairchild® model 10264 precision regulator reduced the pressure to the pylon total injection pressures required. Total temperature and total pressure of the pylon injection gas were measured at the output end of the precision regulator just prior to entering the pylon plenum by the transducer and thermocouple.

Aerothermal Probing

Aerothermal probing is an intrusive technique used to gather pressure and temperature measurements in the wind tunnel flow. From these measurements other basic flow properties can be deduced (Mach number, velocity, and density). The probing apparatus used to collect the data is located at AFRL, and has been successfully implemented in other research. [40, 65, 80] Past efforts using the probing apparatus gathered flow property data on wall transverse or angled injector ports and cavity flow. In current research the probe apparatus was implemented the same as before, measuring flow properties in the wake region of each pylon configuration.

Three probes (thermocouple, cone static, and pitot) were used to measure total temperature, static pressure, and total pressure respectively in the wake region of the pylons at specific point locations. Three separate runs were required to obtain data with the three probes at the same locations. The cone static probe has a 10° half angle cone tip with four small pressure ports at 90° intervals around the cone. The pitot probe tip outer and inner diameter is 3.175 mm (0.125 in) and 1.588 mm (0.0625 in) respectively. The thermocouple probe has the same outer and inner diameter as the pitot probe. The thermocouple probe tip is made of a ceramic material with two small holes in the side at 180° intervals for aspiration. The type-K thermocouple is a small bead just inside the ceramic tip shroud. Figure 4.7 shows the probes used in experiments.

In addition to determining basic flow properties, the probing apparatus was also used to measure the mixing effectiveness of each pylon configuration. This was the first time a mixing measure had been attempted with the probing apparatus in the AFRL wind tunnel. The additional equipment required was a flow heater to heat the pylon injection air to a higher total temperature than the wind tunnel air. A mixing analogy was attempted, using total temperature measurements to evaluate the mixed state of the pylon injection air in the wind tunnel airflow.

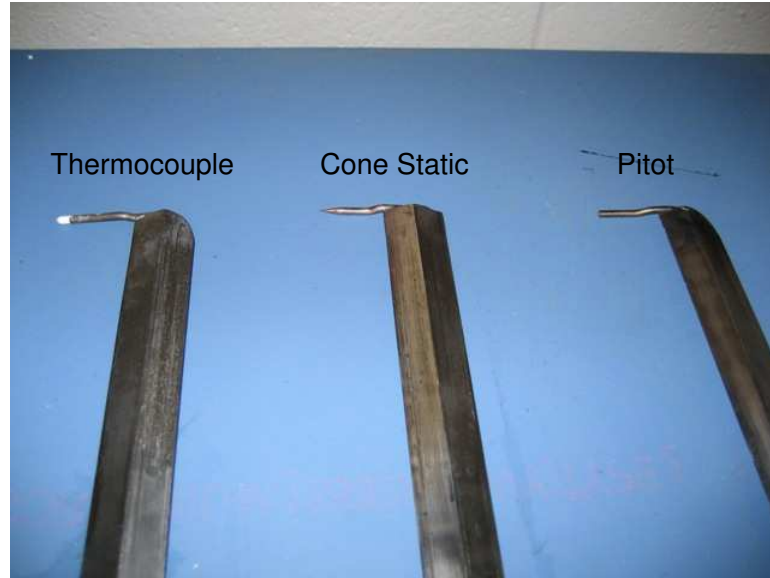


Fig. 4.7 Aerothermal probes.

Experimental Setup. The wind tunnel test section was configured with one metal sidewall and one window sidewall for the aerothermal probing experiments. The metal sidewall incorporated a slide that traversed in the vertical direction, driven by the three axis moveable table. This allowed for vertical probe movement inside the test section. Horizontal movement of the probe was accomplished using a worm gear drive affixed to the movable table. The worm gear traverser and movable table worked together to position the probes in the test section and produce two dimensional grids of data at desired spatial resolution. Figure 4.8 shows the pitot probe setup inside the test section behind the ramp pylon. Figure 4.9 shows the worm gear traverser.

For mixing analogy experiments a heater was required to heat the pylon injection air total temperature to approximately 60°C above the wind tunnel total temperature. The heater used was a Watlow[®] 4.5 kilowatt circulator heater. The 1.4 MPa air entering the wind tunnel room was connected to the circulation heater, and the output from the heater was connected to the precision regulator. The precision regulator had a limitation of 366 K on the air temperature flowing through it due to the diaphragm material inside the regulator. From this limitation and the need to keep the air injection temperature constant throughout the experiment, the circulation heater had

a closed loop control system attached to it. A thermocouple sampled the output from the heater. The signal from the thermocouple was fed to a power controller to regulate the duty cycle of the elements inside the heater, maintaining the desired temperature. Figure 4.10 shows the circulation heater with power controller system connected.

A set of nominal flow conditions were expected for the aerothermal probe experiments. These are shown in Table 4.3. These nominal conditions are based on a momentum flux ratio equal to one between the pylon injection air and the wind tunnel air. The mass flux ratio change between cold and heated air is due to the total temperature difference. There is about 10% less mass flow in the heated case.

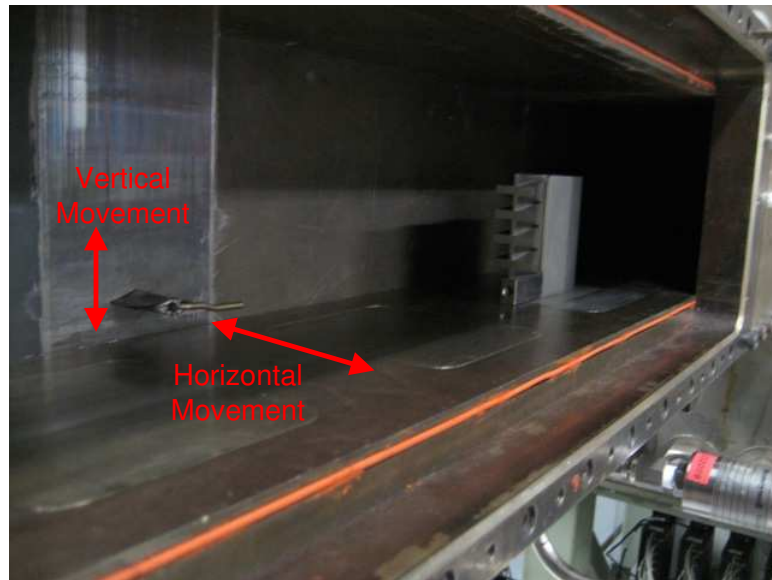


Fig. 4.8 Pitot probe inside test section.

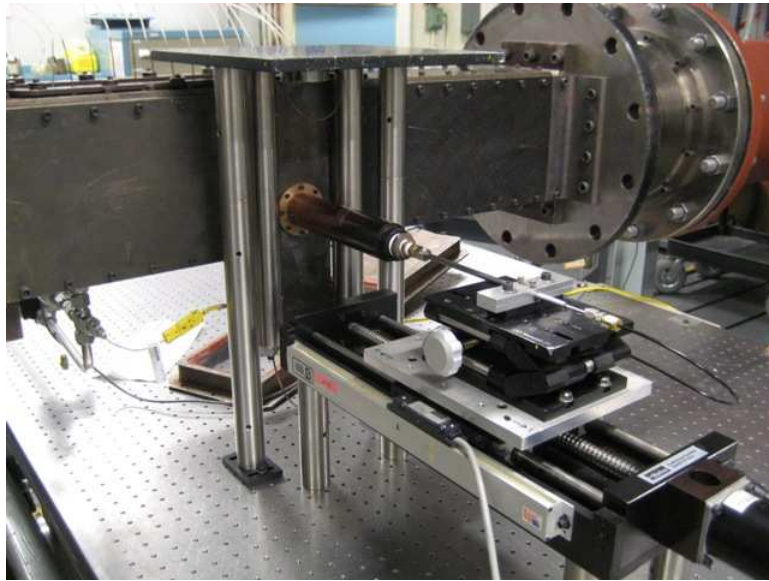


Fig. 4.9 Probe attached to worm gear traverser.

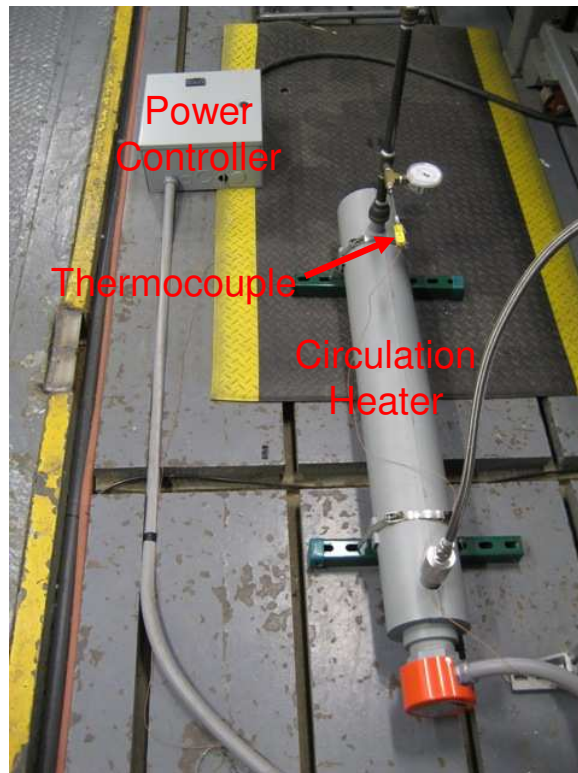


Fig. 4.10 Watlow® 4.5 kilowatt circulation heater.

Table 4.3 Nominal flow conditions for aerothermal probe experiments.

Property/Condition	Tunnel Airflow	Pylon Inj (Cold)	Pylon Inj (Heated)
Momentum Flux Ratio	–	1.0	1.0
Mass Flux Ratio	–	1.61	1.46
Mach Number	1.95	1.0	1.0
Velocity	501 <i>m/s</i>	311 <i>m/s</i>	343 <i>m/s</i>
Mass Flow	7.14 <i>kg/s</i>	0.031 <i>kg/s</i>	0.028 <i>kg/s</i>
Total Temperature	288 <i>K</i>	288 <i>K</i>	350 <i>K</i>
Static Temperature	164 <i>K</i>	240 <i>K</i>	292 <i>K</i>
Total Pressure	241 <i>KPa</i>	240 <i>KPa</i>	240 <i>KPa</i>
Static Pressure	33.3 <i>KPa</i>	127 <i>KPa</i>	127 <i>KPa</i>
Flow Area	20,129 <i>mm</i> ²	53.7 <i>mm</i> ²	53.7 <i>mm</i> ²

Testing. A total of 9 cold air pylon injection experiments and 3 heated air pylon injection experiments were accomplished to gather data with the three aerothermal probes in the wake region of the three pylons at $23.9 d_e$. The general procedure was: 1) start the pylon injection flow (cold or heated), 2) adjust the injection flow with the precision regulator, 3) start the wind tunnel, 4) wait for the wind tunnel total pressure to stabilize, and 5) start the traversing probe. The probe would move to each location, collect data for a period of time, then move to the next location. The data for each location was the average over the acquisition time. The data acquisition time for a single measurement was 0.5 *s* for the pressure probes and 1.0 *s* for the thermocouple probe.

A two dimensional grid of data was constructed at the same array of locations with each probe. Figure 4.11 shows a cartoon of the probing area planar position. Figure 4.12 shows the array of 189 points collected at each planar position.

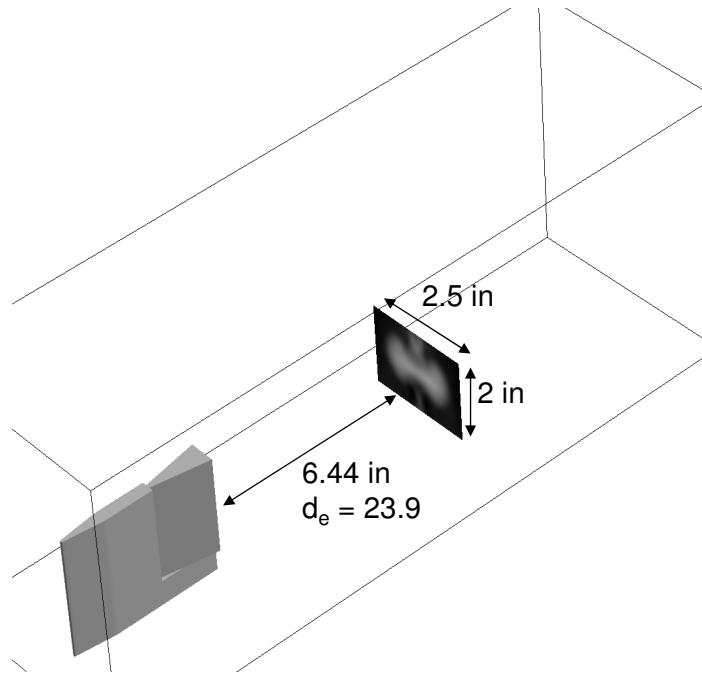


Fig. 4.11 Probing area.

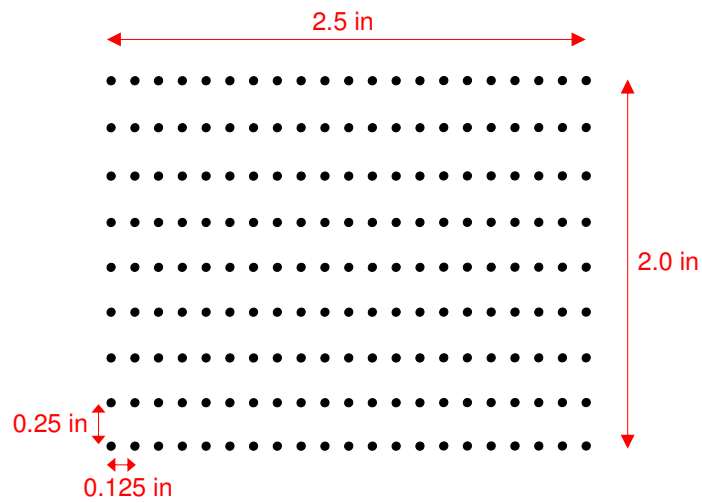


Fig. 4.12 Array of probing locations.

Wind tunnel conditions varied slightly throughout the data runs due mostly to rising total temperature in the wind tunnel. It took about 1 hour of operation for the

wind tunnel to reach and maintain a steady total temperature. The experiments were conducted during the winter. The compressors driving the tunnel take in ambient outside air, compress it, and deliver it to the wind tunnel. During the initial hour of operation, the total temperature of the wind tunnel increased about $1^\circ C$ every 2 minutes. Most probe experimental runs took about 10 minutes, so the wind tunnel mass flow during a test run varied slightly. The wind tunnel total pressure was kept very steady throughout the experiments using the wind tunnel pressure controller.

The total temperature and total pressure of the pylon injection air also varied slightly. The source of the injection air, high pressure bottles outside the facility, decreased in total temperature as they were depleted. The total pressure of the injection air varied due to total temperature variations affecting the precision pressure regulator feeding the pylon plenum.

All these real-world effects caused the experimental wind tunnel and pylon injection conditions to differ slightly from the nominal conditions set forth in the experimental setup. The actual flow condition averages and variations are shown in Table 4.4. The percent variations are the third standard deviations from the means.

Table 4.4 Actual flow conditions for aerothermal probe experiments.

Property/Condition	Tunnel Airflow	Pylon Inj (Cold)	Pylon Inj (Heated)
Momentum Flux Ratio	–	$0.98 \pm 5\%$	$1.0 \pm 1\%$
Mass Flux Ratio	–	$1.58 \pm 6\%$	$1.48 \pm 2\%$
Mass Flow	$7.13 \text{ kg/s} \pm 4\%$	$0.030 \text{ kg/s} \pm 5\%$	$0.028 \text{ kg/s} \pm 1\%$

Data Reduction.

Flow Properties. A methodology to reduced the three probe aerothermal data in a supersonic flow is presented. The probing planar position, $23.9 d_e$, was far enough downstream of the pylon so the flow was supersonic. A normal shock wave is present in front of the pitot and thermocouple probes, and an oblique shock wave is present at the tip of the cone static probe. These shock waves alter the pressure

and temperature fields around the pitot and cone static probes. Assuming an adiabatic process, the thermocouple probe total temperature does not change through the normal shock. However, the total pressure does decrease through the normal shock. The Rayleigh Pitot equation is used to account for the total pressure loss through the normal shock. It is shown in Eq. 4.13. P_{t2} is the total pressure downstream of the normal shock. P_1 is the static pressure upstream of the normal shock. M_1 is the Mach number upstream of the normal shock.

$$\frac{P_{t2}}{P_1} = \left[\frac{(\gamma + 1)M_1^2}{2} \right]^{\frac{\gamma}{\gamma-1}} \left[\frac{\gamma + 1}{2\gamma M_1^2 - (\gamma - 1)} \right]^{\frac{1}{\gamma-1}} \quad (4.13)$$

Along with the Rayleigh Pitot equation, the surrounding flowfield solution for a cone in supersonic flow is required. The surface pressure of a symmetric cone with a given half angle in supersonic flow is obtained from data tables produced using an exact numerical solution. [81] A second order polynomial curve is fit to the surface pressure and flow static pressure ratio data of a 10° half angle cone in a supersonic freestream between Mach numbers 1.116 - 5.0 (Eq. 4.14). P_s is the cone surface pressure. P_1 is the static pressure upstream of the oblique shock. The maximum surface pressure error due to the polynomial curve fit is less than 1% within the Mach number range.

$$\frac{P_s}{P_1} = 0.0425M_1^2 + 0.0405M_1 + 1.0443 \quad (4.14)$$

A suitable ratio of specific heats, γ , is needed to accomplish the probe data reduction calculations. The flow of interest is a Mach number 2.0 wind tunnel airflow with a Mach number 1.0 airflow injected into the pylon wake region. The air temperatures range between 150 K - 350 K. The specific heat ratio of air, γ , varies little within this range ($1.396 < \gamma < 1.400$) [8], and is to a good approximation an ideal gas with $\gamma = 1.4$. This simplification would not be valid if the experiment was done using elevated temperature air, or a gas other than air was injected from the pylon.

The derived expression relating the local Mach number to the pressure measurements from the pitot and cone static probes is shown in Eq. 4.15. An iterative process is required to solve for the local Mach number.

$$\frac{P_{t2}}{P_s} = \frac{[1.2M_1^2]^{3.5} \left[\frac{6}{7M_1^2-1} \right]^{2.5}}{0.0425M_1^2 + 0.0405M_1 + 1.0443} \quad (4.15)$$

Once the local Mach number is found, Eq. 4.14 is used to calculate the local static pressure. With the local static pressure and Mach number, Eq. 4.16 is used to obtain the local total pressure. To calculate velocity and density, static temperature is needed. The total temperature obtained from thermocouple data is used in conjunction with the energy equation and local Mach number to calculate static temperature in Eq. 4.17. T_{t1} is the total temperature from the thermocouple probe and T_1 is the static temperature upstream of the normal shock. R is the gas constant for air. The velocity and density are calculated from Eq. 4.18 and Eq. 4.19 assuming ideal gas. Density, velocity, and total pressure are used to calculate total pressure loss. An automated code developed by Fuller [40] was spot checked for accuracy using a spreadsheet incorporating this probe data reduction methodology, and then used to reduce the wind tunnel probe data.

$$\frac{P_{t1}}{P_1} = \left[1 + \frac{\gamma-1}{2} M_1^2 \right]^{\frac{\gamma}{\gamma-1}} \quad (4.16)$$

$$\frac{T_{t1}}{T_1} = 1 + \frac{\gamma-1}{2} M_1^2 \quad (4.17)$$

$$V_1 = M_1 \sqrt{\gamma R T_1} \quad (4.18)$$

$$\rho_1 = \frac{P_1}{R T_1} \quad (4.19)$$

Mixing Analogy. The mixing analogy is a method to calculate mass fractions of pylon injected air in wind tunnel airflow using local total temperature measurements. [41,82–86] Heated air is injected from the pylons, and total temperature distribution measurements are used as an analogy to concentration measurements of a similar gas (ethylene) injected into a wind tunnel airflow. Ethylene and air have very similar molecular weights and specific heat ratios. The two gases should therefore have similar mixing characteristics. Species and energy equations reveal similar transport mechanisms for mass and energy. The theory supporting this approach is as follows.

The species continuity equation in 1-D is Eq. 4.20. The energy equation in 1-D is Eq. 4.22.

$$\frac{\partial \rho_i}{\partial t} + \frac{\partial}{\partial x} (\rho_i u) = \frac{\partial}{\partial x} \left(D_i \frac{\partial \rho_i}{\partial x} \right) \quad (4.20)$$

$$\rho_i = \rho Y_i \quad (4.21)$$

$$\frac{\partial e_t}{\partial t} + \frac{\partial}{\partial x} (e_t u) = -\frac{\partial P}{\partial x} + \frac{\partial}{\partial x} (\tau_{xx} u) - \frac{\partial q_x}{\partial x} \quad (4.22)$$

$$h_t = e_t + P \quad q_x = -k \frac{\partial T}{\partial x} - C_p T D \frac{\partial \rho}{\partial x} \quad (4.23)$$

$$h_t = \rho C_p T + \frac{\rho u^2}{2} \quad \tau_{xx} = \frac{4\mu}{3} \frac{\partial u}{\partial x} \quad (4.24)$$

The 1-D energy equation is written in terms of total enthalpy (Eq. 4.25) and compared with the 1-D species equation (Eq. 4.28) written in a slightly different form.

$$\frac{Dh_t}{Dt} + h_t \frac{\partial u}{\partial x} = \frac{\partial}{\partial x} \left(a \frac{\partial h_t}{\partial x} \right) \quad (4.25)$$

$$+ \frac{\partial P}{\partial t} + \frac{\partial}{\partial x} \left(\frac{4\mu}{3} u \frac{\partial u}{\partial x} \right) - \frac{\partial}{\partial x} \left(\frac{au^2}{2} \frac{\partial \rho}{\partial x} + \frac{a\rho}{2} \frac{\partial (u^2)}{\partial x} \right)$$

$$h_t = \rho C_p T_t \quad (4.26)$$

$$a = \frac{k}{C_p \rho} \quad (4.27)$$

$$\frac{D\rho_i}{Dt} + \rho_i \frac{\partial u}{\partial x} = \frac{\partial}{\partial x} \left(D_i \frac{\partial \rho_i}{\partial x} \right) \quad (4.28)$$

$$Le = \frac{a}{D_i} \quad (4.29)$$

Assuming a Lewis number (Eq. 4.29) of unity, equating the thermal diffusion coefficient to the mass diffusion coefficient, the species and energy equations are similar. If the right side of both equations was zero, assuming convection was the only phenomenon in the flow, the equations would be identical. The flow would convect total enthalpy and species identically.

There are several terms on the right hand side of the energy equation that have no equivalent in the species equation. These terms are additional enthalpy transport terms due to pressure fluctuations, viscous work, and energy diffusion not associated with temperature gradients. These terms result in mass and energy transport not being identical, and therefore the mixing analogy is only an estimation of the species transport process. However, the analogy should yield some useful information about the dispersion shape and concentration of the pylon injectant in the wind tunnel airflow.

To use the mixing analogy in experiment, two sets of probe measurements are taken at a planar position. One measurement is with cold pylon injection air, where

the primary flow and injectant flow have the same total temperature. Another measurement is with heated pylon injection air, where the injector flow total temperature is raised by about $60^\circ C$. By assuming an enthalpy distribution difference factor, β , at each location which is directly proportional to the total temperature measured at that location, the error of the additional energy transport terms in the energy equation is lessened to some degree. Essentially, the two measurements allow for the enthalpy transport mechanisms not associated with convection to be divided out of the calculation.

Equations 4.30 - 4.32 show the calculation of the mass fraction concentration value at a point location. α is the mass fraction of pylon air injectant in wind tunnel airflow. Subscript p represents the total temperature probe measurement, a represents the wind tunnel airflow total temperature, and j represents the pylon injectant total temperature. Sub-subscript c represents cold pylon airflow and h represents heated pylon airflow.

$$T_{p_c} = [(1 - \alpha)T_{a_c} + \alpha T_{j_c}] \beta \quad (4.30)$$

$$T_{p_h} = [(1 - \alpha)T_{a_h} + \alpha T_{j_h}] \beta \quad (4.31)$$

$$\alpha = \frac{T_{a_c} T_{p_h} - T_{a_h} T_{p_c}}{T_{j_h} T_{p_c} - T_{a_h} T_{p_c} + T_{a_c} T_{p_h} - T_{j_c} T_{p_h}} \quad (4.32)$$

The difference in pylon air injection total temperature between the two measurements leads to slightly different injection mass flows, an experimental error source. To keep the injectant mass flow between cold and heated conditions close (within 10%), the injectant air can only be heated about $60^\circ C$. This limits the resolution of the method. The type-K thermocouple used in experiments has a $1^\circ C$ accuracy, so the smallest mass fraction detectable and the resolution of the method is about $1/60 = 0.017$. The stoichiometric mass fraction for ethylene in air is 4 times larger than this

minimum resolution, so the combustible ethylene mass fraction range is resolvable. However, the resolution of the method is rather course.

Data Adequacy. Mach profiles, total pressure loss, and mass fraction profiles were constructed from the aerothermal probe data. A 50.8 mm (2 in) high x 63.5 mm (2.5 in) wide array of 189 points was arranged with a 6.35 mm (0.25 in) vertical spacing and 3.175 mm (0.125 in) horizontal spacing. The bottom of the array was 12.7 mm (0.5 in) above the wind tunnel floor, and the middle of the array was centered on the wind tunnel centerline. Local Mach numbers, pressures, densities, and velocities were calculated using the procedure outlined previously. Equation 4.6 was used to find the total pressure loss over the probing area. Equation 4.32 was used to find the pylon injection air mass fractions with thermocouple data from the cold and heated pylon injection experiments. MATLAB[®] was used to plot plume mass fraction profiles and accomplish data reduction calculations.

The momentum and mass flux ratio variations were small among test runs, so the total pressure data from the cold air injection experiments yielded adequate total pressure loss comparisons among the three pylons. The pressure loss calculations were straight forward. Integrating over the probing array locations was a simple matter of summing/averaging over 189 equally spaced data.

The adequacy of the mixing analogy data depended not only on variations in the momentum and mass flux ratios, but also on total temperature variations in the wind tunnel and pylon air injection. Total temperatures were used directly to determine the pylon air injection local mass fractions. The wind tunnel and pylon injection total temperature variations proved to be significant sources of error with respect to calculating the local mass fractions using the mixing analogy.

In addition, the probes were located at $23.9 d_e$, where the injected air was already very well mixed into the wind tunnel flow. The resolution of the mixing analogy is limited at the injectant concentration values. The data collected was not adequate to obtain plume mass fraction profiles to compare the pylon mixing

capabilities. However, the data collected did show promise of better results if the total temperature of the wind tunnel and pylon air injection could be held more steady during and between test runs. The method would also yield better results if probing in a higher injectant mass fraction environment closer to the pylon base plane.

In an ideal set of mixing analogy experiments: 1) the wind tunnel total temperatures during the cold and heated pylon injection experiments would be the same and constant, 2) the cold air pylon injection would be equal to the wind tunnel total temperature and constant, and 3) the heated air pylon injection temperature would be elevated over the wind tunnel temperature about $60^{\circ} C$ and constant. In experiments conducted: 1) the wind tunnel temperature varied between cold and heated pylon injection runs, 2) the cold air pylon injection temperature was close to the wind tunnel temperature, but varied about $5^{\circ} C$ during and between runs, and 3) the heated air pylon injection temperature was elevated to the correct level, but varied about $5^{\circ} C$ during and between runs. Figures 4.13, 4.14, and 4.15 show the time history of the total temperature in the cold and heated injector runs for each pylon.

The wind tunnel increasing total temperature the first hour of operation lead to the cold air runs having lower wind tunnel total temperatures than the heated air runs since they were conducted first. The cold and hot air wedge pylon injection runs exhibited the largest variation in wind tunnel total temperatures, and the ramp pylon runs exhibited the smallest variation. As a result, the calculated mass fraction plume profile for the wedge pylon was the least accurate, and the ramp pylon plume profile the most accurate (Fig. 5.17). Since mass fraction plume profiles were not constructed accurately using mixing analogy measurements, mixing effectiveness parameters in the form of plume dilution and plume flammability were not attainable from the plume profiles.

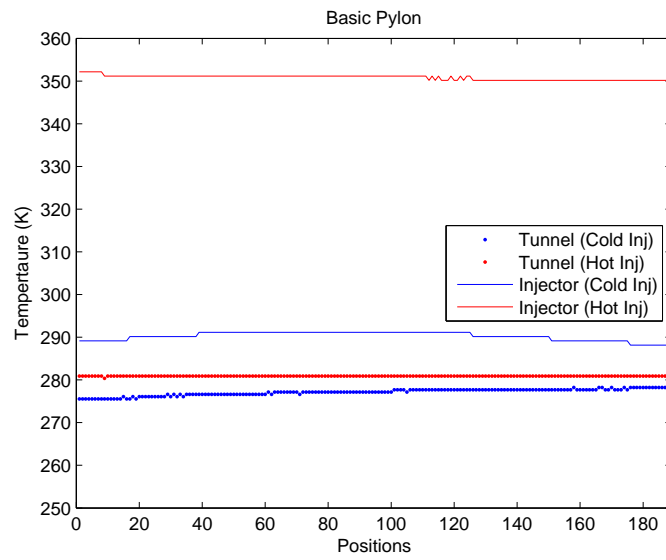


Fig. 4.13 Total temperature history (Basic).

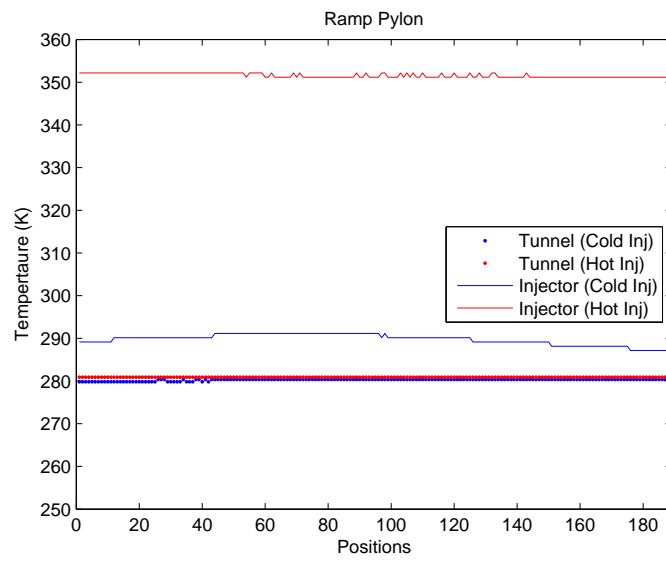


Fig. 4.14 Total temperature history (Ramp).

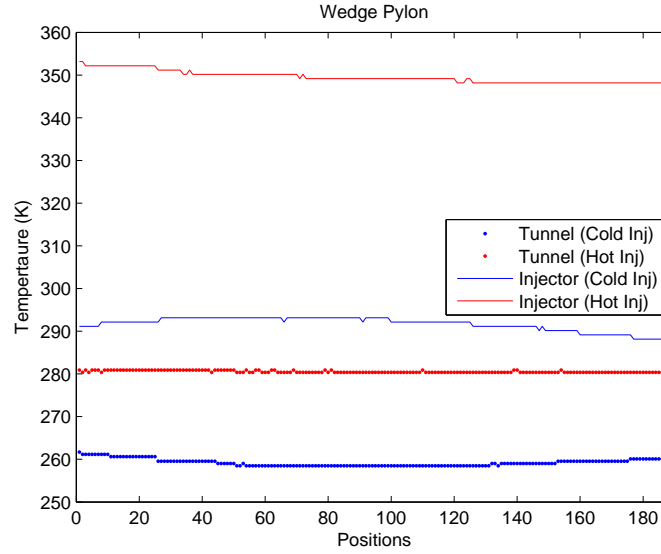


Fig. 4.15 Total temperature history (Wedge).

Raman Spectroscopy

Raman spectroscopy is a non-intrusive light interrogation technique using inelastic light scattering to sample concentrations of gases in the wind tunnel flow by detecting molecular species of interest. [87,88] The experimental apparatus used to collect the data is located at AFRL, and has been successfully implemented in other research. [65,80,89,90] Past efforts using the Raman apparatus have gathered ethylene concentration data in air downstream of wall transverse or angled injector ports. In current research methane concentration data in air was gathered downstream of an intrusive pylon with parallel injector ports. It was the first time the test apparatus had been used to detect Raman scattering from methane in air. The data reduction techniques used were the same as previous research, except methane properties were incorporated instead of ethylene.

A visible green laser beam was used as the light interrogation source. The interrogation light source could theoretically be any wavelength, as long as it was able to pass through the optical windows. Both elastic and inelastic collisions between the

visible laser beam and molecules result. Rayleigh scattering results from elastic collisions where no energy is absorbed by the molecule, and the molecule re-radiates the same laser frequency incident on it. Raman scattering results from inelastic collisions where energy is absorbed by rotational and vibrational modes of the molecule, and the molecule re-radiates a frequency shifted from the original laser frequency.

The frequency shift from Raman scattering could be an increase or decrease from the original depending on whether the molecule is in its ground ro-vibrational state or not, and in practice both occur. A decreased scattering frequency is called Stokes Raman scattering, and an increased scattering frequency is called Anti-Stokes Raman scattering. In general, the Rayleigh signal is much stronger than the Raman signal, and the Stokes Raman signal is stronger than the anti-Stokes Raman signal.

In non-resonant Raman scattering the ro-vibrational excitation of the molecule is small, generally no more than one vibrational level since the molecules are not being excited directly at their ro-vibrational natural frequencies. Ro-vibrational natural frequencies are generally in the infrared frequency range. [91,92] Assuming the molecule is in its ground state, the ro-vibrational energy imparted to the molecule decreases the energy of the scattered light, shifting the frequency down. This Stokes frequency shift for a given single level rotational, single level vibrational, or combined ro-vibrational excitation is depicted in Fig. 4.16. Pure rotational frequency shifts are smaller than ro-vibrational since rotational energy levels are much closer together. A single level rotational energy shift is generally in the far infrared, and a single level vibrational energy shift is generally in the near infrared. The Rayleigh scattering signal can easily overwhelm the pure rotational Raman scattering signal unless a sharp filter is used to isolate the laser frequency. The ro-vibrational frequency shift, centered around a natural vibrational frequency of the molecule, is larger, and is detected in experiments here.

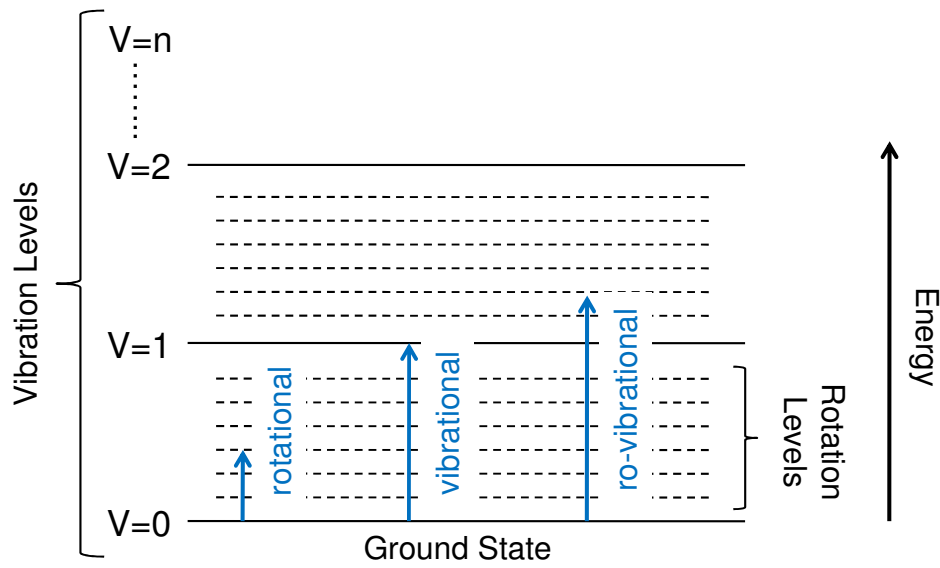


Fig. 4.16 Ro-vibrational molecular energy levels.

Since ro-vibrational natural frequencies of molecules differ, the Raman signal allows one to determine the molecular species present and number density of each species from the amount of frequency shift and scattering intensity respectively. The molecular species of interest are methane, CH_4 , nitrogen, N_2 , and Oxygen, O_2 . Methane has several Raman active vibrational modes, but the one of interest is at approximately 3.31 microns, a frequency of 90.5 THz . The light source used for interrogation is at 532 nm (green) or a frequency of 564 THz . The shifted Stokes Raman signal is therefore at 473.4 THz , or approximately 634 nm . Nitrogen and oxygen are also present in the wind tunnel airflow and are Raman active. Nitrogen has a primary natural vibrational frequency of 69.9 THz (4.29 microns) and oxygen has a primary natural vibrational frequency of 46.7 THz (6.43 microns). Their respective shifted Stokes Raman wavelengths are approximately 607 nm and 580 nm .

Experimental Setup. For Raman experiments the wind tunnel test section was configured with two window sidewalls and a window top wall for optical access into the test section. Top and side view diagrams of the Raman setup are shown in Fig. 4.17. The light source was a Coherent[®] Verdi laser, a 4.5 Watt continuous source

at 532 nm (green). The beam traversed through the test section at a single height above the floor and single planar position behind the pylon. The beam was focused to the center of the test section with a 1.0 m focal length lens.

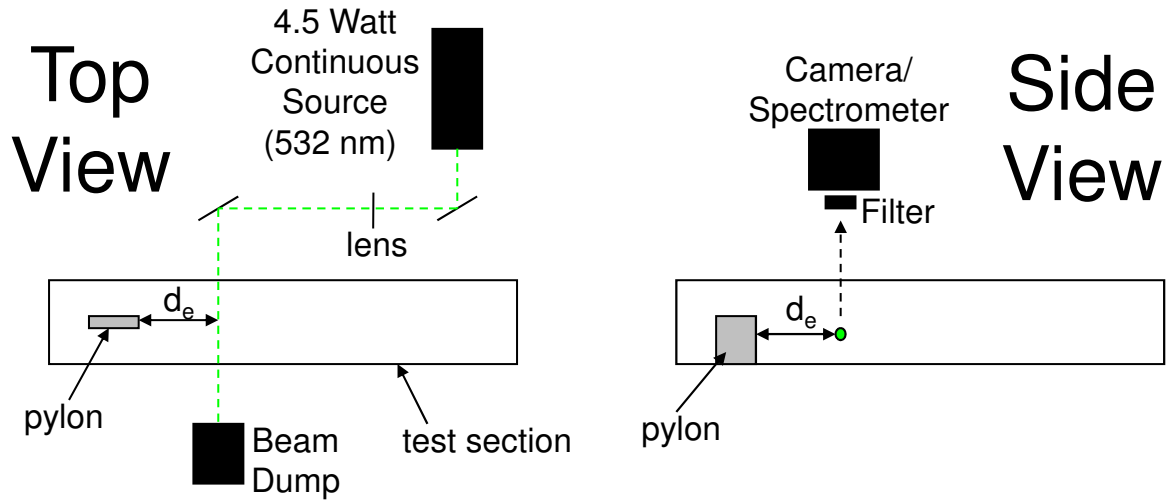


Fig. 4.17 Raman experiment setup.

The camera/spectrometer was located above the test section looking down 90° onto the laser beam. The field of view of the camera captured the middle 63.5 mm (2.5 in) of the test section. The camera/spectrometer equipment was a Kaiser® Holospec, $f/1.8$ aperture size, with an Andor® back-illuminated CCD detector. The imaging spectrometer was configured to record spectra over a range of approximately 550 nm - 650 nm to capture all the Stokes Raman signals from the wind tunnel flow and methane injectant. A mechanical shutter was used to control the exposure time of the imaging spectrometer. A Schott® Glass OG 570 long-pass filter was placed in front of the aperture to attenuate scattering at the laser light frequency (532 nm). The spectrometer also acted as a filter since it was looking in the 550 nm - 650 nm frequency range. Filtering the light source frequency prevented Rayleigh and Mie scattering signals from overwhelming the Raman scattering signal. Pictures of the experimental setup are seen in Fig. 4.18 and 4.19.

To obtain a two dimensional plume profile of the methane mass fractions at a planar position, the laser beam and imaging spectrometer were incrementally moved to several heights above the wind tunnel floor during a single test run using the movable table. The movable table also traversed the Raman setup to different planar positions downstream of the pylon.

The same precision regulator was used to control total pressure into the pylon plenum, flowing methane instead of air during these experiments. The methane was obtained from 32 high pressure k-bottle cylinders outside the facility, fed into the wind tunnel room around 1.4 MPa (200 lb/in^2). A set of nominal flow conditions were expected for the Raman experiments. These are shown in Table 4.5. These nominal conditions are based on a momentum flux ratio equal to one between the pylon injection methane and the wind tunnel air.

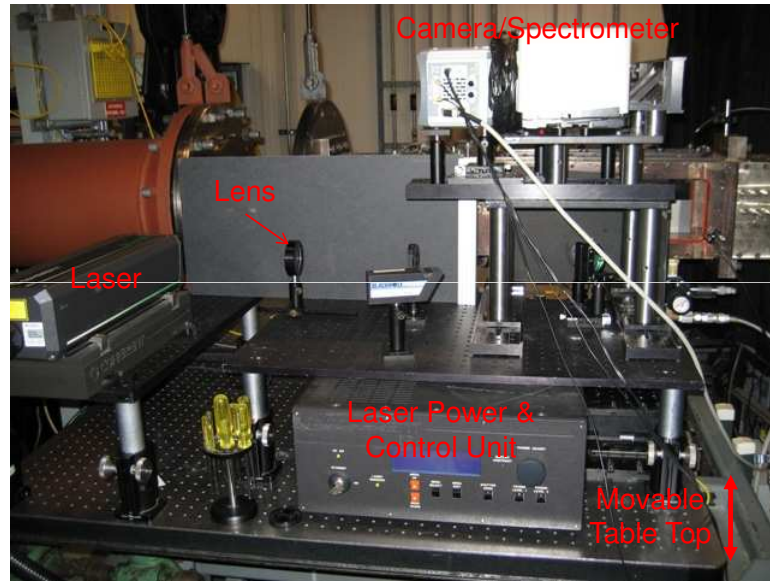


Fig. 4.18 Right side of test section Raman setup.

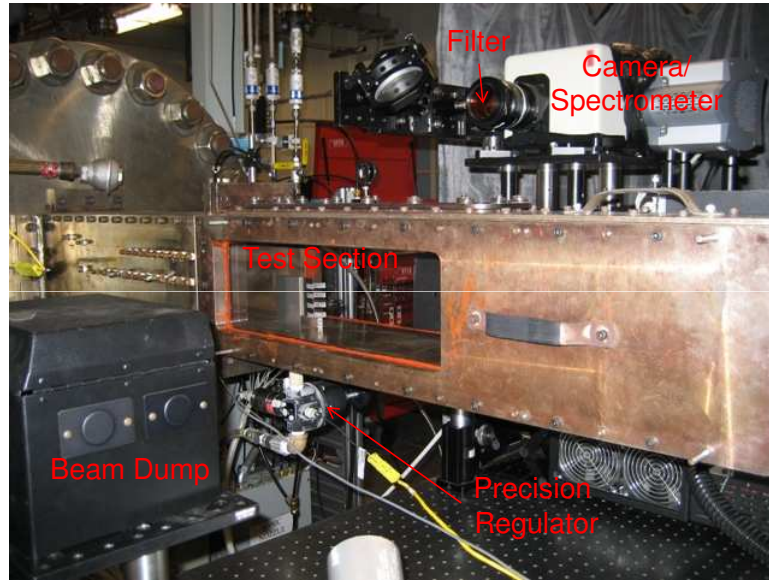


Fig. 4.19 Left side of test section Raman setup.

Table 4.5 Nominal flow conditions for Raman experiments.

Property/Condition	Tunnel Airflow	Pylon Inj (Methane)
Momentum Flux Ratio	—	1.0
Mass Flux Ratio	—	1.22
Mach Number	1.95	1.0
Velocity	501 m/s	411 m/s
Mass Flow	7.14 kg/s	0.023 kg/s
Total Temperature	288 K	288 K
Static Temperature	164 K	249 K
Total Pressure	241 KPa	249 KPa
Static Pressure	33.3 KPa	135 KPa
Flow Area	20,129 mm^2	53.7 mm^2

A calibration was necessary to carry out the Raman experiments. Since the Raman signal is species specific, the Raman signal intensity from a species at a location is a function of the number density of the species present there. The local signal

intensity was used to determine how much of a particular species was present at that location. The Raman signal intensities of nitrogen and methane were used to determine the the mass fraction of methane in air. The molar ratio of nitrogen to oxygen in air is 3.76. This ratio was assumed not to change with the amount of air present, so the amount of nitrogen present was used as a direct measure of the amount of air present.

Testing. Two calibration measurements were accomplished, both with no air flow in the wind tunnel, and the test section loosely isolated from the rest of the wind tunnel by placing foam material upstream and downstream of the test section. The loose barriers were added to keep methane in the test section while calibration data was captured. The first measurement was taken with no methane present in the test section. Raman signals for oxygen and nitrogen were observed in this calibration image. For the second measurement methane was injected into the test section, and a few seconds were allowed for the methane to diffuse throughout prior to taking the measurement. Raman signals for oxygen, nitrogen, and methane were present in this calibration image. The two measurements are seen in Fig. 4.20. Each spectral data image is 128 pixels high and 256 pixels wide. Along with these two spectral data image measurements, the temperature and pressure within the test section were recorded.

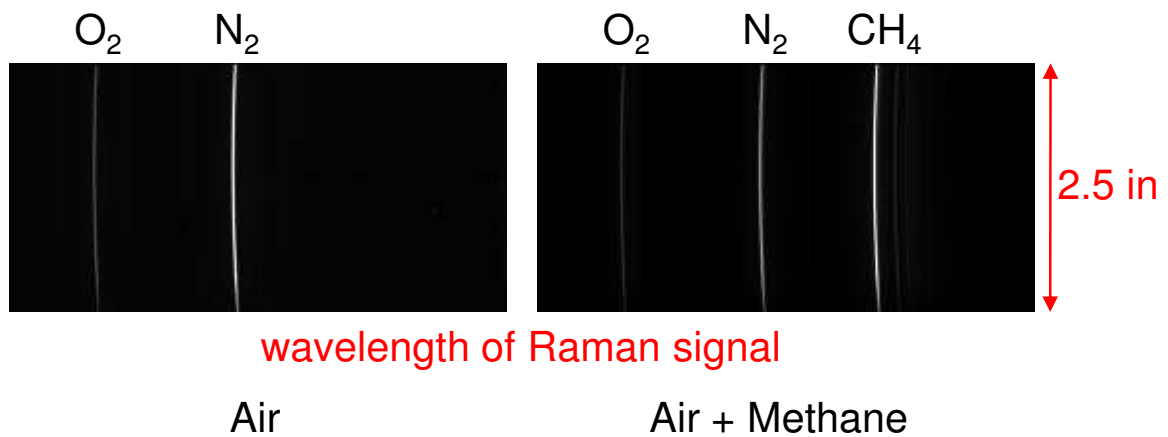


Fig. 4.20 Air and methane calibration.

A total of 6 Raman experiments were accomplished to gather methane plume mass fraction profile data for all three pylons at two planar positions downstream of the pylon base plane: $13.6 d_e$ and $23.9 d_e$ ($1 d_e = 8.52 mm$). Three experiments were accomplished twice: 1) the ramp pylon at $23.9 d_e$, 2) the wedge pylon at $13.6 d_e$, and 3) the wedge pylon at $23.9 d_e$. The second planar position, $23.9 d_e$, was the same as the probe experiments. The general procedure for testing was: 1) turn on the laser, 2) start the pylon methane injection flow and adjust with the precision regulator, 3) start the wind tunnel, 4) wait for the wind tunnel total pressure to stabilize, and 5) begin recording Raman signal data using the imaging spectrometer connected to a laptop for storage. At each height location the mechanical shutter opened for 20 s to allow the Raman signal time to integrate, then the movable table traversed the setup to the next height.

A two dimensional $50.8 mm$ ($2 in$) x $63.5 mm$ ($2.5 in$) grid of data was constructed. Figure 4.21 shows the array of data gathered at each planar position. The vertical resolution was $3.175 mm$ ($0.125 in$). The horizontal resolution was approximately $0.254 mm$ ($0.01 in$), the resolution of the imaging spectrometer images. During data reduction, the horizontal data was adjusted to $3.175 mm$ spacing so the vertical and horizontal resolutions were comparable when constructing plume mass fraction profiles.



Fig. 4.21 Array of Raman data.

Test conditions varied throughout the data runs due mostly to the decreasing total temperature of the pylon injection gas (methane) and the effect of this decreasing temperature on the precision regulator feeding the pylon plenum. The wind tunnel also exhibited increasing total temperature during the first hour of operation as before, but the mass flux ratio was less affected by this than the pylon injection mass flow variations.

For the aerothermal probe experiments, the high pressure air source outside the facility was a very large container cart. The reservoir was large enough that the total temperature of the air did not vary much over those test runs. For the Raman experiments, the high pressure methane source outside the facility was a collection of 32 gas cylinders, a much smaller reservoir, and the total temperature decreased more during the test runs. The injected methane total temperature varied as much as $40^{\circ}C$ during a single test run.

The precision regulator did not hold the set pressure well as the gas flowing through it decreased in temperature (as low as $-25^{\circ}C$). This change in the set pressure of the precision regulator turned out to be the largest source of mass flow variation for the Raman experiments. The wind tunnel and pylon injection conditions differed from the nominal conditions set forth in the experimental setup. The actual flow condition means and variations are shown in Table 4.6. The percent variations are the third standard deviations from the means. The amount of variation in the momentum and mass flux ratios was higher in the Raman experiments than in other experiments due to larger total pressure and total pressure changes in the pylon injection gas. During data reduction, a procedure correcting for these variations in the mass fraction data was accomplished.

Table 4.6 Actual flow conditions for Raman experiments.

Property/Condition	Tunnel Airflow	Pylon Inj (Methane)
Momentum Flux Ratio	–	$0.97 \pm 16\%$
Mass Flux Ratio	–	$1.25 \pm 16\%$
Mass Flow	$7.09 \text{ kg/s} \pm 2\%$	$0.024 \text{ kg/s} \pm 17\%$

Data Reduction. An extensive data reduction process was required to obtain methane mass fraction information from the Raman measurements. Two calibration curves relating Raman signal intensities to number densities of nitrogen and methane were required from the calibration process. Air and methane were both considered to be ideal gases under the range of pressures and temperatures experienced during testing. The total number density of molecules within the test section is a function of the temperature and pressure and is seen in Eq. 4.33. n is the number density and k is Boltzman's constant, $1.38066\text{E-}23 \text{ J/K}$.

$$P = nkT \quad (4.33)$$

The Raman signal intensity is assumed to vary linearly with concentration for both nitrogen and methane. This is an assumption made in all previous research using this Raman setup, due to the relatively small ro-vibrational excitation of the method. The number densities for each species were calculated through a set of simple simultaneous equations, knowing the total number density for each measurement from the test section temperature and pressure, and the signal intensities gathered from the spectral lines of each Raman calibration image. The simultaneous equations were solved for each vertical position in the calibration images, producing a calibration curve. The simultaneous equations are shown in Eqs. 4.34 and 4.35. Each vertical position horizontal slice is a horizontal position in the wind tunnel. A single horizontal slice from the spectral images of each calibration experiment is seen in Fig. 4.22.

$$n_1 = c_1 I_{1\text{N}_2} \quad (4.34)$$

$$n_2 = c_1 I_{2\text{N}_2} + c_2 I_{2\text{CH}_4} \quad (4.35)$$

I_1 and I_2 are the Raman signal intensity values of each respective species from a horizontal slice. To calculate the I_1 and I_2 values of each species, the background signal (floor noise level) was subtracted off within each horizontal slice and the top

four intensity values averaged from the nitrogen and methane Raman signals. Solving for c_1 and c_2 at each vertical position yielded two calibration curves, shown in Fig. 4.23. The calibration is, to a good approximation, constant over a large extent of the horizontal viewing area, except at the left and right ends. This could be due to the camera/spectrometer pixel binning method, viewing path differences into the test section, or sensitivity differences near the edges of the CCD detector array. The reason for the behavior is not a concern, as long as it is accounted for in the calibration curves. The entire 128 pixel horizontal width of each Raman data image was used to construct plume profiles.

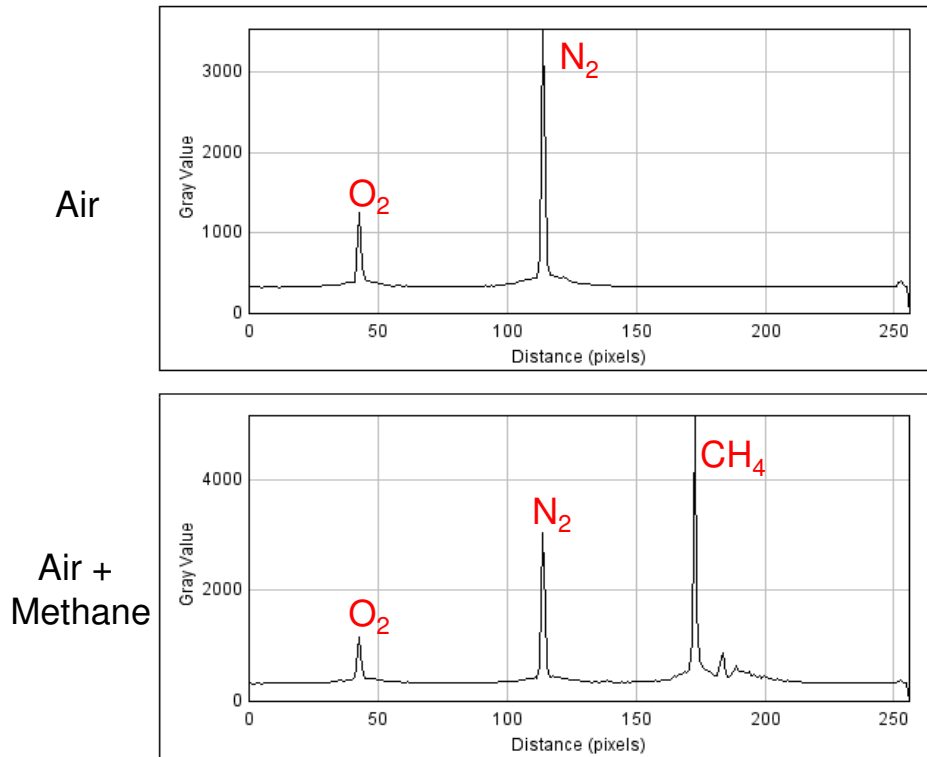


Fig. 4.22 Horizontal slices from Fig. 4.20

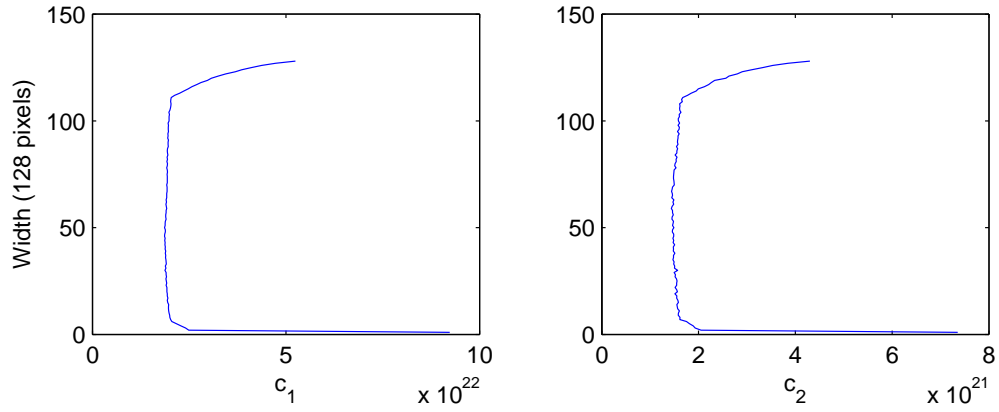


Fig. 4.23 Calibration curves for air and methane.

Figure 4.24 shows a sample of a test run Raman signal data image at a planar position 76.2 mm (3.0 in) behind the wedge pylon and 25.4 mm (1.0 in) above the wind tunnel floor. Each spectral data image is the same size as the calibration images, 128×256 . The Raman data image intensities were transformed into number densities using the calibration. To accomplish this, the background signal was subtracted from each horizontal slice of image data, the top four intensity values for nitrogen and methane averaged, and the intensity values multiplied by their respective calibration curve values.

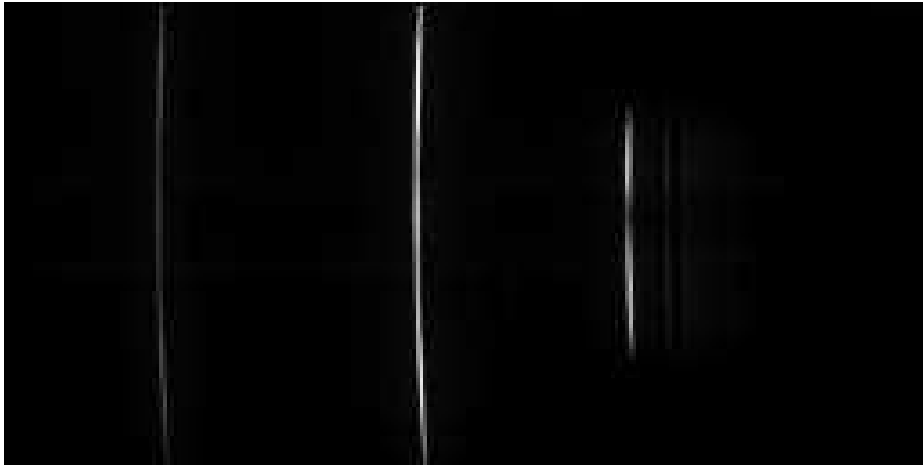


Fig. 4.24 Raman data image.

The next step was to calculate methane mass fractions from the nitrogen and methane number densities. Another expression of the ideal gas relationship is seen in Eq. 4.36. R is the universal gas constant and MW is the molecular weight of the species. Comparing this equation to Eq. 4.33, the density of each species is a function of its number density multiplied by three constants, seen in 4.37. The ratio of the methane density to air density is the methane/air mass ratio, f , and the mass fraction of fuel in air, α , is defined by Eq. 4.10. The number densities calculated with the calibration were changed into mass densities using these equations and divided to yield methane/air mass ratios.

$$P = \rho \frac{R}{MW} T \quad (4.36)$$

$$\rho = n \frac{kMW}{R} \quad (4.37)$$

Since the mass flow variations from the pylon caused the mass flux ratio values to vary much more than in other experiments performed, the methane/air mass ratio values were corrected using the mass flux ratio data. To accomplish this, the methane/air mass ratios were multiplied by the deviation of the mass flux ratio at the time of the measurement from the expected mass flux ratio given in the experimental setup. This procedure normalized the methane/air mass ratios at each location within the fuel plume. For example, at a particular test run time, if the mass flux ratio was 1.25, it was divided into the expected value, 1.22, and the methane/air mass ratios measured at that time were multiplied by $1.22/1.25 = 0.976$. This was repeated for all data at each planar position. The plume profile methane/air mass ratios were then converted into mass fraction values following this correction.

The Raman signal data was reduced to mass fraction data using the above procedures. The two planar positions downstream of the three pylons resulted in 6 total data sets. The data at each position was arranged into 50.8 *mm* (2 *in*) high x 63.5 *mm* (2.5 *in*) wide arrays of mass fractions with 3.175 *mm* (0.125 *in*) spacing in both the vertical and horizontal. The bottom of the array was 12.7 *mm* (0.5 *in*)

above the wind tunnel floor, and the middle of the array was centered on the wind tunnel centerline.

Methane mass fraction plume profiles were constructed at each planar position. The maximum methane mass fraction was calculated at each planar position by averaging the top 1% of local methane mass fraction values at that position. The flammable plume area and flammable plume fraction were calculated from Eqs. 4.11 and 4.12 at each planar position. MATLAB[®] was used to plot methane mass fraction plume profiles and accomplish data reduction calculations. For the three Raman test runs accomplished twice, the methane mass fraction plume profiles were averaged.

The range of mass fractions in the flammable region is about three times smaller for methane than for ethylene. The equivalence ratio flammability limits for methane are $0.53 \leq \phi \leq 1.6$. [72] The stoichiometric methane/air mass ratio is approximately 0.058. Consequently, from Eq. 4.10, the range of flammable mass fractions of methane fuel in air is $0.030 \leq \alpha \leq 0.085$. The flammable plume information for the Raman experiments was calculated using the methane flammability region. The effective fuel injection area for the manufactured pylons, A_e , is $5.37\text{E-}5 \text{ m}^2$.

Planar Laser Induced Fluorescence

Laser Induced Fluorescence (LIF) is a non-intrusive light interrogation technique used to detect gas concentration by deliberate resonant excitation of a molecule of interest. Fluorescence is emitted from the molecule as a response to the direct excitation. [87,88] The experimental apparatus used, again at AFRL, produces ultraviolet radiation spread out in a planar sheet to stimulate an electronic transition in seeded Nitric Oxide (NO-PLIF). The AFRL test apparatus has been used successfully in several past research projects. [22,64,90,93] Past efforts have gathered flow visualization data on wall transverse or angled injector ports and cavity flow. In current research the test apparatus and data reduction was implemented the same as before, but this was the first time NO-PLIF measurements had been gathered downstream of a large intrusive object in the wind tunnel flow.

Unlike Raman spectroscopy, NO-PLIF is not a scattering technique, it is a resonance stimulation. An ultraviolet electronic transition is used to excite the molecule. The electronic excitation also results in rotational and vibrational energy transfers through collisional processes, hence the excitation is ro-vibronic (a combination of rotational, vibrational, and electronic energy modes). Raman excitation was meant to be ro-vibrational as no electronic transition was targeted; so the methane should have remained in one electronic state. An advantage of NO-PLIF over Raman is the fluorescence signal is orders of magnitude more intense than the Raman scattering signal, making it easier to detect.

A generic picture of ro-vibronic molecular energy levels is shown in Fig. 4.25. Fluorescence is produced when an excited ro-vibronic state emits a photon that reduces it to a de-excited ro-vibronic state. The photon frequency emitted can be from any ro-vibronic combination of both states. For instance, a photon emitted from the ground vibrational levels of two electronic states is termed a (0,0) de-excitation; and a photon emitted from the upper electronic ground vibrational level to the lower electronic first vibrational level is termed a (0,1) de-excitation. The photon in the latter case would have less energy (longer wavelength) than the former.

NO has an electronic transition in the ultraviolet around 226 nm, $R_1(8.5)$ transition of the $A^2\Sigma^+ - X^2\Pi$ (0,0) band. Stimulated at the transition wavelength, NO fluoresces at 226 nm (0,0) as well as other wavelengths above 226 nm from the (0,1), (0,2), (0,3), ... (0,n) vibrational levels. A spectrum of NO fluorescence is shown in Fig. 4.26, interrogated at 226 nm, generated from LIFBase for an NO gas temperature of 200 K. The fluorescence wavelengths are at approximately 10 nm intervals starting at 226 nm. The fluorescence signal is strongest around 237 nm (0,1), and above 300 nm the fluorescence signal is very weak. A filter is placed in front of the camera lens to block the laser frequency, as well as (0,0) fluorescence, and avoid capturing scattered radiation not due to fluorescence. Fluorescence from wavelengths greater than 226 nm is captured by the camera.

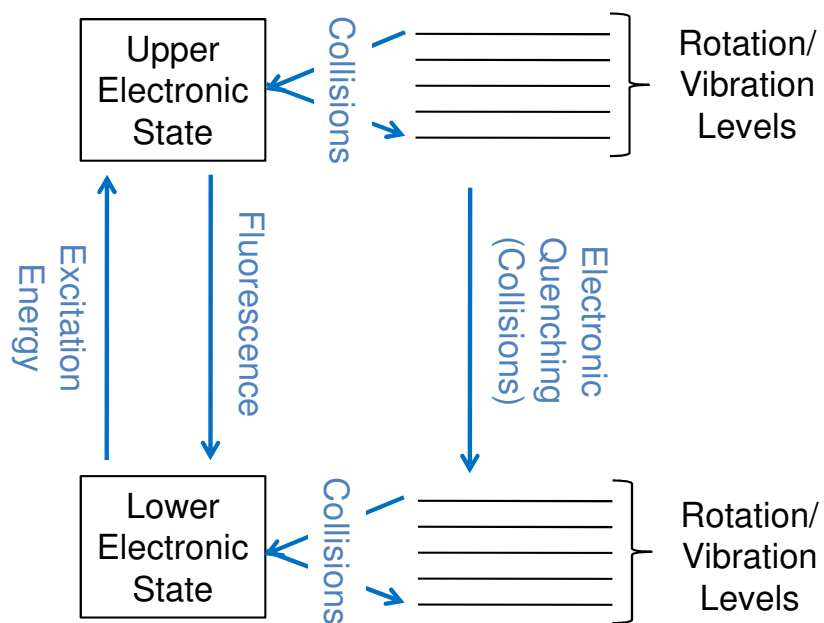


Fig. 4.25 Ro-vibronic molecular energy levels.

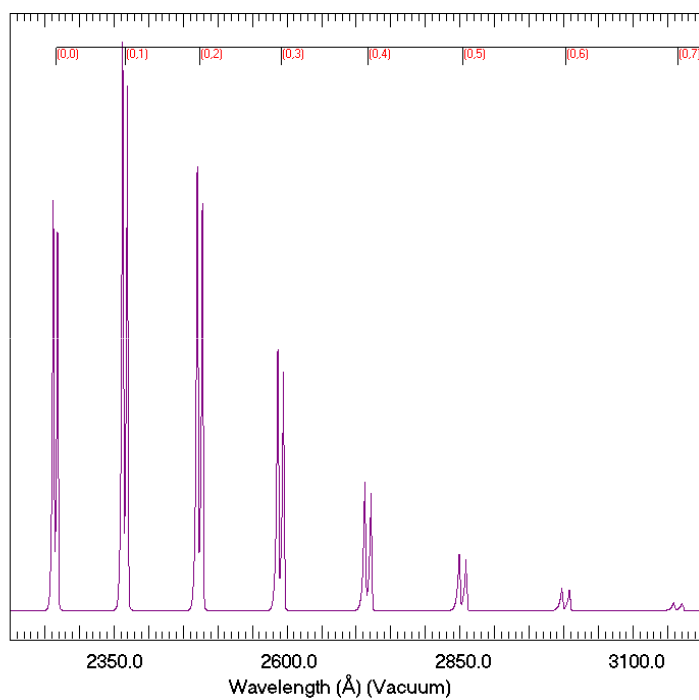


Fig. 4.26 NO fluorescence spectrum at $R_1(8.5)$ ro-vibronic transition.

Instead of producing fluorescence, the molecule can also de-excite through collisions. This is called electronic quenching (Fig. 4.25). It is part of the reason the NO-PLIF intensity results are only qualitative. There is only a probability a de-excitation will produce a photon, based on collision rates. The more collisions there are, the higher the probability a photon will not be produced. Collision rates generally vary directly with pressure and inversely with the square root of temperature. [94] The static pressure and temperature behind an intrusive object like the pylon varies with downstream distance and also within a single planar position. The shock structure in the wind tunnel also varies the static pressure in the wake region. These pressure and temperature variations change the collision rates and therefore the fluorescence signal from one location to another.

In addition to electronic quenching, the frequency band over which an electronic transition is stimulated varies depending on pressure. Typically, as pressure rises, the frequency band for the transition widens. This is called collisional line broadening. Quenching rates and collisional line broadening are two phenomenon that complicate quantitative number density calculations using NO-PLIF. Pressure and temperature measurements were not taken in conjunction with the NO-PLIF measurements, so no corrections were attempted. However, qualitatively, a change in NO-PLIF signal intensity can be interpreted as a monotonically similar change in NO concentration. This monotonic relationship between concentration and fluorescence signal is experimentally confirmed with data portrayed in Chapter 5, allowing for a qualitative mixing (dilution) analysis of the pylon injectant plume based on NO-PLIF signal intensity data.

An advantage of NO-PLIF is the ability to capture instantaneous snapshots of the flow, whereas Raman is time-averaged due to the integration time of the low intensity signal. NO fluorescence times are approximately 10^{-8} to 10^{-10} seconds depending on static pressure and temperature of the gas. Assuming a fluorescence time of 20 ns, and an airflow speed of 500 m/s (approximate wind tunnel condition), the fluorescence radiation can be detected within a flow traversing distance of approxi-

mately $.01\text{ mm}$. This distance is much smaller than the typical extent of a focused laser beam ($0.1 - 0.5\text{ mm}$). The response time of the technique relative to the flow speed allows the instantaneous capture of flowfields.

Experimental Setup. For NO-PLIF experiments, the test section was configured with two window sidewalls and a metal top wall. The laser penetrated one sidewall and was caught by a beam dump after passing through the other sidewall. The radiation source was created through a combination of a Spectra Physics® Quanta Ray Nd:YAG laser (GCR-170) and a Lumonics® Hyperdye dye laser (HD-300). The primary wavelength of the Nd:YAG laser was 1064 nm (infrared), and was not used. The second and third harmonics of the Nd:YAG laser were 532 nm and 355 nm respectively. The second harmonic pumped the tunable dye laser. The output of the dye laser was around 622 nm . The 622 nm radiation from the dye laser and the 355 nm radiation from the Nd:YAG were mixed to produce 226 nm radiation (ultraviolet) using a INRAD® Autotracker III system. The Nd:YAG was a pulsed source. The laser had a 10 ns pulse length and a 10 Hz rate. The power output of the laser was 5 mJ per pulse. This setup provides instantaneous spatial pictures, however, the pulsing frequency is not fast enough to capture flow changes at the appropriate time resolution. One obtains temporally resolved images that are uncorrelated (no relation between one another). Figure 4.27 shows the laser setup.

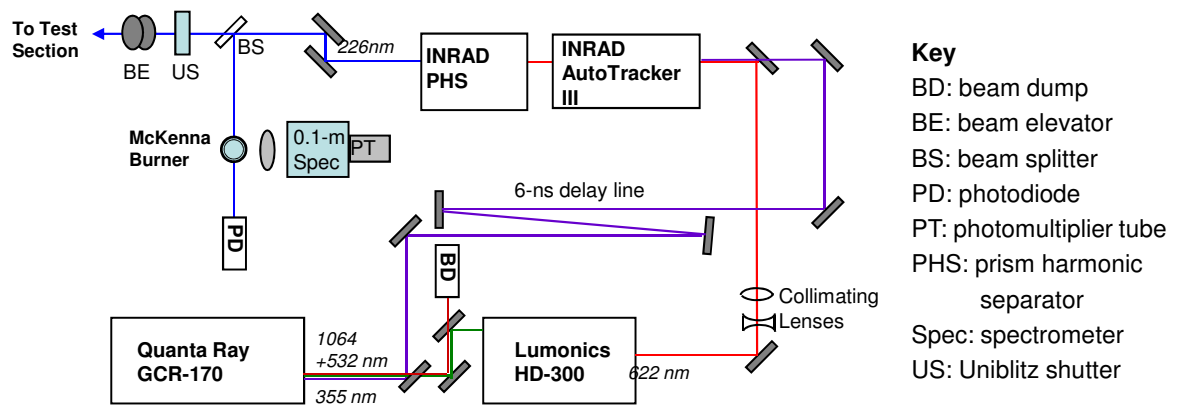


Fig. 4.27 NO-PLIF laser setup.

The resultant radiation source was sampled using a beam splitter. The sample was diverted through a burning methane flame. The methane flame had enough internal NO at the hot flame front for a spectrometer to detect a fluorescence signal from the interaction. The spectrometer with attached oscilloscope monitored the interaction between the sampled radiation and the flame. The dye laser was tuned until a peak signal was obtained at the correct ro-vibronic transition state of the NO. This tuning process was accomplished to ensure a strong fluorescence signal from the seeded NO in the pylon injection air. The oscilloscope was continually monitored throughout testing to ensure good overlap between the laser frequency and electronic transition.

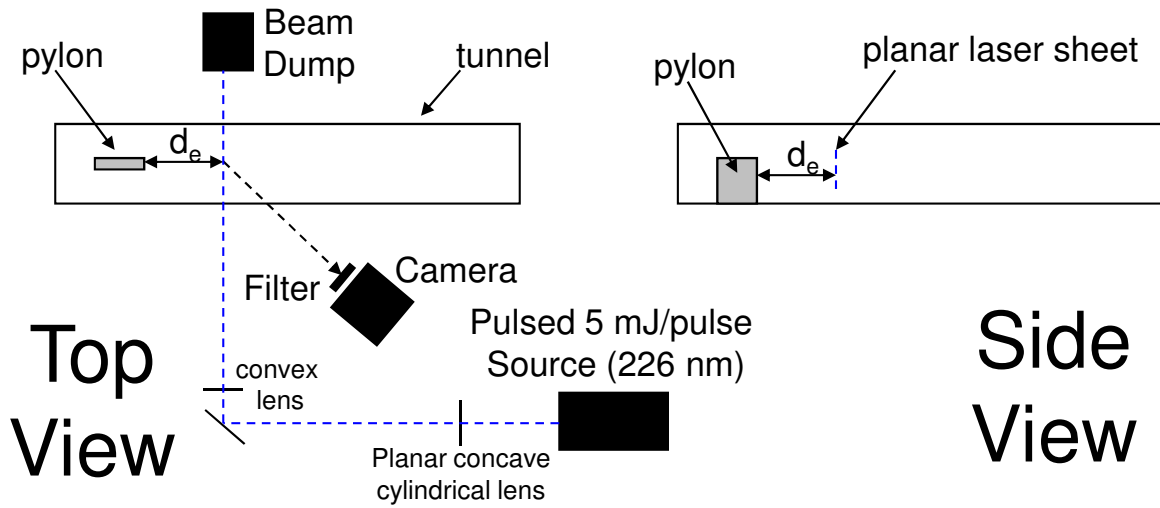


Fig. 4.28 NO-PLIF experiment setup.

A top and side view diagram of the NO-PLIF setup is seen in Fig. 4.28. The beam traversed from the light source setup through a -50 mm focal length planar concave cylindrical lens that spread the beam out in the wind tunnel height dimension. The light was then reflected onto a 1.0 m focal length spherical convex lens that straightened the light rays in the wind tunnel height dimension and focused the light rays in the axial dimension at the wind tunnel centerline.

The imaging camera was a Roper PIMAX[®] CCD with a Superblue intensifier, and incorporated a Cerco 45 *mm* f/1.8 UV lens. The planar laser sheet (101.6 *mm* high within the test section) was imaged by the camera at approximately a 45° angle. The camera was attached to a Scheimpflug mount to mitigate image blur from the off-normal viewing angle. A two dimensional area profile 88.9 *mm* (3.5 *in*) high and 101.6 *mm* wide was captured by the camera. The camera gate time was set at 200 *ns* to capture the fluorescence signals from the flowfield. A UG 5 band-pass filter was placed in front of the camera lens to attenuate scattering at the frequency of the laser source. The filter also attenuated some fluorescence signal at the laser frequency.

The movable table traversed the laser sheet and camera setup to planar positions within the viewing access of the test section sidewall windows. Pictures of the experimental setup are shown in Fig. 4.29 and 4.30.

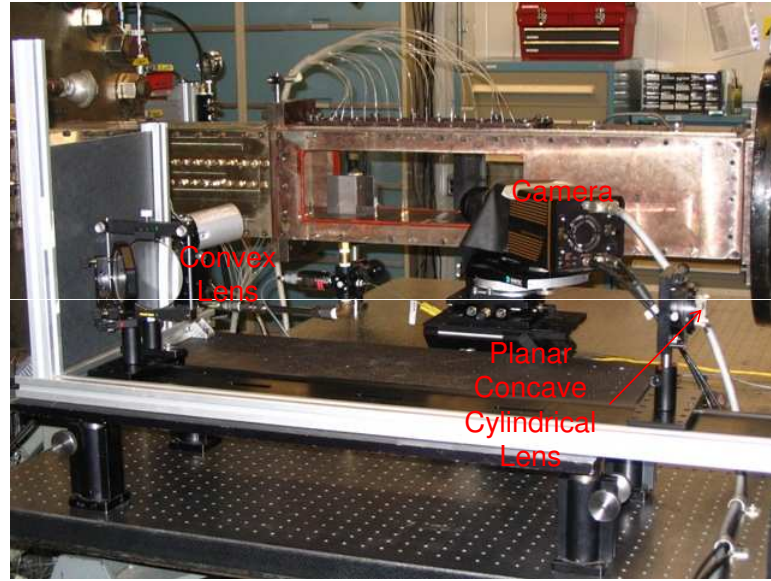


Fig. 4.29 Test section with NO-PLIF setup.

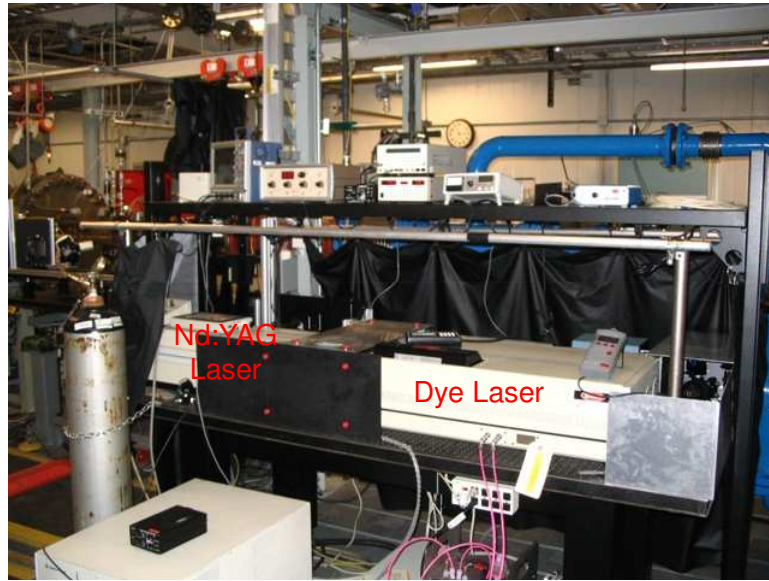


Fig. 4.30 NO-PLIF radiation source setup.

The airflow to the pylon was supplied from the outside air cart using the same precision regulator used in the aerothermal probe and Raman experiments. The NO seeding flow to the pylon was controlled using a calibrated mass flow controller, and kept at the same flow rate throughout the NO-PLIF experiments to minimize the amount of variance in the fluorescence signal due to the amount of NO present. The air was seeded with a 1% by volume NO in N₂ mixture far upstream of the precision regulator to allow time for the seeding flow to distribute evenly within the pylon injection air. The amount of NO present in the pylon injection air was approximately 0.07% by mass.

Due to the low NO concentration, the properties of the injected mixture were considered to be air for all pylon mass flow calculations. A set of nominal flow conditions were expected for the NO-PLIF experiments. These are shown in Table 4.7. These nominal conditions are based on a momentum flux ratio equal to one between the pylon injection air and the wind tunnel air.

Table 4.7 Nominal flow conditions for NO-PLIF experiments.

Property/Condition	Tunnel Airflow	Pylon Inj (Air)
Momentum Flux Ratio	–	1.0
Mass Flux Ratio	–	1.61
Mach Number	1.95	1.0
Velocity	501 m/s	311 m/s
Mass Flow	7.14 kg/s	0.031 kg/s
Total Temperature	288 K	288 K
Static Temperature	164 K	240 K
Total Pressure	241 KPa	240 KPa
Static Pressure	33.3 KPa	127 KPa
Flow Area	20,129 mm^2	53.7 mm^2

As discussed previously, the NO-PLIF data was not corrected for electronic quenching and spectral line broadening. However, the data was corrected for the camera viewing angle, background noise, and image non-uniformity. Since the camera was viewing the laser sheet at an off-normal angle, a spatial calibration of the camera using a uniform grid reference at the same planar position as the laser sheet was necessary in order to perform perspective distortion corrections (de-warping). Also, the camera, observing a uniform area of signal intensity, does not produce an exactly uniform flatfield image of intensities due to laser sheet fluence, window transmission, and camera detector array non-uniformities. Flatfield images were used to help remove these errors by normalizing the data images.

Testing. Prior to testing, two spatial calibration images were taken. The first was an image of the grid reference block and a small ruler situated vertically on the block. The grid reference block had a paper grid attached to one side with 2.54 mm (0.1 in) vertical and horizontal line spacing. The ruler was touching the wind tunnel floor to obtain an absolute height measurement of the camera field of view. The

second image was the same small ruler situated horizontally across the wind tunnel test section without the reference grid block. The ruler was touching the left window to obtain an absolute horizontal measurement of the camera field of view.

These two images were corrected using a linear de-warping algorithm written and executed in MATLAB[®] script. The resulting images are seen in Figs. 4.31 and 4.32. All NO-PLIF data images were de-warped prior to accomplishing any data reduction. Each spatial calibration image was 256 x 256 pixels prior to de-warping, and 346 x 316 pixels after de-warping. The resolution in the vertical and horizontal of the de-warped images is approximately 0.254 mm/pixel (0.01 in/pixel).

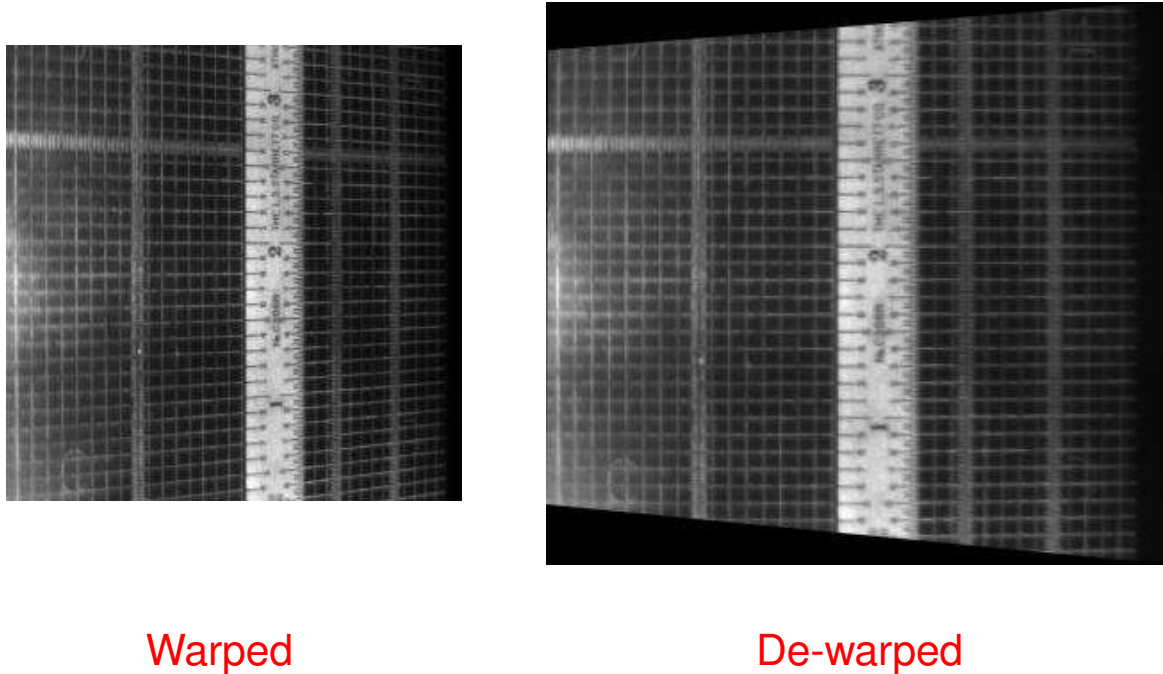


Fig. 4.31 De-warping of image with grid reference and vertical ruler.

Also prior to testing, the test section was injected with NO under stagnant wind tunnel flow conditions. The same loose foam inserts from the Raman experiments were used to isolate the test section and keep the NO within the volume. The NO was allowed to diffuse throughout the test section so a uniform amount was present. A flatfield image was then taken at each planar position used for data collection. The

flatfield image at each planar position was used in data reduction to normalize the pixel intensities in the data images.

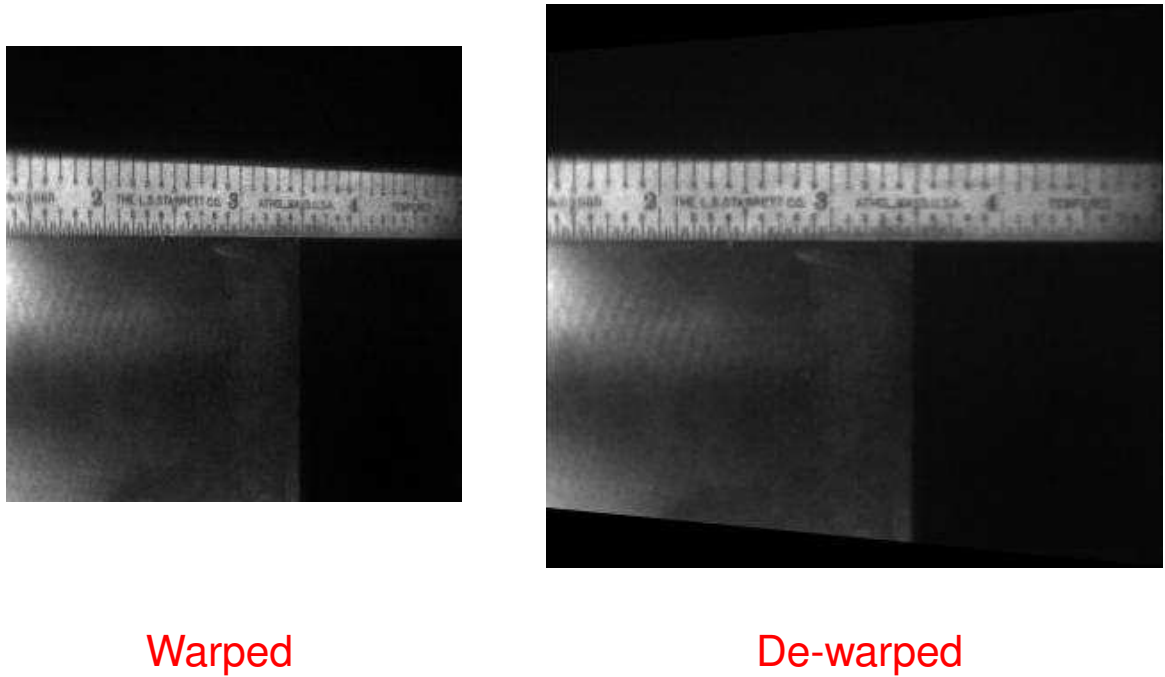


Fig. 4.32 De-warping of image with horizontal ruler.

A total of 18 NO-PLIF experiments were accomplished to gather fuel plume signal intensity data on all three pylons at 6 planar positions downstream of the pylon base plane: $7.7 d_e$, $10.7 d_e$, $13.6 d_e$, $16.6 d_e$, $19.6 d_e$, and $23.9 d_e$ ($1 d_e = 8.52 \text{ mm}$). The third and sixth positions, $13.6 d_e$ and $23.9 d_e$, were the same as the Raman experiments; and the sixth position was the same as the probe experiments. The laser was turned on and kept on the entire length of the experiments (all NO-PLIF data was collected the same night) to ensure the light source intensity and frequency output stayed constant throughout the experiments.

The general procedure for testing was: 1) start the pylon air injection flow and adjust with the precision regulator, 2) start the wind tunnel, 3) wait for the wind tunnel total pressure to stabilize, 4) take a set of background images with only air flowing through the pylon, 5) start the NO seeding, 6) record images for 30 s at a rate

of 10 Hz (300 images). After data was collected at one planar position, the movable table traversed the setup to the next position. Test conditions varied throughout the data runs from those set forth in the experimental setup, but the amount of variation was lower in the NO-PLIF experiments than any other experiments. The actual flow condition means and variations are shown in Table 4.8. The percent variations are the third standard deviations from the means.

Table 4.8 Actual flow conditions for NO-PLIF experiments.

Property/Condition	Tunnel Airflow	Pylon Inj (Air)
Momentum Flux Ratio	–	$1.03 \pm 3\%$
Mass Flux Ratio	–	$1.67 \pm 3\%$
Mass Flow	$6.98 \text{ kg/s} \pm 2\%$	$0.031 \text{ kg/s} \pm 3\%$

Data Reduction. The software used to manipulate the NO-PLIF data images was a freeware called ImageJ[®]. NO-PLIF images were taken for each of the three pylons at 6 planar positions, 18 total sets of images. At each planar position 300 images were collected over a 30 s period (10 Hz image rate). A total of 5,400 individual data images were collected and used in data reduction. An example of a de-warped data image is shown in Fig. 4.33.

The first step in data reduction was to subtract the de-warped background images from the de-warped data images. The average background image for each pylon and planar position was subtracted from the 300 de-warped data images for that same pylon and planar position. The second step was to use the de-warped flatfield images to normalize the data images. The flatfield image for each pylon and planar position was normalized so the average pixel intensity in the image was approximately 1.0 magnitude. Then the normalized image was divided into the 300 background subtracted data images for that same pylon and planar position. An example of a background image is shown in Fig. 4.34. The observable darker area in the middle is the result of the Mie scattering difference of the wind tunnel air (moist) and the pylon injection air (dry) from the supply cart outside the test cell.

An example of a de-warped flatfield image is shown in Fig. 4.35. The non-uniformity of the flatfield image is visually apparent although a uniform concentration of NO is present in the test section.

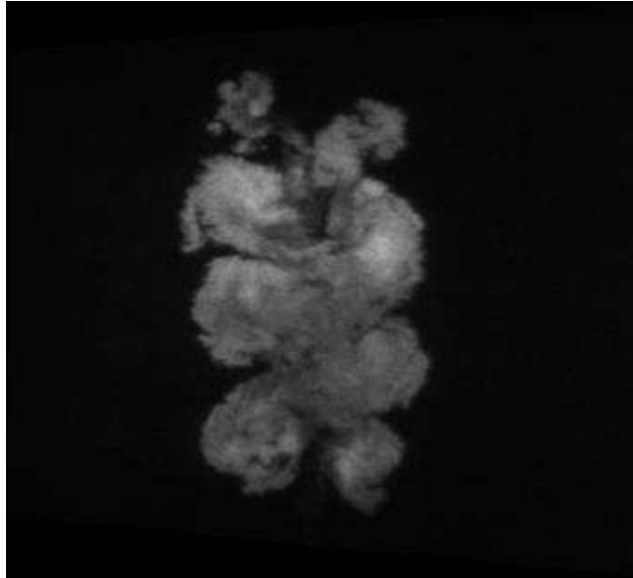


Fig. 4.33 De-warped data image.

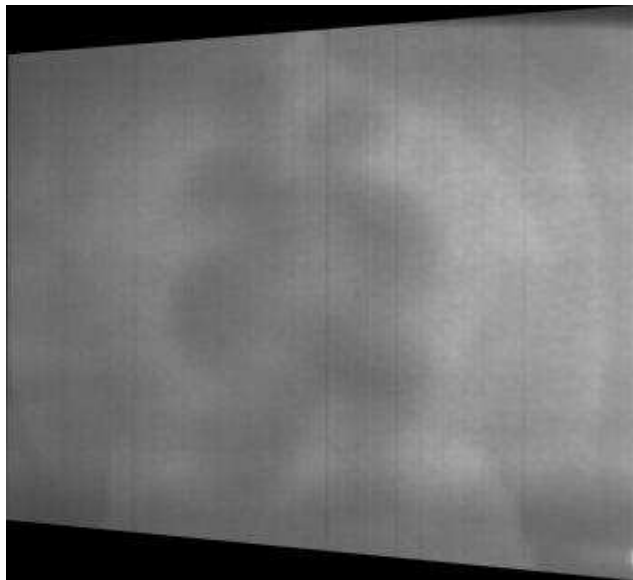


Fig. 4.34 De-warped background image.

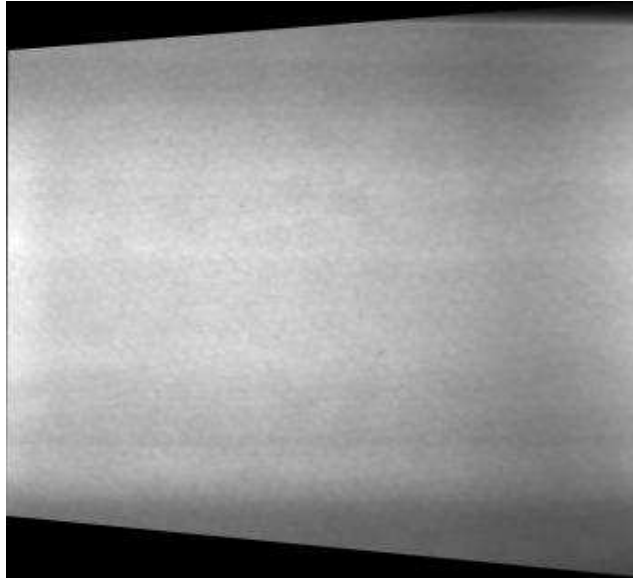


Fig. 4.35 De-warped flatfield image.

The third step was to flip the data images horizontally (looking downstream instead of upstream) so they matched the probe and Raman experimental data profile orientations. The resultant 18 data images sets contained 300 instantaneous snapshots each, providing flowfield instantaneous spatial information. Spatial statistics of the images were accomplished by taking the ensemble averages and standard deviations of the 18 image sets. The statistical images provide the average pylon injectant plume shape through the ensemble averages and the amount of unsteadiness in the pylon injectant plume through the standard deviations. Both the instantaneous and statistical images are shown in the results section.

The instantaneous and averaged images were cropped and read into MATLAB® for further analysis. The height dimension of the de-warped images varied from right to left due to their keyhole shape. After cropping the height was 66.04 mm (2.6 in) (12.7 mm - 78.74 mm from the floor of wind tunnel). The horizontal cropped width was the center 76.2 mm (3 in), more than enough to encompass the horizontal extend of the pylon injectant plumes. Figure 4.36 shows the cropped area overlayed on the de-warped reference grid.

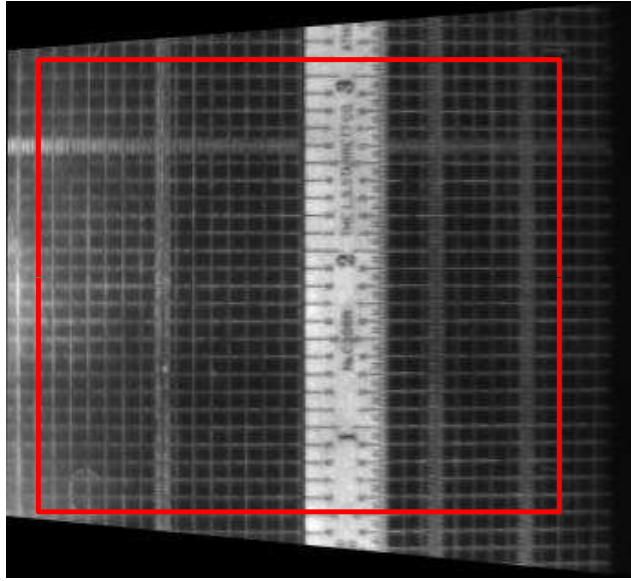


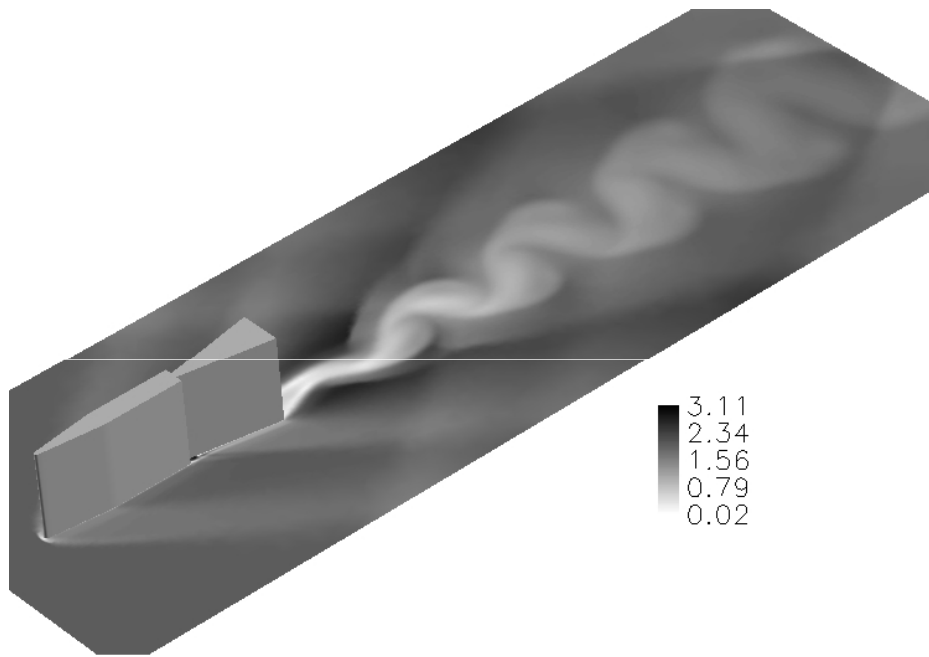
Fig. 4.36 Cropped image area.

MATLAB[®] was used to plot signal intensity plume profiles next to each other, accomplish plume dilution calculations, and observe the differences between average and instantaneous flowfield information. Signal intensity plume profiles were constructed in order to visualize the wake region flow of the pylons and determine the diluted state of the injectant/wind tunnel air mixture at each planar position. Maximum mass fraction calculations were accomplished the same way as for the Raman data. However, instead of mass fraction values, the maximum concentration measurement was the averaged top 1% of pixel intensities within the images. These maximum pixel intensity measurements were compared between planar positions to observe qualitatively how quickly the fuel plume diluted into the wind tunnel airstream.

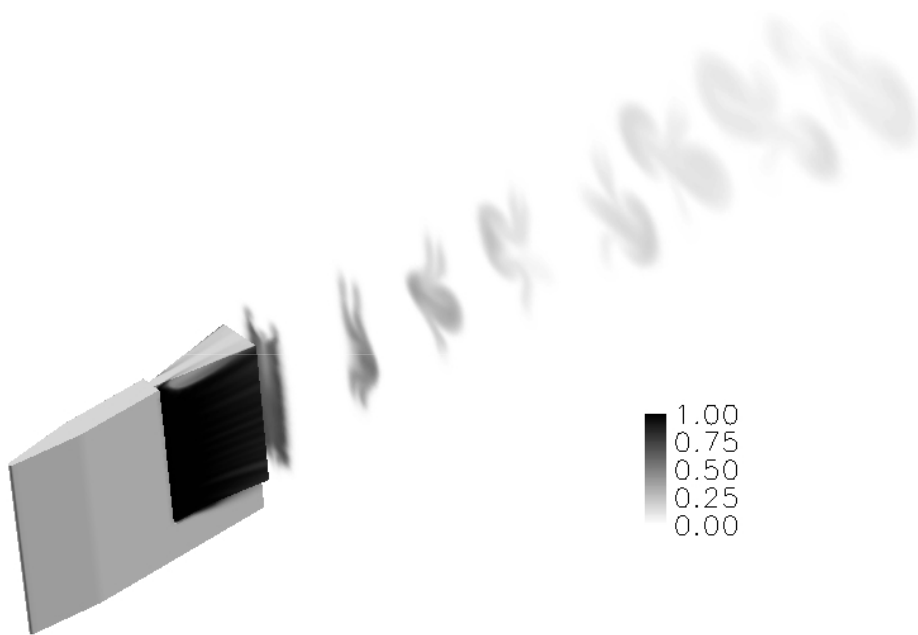
V. Results and Analysis

Pylon Wake Region Flowfields

CFD simulation flowfields and NO-PLIF plume profile data taken together are adequate to visualize and verify the characteristics of the wake region flowfields for the three pylon configurations. CFD simulation flowfields are shown first. Figure 5.1a shows a planar cut of Mach number in the horizontal direction half way up the basic pylon height, and Fig. 5.1b shows eight planar cuts of ethylene mass fraction plume profiles in the vertical direction downstream of the pylon. The basic pylon has a highly unsteady wake region that required a time accurate solution. One time snapshot of the solution is displayed. Vortex shedding in the wake region of the basic pylon is apparent in the Mach number profile (Fig. 5.1a) as well as the unsteady mass distributions in the ethylene plume profiles (Fig. 5.1b). Similar planar cuts of Mach number and ethylene mass fraction plume profiles are displayed for the ramp and alternating wedge pylons in Figs. 5.2 and 5.3. Both of these pylons have a steady state CFD solution rather than a time accurate one. The added axial vortical motion produced in the wake region behind the hypermixer pylons is apparent in the near-field region behind the pylons from the ethylene plume profile shapes (Figs. 5.2b and 5.3b). The wake region flowfields of the hypermixer pylons are more steady than the basic pylon (Figs. 5.2a and 5.3a). All ethylene profiles decrease in mass fraction values with downstream distance, demonstrating dilution of the ethylene injectant into the airstream.

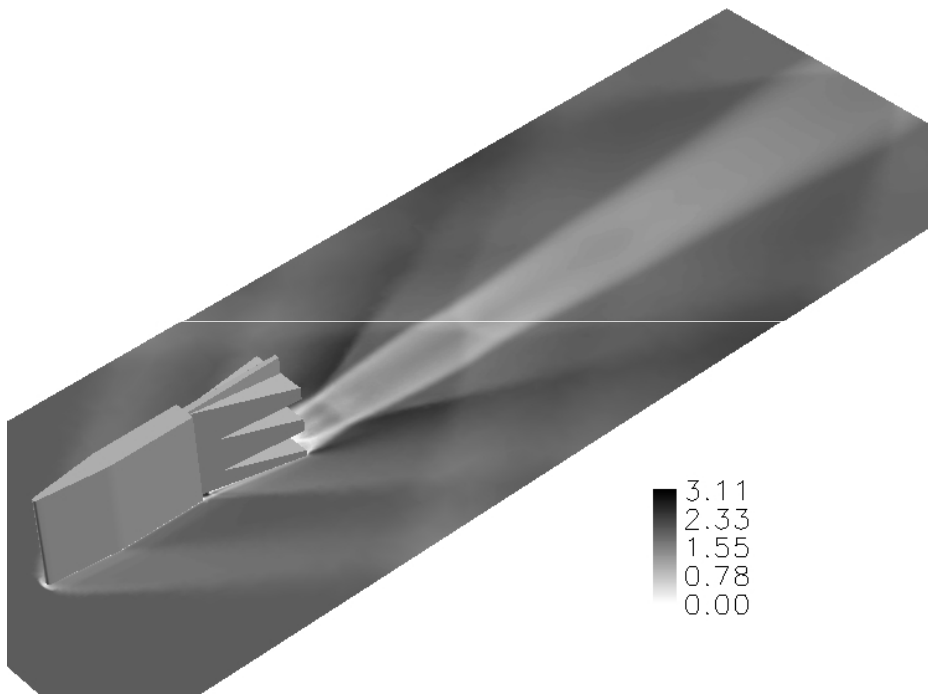


(a) Mach number in one horizontal plane.

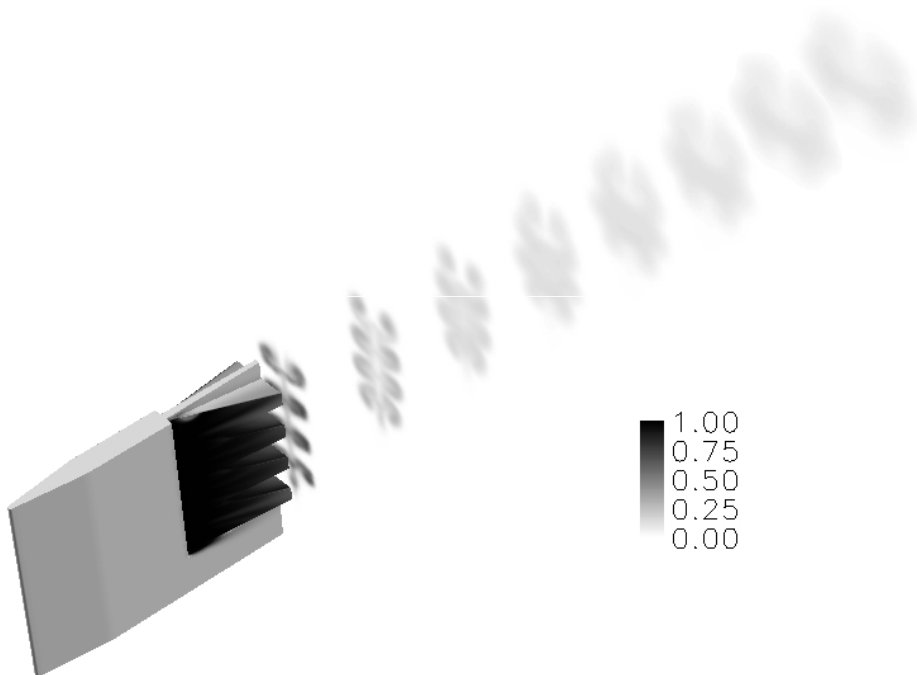


(b) Ethylene plume in eight vertical planes.

Fig. 5.1 Basic pylon CFD visualization.

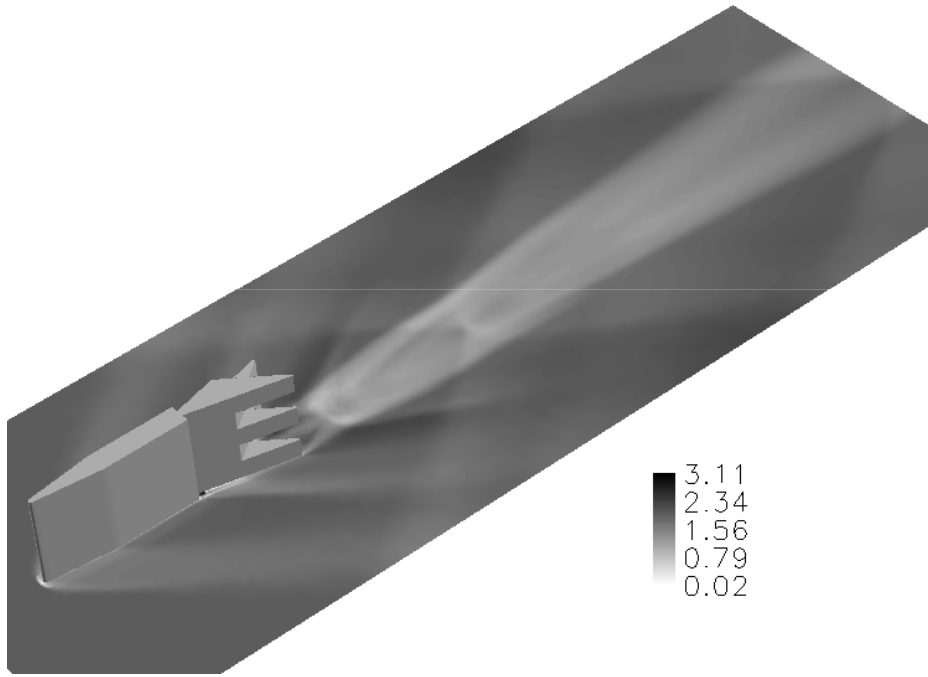


(a) Mach number in one horizontal plane.

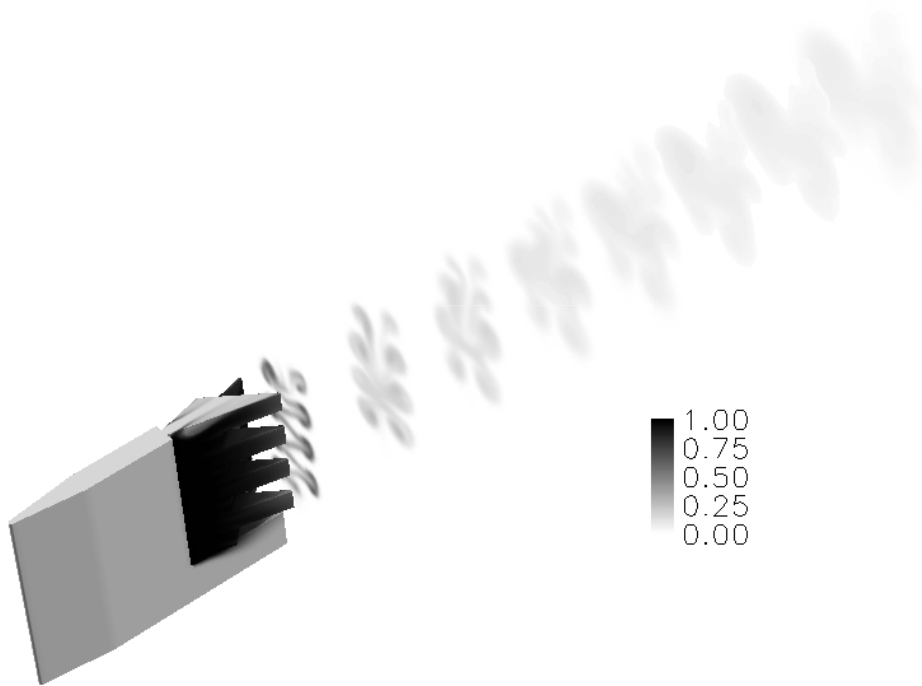


(b) Ethylene plume in eight vertical planes.

Fig. 5.2 Ramp pylon CFD visualization.



(a) Mach number in one horizontal plane.



(b) Ethylene plume in eight vertical planes.

Fig. 5.3 Alternating wedge pylon CFD visualization.

To corroborate the accuracy of the flowfields observed in CFD simulations, NO-PLIF plume profile images are examined (contained in Appendix D). Ensemble averaged plume shapes at six planar positions in the wake region of each pylon configuration are shown in the appendix. Six instantaneous images (out of 300) for each pylon configuration at $13.6 d_e$ are also displayed in Appendix D so the reader can view how the plume shapes change over time. As an example, Fig. 5.4 shows one instantaneous image for each pylon configuration at $13.6 d_e$ along with the ensemble averaged image of all 300 instantaneous images.

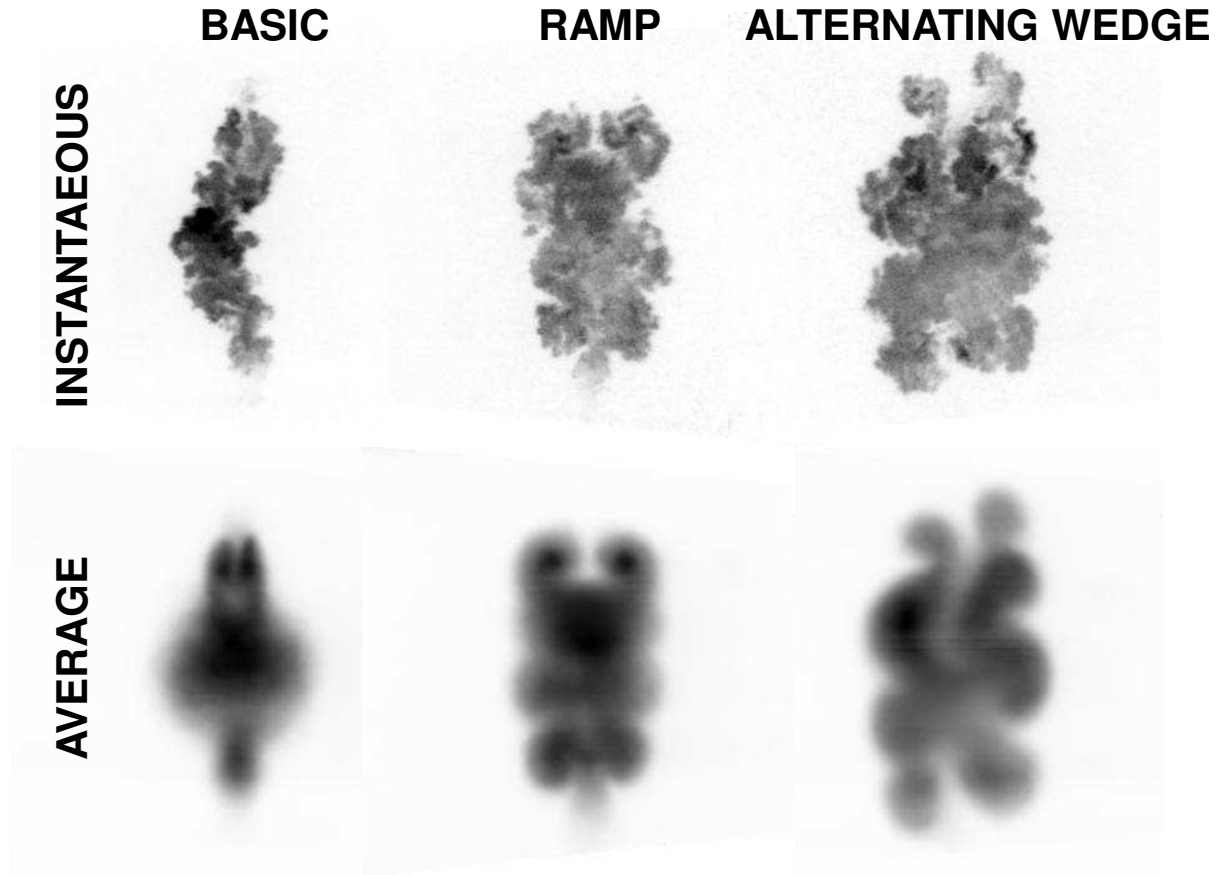


Fig. 5.4 NO-PLIF images at $13.6 d_e$.

The basic pylon injectant plume is highly unsteady, exhibiting side-to-side movement about the centerline of the plume. This is experimental verification of the vortex shedding observed in CFD simulation results for the basic pylon. An instantaneous NO-PLIF image of a basic pylon plume profile varies substantially from the ensemble

ble averaged image. An instantaneous image from the ramp and alternating wedge pylons also shows some variation from the ensemble averaged image, but it is much less pronounced than the basic pylon. The wake region flow of the two hypermixer pylons is much steadier than that of the basic pylon. For additional help visualizing unsteadiness in the plume profiles, standard deviation images are also constructed.

Normalized standard deviation images are shown for three planar positions in Appendix D (Fig. D.7). The standard deviation images are normalized to the maximum pixel intensity present at each planar position. The standard deviation images are a good visual representation of the amount of unsteadiness present in the plume shape at each planar position since the standard deviation is a measure of spatial intensity change among the 300 instantaneous images. At each planar position the basic pylon exhibits the darkest standard deviation image, corresponding to the most unsteady plume. The darkest (most unsteady) part of the basic pylon standard deviation plume image is located at the mid-height of the plume’s vertical extent, where the vortex shedding is occurring. Since vortex shedding is not present in the wake region of the hypermixer pylons, the outer edges of the injectant plume are the darkest, most unsteady area for those pylons, where the injectant and wind tunnel air meet.

The NO-PLIF instantaneous, averaged, and standard deviation plume profile images verify the characteristics of the pylon wake flows seen in the CFD simulation results for each pylon configuration. A steady state CFD solution was found for the ramp and alternating wedge pylons, and a time accurate solution with vortex shedding was found for the basic pylon. The NO-PLIF images verify the basic pylon exhibits unsteady vortex shedding, and the hypermixer pylons have steadier wake regions compared to the basic pylon.

Plume Profiles

Fuel plume profiles visualize the concentration of pylon injectant at downstream planar positions. They are the primary source of data for determining mixing effectiveness. Plume profiles were constructed using fluorescence signal data from the

NO-PLIF experiments (a qualitative measure), methane mass fraction data from the Raman experiments (a quantitative measure), and ethylene mass fraction data from CFD simulations (a quantitative simulation measure). Mach number data from the aerothermal probe experiments also offer visual plume profiles, but are not used in the mixing analysis. There were differences between plume profiles from different simulation and experimental data sources.

Plume profiles from simulation and experiment do not match precisely due primarily to test condition differences. Flow conditions in the CFD simulation wind tunnel were Mach number 2.0 and a Reynolds number of $2.9\text{E}7\text{ m}^{-1}$. The average flow conditions in the wind tunnel experiments were Mach number 1.95 and a Reynolds number of $2.4\text{E}7\text{ m}^{-1}$. The CFD wind tunnel was slightly larger than the actual wind tunnel, and viscous effects were not modeled on the walls of the simulation wind tunnel. The test conditions between simulation and experiment were not meant to match precisely. The simulations were accomplished as a precursor to wind tunnel experiments to gain knowledge of the pylon wake region flowfields prior to wind tunnel experiments.

Plume profiles also vary due to pylon injectant gas differences. The Raman experiments used methane injection, the NO-PLIF and aerothermal probe experiments air injection, and the CFD simulations ethylene injection from the pylon. In all cases the momentum ratios of the injectant gases to wind tunnel airflow were kept the same, but the mass flux ratios varied depending on injectant gas. The mass flux ratio of methane injection varied more than 25% from air or ethylene injection, resulting in plume profile concentration differences at the same planar position from each simulation and experiment.

Although these differences existed, meaningful data comparing the mixing effectiveness of the pylon configurations using all the plume profile data sources was possible. The same pylon mixing comparisons could be observed regardless of differences in mass flux ratios or test conditions. Whether simulation and experimental

calculated mixing quantities were directly comparable to one another, as long as each technique produced the same comparisons between the pylons, the objective was met.

There were some, at least qualitative, direct comparisons possible between simulation and experimental data. The test conditions between the NO-PLIF and Raman experiments were similar since they were both accomplished in the same wind tunnel environment, at the same wind tunnel test conditions, having the same momentum flux ratio. Although mixing quantities from the Raman plume profiles were not compared directly to mixing quantities from NO-PLIF or CFD plume profiles, the plume shapes and concentration distributions within the plume boundaries were directly compared between experiments due to the test condition similarities.

Another direct (qualitative) comparison was between mixing quantities of NO-PLIF experiments and CFD simulations. The NO-PLIF experiments and CFD simulations were similar in their injectant gases. The NO-PLIF experiments injected air seeded with a small amount NO. The CFD simulations incorporated ethylene injection. Ethylene and air have very similar molecular weights, and therefore have very similar mass flux ratios. However, test conditions between NO-PLIF experiments and CFD simulations varied, resulting in somewhat different plume profile shapes. Even though the CFD and NO-PLIF plume profile shapes could not be compared directly, the mixing quantities from each were qualitatively similar.

NO-PLIF Signal Intensity Profiles. Figures 5.5 and 5.6 show averaged NO-PLIF plume images of all three pylon configurations at six planar positions. The basic pylon plume close to the pylon base plane is a vertically long, thin strip of injectant gas. The plume spreads out horizontally and contracts in height as it grows in size with downstream distance. This vertical to horizontal plume shape change is called axis switching. The ramp pylon has tightly concentrated axial vortical structures close to the pylon base plane that help preserve the vertical extent of the ramp plume with downstream distance. The alternating wedge pylon also has vortical structures close to the pylon base plane that help preserve the vertical extent of the alternating

wedge plume moving downstream. Axis switching is not observed as much in the downstream development of the hypermixer pylons. The axis switching of the basic pylon is mostly a result of the ensemble averaging. The basic pylon instantaneous plume images are shifting left and right across the centerline of the plume due to the vortex shedding. The horizontal extent of the ensemble averaged plume image for the basic pylon is the mean horizontal variation over time. The plume is not actually present in the full horizontal extent at any one instant.

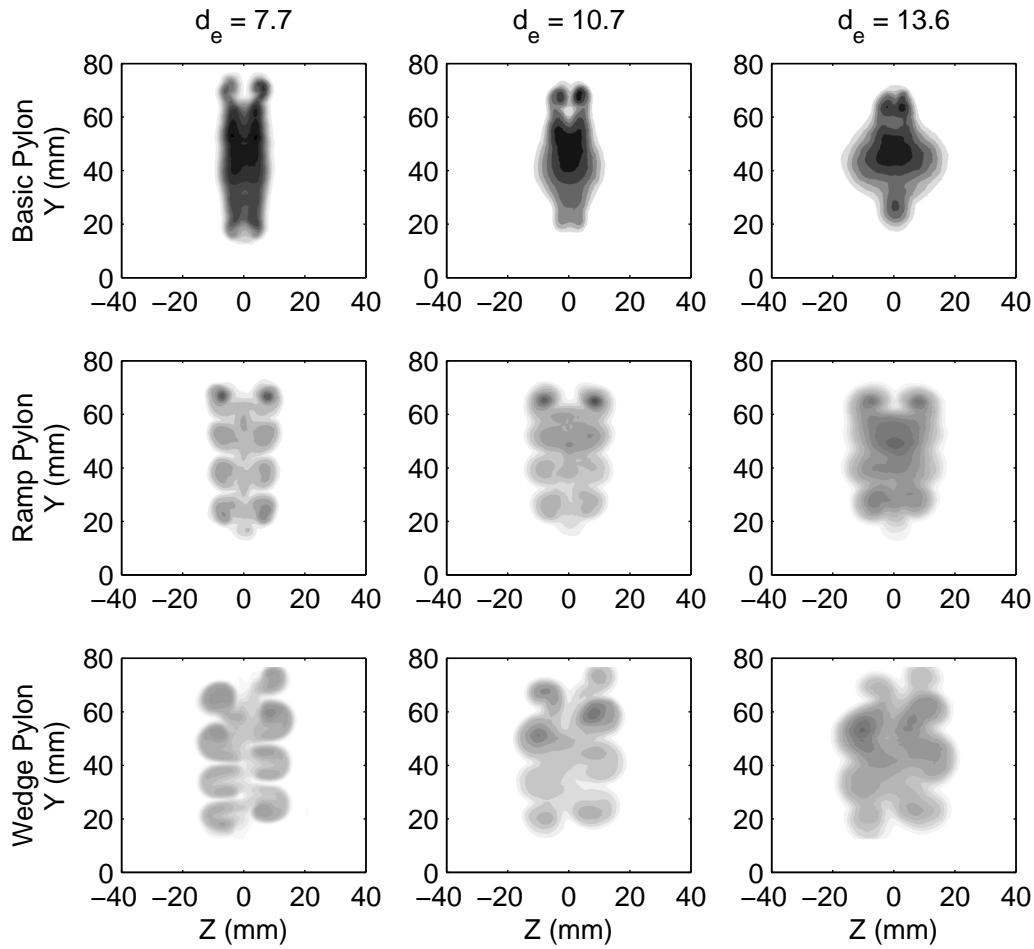


Fig. 5.5 NO-PLIF averaged plume profiles at $7.7 d_e$, $10.7 d_e$, and $13.6 d_e$.

From the NO-PLIF plume profiles in Figs. 5.5 and 5.6, an initial visual comparison of mixing is done. The pixel intensities of each image are normalized by the maximum pixel intensity present at each respective planar position. The darkest

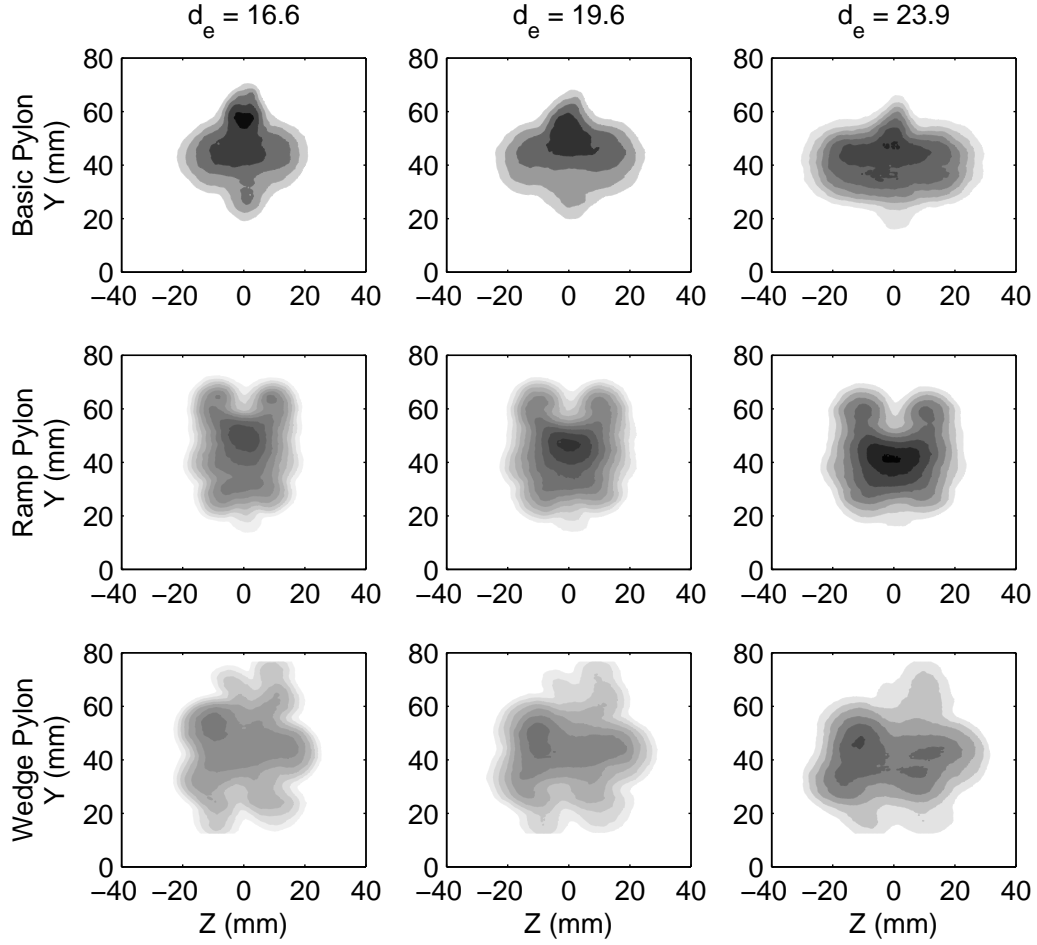


Fig. 5.6 NO-PLIF averaged plume profiles at $16.6 d_e$, $19.6 d_e$, and $23.9 d_e$.

image at a planar position corresponds to the least mixed injectant plume, and the lightest image corresponds to the most well mixed. Since the injectant plume intensity profiles are normalized globally, comparison between positions cannot be made with these plots. An attempt to globally normalize all plume intensity profiles was done, but the mixing rate behind the pylons was rapid enough that the pixel intensities at planar positions farther downstream were too white in the gray scale to be observed visually.

At the three planar positions closest to the pylon base plane in Fig. 5.5, the basic pylon has the darkest plume and is therefore the least mixed of the three. The ramp and alternating wedge pylons are lighter and similar in contrast, indicating

they have similar mixed states at these planar positions. At planar positions farther downstream in Fig. 5.6, there is less of a contrast difference between the three pylon injectant plumes, indicating less of a mixed state difference between the three. At the farthest planar position, $23.9 d_e$, the basic and ramp pylon injectant plumes are similar in darkness, indicating their mixed states are similar, while the alternating wedge appears slightly lighter, indicating a more mixed state than the other two.

Raman Methane Mass Fraction Profiles. Figure 5.7 shows methane mass fraction plume profiles constructed using Raman data at $13.6 d_e$ and $23.9 d_e$. Blowups of each profile are seen in Appendix C. Three of the methane mass fraction profiles are averaged because two test runs were accomplished for three of the six Raman experiments. The individual profiles of the three averaged profiles are shown in Appendix C side-by-side. In all three cases where multiple test runs are accomplished the two individual profiles are practically identical to the averaged profile. This shows good repeatability in the Raman measurements and data reduction procedure.

From the methane mass fraction profiles in Fig. 5.7, an initial visual comparison of mixing is done. Lower methane mass fractions indicate a better mixed, and therefore more diluted methane plume. The methane mass fractions are generally smaller at $23.9 d_e$ than at $13.6 d_e$, indicating more mixing with downstream distance. At $13.6 d_e$, the ramp and alternating wedge pylons result in noticeably lower mass fractions than the basic pylon, with the alternating wedge having the lowest methane mass fractions. At $23.9 d_e$, the alternating wedge pylon is still the most diluted of the three, and the ramp and basic pylons exhibit about the same dilution visually.

This is the same trend observed in the NO-PLIF plume profiles at $13.6 d_e$ and $23.9 d_e$. The ramp and alternating wedge pylons mix the injectant and wind tunnel airstream in a shorter distance, but the basic pylon eventually achieves a similar level of mixing to the hypermixer pylons as downstream distance increases.

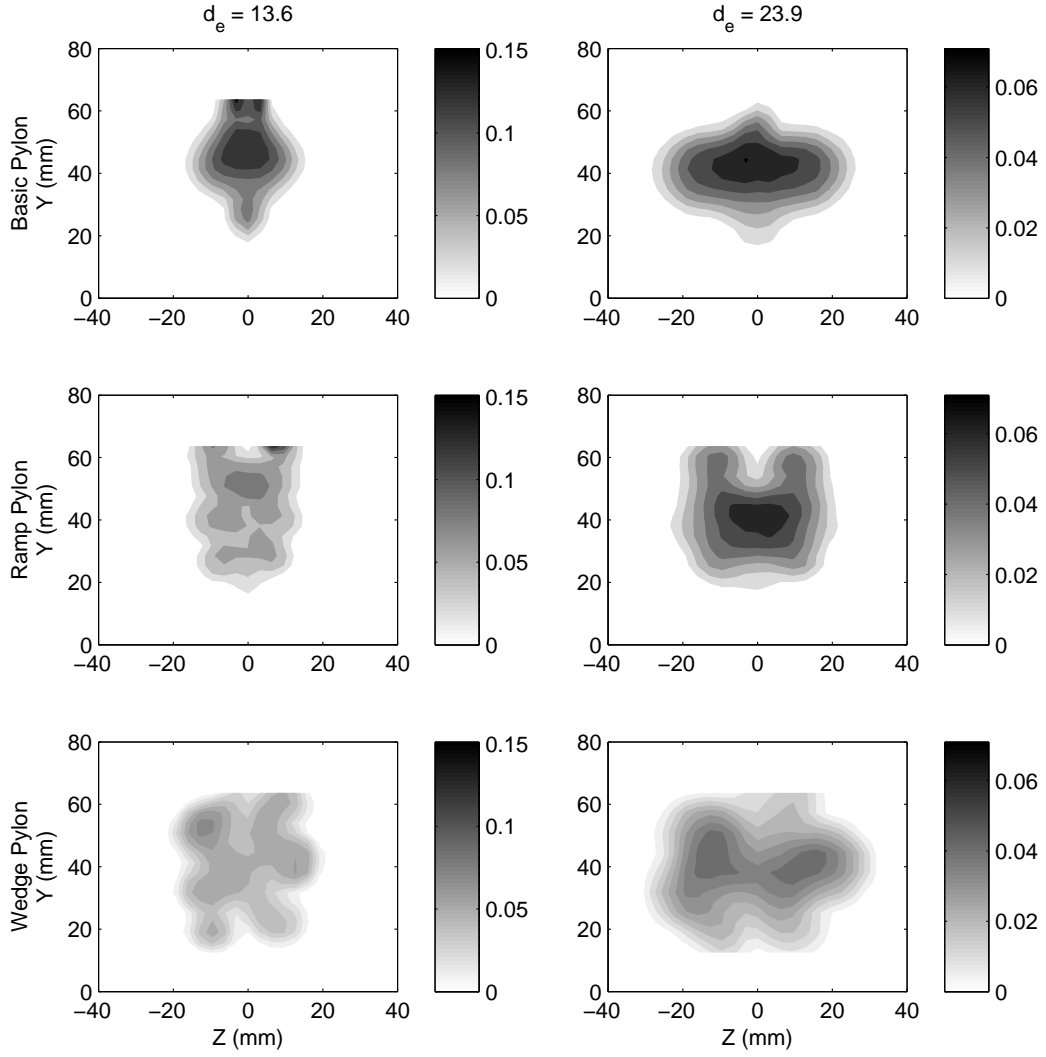


Fig. 5.7 Raman plume profiles at $13.6 d_e$ and $23.9 d_e$.

Raman and NO-PLIF Profile Comparisons. In order to show the monotonic, although qualitative, relationship between NO-PLIF fluorescence signal data and pylon injectant concentration described in Chapter 4, a direct comparison between Raman and NO-PLIF plume profiles is accomplished. The Raman plume profiles are very similar in size and shape to the NO-PLIF plume profiles at $13.6 d_e$ and $23.9 d_e$. This is due to the test condition similarities between the two experiments. Concentration data from the Raman experiments is in the form of mass fractions, and concentration data from the NO-PLIF experiments is in the form of fluorescence

signal intensities. The data is normalized for each planar position by the maximum concentration value at that position in each experiment. The average plume profile shapes from both experiments are shown in Figs. 5.8 and 5.9.

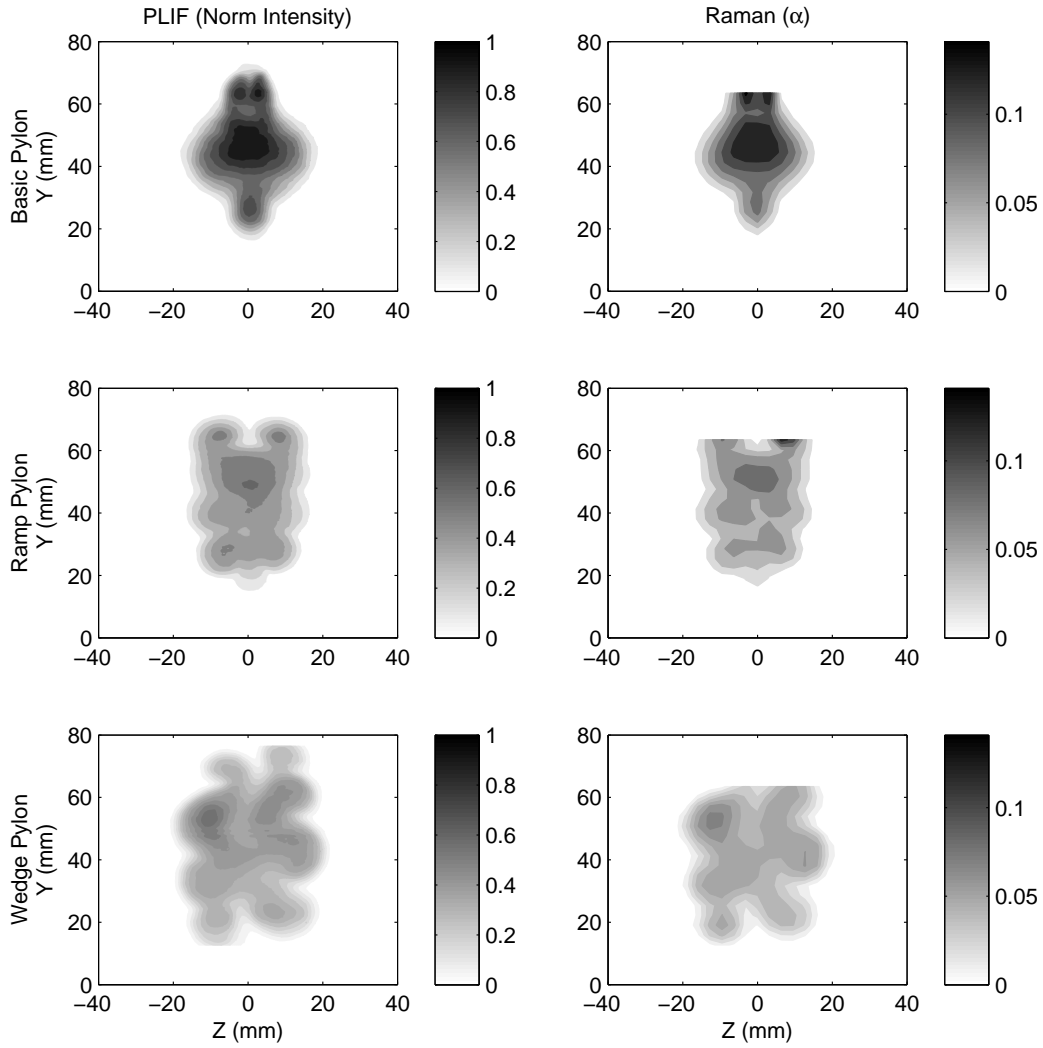


Fig. 5.8 Raman and NO-PLIF plume profile comparison at $13.6 d_e$.

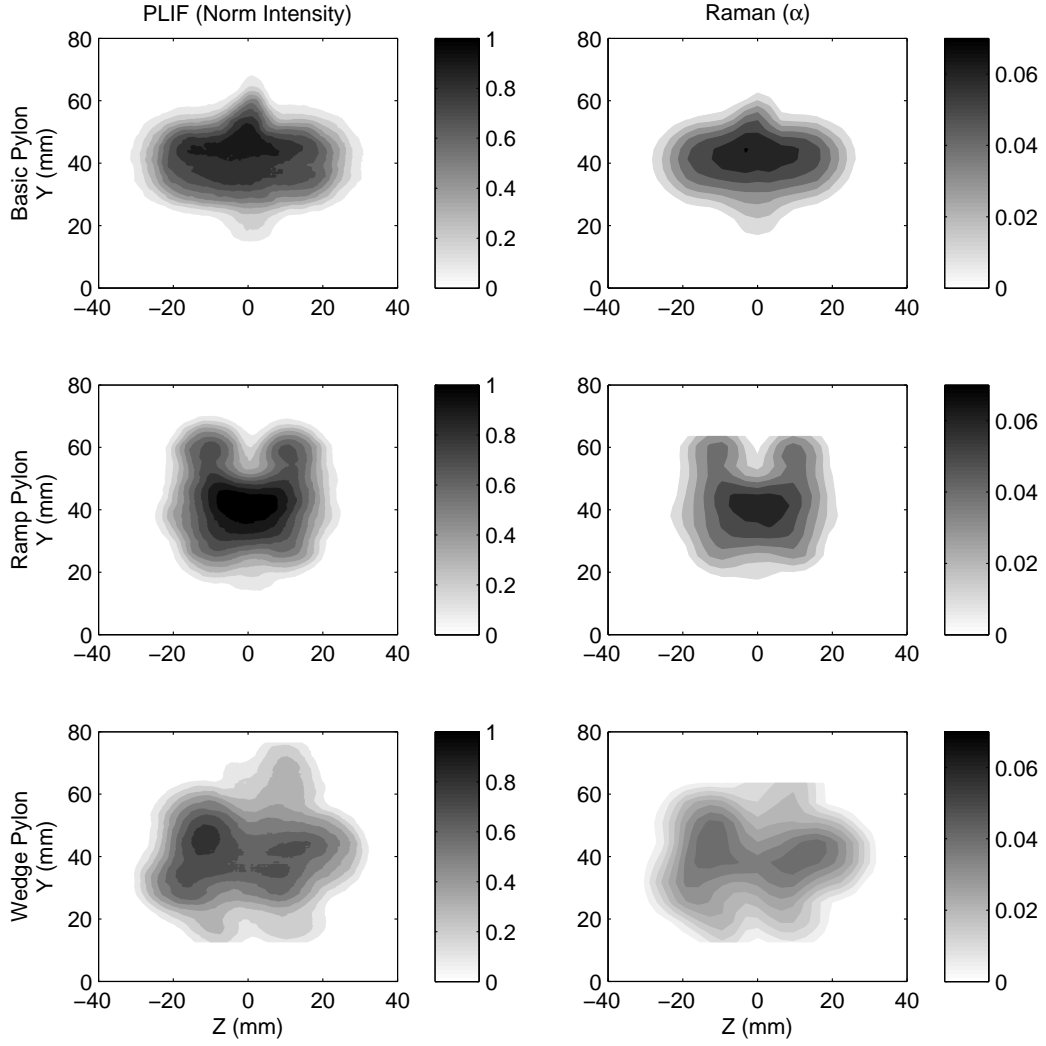


Fig. 5.9 Raman and NO-PLIF plume profile comparison at $23.9 d_e$.

The resolution and area extent of the plume profiles computed with concentration data from each experimental technique are different. The Raman data is plotted at 0.125 in space intervals in both the vertical and horizontal, and the NO-PLIF data is plotted at 0.254 mm space intervals in both the vertical and horizontal. The NO-PLIF plume data has an order of magnitude better resolution than the Raman data, so the edges of the plume are resolved more finely. Also, in the vertical direction

the Raman data is present up to 63.5 *mm* above the wind tunnel floor, whereas the NO-PLIF data is present up to 78.74 *mm* above the wind tunnel floor. More of the plume vertical extent is captured in the NO-PLIF images.

In Chapter 4 it was argued that although NO-PLIF fluorescence signals are qualitative (due to variations of the fluorescence signal with temperature and pressure), the fluorescence signal could be considered to monotonically increase with increasing pylon injectant concentrations. This allows a general plume mixing comparison between the pylons using NO-PLIF signal data. Figures 5.8 and 5.9 both visually appear to support this monotonic relationship. The increasing and decreasing concentration areas in the Raman plume profiles appear to be mirrored by increasing and decreasing fluorescence in the NO-PLIF plumes. A direct location by location comparison between the Raman and averaged NO-PLIF plume profiles is done to show this relationship. Raman mass fraction data are considered a quantitative concentration truth source to compare against the ensemble averaged NO-PLIF signal data in this analysis.

The comparison was accomplished as follows. The ensemble averaged NO-PLIF data was sampled at the resolution of the Raman data, the comparison region extending to the edges of the Raman plume profile. Figure 5.10 shows the Raman-calculated methane mass fraction against the NO-PLIF fluorescence signal intensity for all locations inside the comparison region at planar positions 13.6 d_e and 23.9 d_e . A monotonic (generally linear) relationship between pylon injectant concentration and NO-PLIF signal intensity is observed. There is scatter in the data since the NO-PLIF measurements are qualitative, but the trend is apparent. More scatter is present at 13.6 d_e than at 23.9 d_e . This is expected because pressure and temperature variations are larger at planar positions closer to the base plane of the pylon.

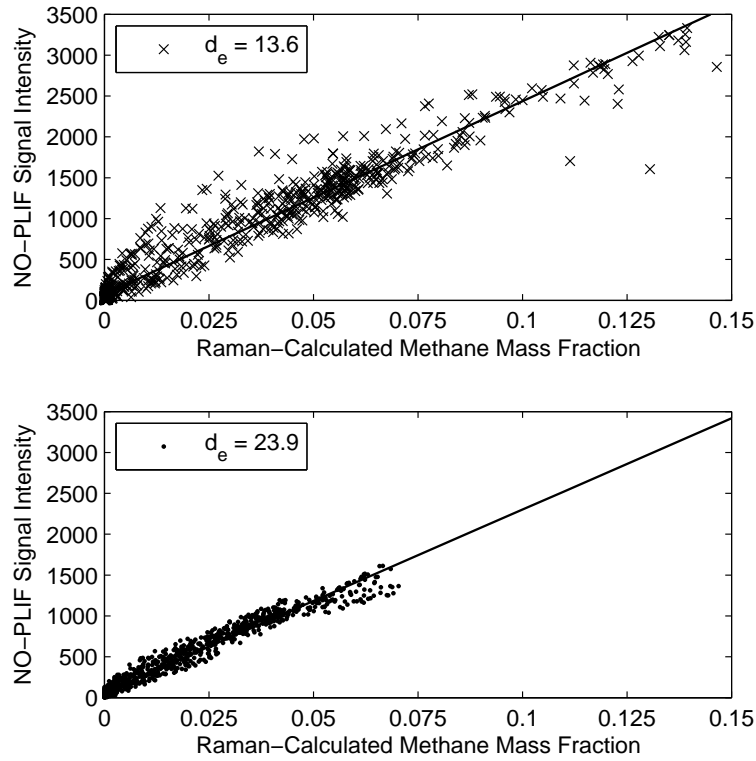


Fig. 5.10 NO-PLIF signal comparison to Raman concentration data.

Figure 5.11 breaks out the comparison for each pylon configuration. The difference in scatter present at $13.6 d_e$ compared to $23.9 d_e$ is apparent with all the pylon configurations. In addition, there are differences among the pylons. The basic pylon NO-PLIF signal data appears to have more overall scatter than the ramp and alternating wedge pylons at $13.6 d_e$, and at both $13.6 d_e$ and $23.9 d_e$ the basic pylon NO-PLIF signal data has more of a concave shape with rising concentration compared to a linear one with the other pylon configurations. The ramp and alternating wedge pylon NO-PLIF signal data are practically linear with less scatter than basic pylon; however, the ramp pylon at $13.6 d_e$ has two outlier data points that do not follow the linear trend.

The increased scatter and non-linear behavior of the basic pylon NO-PLIF signal data is most likely due to variable pressure in the unsteady characteristics of

its wake flow. It was confirmed by both simulation and experiment that the wake region flowfield of the basic pylon is highly unsteady. Pressure variations from the unsteady flow lead to collisional variations that vary the fluorescence signal due to both collisional de-activation rate changes (electronic quenching) and collisional line broadening changes (see Chapter 4).

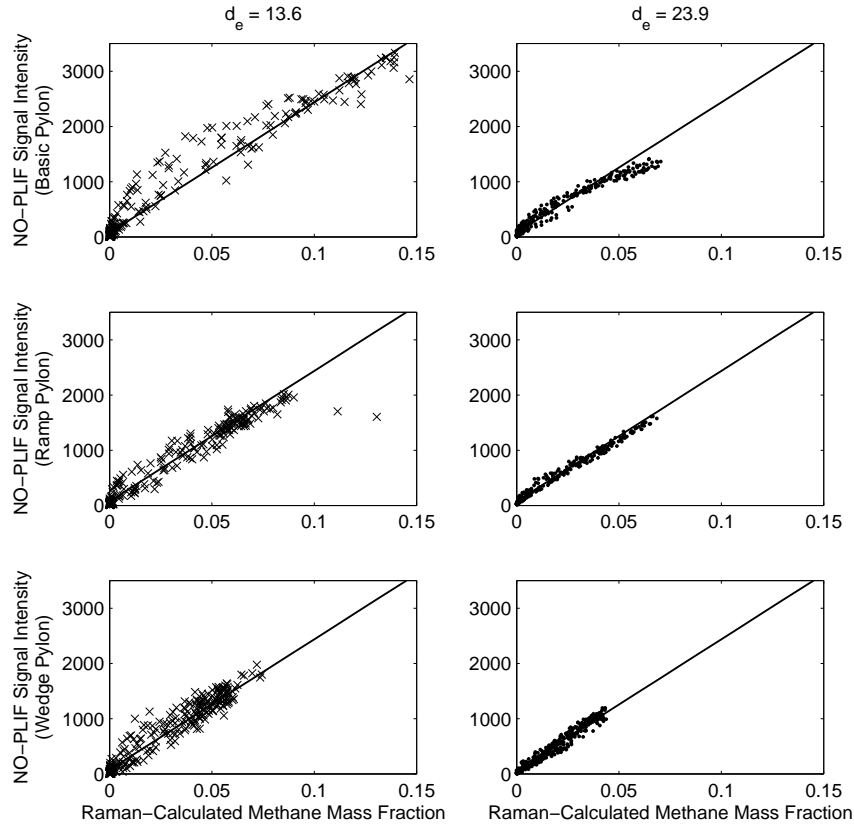


Fig. 5.11 NO-PLIF comparison with Raman for pylon configurations (summarized in 5.10)

CFD Ethylene Mass Fraction Profiles. Figures 5.12 and 5.13 show CFD ethylene mass fraction plume profiles of all three pylon configurations at the same six planar positions where NO-PLIF fluorescence data was gathered. Both an instantaneous and ensemble averaged (over one vortex shedding period) plume profile is shown for the basic pylon due to its unsteady wake region. The averaged plume profiles are somewhat similar in shape to the NO-PLIF plume profiles in Figs. 5.5

and 5.6, however, the plume shapes are not precisely similar due to test condition differences. There is more similarity in the plume shapes closer to the pylon base plane, prior to where shocks bouncing off the wind tunnel side walls intersect the pylon wake region.

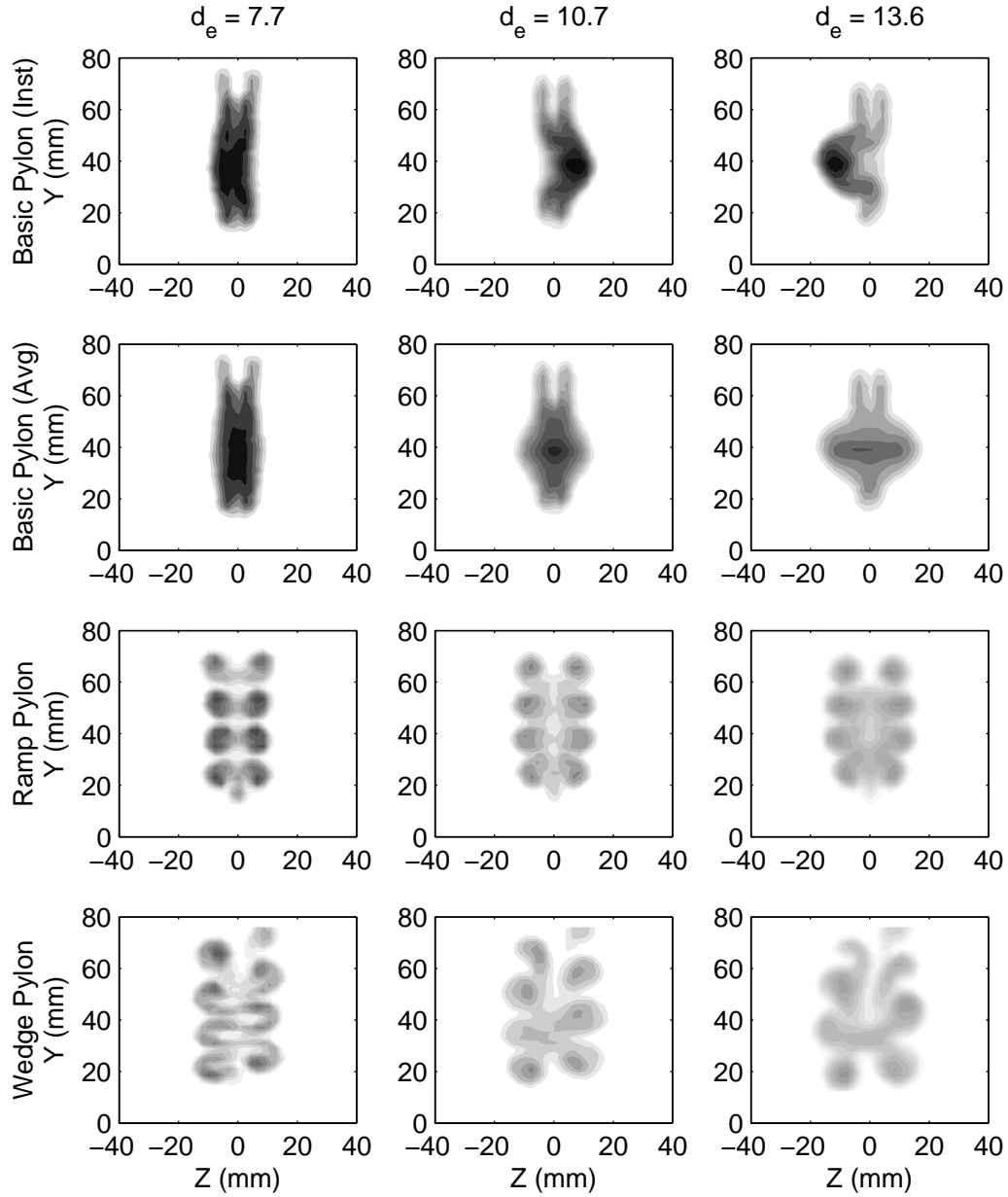


Fig. 5.12 CFD plume profiles at $7.7 d_e$, $10.7 d_e$, and $13.6 d_e$.

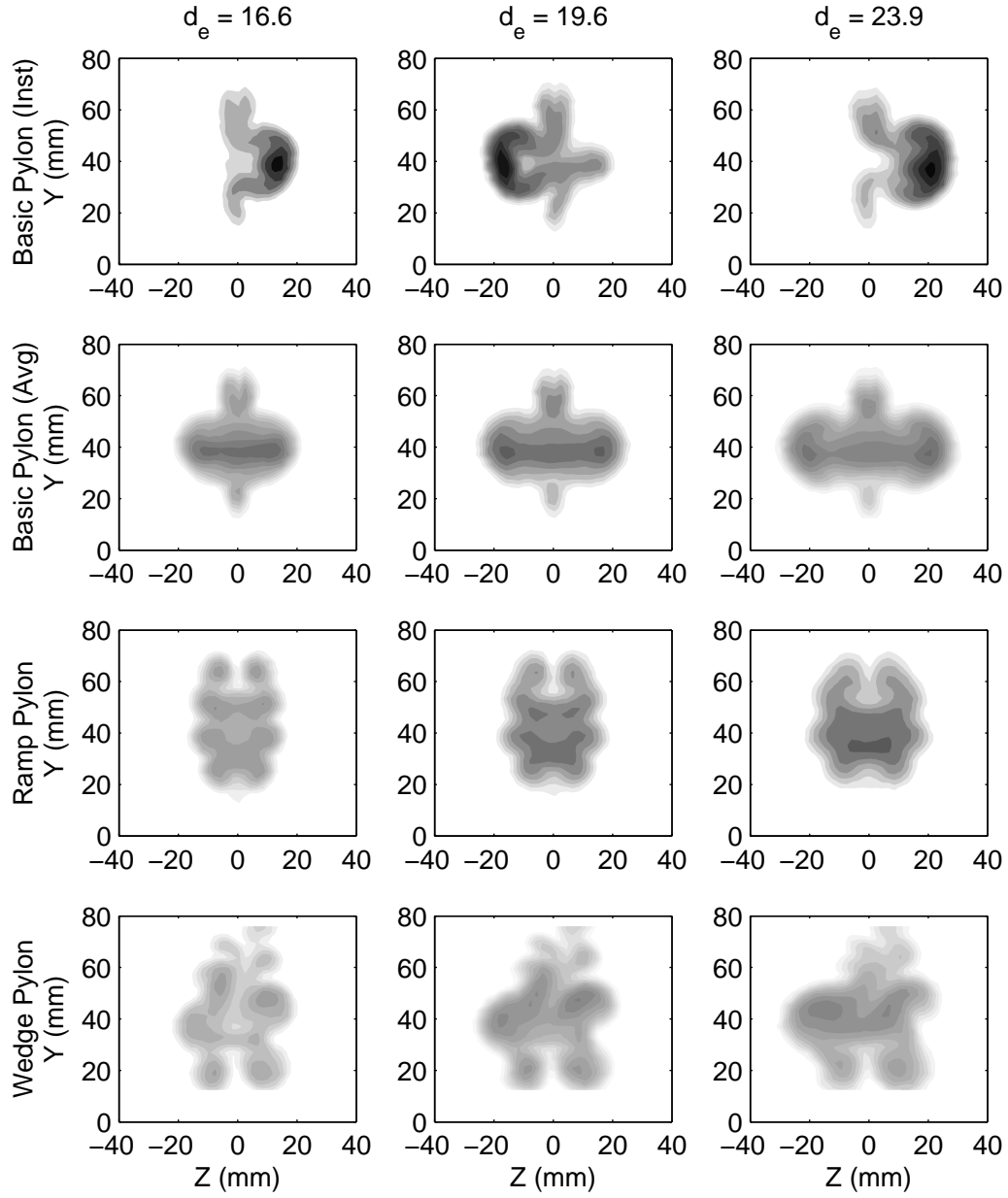


Fig. 5.13 CFD plume profiles at $16.6 d_e$, $19.6 d_e$, and $23.9 d_e$.

As with the Raman and NO-PLIF plume profiles, an initial visual comparison of mixing is made using Figs. 5.5 and 5.6. The ethylene mass fractions in each figure are normalized by the maximum ethylene mass fraction present at each planar position

from the three pylons. The darkest images correspond to the least mixed injectant plumes at each planar position. It is visually evident that the instantaneous plume profile of the basic pylon is the least mixed at every planar position. It is darker than the ensemble averaged basic, ramp, and alternating wedge plume profiles at every planar position. This difference between instantaneous plume data and averaged plume data for the basic pylon is explored in depth in a subsequent section.

Ignoring the instantaneous basic pylon plume image for now, the general mixing trend matches that seen in the NO-PLIF and Raman plume profiles. Closer to the pylon base, the basic pylon exhibits the darkest plume images, indicating it is the least mixed fuel plume of the three. Farther away from the pylon base, there is less of a contrast difference between the three pylon configurations, indicating less of a mixed difference in the fuel plumes.

Aerothermal Probe Profiles. Figures 5.14, 5.15, and 5.16 show Mach number profiles constructed from aerothermal probe data at $23.9 d_e$. The Mach number profiles for all three pylon configurations at this planar position are supersonic throughout. The shapes of the Mach number profiles are very similar to the fuel plume shapes from Raman and NO-PLIF data at $23.9 d_e$ (Fig. 5.9). In the absence of injectant concentration measurements, one could use these Mach number profiles as a visual, qualitative assessment of the size and shape of the fuel plumes. The Mach number profiles are not, however, used for any type of mixing analysis.

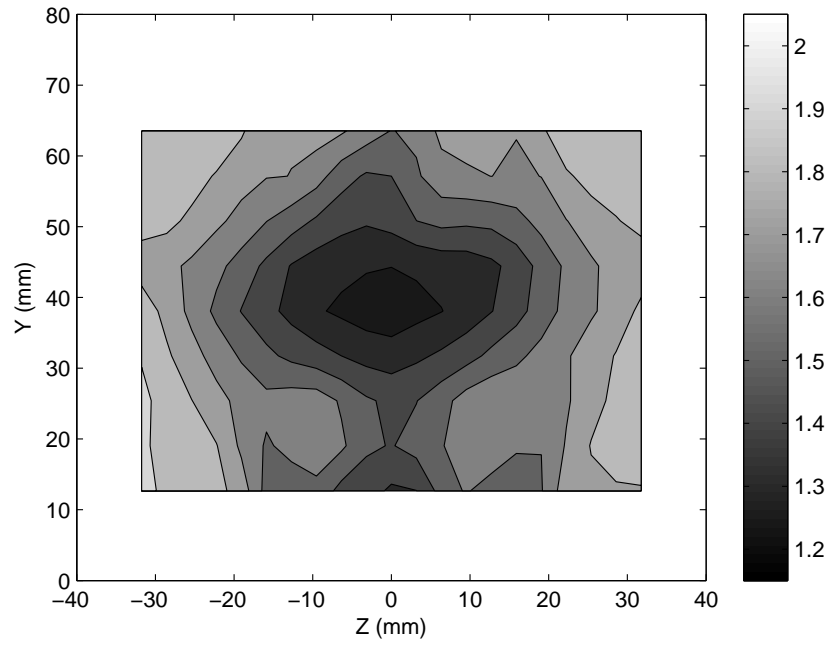


Fig. 5.14 Basic pylon Mach profile at $23.9 d_e$.

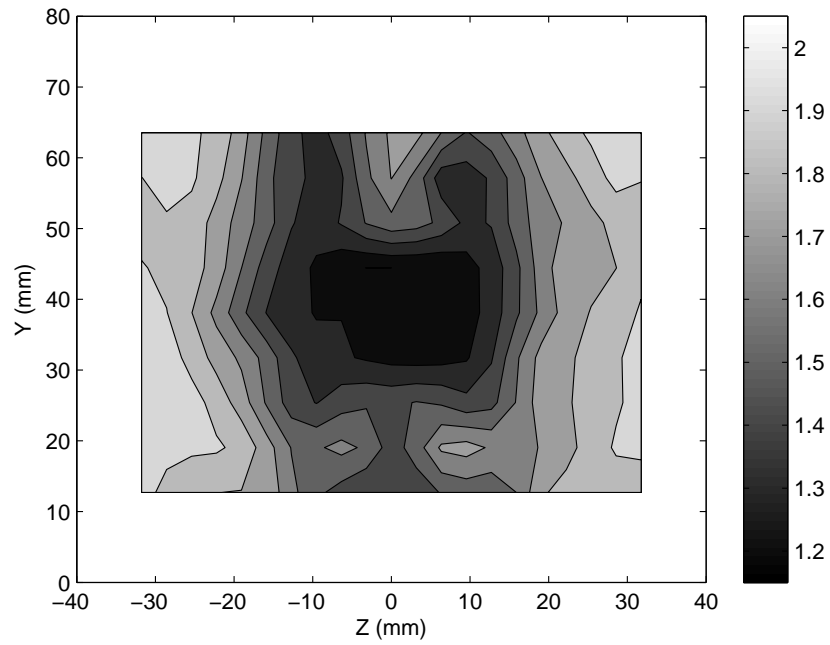


Fig. 5.15 Ramp pylon Mach profile at $23.9 d_e$.

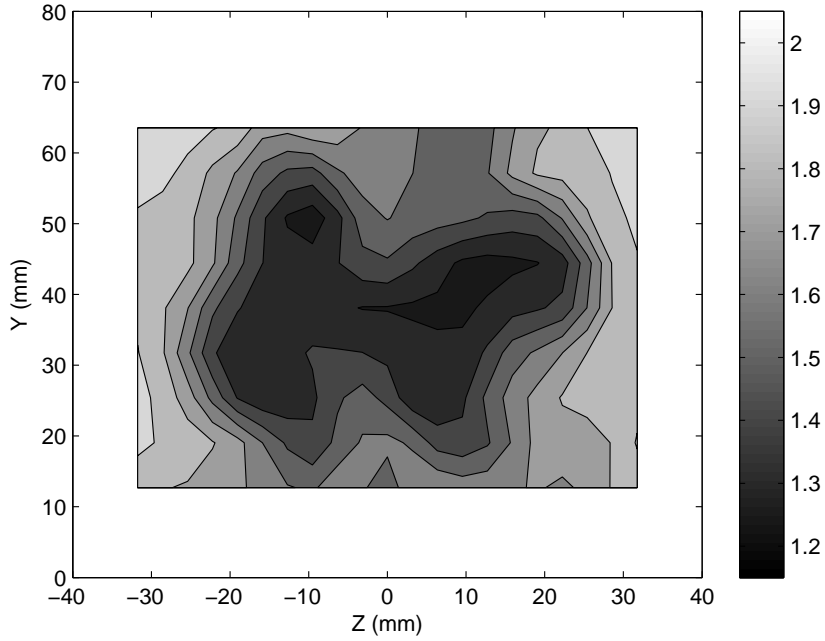


Fig. 5.16 Alternating wedge pylon Mach profile at $23.9 d_e$.

Concentration measurements using the aerothermal probes were attempted in wind tunnel experiments using total temperature distributions with the mixing analogy. Unfortunately, the concentration measurements were not successful. Pylon injectant mass fraction plume profiles constructed from the aerothermal probe data at $23.9 d_e$ are shown in Fig. 5.17. A side-by-side shape comparison is made between mixing analogy mass fraction plume profiles and those obtained in Raman experiments at the same planar positions. Due to total temperature variations in the wind tunnel and pylon injection gas during testing, the mass fraction plume profiles produced are not adequate to compare the pylon mixing capabilities. However, the ramp pylon mass fraction plume profile in particular shows some promise for the mixing analogy method if the wind tunnel and pylon total temperatures could be regulated more precisely.

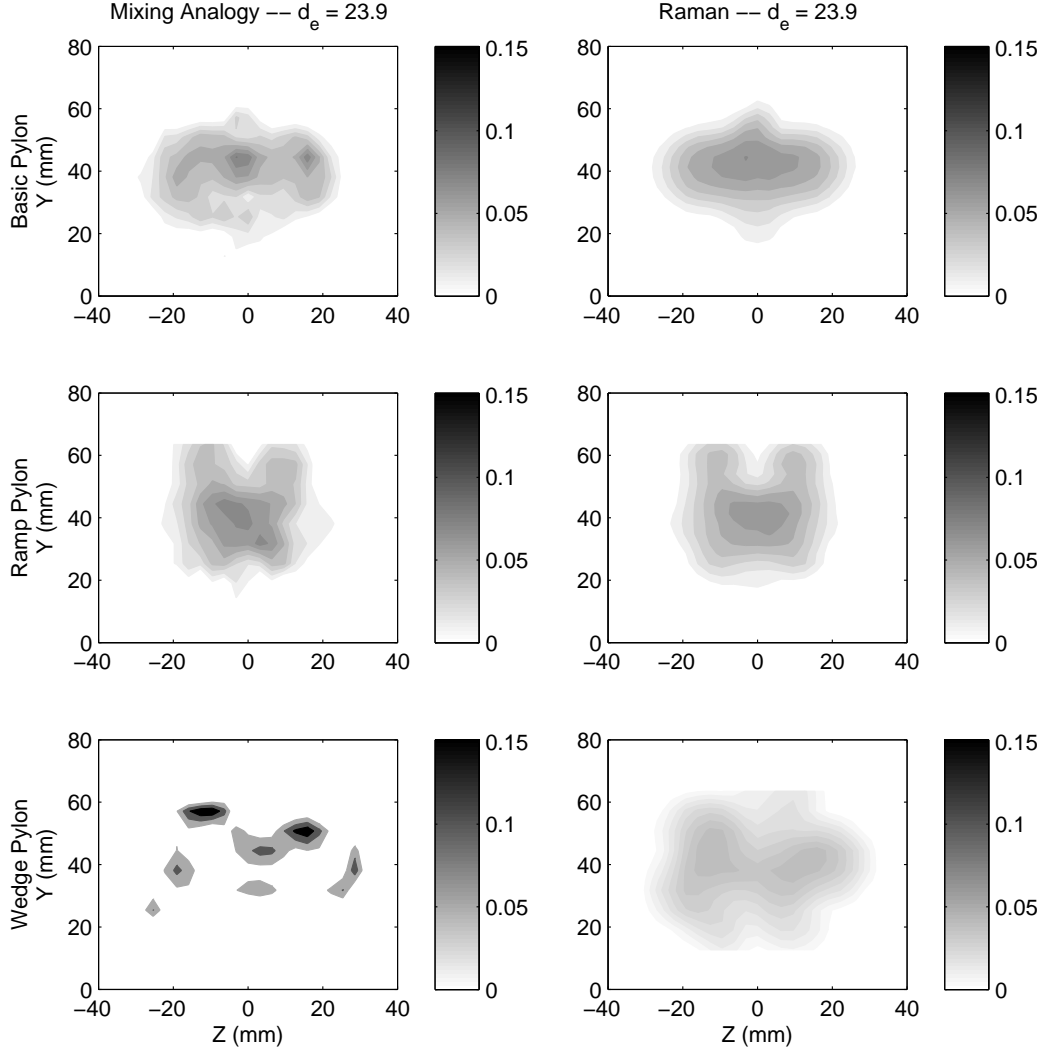


Fig. 5.17 Mixing analogy plume profiles at $23.9 d_e$.

Mixing Analysis

A mixing analysis of the three pylon configurations includes the calculated mixing parameters of streamwise vortex magnitudes from CFD simulation data; plume dilution from CFD simulation data and NO-PLIF and Raman concentration measurements; and plume flammability from CFD simulation data and Raman concentration measurements. The mixing parameters are used to compare the pylon configurations and determine which one is a more effective mixer. An initial, visual comparison

of mixing between the basic, ramp, and alternating wedge pylons was done in the previous section. The goal of this section is to put some quantitative analysis behind those visual comparisons.

Streamwise Vortex Magnitudes. The streamwise vortex magnitudes produced by the three pylons are compared in Fig. 5.18 from CFD simulation data. It is difficult to make direct planar position comparisons between the basic pylon and the other two given the slight mass flow variations (shown in Chapter 4) in the basic pylon time accurate CFD solution. However, there are general trends.

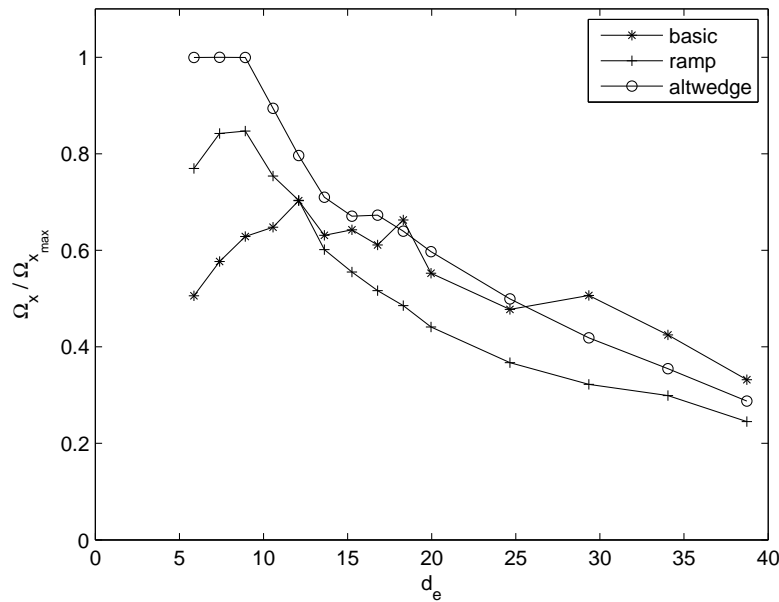


Fig. 5.18 Streamwise vortex magnitude comparison.

The streamwise vortical motion immediately downstream (in the near-field) of the ramp and alternating wedge pylons is increased over the basic pylon due to the vortical inducing geometries at the aft end of those pylons. The alternating wedge pylon exhibits the largest streamwise vortex magnitudes overall. Looking past the near-field, the difference in streamwise vortical motion among the pylon configurations is less. The heightened streamwise vortex magnitudes in the near-field region of the

ramp and alternating wedge pylons are shown in the next section to increase the fuel dilution rate into the airstream compared to the basic pylon.

Plume Dilution. The link between larger streamwise vortex magnitudes and increased mixing effectiveness is seen in fuel plume dilution parameters. One method of determining plume dilution, the mixing efficiency quantity (discussed in Chapter 4), is shown in Fig. 5.19. Only CFD simulation data is used to calculate the mixing efficiency quantity because it is the only data collection method where all the flowfield data are available for the complicated calculation. The other method of determining plume dilution, maximum concentration (fuel mass fraction or signal intensity) at a planar position, is used with CFD simulation data and Raman and NO-PLIF concentration measurements.

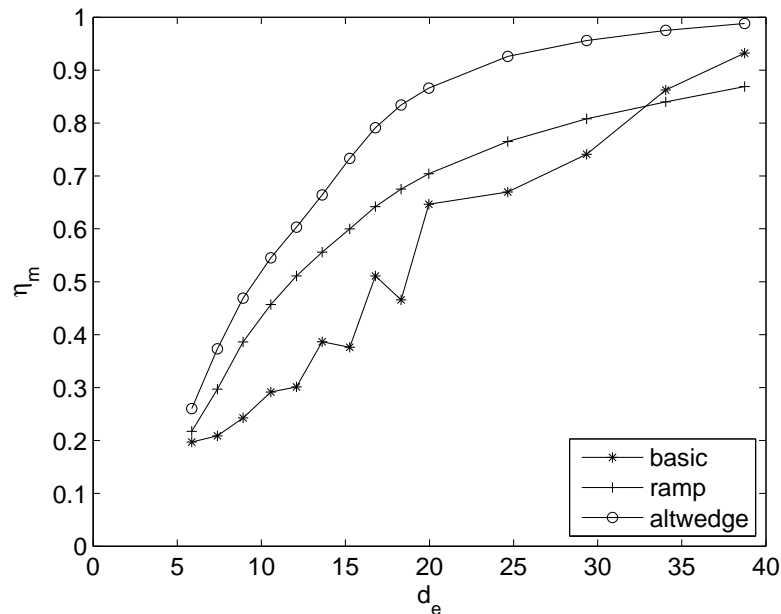


Fig. 5.19 Ethylene/air mixing efficiency comparison.

Observing the mixing efficiency quantity throughout the pylon wake region in Fig. 5.19, the mixing efficiency of all pylon configurations increases with downstream distance. The alternating wedge pylon exhibits the greatest mixing efficiency through-

out the wake region. The ramp pylon has the second largest mixing efficiency throughout the near-field and most of the far-field region. The basic pylon has the least mixing efficiency in the near-field and matches the mixing efficiency of the ramp pylon at the end of the calculated far-field region.

The mixing efficiency quantity comparison between the pylons shows that in simulation results, streamwise vortex enhancement in the pylon wake flow increases mixing effectiveness. The pylon having the largest magnitude of streamwise vortices (the alternating wedge) in the near-field exhibits the largest mixing efficiencies in the near-field and throughout the wake region calculated in the simulation. The pylon with the smallest magnitude of streamwise vortices in the near-field (the basic pylon) exhibits the smallest mixing efficiencies in the near-field and throughout most the far-field wake region calculated in the simulation. This mixing effectiveness comparison between the pylon configurations using simulation results is verified by experimental data in subsequent subsections.

Instantaneous versus Averaged Concentration Data. Before discussing the rest of the fuel plume dilution parameter data, a distinction should be made between ensemble averaged concentration data and instantaneous concentration data. As seen previously from a visual comparison between instantaneous and ensemble averaged CFD simulation plume profiles of the basic pylon, the instantaneous plume profiles (using ethylene mass fraction data) were darker in contrast to the ensemble averaged plume profiles at the same planar positions, indicating the instantaneous plumes were less diluted into the airstream than the ensemble averaged ones. This visual observation is verifiable through quantitative analysis.

Using NO-PLIF fluorescence signal image data, maximum pixel intensity values for both the ensemble averaged as well as the instantaneous plume profiles are calculated, but determined differently in each case. The maximum pixel intensities for the ensemble averaged plume profiles are calculated by averaging the top 1% of pixel intensities (a sample of data) in the ensemble averaged plume images. The maximum

pixel intensities for the instantaneous profiles are calculated by averaging the top 1% of pixel intensities in each of the 300 instantaneous plume images for each planar position, then averaging the 300 maximum intensity values to obtain a representative maximum pixel intensity for each position.

Since an average was calculated in each case, it is important to understand whether there is statistical significance between the maximum pixel intensities (the top 1% sample averages). This is determined using the standard deviation of each sample. The averaged maximum pixel intensities are statistically different at the 90% confidence level if they are separated by more than their standard deviations summed multiplied by 1.282. [95]

A statistical difference between the maximum pixel intensities of the instantaneous plume profiles and averaged plume profile at a planar position would not be present if the fuel plumes were perfectly steady. One calculation is the maximum of the instantaneous plume information averaged, and the other calculation is the maximum of the averaged plume information. However, in an unsteady flow, the two calculations produce different results.

To illustrate the difference, Fig. 5.20 shows the normalized maximum pixel intensities using the ensemble averaged and instantaneous averaged methods for the three pylon configurations at six planar positions. The maximum pixel intensity globally is located in the the $7.7 d_e$ plane for the NO-PLIF instantaneous image data of the basic pylon. The normalized average and standard deviation values for each sample are shown in Table 5.1, and Table 5.2 shows whether the maximum plume pixel intensity values are statistically different at the 90% confidence level ("Y" = yes and "N" = no).

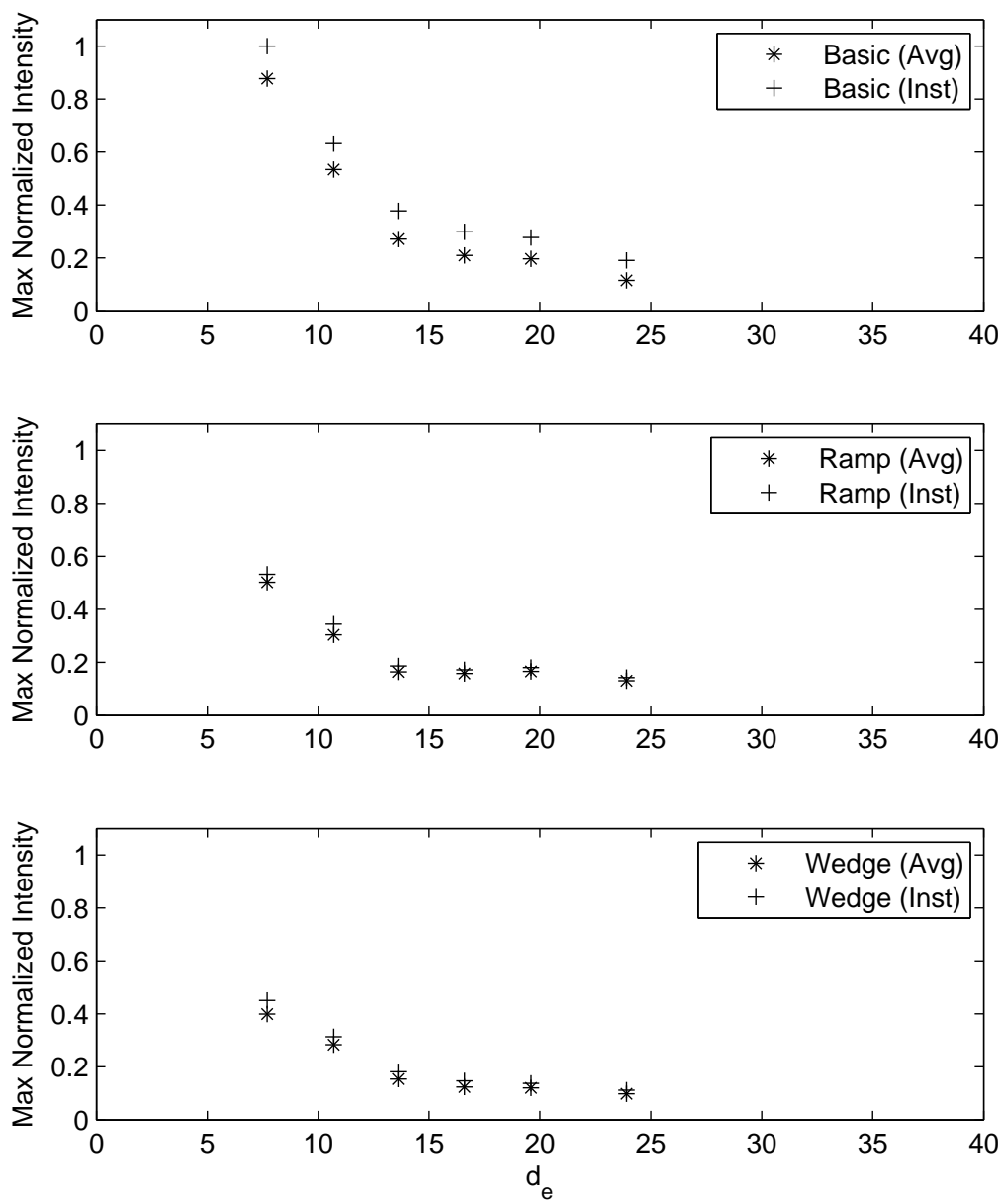


Fig. 5.20 NO-PLIF averaged versus instantaneous maximum pixel intensities.

Table 5.1 NO-PLIF averaged versus instantaneous maximum pixel intensity data.

Pylon	Statistic	7.7 d_e	10.7 d_e	13.6 d_e	16.6 d_e	19.6 d_e	23.9 d_e
Basic(Inst)	Mean	1.0000	0.6312	0.3776	0.2981	0.2767	0.1902
	Sdev	0.0546	0.0284	0.0181	0.0144	0.0132	0.0091
Basic(Avg)	Mean	0.8776	0.5335	0.2706	0.2095	0.1965	0.1142
	Sdev	0.0133	0.0040	0.0032	0.0047	0.0037	0.0012
Ramp(Inst)	Mean	0.5327	0.3441	0.1867	0.1720	0.1805	0.1428
	Sdev	0.0575	0.0394	0.0092	0.0057	0.0055	0.0045
Ramp(Avg)	Mean	0.5025	0.3038	0.1647	0.1586	0.1658	0.1310
	Sdev	0.0572	0.0345	0.0029	0.0025	0.0017	0.0017
Wedge(Inst)	Mean	0.4505	0.3134	0.1811	0.1467	0.1376	0.1119
	Sdev	0.0281	0.0180	0.0098	0.0065	0.0048	0.0037
Wedge(Avg)	Mean	0.3996	0.2840	0.1537	0.1240	0.1208	0.0980
	Sdev	0.0121	0.0129	0.0062	0.0029	0.0017	0.0014

Table 5.2 NO-PLIF averaged versus instantaneous maximum pixel intensity statistical difference.

Comparison	7.7 d_e	10.7 d_e	13.6 d_e	16.6 d_e	19.6 d_e	23.9 d_e
Basic(Inst)/Basic(Avg)	Y	Y	Y	Y	Y	Y
Ramp(Inst)/Ramp(Avg)	N	N	Y	Y	Y	Y
Wedge(Inst)/Wedge(Avg)	N	N	Y	Y	Y	Y

The basic pylon instantaneous and averaged maximum pixel intensity data are statistically different at the 90% confidence level at all planar positions. The instantaneous data is consistently higher compared to the averaged data. The ramp and alternating wedge pylon instantaneous and averaged data are not statistically different from one another at all planar positions. The ramp and alternating wedge pylons

show much less difference overall between instantaneous and averaged maximum pixel intensity data compared to the basic pylon.

Figure 5.20 shows the ensemble averaged concentration data overestimates the mixed state of the fuel plume compared to instantaneous data by depicting a more diluted fuel plume than reality. Spatially averaging unsteady flow quantities tends to depress peaks in the concentration data. Since the basic pylon has more unsteadiness in its wake region compared to the hypermixer pylons, the ensemble averaged images depress the maximum pixel intensities to a greater extent. This results in an over-estimation of the mixing capability of the basic pylon more so than the hypermixer pylons.

The logical question to ask is whether the instantaneous information or the ensemble averaged information is more indicative of the plume's susceptibility to combustion over time. That question cannot be answered by these experiments. Combustion experiments are required. However, the instantaneous composition of fuel and air mixtures should be a better indication of combustion potential over time because the instantaneous flowfield is physically where the fuel and air meet. They do not physically meet in an ensemble averaged sense.

The difference between averaged and instantaneous data has ramifications for other experiments and direct simulation/experiment comparisons. The Raman experiments measured average quantities due to the data integration time of that experimental technique, so those measured concentrations overestimate the basic pylon fuel plume dilution rate. The CFD results for the basic pylon were presented previously using data from instantaneous snapshots of the wake flow instead of ensemble averaged data, so ethylene mass fraction data from those results accurately reflect the basic pylon mixing. The aerothermal probe experiments measured averaged flow quantities due to the integration time of that method, so the total pressure calculation comparisons between simulation and experiment is done with ensemble averaged simulation data.

As it turns out, regardless of whether instantaneous or averaged concentration data is used for the basic pylon, the ramp and alternating wedge pylons still show a mixing advantage over the basic pylon in the near-field. In the far-field the mixing advantage of the hypermixer pylons over the basic pylon extends farther downstream using the instantaneous concentration data for the basic pylon. Since the differences in instantaneous and averaged concentration data between the ramp and alternating wedge pylons are much less, averaged concentration data only is used for their mixing effectiveness comparison.

NO-PLIF Maximum Concentration Calculations. Figure 5.21 shows a plume dilution comparison among the three pylon configurations using NO-PLIF maximum pixel intensity data. The maximum pixel intensity values in each plume profile are normalized by the maximum pixel intensity globally. The maximum pixel intensity globally is located in the $7.7 d_e$ instantaneous maximum pixel data of the basic pylon. Since all maximum pixel intensities are normalized across planar positions, comparisons among positions are made using Fig. 5.21. The normalized average and standard deviation values for each sample are shown in Table 5.5, and Table 5.6 shows whether the maximum plume pixel intensity values are statistically different at the 90% confidence level ("Y" = yes and "N" = no).

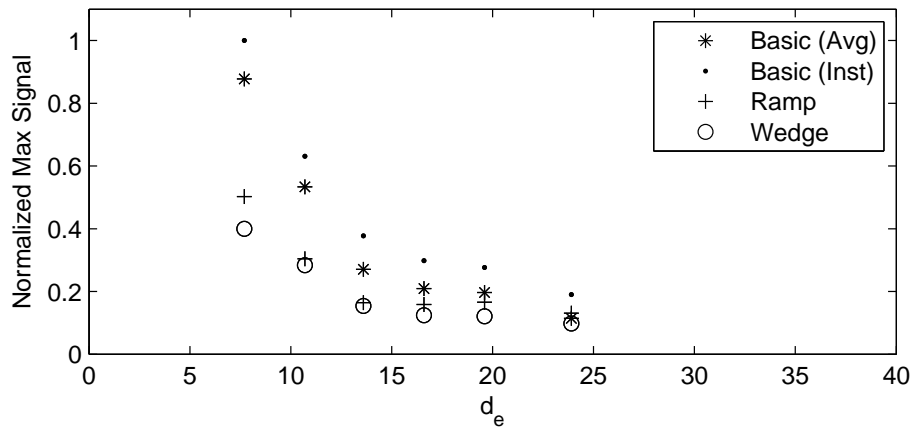


Fig. 5.21 NO-PLIF normalized maximum pixel intensity comparison.

Table 5.3 NO-PLIF normalized maximum pixel intensity data.

Pylon	Statistic	7.7 d_e	10.7 d_e	13.6 d_e	16.6 d_e	19.6 d_e	23.9 d_e
Basic(Inst)	Mean	1.0000	0.6312	0.3776	0.2981	0.2767	0.1902
	Sdev	0.0546	0.0284	0.0181	0.0144	0.0132	0.0091
Basic(Avg)	Mean	0.8776	0.5335	0.2706	0.2095	0.1965	0.1142
	Sdev	0.0133	0.0040	0.0032	0.0047	0.0037	0.0012
Ramp(Avg)	Mean	0.5025	0.3038	0.1647	0.1586	0.1658	0.1310
	Sdev	0.0572	0.0345	0.0029	0.0025	0.0017	0.0017
Wedge(Avg)	Mean	0.3996	0.2840	0.1537	0.1240	0.1208	0.0980
	Sdev	0.0121	0.0129	0.0062	0.0029	0.0017	0.0014

Table 5.4 NO-PLIF normalized maximum pixel intensity statistical difference.

Comparison	7.7 d_e	10.7 d_e	13.6 d_e	16.6 d_e	19.6 d_e	23.9 d_e
Basic(Avg)/Ramp(Avg)	Y	Y	Y	Y	Y	Y
Ramp(Avg)/Wedge(Avg)	Y	N	N	Y	Y	Y

The basic pylon and ramp pylon are statistically different at the 90% confidence level at all planar positions. The basic pylon has consistently higher maximum plume pixel intensities compared to the ramp pylon. The ramp and alternating wedge pylon maximum pixel intensities are not statistically different from one another at all planar positions, but those positions that are statistically different show the alternating wedge has lower maximum plume pixel intensities compared to the ramp.

The trends from Fig. 5.21 match the visual observations of the plume intensity profiles in Figs. 5.5 and 5.6. The ramp and alternating wedge pylons mix the injectant into the wind tunnel flow more quickly in the near-field, resulting in lower maximum pixel intensities compared to the basic pylon. However, the basic pylon eventually matches the mixing capability of the hypermixers further downstream. The ramp and alternating wedge pylons are very close in their maximum pixel intensities at every

planar position, but the alternating wedge does show a slight mixing advantage at most positions.

CFD Maximum Concentration Calculations. Figure 5.22 shows a plume dilution comparison among pylon configurations using CFD simulation maximum ethylene mass fraction data. The maximum ethylene mass fractions are shown at the same planar positions as the NO-PLIF maximum pixel intensities in Fig. 5.21. The maximum ethylene mass fraction values are all normalized by the maximum global ethylene mass fraction at any planar position, here at $7.7 d_e$ in the basic pylon instantaneous image. The non-normalized average and standard deviation values for each maximum ethylene mass fraction sample are shown in Table 5.5, and Table 5.6 shows whether the maximum plume pixel intensity values are statistically different at the 90% confidence level ("Y" = yes and "N" = no).

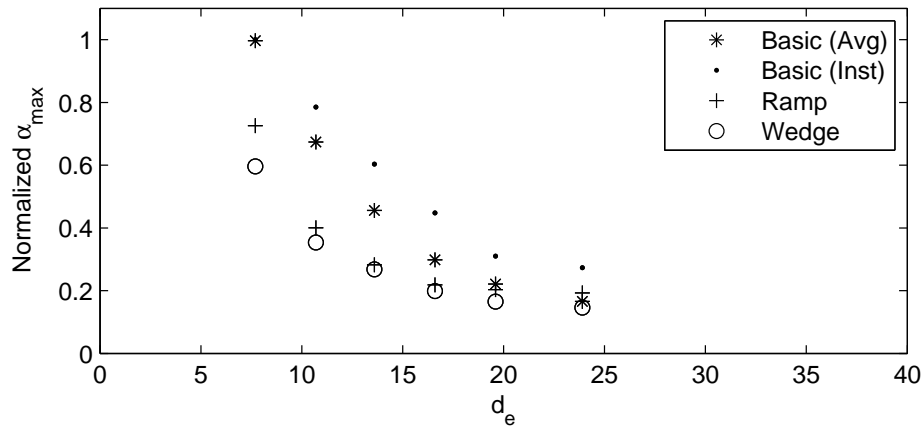


Fig. 5.22 CFD normalized maximum ethylene mass fraction comparison.

Table 5.5 CFD maximum ethylene mass fraction data.

Pylon	Statistic	7.7 d_e	10.7 d_e	13.6 d_e	16.6 d_e	19.6 d_e	23.9 d_e
Basic(Inst)	Mean	0.6315	0.4958	0.3810	0.2828	0.1958	0.1723
	Sdev	0.0076	0.0221	0.0299	0.0230	0.0152	0.0084
Basic(Avg)	Mean	0.6297	0.4258	0.2879	0.1882	0.1396	0.1045
	Sdev	0.0072	0.0234	0.0098	0.0040	0.0036	0.0034
Ramp(Avg)	Mean	0.4587	0.2530	0.1748	0.1378	0.1284	0.1217
	Sdev	0.0209	0.0070	0.0052	0.0014	0.0027	0.0012
Wedge(Avg)	Mean	0.3766	0.2234	0.1693	0.1256	0.1041	0.0921
	Sdev	0.0289	0.0143	0.0073	0.0049	0.0037	0.0014

Table 5.6 CFD maximum ethylene mass fraction statistical difference.

Comparison	7.7 d_e	10.7 d_e	13.6 d_e	16.6 d_e	19.6 d_e	23.9 d_e
Basic(Inst)/Basic(Avg)	N	Y	Y	Y	Y	Y
Basic(Avg)/Ramp(Avg)	Y	Y	Y	Y	Y	Y
Ramp(Avg)/Wedge(Avg)	Y	Y	N	Y	Y	Y

The statistical differences between the maximum ethylene mass fraction values are similar to that seen with NO-PLIF maximum pixel intensities. Most of the maximum concentration calculations (except for a few) are statistically different at the 90% confidence level. The basic and ramp pylon maximum ethylene mass fractions are statistically different at all planar positions. The basic pylon instantaneous and averaged concentration data are statistically different at all but one planar position. The ramp and alternating wedge ethylene mass fraction data are statistically different at all but one planar position.

The maximum ethylene mass fraction data in Fig. 5.22 from the CFD simulation data exhibits the same qualitative trend among the pylon configurations as the maximum plume pixel intensity data in Fig. 5.21 from the NO-PLIF concentration

measurements. The hypermixer pylons mix the injectant more quickly than the basic pylon, but the difference in mixing capabilities lessen with downstream distance. The ensemble averaged ethylene mass fractions overestimate the mixing capability of the basic pylon compared to the instantaneous concentration data. The ramp and alternating wedge pylons are very close in their mixing ability, but the alternating wedge plume is mixed slightly better at most planar positions.

Raman Maximum Concentration Calculations. Figure 5.23 shows the maximum methane mass fraction at $13.6 d_e$ and $23.9 d_e$ for each pylon configuration. Table 5.7 shows the averages and standard deviations of the maximum methane mass fraction samples, and Table 5.8 shows which maximum mass fraction values are statistically different at the 90% confidence level ("Y" = yes and "N" = no). In this case the only maximum mass fractions that are not statistically different are from the basic and ramp pylons at $23.9 d_e$.

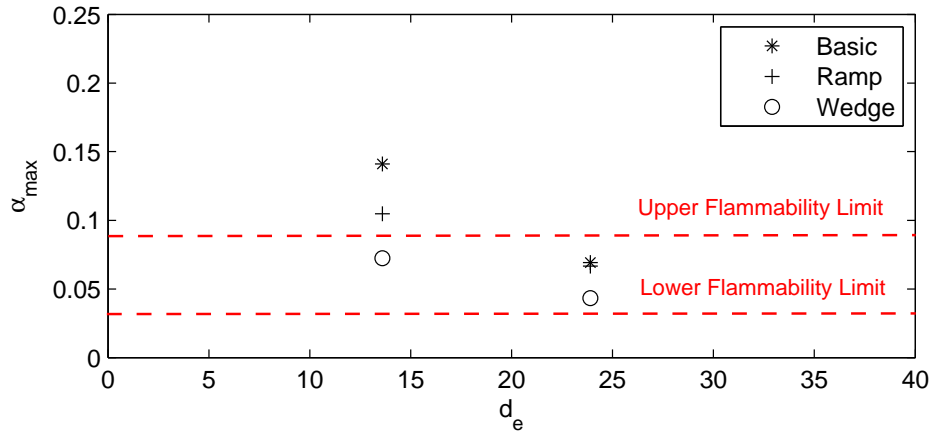


Fig. 5.23 Raman maximum methane mass fraction comparison.

Table 5.7 Raman maximum methane mass fraction data.

Pylon	Statistic	13.6 d_e	23.9 d_e
Basic	Mean	0.1410	0.0692
	Sdev	0.0037	0.0008
Ramp	Mean	0.1048	0.0666
	Sdev	0.0202	0.0014
Wedge	Mean	0.0724	0.0433
	Sdev	0.0020	0.0004

Table 5.8 Raman maximum methane mass fraction statistical difference.

Comparison	13.6 d_e	23.9 d_e
Basic/Ramp	Y	N
Ramp/Wedge	Y	Y

Raman methane mass fraction data cannot be directly compared to NO-PLIF signal intensity data or CFD ethylene mass fraction data due both mass flux differences and test condition differences. However, the same plume dilution trends among the pylon configurations are still be present using Raman methane mass fraction data as the plume dilution parameter. All the fuel plumes become better mixed progressing downstream. At 13.6 d_e the hypermixer pylons have a better mixed plume than the basic pylon. At 23.9 d_e there is less overall mixing difference between the pylon plumes, but the alternating wedge has a slightly more diluted state. The same overall trend is the hypermixer pylons dilute the fuel into the airstream in a shorter downstream distance than the basic pylon, and between the two hypermixer pylons, the alternating wedge dilutes the fuel into the airstream slightly faster.

Plume Dilution Comparison to Other Work. In order to bolster the validity of plume dilution measurements attained in current research, a comparison between the CFD ethylene mass fraction data from pylon injection in current research is compared

to a single hole transverse wall injector contained in past experimental research. [65,80] The past experimental data comes from plane wall transverse ethylene injection into a Mach number 2.0 airflow with a momentum ratio of 1.0, the same equivalency parameters used here. No concentration data for methane or ethylene injection from a strut or pylon fuel injector in a supersonic airflow has been found in open literature, so this the closest data comparison possible.

The plume dilution parameter used in the past research is ethylene/air maximum equivalence ratio, ϕ_{\max} , at a planar position downstream of the injection plane. The past research states the decay rate of the maximum equivalence ratio downstream of a single transverse injection hole at a momentum ratio of one is a power law function defined by Eq. 5.1. The plume dilution parameter used in current research is the maximum ethylene mass fraction, α_{\max} , at a planar position downstream. A conversion between the two measures is shown in Eq. 5.2. This equation is derived from Eq. 4.10. $f_s = 0.068$ for an ethylene/air mixture.

$$\phi_{\max} = 21.7d_e^{-0.78} \quad (5.1)$$

$$\phi_{\max} = \frac{\alpha_{\max}}{f_s(1 - \alpha_{\max})} \quad (5.2)$$

Figure 5.24 shows the ethylene concentration with downstream distance comparison between the single hole transverse injector and pylon injectors in current research. Instantaneous concentration information is used for the basic pylon instead of averaged information. The spatial comparison is from the point where the ethylene is injected. For the single hole transverse injector this is from the center of the hole. For the pylons this is $4.7 d_e$ upstream of the base plane of the pylon, where the fueling slots are located.

The plume dilution data in Fig. 5.24 show the hypermixer pylon injectors equal the mixed state of the transverse injector around $10 - 15 d_e$. Upstream of this planar position the single hole transverse injection does a better job mixing the ethylene and air, and downstream of this planar position the hypermixer pylons equal or better the transverse injector. This is a promising result. The hypermixer geometries were placed on the parallel injection pylons to better their mixing capability since pure parallel injection does not mix as well as transverse injection. The ethylene/air mixture behind the hypermixer pylons matches that from a single transverse injection hole in a short distance behind the pylon base plane.

If the location of comparison between the two injectors was different, say the hole location (transverse injector) and the pylon base plane (pylon injector), the pylon mixing would fair much better in the comparison. All the pylon plume dilution data would shift $4.7 d_e$ to the left, and the alternating wedge pylon would equal the mixing effectiveness of the transverse hold injector at all planar positions. However, in fairness to the transverse hole injector, the location of ethylene injection is the most logical place to compare the two injectors.

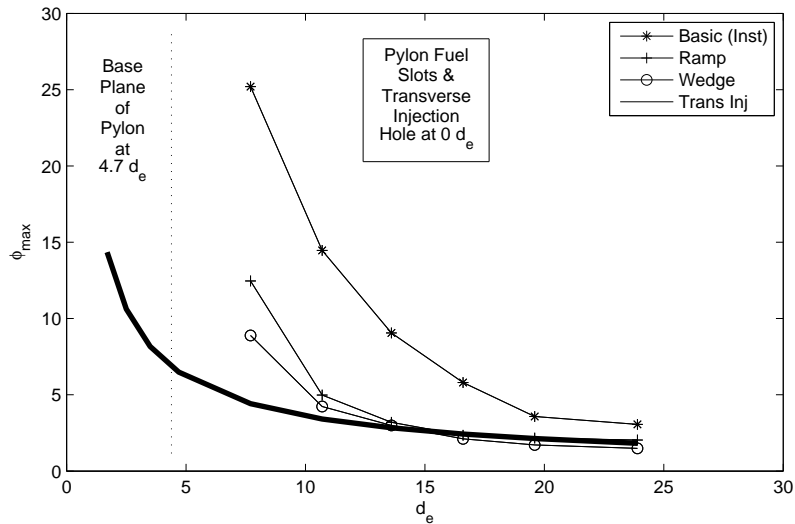


Fig. 5.24 Plume dilution comparison between pylons and transverse injection.

Plume Flammability. Fuel plume dilution into the airstream is not the best overall measure of mixing effectiveness, although it is used quite often by researchers. The amount of fuel plume dilution is an indicator of how mixed the fuel is in the airstream, but there is a narrow range of flammable fuel concentrations (fuel mass fractions) over which a fuel/air mixture is able to combust. If the fuel mass fraction is too high, the mixture is too rich for combustion, and if the fuel mass fraction is too low, the mixture is too lean for combustion. Instead of examining just the diluted, mixed state of the fuel plume, it is important to also examine the combustible mixture state.

The combustible mixture state, or flammable plume extent, was calculated using both CFD ethylene mass fraction data and Raman methane mass fraction data. The flammable plume extent results from each data source are compared only qualitatively due to mass flux ratio differences, test condition differences, and flammability limit differences. However, comparisons among the pylon configurations follow the same trends using either data source.

Figure 5.25 shows the ethylene flammable plume extent with both flammable plume area and flammable plume fraction parameters using CFD simulation data. Moving downstream the flammable plume area/fraction generally increases while the ethylene is being diluted to within flammability limits, then decreases as increasing portions of the ethylene plume fall below flammability limits. Looking specifically at the flammable plume area parameter, the alternating wedge pylon has the largest area throughout the wake region. The ramp pylon has the second largest flammable plume area throughout the near-field and most of the far-field region. The basic pylon has the smallest flammable plume area in the near-field and matches the flammable plume area of the ramp pylon at the end of the far-field region calculated in simulation.

Looking specifically at the flammable plume fraction parameter in Fig. 5.25, the alternating wedge and ramp pylons both show a maximum fraction around $10 d_e$, upstream of the basic pylon maximum flammable plume fraction around $20 d_e$. Both

hypermixer pylons have larger fractions of fuel plume ready for combustion closer to the pylon base plane compared to the basic pylon, and the alternating wedge pylon has a slightly higher flammable plume fraction compared to the ramp pylon upstream of $10 d_e$. An obvious link exists in simulation data between plume dilution and plume flammability. Pylon configurations with increased plume dilution draw the largest flammable plume region of the fuel/air mixture closer to the base plane of the pylon. Plume flammability calculations using experimental Raman methane mass fraction data also support this link between plume dilution and plume flammability.

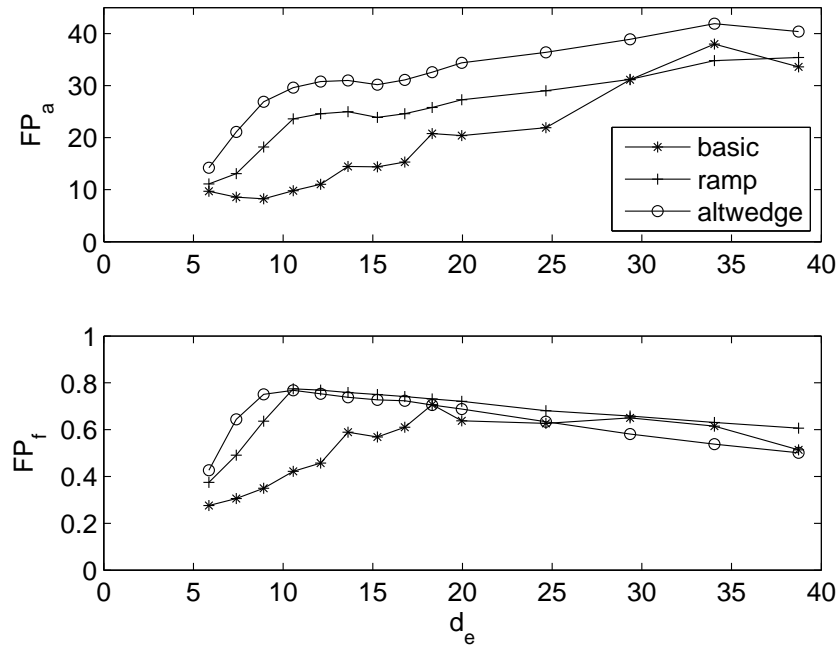


Fig. 5.25 CFD plume flammability comparison.

Figure 5.26 shows the flammable plume areas and flammable plume fractions for methane mass fraction plume profiles at $13.6 d_e$ and $23.9 d_e$. The largest flammable plume area and highest flammable plume fraction are found in the alternating wedge pylon case at $13.6 d_e$. At this planar position about 65% of the methane/air plume is combustibile. At this same planar position the ramp pylon has the second largest flammable plume area/fraction, almost matching the alternating wedge pylon, and

the basic pylon has the smallest flammable plume area/fraction. About 25% of the basic pylon plume is flammable at $13.6 d_e$.

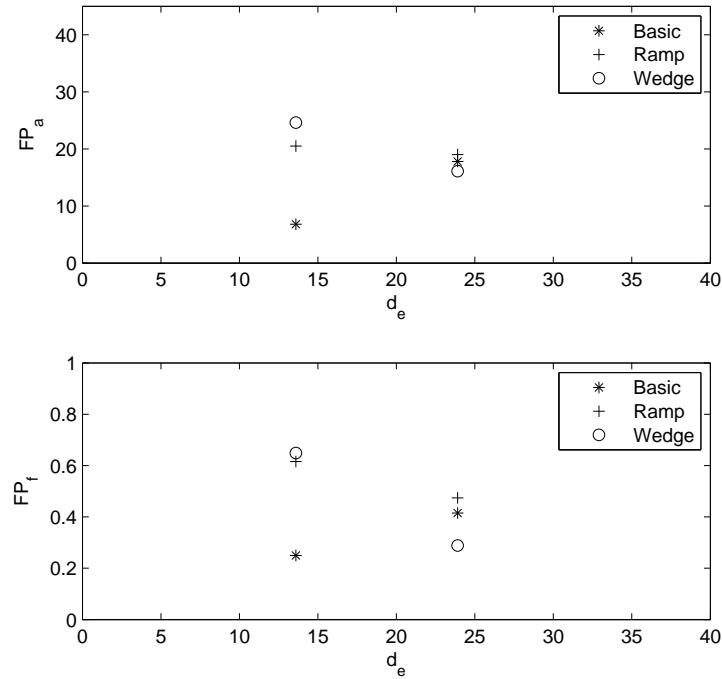


Fig. 5.26 Raman plume flammability comparison.

The story is much different at $23.9 d_e$. The flammable plume measures from the three pylons are closer. The alternating wedge has the smallest flammable plume area/fraction now since a large portion of the fuel plume has dropped below flammability limits. The ramp pylon has the largest flammable plume area/fraction, although smaller than at $13.6 d_e$ since some of its fuel plume area has also dropped below flammability limits. The basic pylon has the second largest flammable plume area/fraction, as more of the fuel plume has fallen into flammability limits farther away from the pylon base plane.

The flammable plume extent parameters calculated with Raman methane mass fraction data support the CFD simulation results. The alternating wedge and ramp pylons create a larger flammable mixture of fuel in a shorter downstream distance

compared to the basic pylon, drawing the largest flammable plume area and highest flammable plume fraction closer to the base plane of the pylon. Between the ramp and alternating wedge pylons, the alternating wedge creates a slightly larger flammable plume and reaches a higher flammable plume fraction in a slightly shorter distance. The plume flammability differences between the two hypermixer pylons are much less pronounced than the differences between the hypermixer pylons and the basic pylon.

Total Pressure Loss Analysis

There is an expected increase in total pressure loss accompanying an increase in mixing effectiveness. A relative comparison between the pylon configurations is accomplished to examine whether total pressure loss increase from the hypermixer pylons compared to the basic pylon is significant or negligible. Total pressure measurements were accomplished using both CFD simulation data and aerothermal probe measurements. The probing area in the wind tunnel was limited to a small patch of area behind the pylon at $23.9 d_e$. The CFD total pressure data were available throughout the simulation wind tunnel volume. A comparison between the two total pressure data sources can only be done qualitatively due to the different test conditions between simulation and experiment; however, the relative total pressure loss between pylon configurations has the same trend in either case.

Figure 5.27 compares the total pressure loss of the pylon configurations using CFD simulation data integrated over the entire cross-section of the simulation wind tunnel at fourteen planar positions downstream of the pylon base plane. In general, total pressure loss increases with downstream distance as the pylon wake region grows and viscous losses from mixing increase. The wind tunnel walls are inviscid boundary surfaces, so no additional total pressure losses occur there. The total pressure loss of the alternating wedge pylon exceeds that of the basic and ramp pylons throughout the wake region. The ramp pylon total pressure loss is greater than the basic pylon in the near-field, but the total pressure loss of the basic pylon exceeds that of the ramp pylon as downstream distance increases into the far-field.

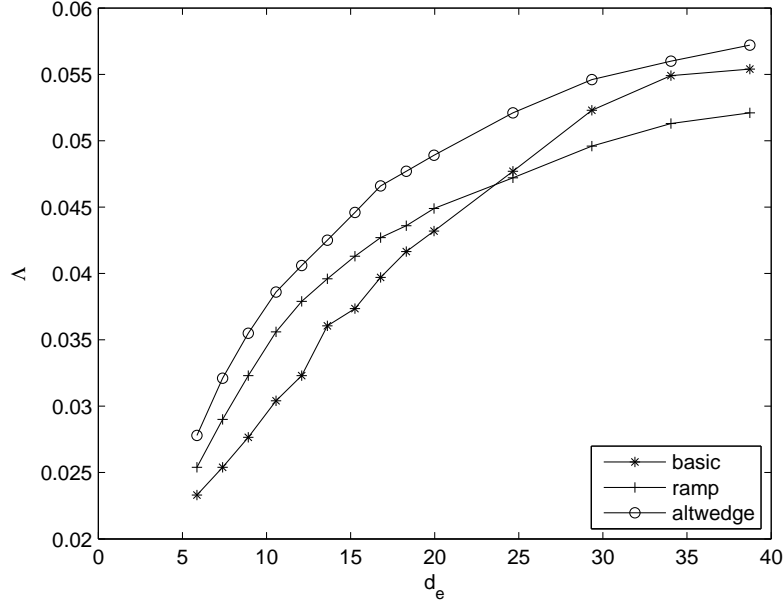


Fig. 5.27 CFD total pressure loss comparison.

Along with total pressure loss measurements, a drag calculation is accomplished on the pylon surfaces using CFD simulation data. The non-dimensional drag from surface pressures and viscosity is the drag coefficient, which is defined in Eq. 5.3. The dynamic pressure multiplied by the pylon frontal area is 134.9 N in the simulation cold flow for all pylons since each has the same frontal area by design. The drag coefficients are presented in Table 5.9. The alternating wedge has the highest drag penalty, followed by the basic pylon, and then the ramp pylon.

$$C_d = \frac{Drag}{\frac{1}{2}\rho u^2(Area)} = \frac{Drag}{134.9N} \quad (5.3)$$

Table 5.9 CFD drag comparison.

Pylon	C_d	Drag (N)
Basic	0.61	82
Ramp	0.59	80
Alternating Wedge	0.66	89

The CFD simulation total pressure losses had to be recalculated so aerothermal probe total pressure loss measurements could be compared to it. The aerothermal probes only sampled the pylon wake region over a small area 50.8 mm high x 63.5 mm wide, so simulation total pressure loss was recalculated using flow quantities from this small area. In addition, aerothermal probe flow quantities were temporally averaged due to the acquisition time of the probes. The instantaneous CFD flow quantities were ensemble averaged over one vortex shedding period to account for this averaging.

The second column of Table 5.10 shows the recalculated total pressure loss for the CFD simulations at $23.9\text{ }d_e$. The first column of Table 5.10 shows the aerothermal probe total pressure loss using the aerothermal probe measurements at $23.9\text{ }d_e$. The experimental aerothermal probe total pressure loss measurements support the CFD simulation total pressure loss trends among the pylon configurations. Even though the numerical total pressure loss values from CFD and aerothermal probe data are not very close due to test condition differences between simulation and experiment, there are striking similarities among the pylons.

Table 5.10 Total pressure loss comparison at $23.9\text{ }d_e$.

Pylon	Λ (probes)	Λ (CFD)
Basic	0.184	0.243
Ramp	0.200	0.244
Alternating Wedge	0.244	0.288

The ramp and basic pylons both have very similar total pressure losses at $23 d_e$ in simulation and experiment. In the case of the aerothermal probes the difference is a little greater than in simulation, but in both cases the total pressure loss of the basic and ramp pylons are close. The alternating wedge pylon consistently shows a greater total pressure loss than the basic and ramp pylons at $23 d_e$ in simulation and experiment. The same trend is seen throughout the pylon wake region in simulation results (Fig. 5.27). The alternating wedge has a larger total pressure loss compared to the basic and ramp pylons, and the basic and ramp pylons are more similar in their total pressure loss.

Mixing Effectiveness and Total Pressure Loss Tradeoff

It is now apparent the pylon configurations that produce the most streamwise vortices have the most rapid plume dilution and create a larger area of flammable fuel/air mixture closer to the pylon base plane. However, in general they also produce more total pressure loss in the airstream. The alternating wedge pylon has a greater total pressure loss compared to both the ramp and basic pylons, and the ramp has a slight to negligible increased total pressure loss compared to the basic pylon.

Given this information, a conclusion could be drawn that the ramp pylon configuration is the overall best performer since it offers a heightened mixing effectiveness with a small to negligible increase in total pressure loss. However, this would involve an assumption since a direct link between cold flow total pressure loss, cold flow mixing efficiency, and scramjet combustor performance has not been established. The overall performance of a scramjet combustor section is hard to gauge from cold flow measurements.

It is the combustion efficiency and total pressure loss tradeoff that is important to actual scramjet combustor performance. It is not known precisely how mixing effectiveness correlates to combustion efficiency. However, in general combustion efficiency increases with increased mixing effectiveness as seen in Fig. 2.8, a comparison of combustion efficiency using parallel, transverse, and ramp hypermixer injection in

a scramjet combustor. Transverse injection, having the best mixing effectiveness, has the highest combustion efficiencies; and parallel injection, having the worst mixing effectiveness, has the lowest combustion efficiencies.

Mixing effectiveness itself also changes with heat release due to changes in flow-field temperatures, pressures, velocities, and physical properties. The mixing effectiveness measures of plume dilution and plume flammability change in a combustor flow compared to a cold flow. However, cold flow mixing studies are a good first step in determining mixing capabilities of different fuel injection strategies, and have often been used by researchers to study fuel mixing prior to conducting combustion studies.

In addition to mixing effectiveness differences between hot and cold flow, the complete total pressure loss is not known from a cold flow study since a large amount of total pressure loss accompanies heat release in a scramjet combustor. Due to both mixing effectiveness and total pressure loss differences between cold and hot flow, further research with these pylon configurations in hot combustor flows is needed to answer the question of which pylon configuration offers the best overall performance in a scramjet combustor.

The cold flow mixing and total pressure loss analysis conducted here is a good initial assessment of the supersonic fuel injection effectiveness and suitability of these pylon configurations. In general increased cold flow mixing effectiveness leads to a combustion flame in a shorter downstream distance, and this was shown in current research through plume dilution and flammability calculations. In turn, a shorter distance to a combustion flame shortens the combustor section, reducing total pressure loss by allowing a shorter combustor length. Also, a large combustible region closer to the pylon base where slower subsonic speeds exist allows the pylon to act as a flameholder, anchoring a combustion flame in the supersonic airflow of the scramjet combustor.

Energy Analysis. If a total pressure loss and combustion efficiency were calculated from a hot combustor flow for each pylon configuration, the following is a

simple methodology one could follow to do an approximated energy tradeoff analysis. The analysis is accomplished here using cold flow measurements since that is all that is currently available. All the data used comes from the CFD simulations with ethylene injection from the pylon configurations.

There is kinetic energy loss due to flow obstruction from the pylon and other total pressure loss sources, and there is thermal energy gain from heat release due to fuel burning. The combination of energy loss and gain is an energy change to the combustor flow. Total pressure losses result in entropy gains, as derived from the Gibbs equation, first law of thermodynamics, and the ideal gas law (Eq. 5.4). Entropy gain results in a reduction in energy of the ideal gas approximated combustor flow (Eq. 5.5).

$$\Delta s = R \ln \left(\frac{P_{t_1}}{P_{t_2}} \right) \quad (5.4)$$

$$\Delta W_L = -\dot{m}T_1\Delta s = -\dot{m}T_1R \ln \left(\frac{P_{t_1}}{P_{t_2}} \right) \quad (5.5)$$

Energy gain from heat release in the combustor is expressed through the first law of thermodynamics in Eq. 5.6. Heat addition is an addition to the energy of the combustor flow. Since there is no combustion efficiency derived from cold flow simulations, one is constructed from the mixing effectiveness calculations. The mixing efficiency, η_m , multiplied by the flammable plume fraction, FP_f , is substituted for the combustion efficiency in Eq. 5.6. \dot{m}_f is the mass flow of fuel. h_f is heat release per kilogram of fuel. The summation of energy gain due to heat addition and energy loss due to entropy gain is the energy tradeoff, ΔW , of the combustor flow due to pylon fueling (Eq. 5.7).

$$\Delta W_Q = \Delta Q = \dot{m}_f \eta_m FP_f h_f \quad (5.6)$$

$$\Delta W = \Delta W_L + \Delta W_Q = \dot{m}_f \eta_m \text{FP}_f h_f - \dot{m} T_1 R \ln \left(\frac{P_{t_1}}{P_{t_2}} \right) \quad (5.7)$$

Using CFD cold flow simulation data calculated at each axial position in the wake region, the following data parameters are used in Eq. 5.7: the mass flow of ethylene (\dot{m}_f), the total mass flow (\dot{m}), the total pressure loss ratio (P_{t_1}/P_{t_2}), the mixing efficiency (η_m), and the flammable plume fraction (FP_f). The other variables in the equation (h_f , R , and T_1) are held constant. $h_f = 4.5\text{E}7 \text{ J/kg}$ is a typical heating value for a hydrocarbon fuel. $R = 287 \text{ J/kg K}$ is the gas constant for air. Although ethylene has a different gas constant, it is a small fraction of the total flow, so the gas constant of air is used. $T_1 = 712 \text{ K}$ is the combustor inlet static temperature calculated for case 1 operational conditions in Chapter 3.

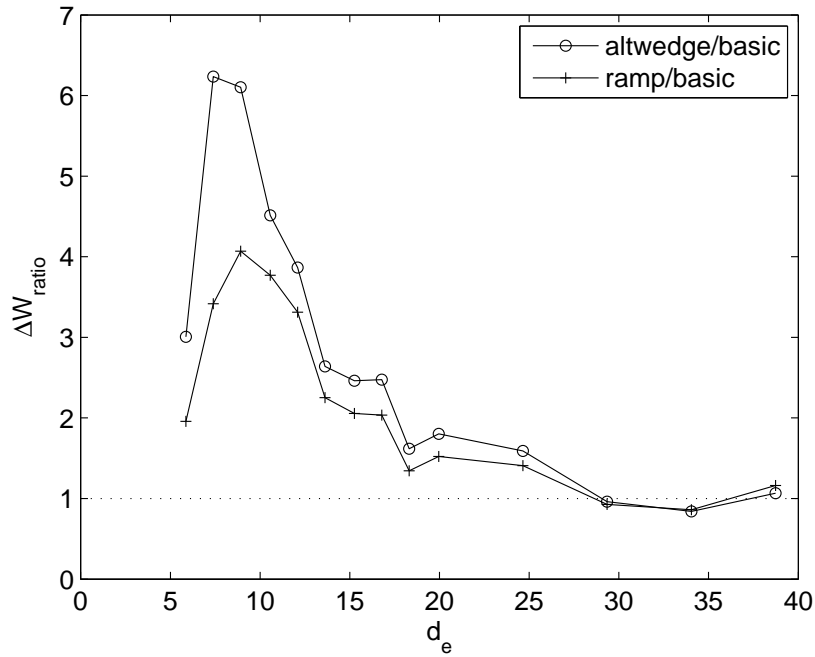


Fig. 5.28 Energy summation ratio comparison.

The energy summation, ΔW , of each pylon configuration is placed into a ratio comparing the energy summation of the basic pylon to that of the ramp and alternating wedge pylons. This ratio comparison is shown in Fig. 5.28. In this example analysis the alternating wedge and ramp pylons both exceed the basic pylon in energy summation for a large portion of the wake region; however, the basic pylon matches the ramp and alternating wedge pylons around $29 d_e$. There is a finite downstream distance where the alternating wedge and ramp pylons have an energy advantage compared to the basic pylon. For this example analysis the alternating wedge pylon has a slight energy advantage over the ramp pylon.

VI. Conclusions and Recommendations

The objective of this research was to assess the mixing effectiveness and total pressure loss of a new fuel injection pylon for low aspect ratio circular or elliptical combustor cross-sections. The intrusive pylon distributes hydrocarbon fuel into a supersonic airflow, mixing the fuel and air to a sufficient concentration for combustion. Three geometric variants of the pylon concept were tested: a basic pylon, a ramp pylon, and an alternating wedge pylon.

Mixing effectiveness was evaluated through a calculation of streamwise vortex magnitudes, plume dilution, and plume flammability in the pylon wake region. Streamwise vortex magnitudes were calculated using velocity vector data from CFD simulation solutions. Plume dilution and flammability were successfully calculated using pylon injectant concentration data from CFD simulation solutions, Raman spectroscopy quantitative methane concentration measurements, and NO-PLIF qualitative pylon injectant concentration measurements. Total pressure loss was gathered using total pressure data from simulation and wind tunnel aerothermal probe measurements.

Conclusions

The characteristics of the flowfields in the wake region of the pylon configurations were determined initially through simulation results and then verified using NO-PLIF instantaneous fuel plume images. The flowfield behind the basic pylon is highly unsteady and exhibits vortex shedding at about a 6900 Hz frequency. The ramp and alternating wedge pylons (hypermixer pylons) exhibited a much more steady flowfield. The streamwise vortices produced by the hypermixer pylons helped to stabilize the pylon wake region flowfield. Understanding the overall characteristics of the pylon wake flowfields made it easier to interpret data from fuel plume profiles downstream of the pylon base plane.

Fuel plume profiles in the wake region of all three pylon configurations were constructed using CFD ethylene mass fractions, Raman methane mass fractions, and

NO-PLIF fluorescence signal data. All these data were either from simulation or experimental measures of fuel concentration in the airstream. Since Raman and NO-PLIF data were both experimentally captured at the same test conditions, a direct comparison of those plume shapes was accomplished. Although NO-PLIF fluorescence is a qualitative measure of pylon injectant concentration, it was verified by comparison to quantitative Raman methane mass fractions that measured fluorescence signals monotonically change with pylon injectant concentration, and can therefore be used in a qualitative mixing analysis.

A mixing analysis was conducted using the plume profiles and comparisons drawn among the pylon configurations by examining three calculated parameters: streamwise vortex magnitude, fuel plume dilution, and fuel plume flammability. The difference between instantaneous and averaged concentration data was notable in this mixing analysis. The averaged concentration data from averaged plume profiles overestimated the mixing capability of the basic pylon because the wake region flowfield was highly unsteady. Since the alternating wedge and ramp pylons had more steady pylon wake flows, this affect was not seen as much in their concentration data. This averaging affect on concentration data, fortunately, did not change the overall fuel plume dilution comparisons among the pylon configurations.

Streamwise vortex magnitude calculations showed the alternating wedge and ramp pylon configurations produced an increased amount of streamwise vortices in the near-field wake region of the pylon compared to the basic pylon. The alternating wedge pylon exhibited the largest magnitude of streamwise vortices in the near-field region. In the far-field region (beyond $15 d_e$) the streamwise vortex magnitude of each pylon configuration was approximately the same. The next mixing analysis parameter examined how streamwise vortex magnitudes influenced fuel plume dilution.

Fuel plume dilution calculations showed there was a direct correlation between the magnitude of streamwise vortices produced and the quickness to which the fuel was diluted into the airstream in the pylon wake region. The alternating wedge

pylon, having the largest amount of streamwise vortex production in the near-field, also exhibited the fastest fuel plume dilution. The ramp pylon had the second fastest fuel plume dilution (very close to the alternating wedge pylon), followed by the basic pylon. However, in the distant far-field the diluted state of the basic pylon fuel plume matches the diluted state of the hypermixer pylon fuel plumes. The plume dilution enhancement of the hypermixer pylons over the basic pylon was observed for only a finite distance behind the pylon. A comparison between the calculated fuel plume dilution data in current research and some past research data was possible.

The fuel plume dilution data of the three pylon configurations was compared to a transverse wall injector using CFD ethylene maximum mass fractions. Transverse injection in a supersonic airflow has a faster mixing rate than pure parallel injection in a supersonic airflow. The hypermixer geometries placed on the pylon aft area were meant to increase the mixing rate of parallel injection to be closer to transverse injection. The comparison showed the pylon with the fastest mixing rate, the alternating wedge, equaled or bettered the dilution state of the transverse injector by 10 - 15 d_e downstream. The last mixing analysis parameter showed how fuel plume dilution rates influenced the size and location of flammable plume mixtures.

Plume flammability is a more important measure than fuel plume dilution because it reveals where in the pylon wake region the fuel/air mixture is ready for combustion. The alternating wedge pylon, having the fastest rate of fuel plume dilution, had the largest flammable fuel plume area closest to the pylon base plane compared to the other pylon configurations. Using Raman methane mass fraction data, at 13.6 d_e the alternating wedge fuel plume was 65% flammable, the ramp fuel plume was 62% flammable, and the basic fuel plume was 25% flammable. Further downstream at 23.9 d_e the alternating wedge fuel plume was 29% flammable, the ramp pylon fuel plume 47% flammable, and the basic pylon fuel plume 41% flammable. The ramp pylon flammable plume behavior was very similar to the alternating wedge, larger closer to the pylon base plane and dropping off farther away. The flammable plume

for the basic pylon was larger farther downstream compared to both the hypermixer pylons because of its slower fuel dilution rate.

The mixing analysis showed the importance of streamwise vortex production to rapid fuel dilution, and also showed the relationship between fuel plume flammability and fuel plume dilution. The hypermixer pylons diluted the fuel faster than the basic pylon and brought the largest plume flammability region closer to the pylon base plane. Bringing the largest flammable plume area closer to the base plane of the pylon is advantageous for the pylon's use as a flameholder. The slower velocities (subsonic) just behind the pylon allow a region for the fuel/air mixture to ignite and anchor a flame. Having more plume flammability in this slower velocity region is a promising results for using the pylons themselves as a flame holding source in the scramjet combustor.

In addition to the thorough mixing analysis, a total pressure loss analysis of each pylon configuration was also accomplished. Both numerical and experimental results agreed that the alternating wedge pylon produced the largest total pressure loss. The ramp and basic pylons exhibited less total pressure loss and were very close in comparison. From experimental aerothermal probe total pressure data, the ramp had a 9% greater total pressure loss and the alternating wedge a 33% greater total pressure loss compared to the basic pylon at $23.9 d_e$. The simulation results of total pressure loss agreed with this trend. Also, the computed drags on the pylon configurations from numerical simulation results showed the alternating wedge had the largest drag overall, the basic pylon had the second largest drag, and the ramp pylon had the least drag.

In summary, both the hypermixer pylons showed an increase in mixing effectiveness compared to the basic pylon. The basic pylon showed both the lowest mixing effectiveness and the lowest total pressure loss of the three pylon configurations. Between the two hypermixer pylons, the alternating wedge had a slightly better mixing effectiveness. However, along with the highest mixing effectiveness, the alternating

wedge pylon also had the largest total pressure loss. The ramp pylon showed the second highest mixing effectiveness, very close to that of the alternating wedge pylon. The ramp pylon did not, however, show a significant total pressure loss increase compared to the basic pylon.

Recommendations

The following are five recommended paths for future research. They are by no means the only paths. Any one or combination of these recommendations could be implemented as a future branch of research on this new scramjet combustor fueling pylon design.

Questions arose during current research, including what the scramjet combustor performance tradeoffs are between total pressure loss and mixing effectiveness, and whether mixing effectiveness can be related to combustion effectiveness. In the cold flow research accomplished here, these questions could not be answered. Hot flow combustion simulations or experiments need to be performed.

The first recommendation is to perform hydrocarbon fuel combustion simulations or experiments with the three pylon configurations at the same equivalency parameter test conditions (Mach number 2.0 and momentum flux ratio of 1.0). A combustion efficiency could be measured, and then a relationship between mixing effectiveness and combustion efficiency explored. Another comparison could be the relationship between cold flow mixing effectiveness from current research and hot flow mixing effectiveness.

The second recommendation is to explore other test conditions relating to other operational conditions of a scramjet combustor, like the case 2 operational condition given in Chapter 3. In addition to another supersonic fuel mixing test condition, an elevated back pressure (dual-mode scramjet combustor environment) test condition could be studied to explore mixing and total pressure loss characteristics under those conditions. The dual-mode scramjet combustor environment occurs at low hypersonic

freestream speeds where the combustor environment is a mixture of subsonic and supersonic flow with shock interactions.

The third recommendation is to study the presence of a wall-based flameholder just behind the pylon and its affect on the fuel injection flowfield, mixing effectiveness of the pylon, and combustion efficiency of the combined pylon/wall-based flameholder configuration. The pylons will probably not be the only sources of flame holding in the scramjet combustor, so exploring other flame holding techniques in concert with the pylons is prudent.

The fourth recommendation is to explore multiple pylon configurations. The individual pylon configurations researched here will not be used alone. Several pylons will be placed in a scramjet combustor section. The interaction of the pylon wake regions and how that interaction changes fuel mixing, total pressure loss, and combustion efficiency is unknown.

The fifth recommendation is to determine the cooling requirements for the pylon configurations. These pylons will be placed in a high enthalpy flow with very high stagnation temperatures. The hypermixer pylon aft areas are vulnerable. Upstream fueling of these hypermixer geometries provide some thermal protection through fuel cooling, but how much fuel flowing over the geometries is required, or materials one should construct the pylons out for thermal protection has not been explored.

Appendix A. Pylon and Wind Tunnel Mounting Plug Designs

The pylons are constructed from two basic pieces, the front and the back. The front piece contains the pedestal that attaches to the wind tunnel. It also contains an injection gas supply tube, the front aerodynamic outer shell, and the internal plenum area. The front piece is common to all pylons. The back piece is interchangeable and consists of either the basic wedge geometry, a ramp geometry, or an alternating wedge geometry. Figures A.1, A.2, A.3, and A.4 show the design drawings created in SOLIDWORKS® for the three pylons. All dimensions are in millimeters.

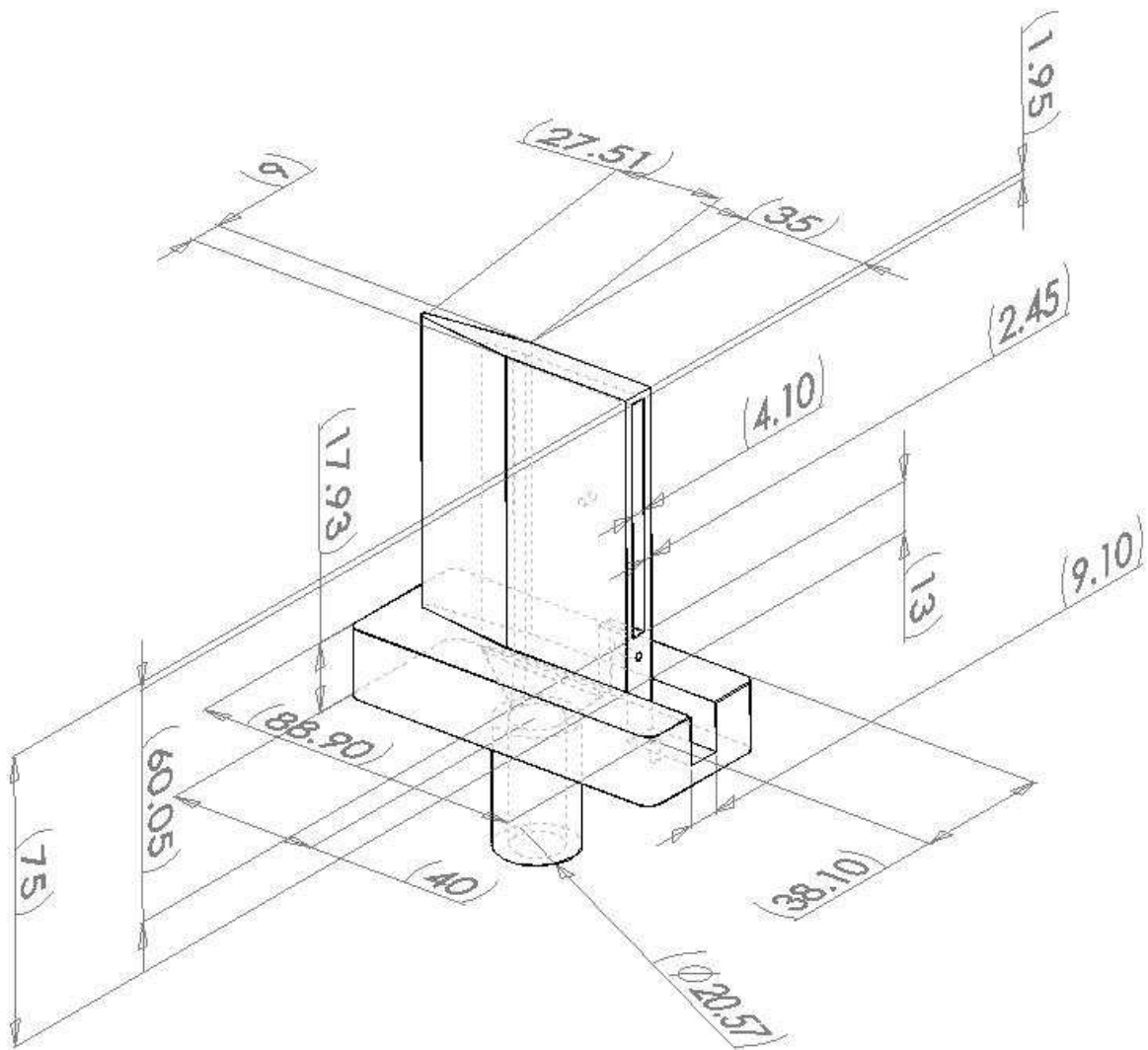


Fig. A.1 Front piece of pylon design.

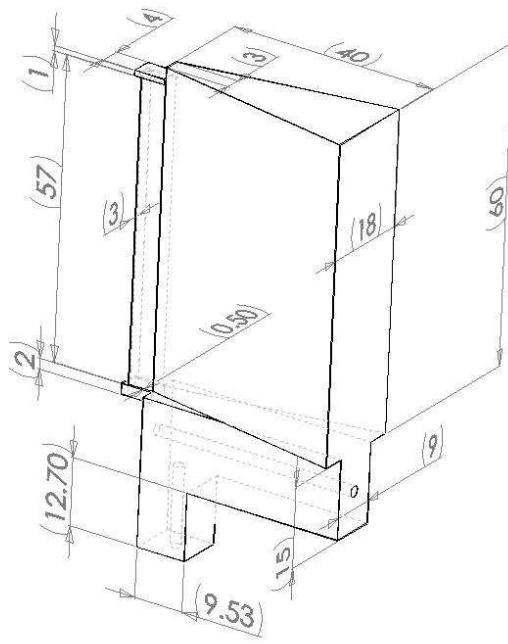


Fig. A.2 Back piece of basic pylon design.

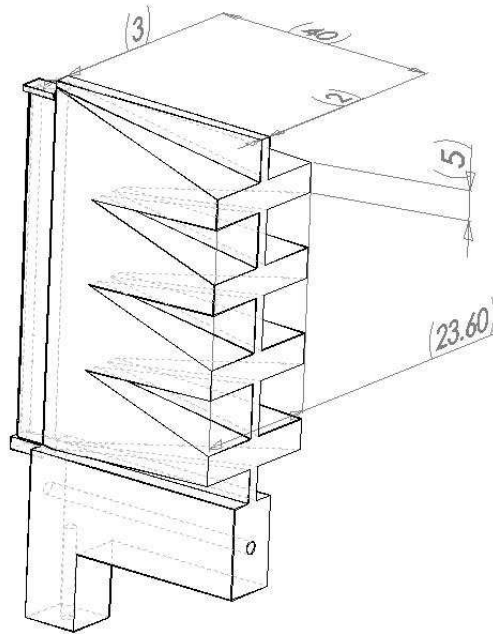


Fig. A.3 Back piece of ramp pylon design.

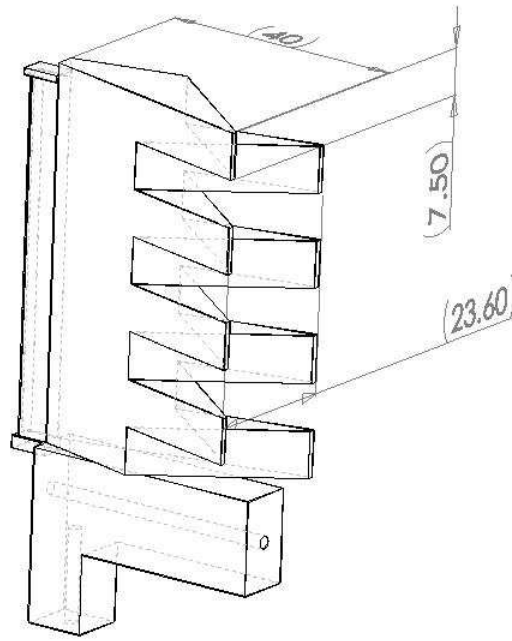


Fig. A.4 Back piece of alternating wedge pylon design.

The two pieces are joined by two 6-32 screws, through holes located in the bottom half of the back piece, the back portion of the aerodynamic shell front, and the bottom surface of the pylon pedestal. The forward portion of the back piece fits into the rear portion of the front piece with 6 *mm* of overlap. This is shown in Fig. A.5. Two small gaps are created by the joining of the front and back pieces. Each gap (slot) has a very large aspect ratio, 0.5 *mm* wide x 57 *mm* long. Combined, the two slots create a geometric fuel port area of 57 *mm*². These fuel ports provide thin film fueling over the pylon back piece. The frontal area of each assembled pylon is the same. The ramp geometry sizes/angles as well as the alternating wedge geometry sizes/angles were chosen so each pylon frontal area is precisely the same as the basic pylon, 1215 *mm*².

The plenum area in the front piece is under pressure and turns the incoming injection flow from the pedestal 90° to orient it downstream through the fueling slots. The injector flow exits the front piece onto the back piece of the pylon, mixing the injectant with the primary airflow around the pylon. The back piece of the

basic pylon is a plain wedge shape with a compression angle of 10.6° half-angle to the flow. The ramp and the alternating wedge geometries (hypermixer geometries) both incorporate compression angles of 14.4° half-angle to the flow. The streamwise vorticity production of the ramp and alternating wedge pylons depends on the pressure difference achieved between the compression surfaces and the valleys between the compression surfaces.

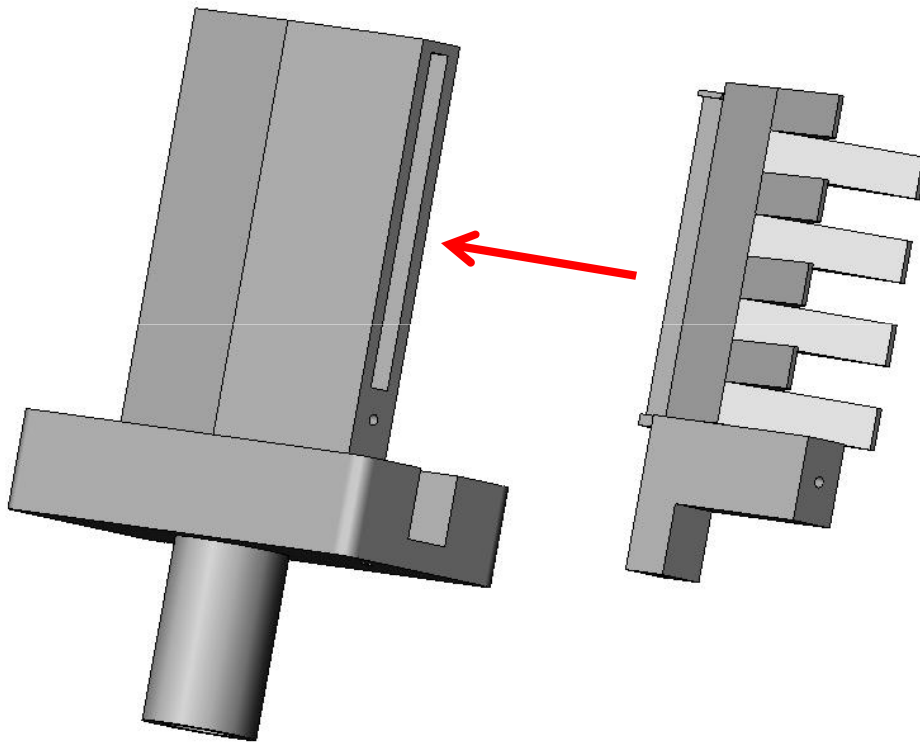


Fig. A.5 Joining front and back pieces.

The four total parts: 1 front piece, and 3 back pieces, were all manufactured by Morris Technologies in Cincinnati, OH using their Direct Metal Laser Sintering (DMLS) process. DMLS machines layer up each part 0.0008 in at a time, using a laser beam to melt millimeter-sized metal balls into place to build the part layer by layer. The advertised accuracy of the process is $\pm 0.005\text{ in}$ for the first inch of layer building, then $\pm 0.002\text{ in}$ thereafter. There is supporting structure material constructed around

the parts to hold them up during the manufacturing process. Once a part is built, the supporting material is shaved off through conventional tooling. The part is then polished and inspected for dimensional accuracy.

A few different metals were available for use in the DMLS process. Morris offered a Bronze semi-porous metal, a 17-4 stainless steel, and a Cobalt Chromium alloy. Morris was the most confident in the Bronze and Cobalt Chromium for making very complicated parts as those designed here. Cobalt Chromium was selected since it is not porous (like the Bronze), the manufacturer was comfortable using the material, and it is durable enough to survive combustion testing if the pylons were to be used for that in the future. The density of the Cobalt Chromium alloy is 8.29 g/cm^3 , the yield strength is between 880 - 980 *MPa*, and the maximum continuous operating temperature is 1150 ° *C*.

The manufacturing process took a couple weeks. Morris had some difficulties manufacturing the front piece and had to redo it, but the final products were within tolerances in the critical areas required – the fuel port area and hypermixer geometries. There are internal thermal stresses that build up during DMLS manufacturing and can cause part bending. This is a danger when parts have a high aspect ratio, have high aspect ratio appendages, or are not supported well during layer buildup. This technology is still maturing, but the parts built for this testing are remarkably accurate given their complexity. The turn-around-time was much faster than available conventional tooling shops, and it was cheaper than using conventional tooling shops. All four parts cost a total of \$10,400, bought by AFRL/RZ. Conventional tooling shops quoted \$15,000 - \$20,000 for the same parts. Figures A.6 - A.11 show the manufactured pylon parts, assembled and disassembled.

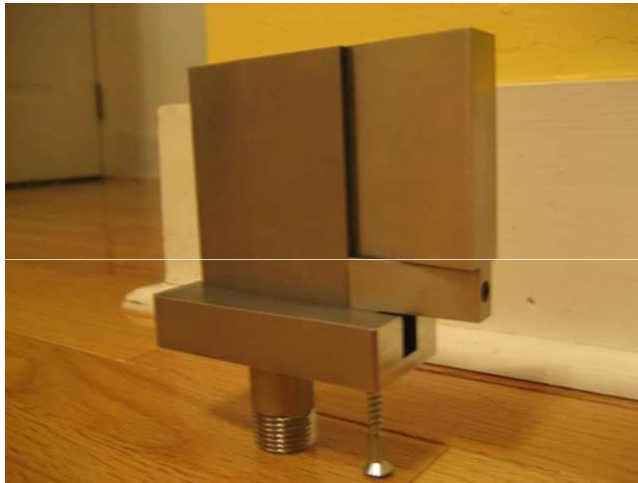


Fig. A.6 Basic pylon assembled picture.

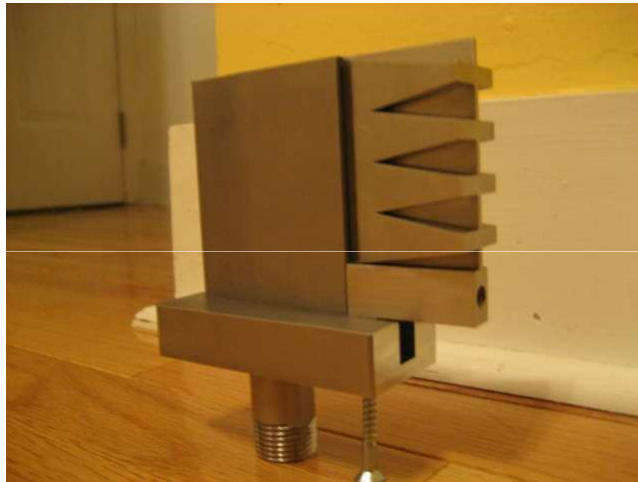


Fig. A.7 Ramp pylon assembled picture.

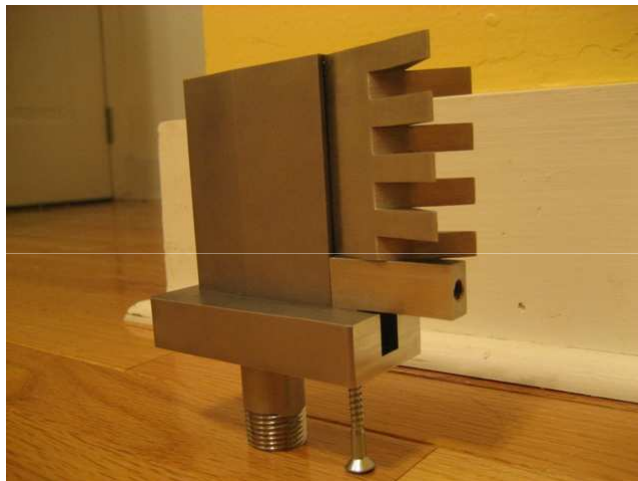


Fig. A.8 Alternating wedge pylon assembled picture.

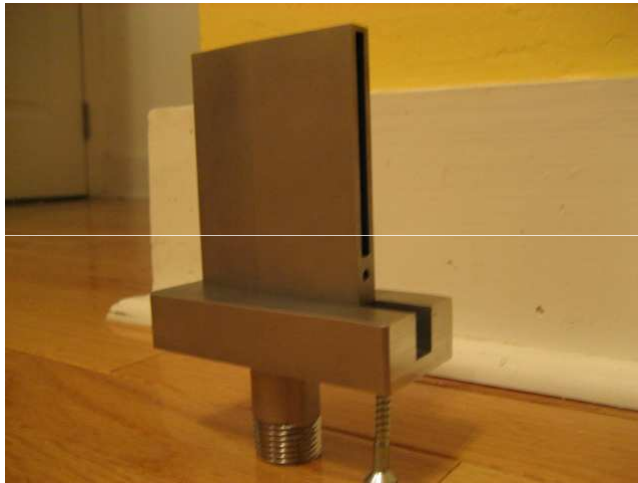


Fig. A.9 Front piece of pylon picture.



Fig. A.10 Back pieces of pylon picture.



Fig. A.11 All pylon pieces picture.

The wind tunnel mounting plug was designed in conjunction with AFRL so the plug would meet the required dimensions to hold the pylon pedestal as well as fit into the AFRL wind tunnel floor opening. The mounting plug is a single piece. It uses four 10-24 screws to secure the pylon pedestal in the mounting plug and four 1/4-20 screws to secure the mounting plug to the floor of the wind tunnel. The mounting plug was manufactured out of steel at a conventional tooling shop in the local area. The mounting plug was placed into the wind tunnel and fit checked prior to testing. The wind tunnel floor and the mounting plug top surface were flush. The pylon pedestal fit into the mounting plug snugly, and the pedestal top was flush with the mounting plug top surface. Once the mounting plug and pylon pedestal were inserted into the wind tunnel floor opening, they were there for the remainder of testing. The only part swapped out during test was the pylon back piece. Between wind tunnel runs it required about 5 minutes to change out the basic, ramp, or alternating wedge back piece for the next test run. Figure A.12 is an isometric view of the wind tunnel mounting plug. Figure A.13 is a top down view of the mounting plug. A crush gasket was placed between the pylon pedestal bottom surface and the floor of the mounting plug to prevent air leakage into the wind tunnel test section. The gasket is shown in Fig. A.14

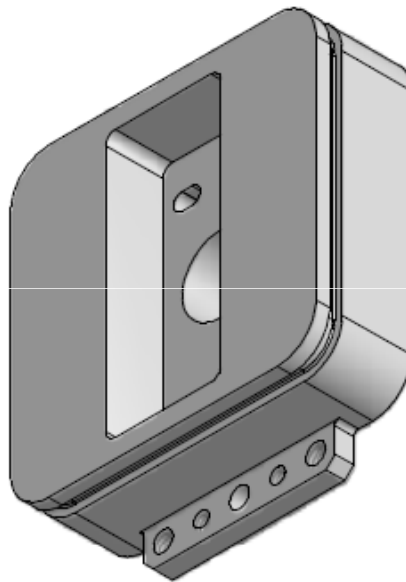


Fig. A.12 Wind tunnel mounting plug isometric view.

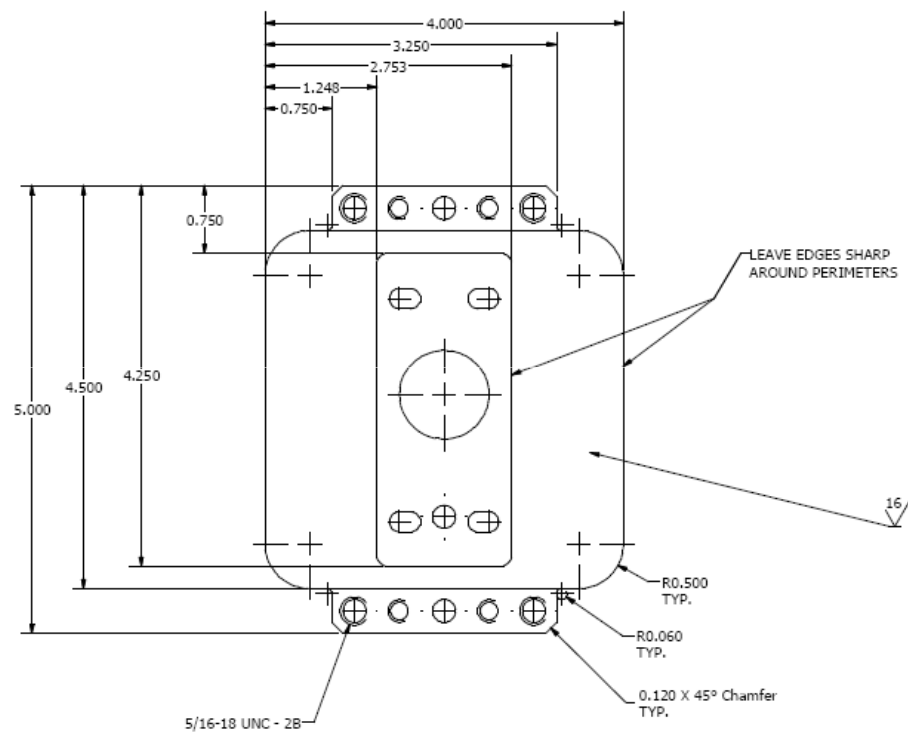


Fig. A.13 Wind tunnel mounting plug top view.

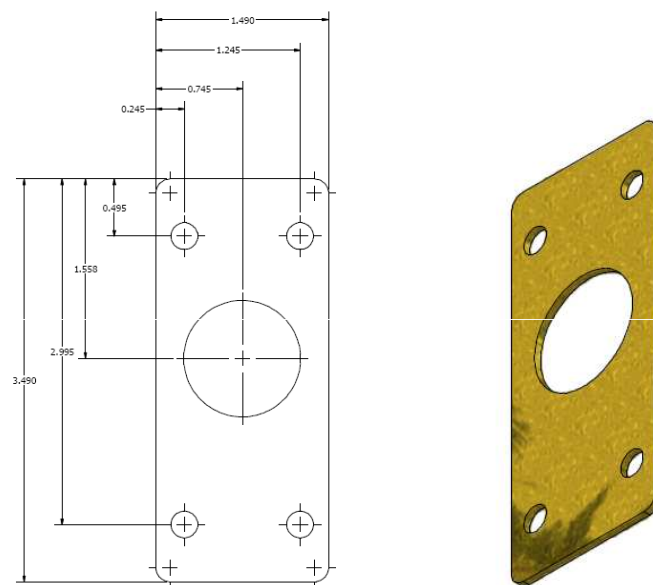


Fig. A.14 Gasket.

Appendix B. Fuel Injection and Inlet Calculation Codes

Listing B.1 Air Properties Function

```
function [Cp, Gamma] = air(temp)
D = temp/100;
MWN2 = 28.01348;
MW02 = 31.9988;
5 CpN2 = (39.060 - 512.79*D^-1.5 + 1072.7*D^-2 - 820.40*D^-3)/MWN2...
    *1000;
CpO2 = (37.432 + 0.020102*D^1.5 - 178.57*D^-1.5 + 236.88*D^-2)/...
    MW02*1000;
Cp = 0.79*CpN2 + 0.21*CpO2;
MW = 0.79*MWN2 + 0.21*MW02;
R = 8314/MW;
10 Cv = Cp - R;
Gamma = Cp/Cv;
```

Listing B.2 Combustor Inlet Conditions

```
clear;clc;
% Mach 8 at 1000 lb/ft^2 (~100,000 ft)
R = 287;
M0 = 8;
5 q_bar = 1000/144*6894.75729;
T0 = 227;
P0 = 2*q_bar/(1.4*M0^2);
HT = 1004*T0 + 1.4*M0^2*R*T0/2;

10 for j = 1:6
    for i = 1:1001
        T2(i,j) = 499 + i;
        T2a(i,j) = T2(i,j);
        CR(i,j) = j*5;
15 [Cp,G] = air(T2(i,j));
        M2(i,j) = sqrt(2/(G*R*T2(i,j))*(HT - Cp*T2(i,j)));
        P2(i,j) = CR(i,j)*(M0/M2(i,j))*sqrt(1.4/G)*sqrt(T2(i,j)/...
            T0)*P0;
        P2a(i,j) = P2(i,j);
        SR(i,j) = (1004 + Cp)/(2*R)*log(T2(i,j)/T0) - log(P2(i,j)...
            /P0);
20 NKE(i,j) = 1 - 2/(1.4*M0^2)*SR(i,j);
        if SR(i,j) < 0
            T2(i,j) = NaN;
            P2(i,j) = NaN;
        end
25 end
end

P2 = P2/1000;
P2a = P2a/1000;
30
```

```

figure(1),clf
for k = 1:size(T2,2)
    h1(k) = plot(P2(:,k),T2(:,k),'b');
    id = find(T2(:,k)==1450);
35    angle = 180/pi*(atan((T2(id+2,k) - T2(id-2,k))/(P2(id+2,k) - P2...
        (id-2,k)).222));
    if k == 1
        text(P2(id,k),T2(id,k),['CR= ',num2str(k*5)],'Rotation',...
            angle,'Vert','bottom','BackgroundColor','none');
    hold on
40    else
        text(P2(id,k),T2(id,k),num2str(k*5),'Rotation',...
            angle,'Vert','bottom','BackgroundColor','none');
    end
end
45 [c,h] = contour(P2,T2,M2,[2.5,3,3.5,4,4.5],'k');
for k = 1:size(c,2)/7
    id = k*7 - 5;
    if k == 1
        text(c(1,id)-15,c(2,id),['M_{comb} = ',num2str(c(1,id-1),'%.1f...
            ')],'Vert','middle','BackgroundColor','white');
50    else
        text(c(1,id)-15,c(2,id),num2str(c(1,id-1),'%.1f'),'Vert','...
            middle','BackgroundColor','none');
    end
end
[c2,h2] = contour(P2a,T2a,NKE,[1,0.99,0.98,0.97],'r');
55 for k = 1:4
    if k == 4
        id = size(c2,2);
        text(c2(1,id)+7,c2(2,id),['n_{KE} = 1.0'],'Vert','middle',...
            'BackgroundColor','none');
    else
60        num = 0.97 + k/100;
        id = find(c2 == num)/2 - 1.5;
        text(c2(1,id)+7,c2(2,id),num2str(num-0.01),'Vert','middle'...
            , 'BackgroundColor','none');
    end
end
65 plot(48,901,'*')
text(50,500,'* Static Pressure = 48 KPa / Static Temperature...
    = 901 K')
axis([0 350 400 1800])
title({'Combustor Inlet Static Conditions', '', '(M_0 = 8, q_0...
    = 1000 lb/ft^2)'})
xlabel('Combustor Static Pressure (KPa)')
70 ylabel('Combustor Static Temperature (K)')
hold off

clear;clc;
75 % Mach 5 at 1000 lb/ft^2 (~80,000 ft)

```

```

R = 287;
M0 = 5;
q_bar = 1000/144*6894.75729;
T0 = 221;
80 P0 = 2*q_bar/(1.4*M0^2);
HT = 1004*T0 + 1.4*M0^2*R*T0/2;

for j = 1:3
    for i = 1:501
85         T2(i,j) = 499 + i;
            T2a(i,j) = T2(i,j);
            CR(i,j) = j*5;
            [Cp,G] = air(T2(i,j));
            M2(i,j) = sqrt(2/(G*R*T2(i,j))*(HT - Cp*T2(i,j)));
90         P2(i,j) = CR(i,j)*(M0/M2(i,j))*sqrt(1.4/G)*sqrt(T2(i,j)/...
                T0)*P0;
            P2a(i,j) = P2(i,j);
            SR(i,j) = (1004 + Cp)/(2*R)*log(T2(i,j)/T0) - log(P2(i,j)...
                /P0);
            NKE(i,j) = 1 - 2/(1.4*M0^2)*SR(i,j);
            if SR(i,j) < 0
95                 T2(i,j) = NaN;
                 P2(i,j) = NaN;
            end
        end
    end
100 end

P2 = P2/1000;
P2a = P2a/1000;

figure(2),clf
105 for k = 1:size(T2,2)
    h1(k) = plot(P2(:,k),T2(:,k),'b');
    id = find(T2(:,k)==975);
    angle = 180/pi*(atan((T2(id+2,k) - T2(id-2,k))/(P2(id+2,k) - P2...
        (id-2,k))*0.5));
    if k == 1
110 text(P2(id,k),T2(id,k),['CR= ',num2str(k*5)],'Rotation',...
        angle,'Vert','bottom','BackgroundColor','none');
        hold on
    else
        text(P2(id,k),T2(id,k),num2str(k*5),'Rotation',...
115         angle,'Vert','bottom','BackgroundColor','none');
    end
end
[c,h] = contour(P2,T2,M2,[1.5,1.75,2,2.25,2.5],'k');
for k = 1:size(c,2)/4
120     id = k*4 - 2;
        if k == 1
            text(c(1,id)-30,c(2,id),['M_{comb} = ',num2str(c(1,id-1)),'%2f...
                ']),'Vert','middle','BackgroundColor','white');
        else

```

```

        text(c(1,id)-30,c(2,id),num2str(c(1,id-1), '%.2f'), 'Vert', '...
            middle', 'BackgroundColor', 'none');
125     end
    end
    [c2,h2] = contour(P2a,T2a,NKE,[1,0.99,0.98,0.97], 'r');
    for k = 1:4
        if k == 4
130            id = size(c2,2);
            text(c2(1,id)+7,c2(2,id),['n_{KE} = 1.0'], 'Vert', 'middle',...
                'BackgroundColor', 'none');
        else
            num = 0.97 + k/100;
            id = find(c2 == num)/2 - 1.5;
135            text(c2(1,id)+7,c2(2,id),num2str(num-0.01), 'Vert', 'middle'...
                , 'BackgroundColor', 'none');
        end
    end
    plot(118,712, '*')
    text(75,450, '* Static Pressure = 118 KPa / Static Temperature...
        = 712 K')
140    axis([0 500 400 1200])
    title({'Combustor Inlet Static Conditions', '', '(M_0 = 5, q_0...
        = 1000 lb/ft^2)'}))
    xlabel('Combustor Static Pressure (KPa)')
    ylabel('Combustor Static Temperature (K)')
    hold off
145    'Mach 8 and 100,000 ft'
    Static_Temperature = 901
    Static_Pressure = 48*1000
    Mach = 3.5
150    [Cp,G] = air(Static_Temperature)
    Total_Temperature = (1 + (G - 1)/2*Mach^2)*Static_Temperature
    Total_Pressure = (1 + (G - 1)/2*Mach^2)^(G/(G - 1))*...
        Static_Pressure
    Velocity = Mach*sqrt(G*R*Static_Temperature)
    Density = Static_Pressure/(R*Static_Temperature)
155    Area = (0.254)^2*pi/4
    Mass_Flow = Density*Velocity*Area

    'Mach 5 and 80,000 ft'
    Static_Temperature = 712
160    Static_Pressure = 118*1000
    Mach = 2.0
    [Cp,G] = air(Static_Temperature)
    Total_Temperature = (1 + (G - 1)/2*Mach^2)*Static_Temperature
    Total_Pressure = (1 + (G - 1)/2*Mach^2)^(G/(G - 1))*...
        Static_Pressure
165    Velocity = Mach*sqrt(G*R*Static_Temperature)
    Density = Static_Pressure/(R*Static_Temperature)
    Area = (0.254)^2*pi/4
    Mass_Flow = Density*Velocity*Area

```


Listing B.3 Fuel Injector Conditions

```

clear;clc

% Pylon Injector Parameters (all units in metric)
GAMMA = 1.02;
5 MW = 154;
R = 56;
P_total_inlet = 8.5E5;
T_total_inlet = 900;
Rho_total_inlet = P_total_inlet/R/T_total_inlet;
10 P_tunnel = 4.8E4;
A_inlet = 1.30E-4;
A_outlet = 5.7E-5;
Internal_height = 1.0E-2;
Volume = A_inlet*Internal_height + 4*4*57/1000^3;
15 dt = 1E-6;

% Initial Conditions
P_internal(1) = P_tunnel;
time(1) = 0;
20

% Calculations

for i = 2:500
    i
25 % Inlet Conditions
    Mach_inlet = -0.0001;
    tol = 1;
    while tol > 0.003
        Mach_inlet = Mach_inlet + .0001;
30        P_ratio_inlet = (1 + (GAMMA-1)/2*Mach_inlet^2)^(GAMMA/(...
            GAMMA-1));
        tol = abs(P_ratio_inlet-P_total_inlet/P_internal(i-1));
    end
    if Mach_inlet > 1.0
        Mach_inlet = 1.0;
35    end
    Rho_inlet = Rho_total_inlet/(1 + (GAMMA-1)/2*Mach_inlet^2)...
        ^((1/(GAMMA-1)));
    T_inlet = T_total_inlet/(1 + (GAMMA-1)/2*Mach_inlet^2);
    m_inlet = Rho_inlet*Mach_inlet*sqrt(GAMMA*R*T_inlet)*A_inlet;

40 % Outlet Conditions
    Mach_outlet = -0.0001;
    tol = 1;
    while tol > 0.003
        Mach_outlet = Mach_outlet + .0001;
45        P_ratio_outlet = (1 + (GAMMA-1)/2*Mach_outlet^2)^(GAMMA/(...
            GAMMA-1));
        tol = abs(P_ratio_outlet-P_internal(i-1)/P_tunnel);
    end
    if Mach_outlet > 1.0

```

```

        Mach_outlet = 1.0;
50     end
    Rho_outlet = Rho_total_inlet/((1 + (GAMMA-1)/2*Mach_outlet^2)...
        ^((1/(GAMMA-1))));
    T_outlet = T_total_inlet/(1 + (GAMMA-1)/2*Mach_outlet^2);
    m_outlet = Rho_outlet*Mach_outlet*sqrt(GAMMA*R*T_outlet)*...
        A_outlet;
    P_outlet = P_total_inlet/((1 + (GAMMA-1)/2*Mach_outlet^2)^(...
        GAMMA/(GAMMA-1)));
55     % Updated Internal Pressure Calculation
        dm = m_inlet - m_outlet;
        dP = (R*T_total_inlet/Volume)*dm;
        P_internal(i) = P_internal(i-1) + dP*dt;
60     time(i) = time(i-1) + dt;
    end

    plot(time,P_internal/1000-P_tunnel/1000)
    xlabel('Seconds')
65     ylabel('Plenum gauge pressure (kPa)')
    title('Pylon internal pressure over time')
    m_outlet_sonic_check = A_outlet*P_total_inlet/sqrt(T_total_inlet)*...
        sqrt(GAMMA/R)*(1+(GAMMA-1)/2)^(-(GAMMA+1)/(2*(GAMMA-1)))
    Mach_inlet
    V_inlet=Mach_inlet*sqrt(GAMMA*R*T_inlet)
70     P_internal_ss = P_internal(i)
    P_internal_gauge_ss = P_internal(i) - P_tunnel
    Mach_outlet
    V_outlet=Mach_outlet*sqrt(GAMMA*R*T_outlet)
    m_outlet
75     P_outlet
    P_tunnel

```

Appendix C. Raman Spectroscopy Mass Fraction Profiles

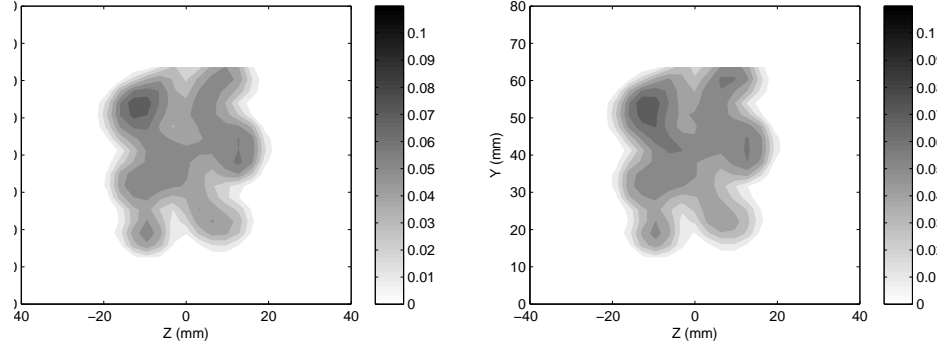


Fig. C.1 Two alternating wedge plume profile measurements at $13.6 d_e$.

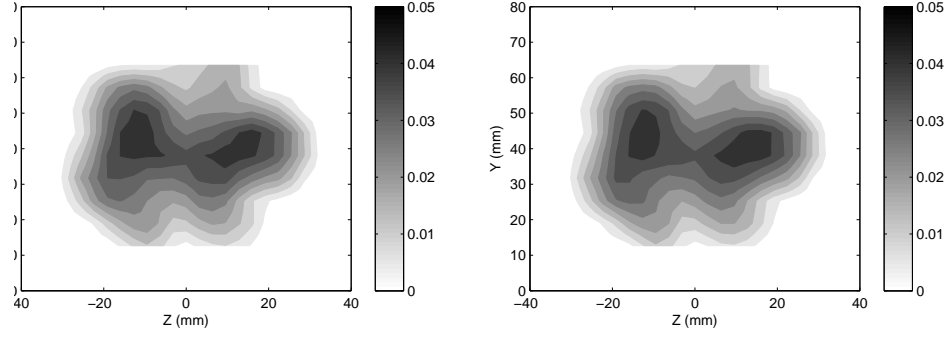


Fig. C.2 Two alternating wedge plume profile measurements at $23.9 d_e$.

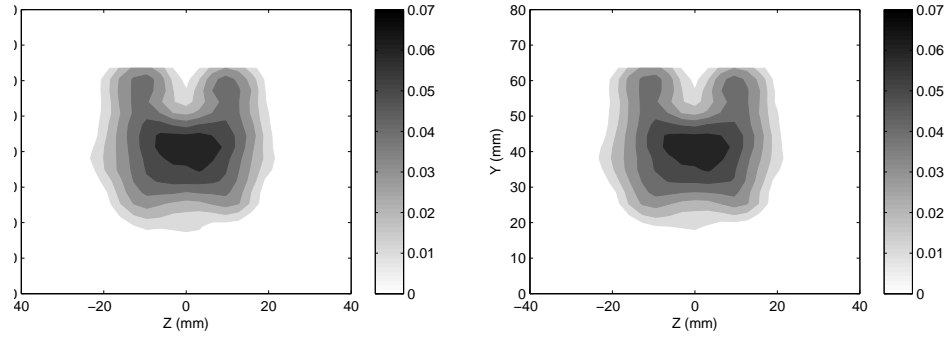


Fig. C.3 Two ramp plume profile measurements at $23.9 d_e$.

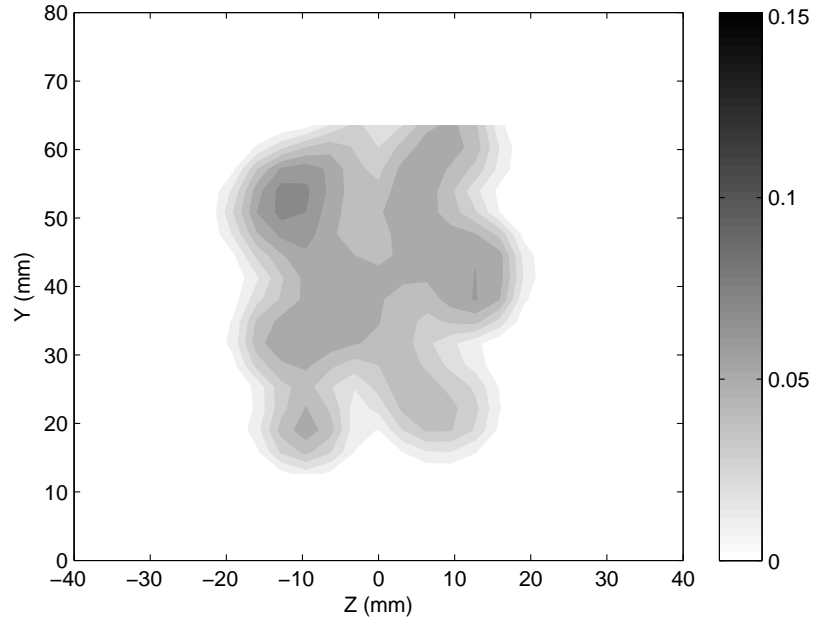


Fig. C.4 Average alternating wedge plume profile measurement at $13.6 d_e$.

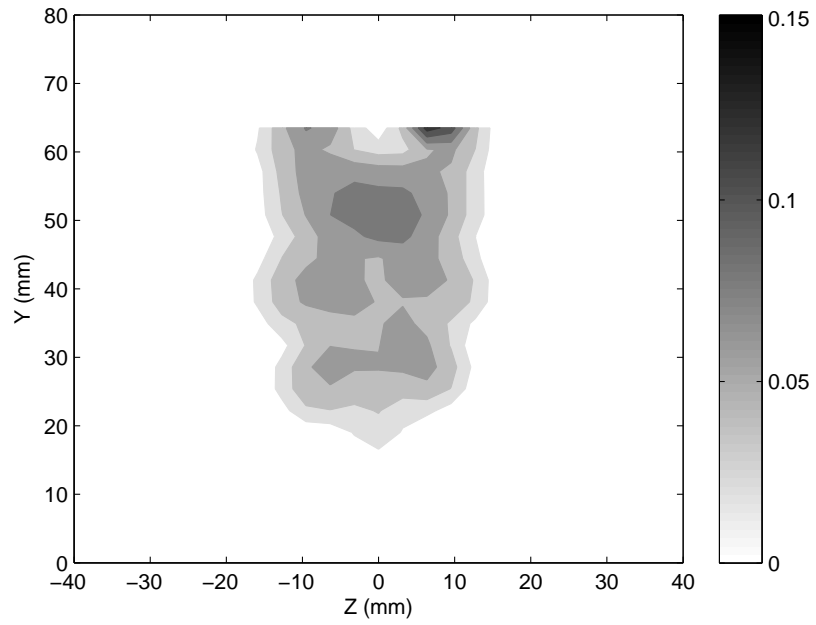


Fig. C.5 Ramp plume profile measurement at $13.6 d_e$.

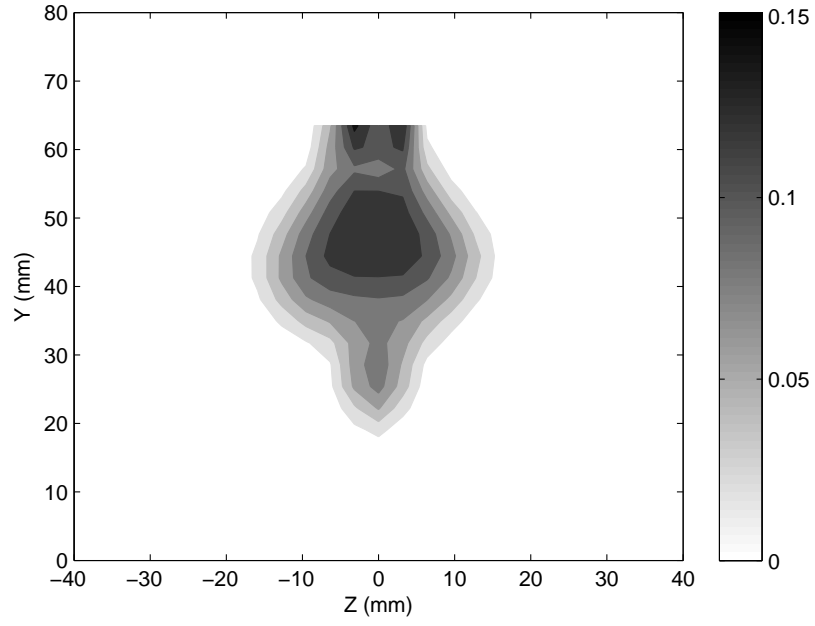


Fig. C.6 Basic plume profile measurement at $13.6 d_e$.

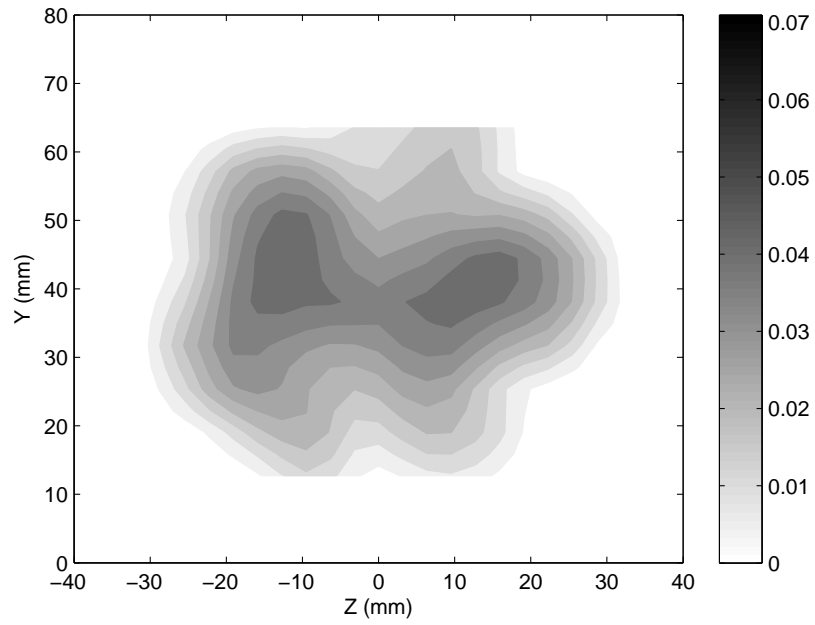


Fig. C.7 Average alternating wedge plume profile measurement at $23.9 d_e$.

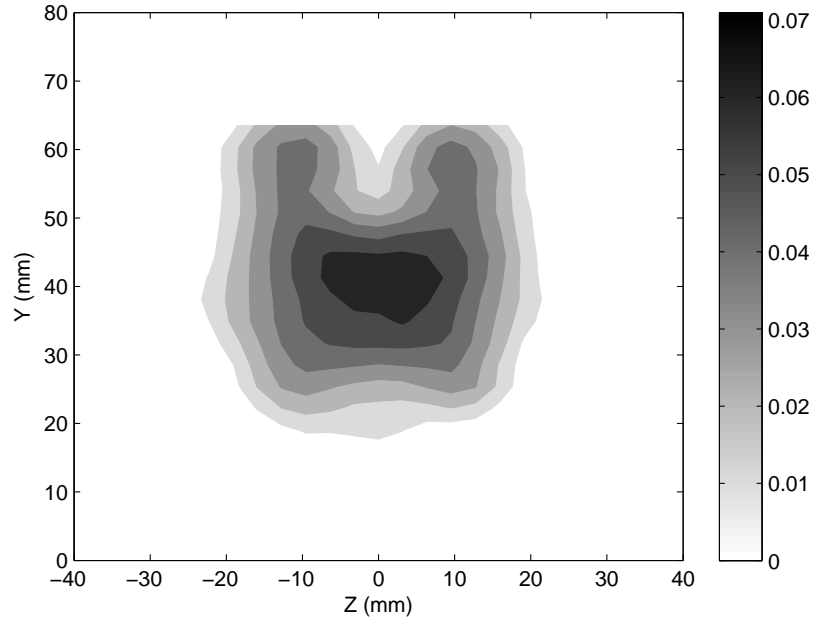


Fig. C.8 Average ramp plume profile measurement at $23.9 d_e$.

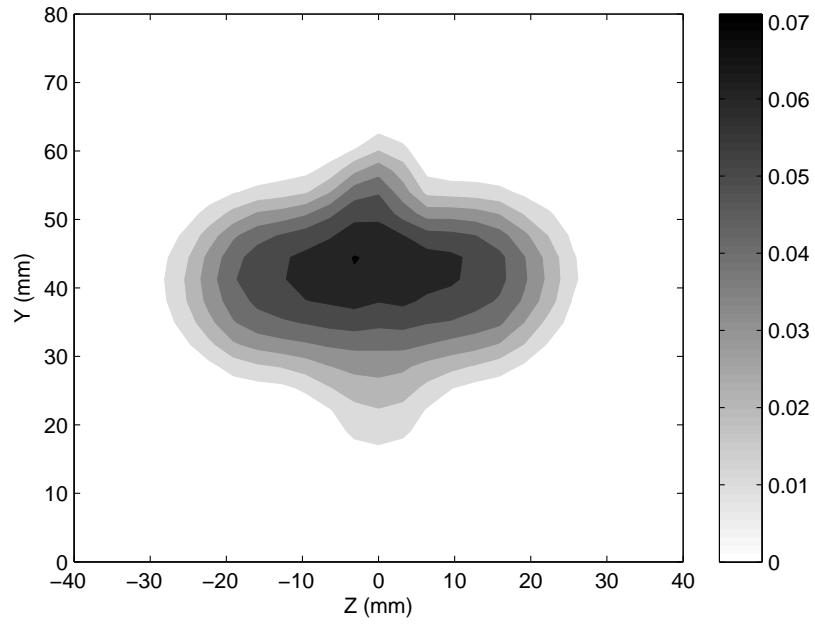


Fig. C.9 Basic plume profile measurement at $23.9 d_e$.

Appendix D. NO-PLIF Intensity Profiles

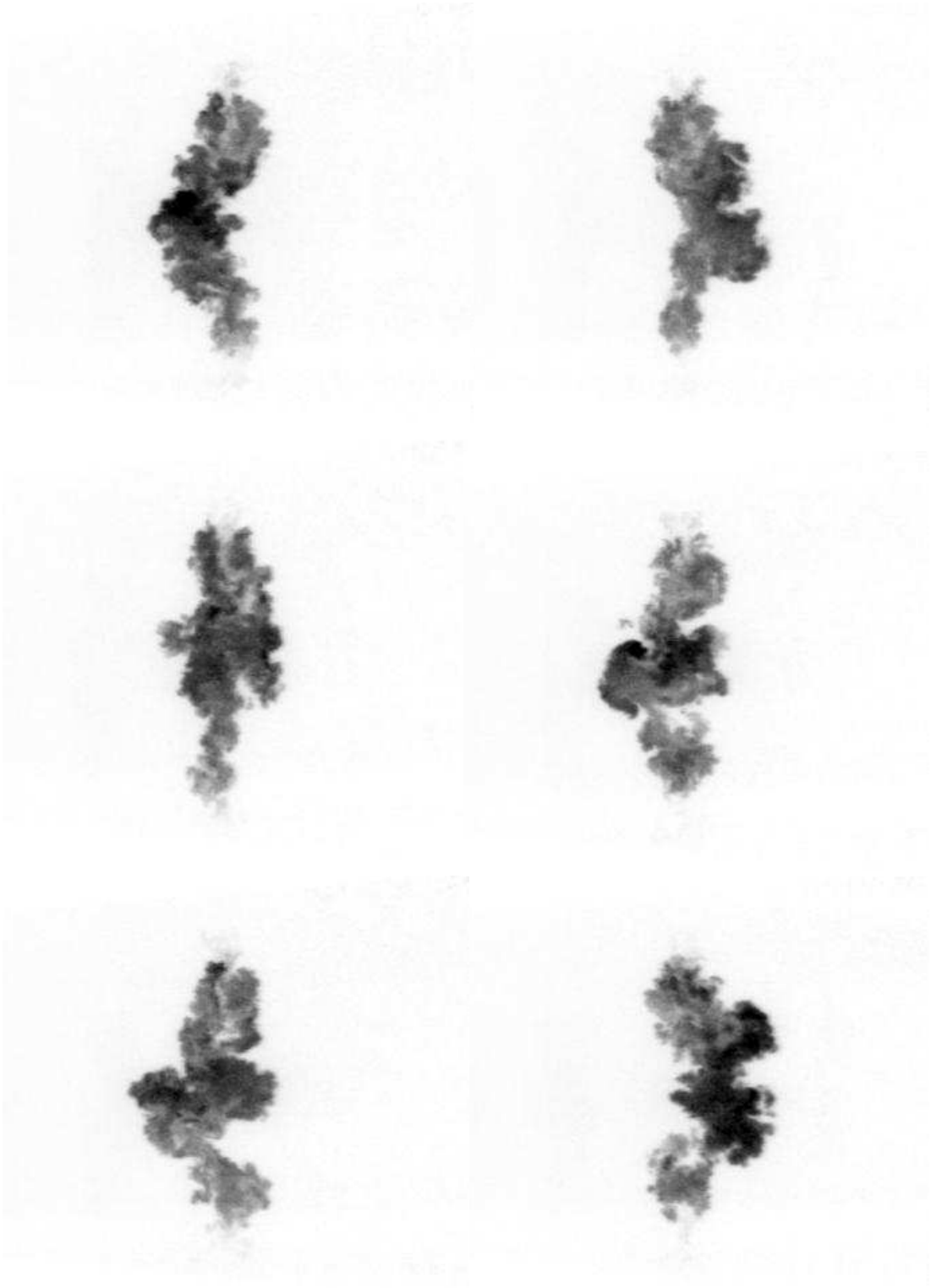


Fig. D.1 Basic pylon instantaneous plume images at $13.6 d_e$.

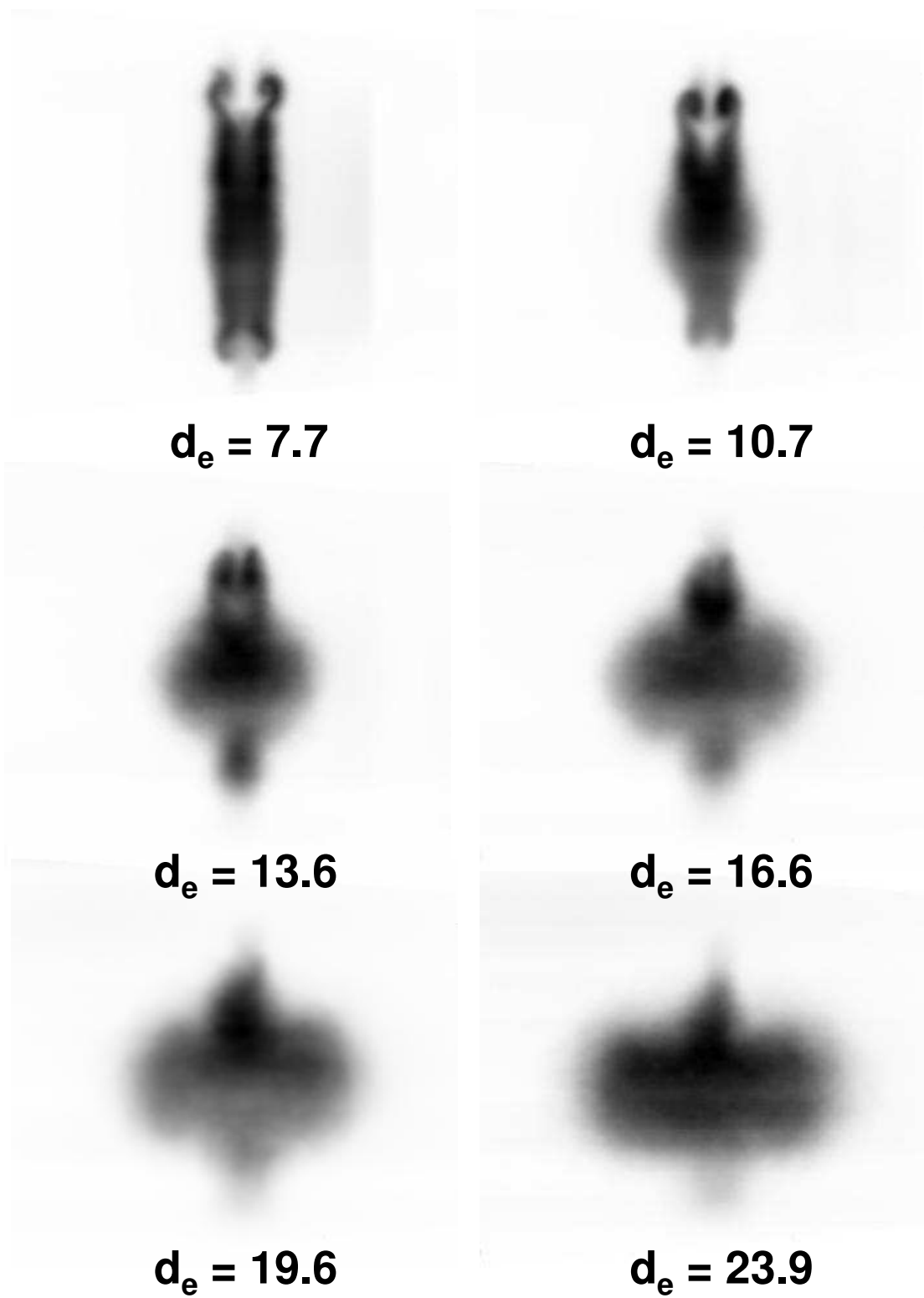


Fig. D.2 Basic pylon ensemble averaged plume images.

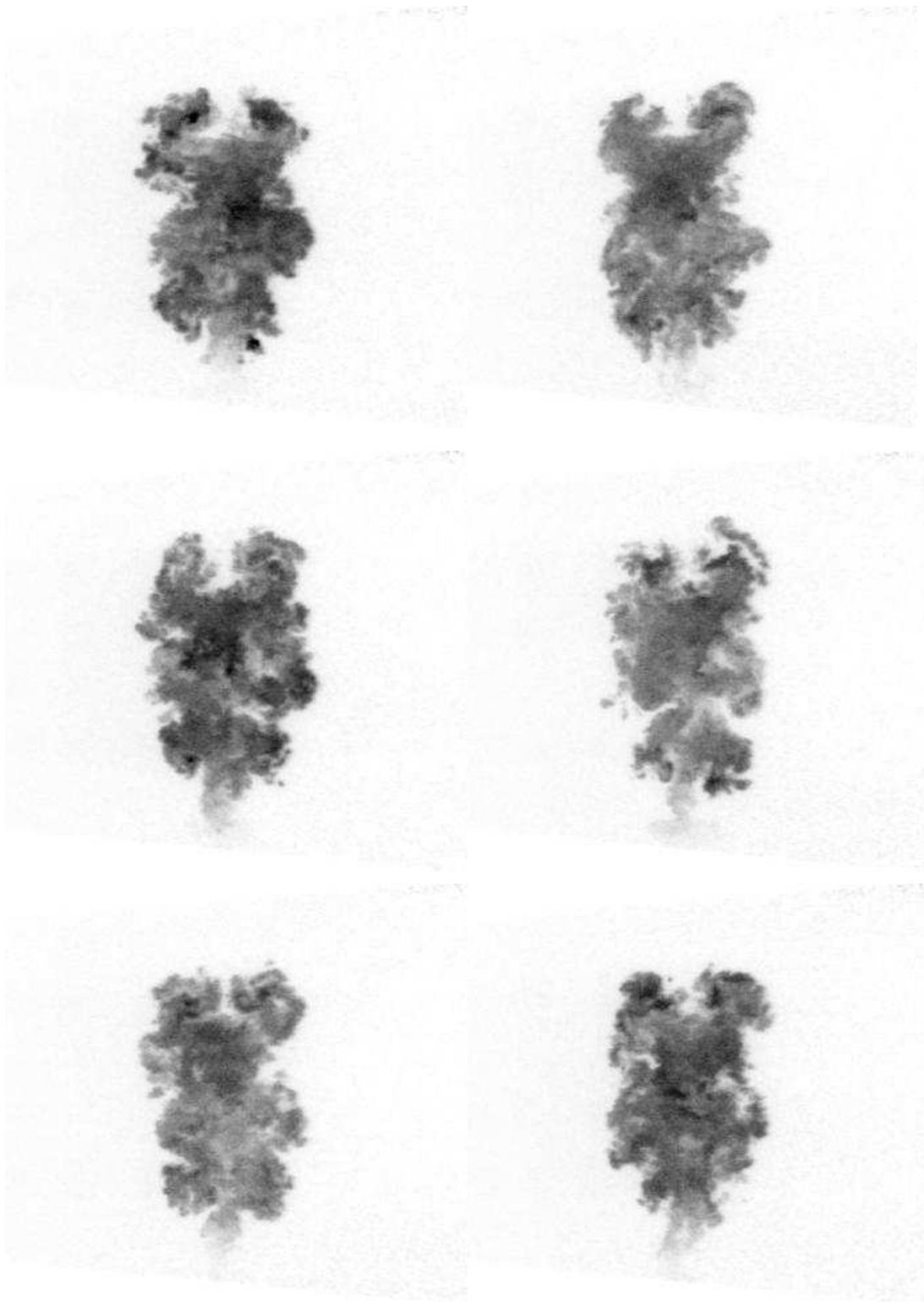


Fig. D.3 Ramp pylon instantaneous plume images at $13.6 d_e$.

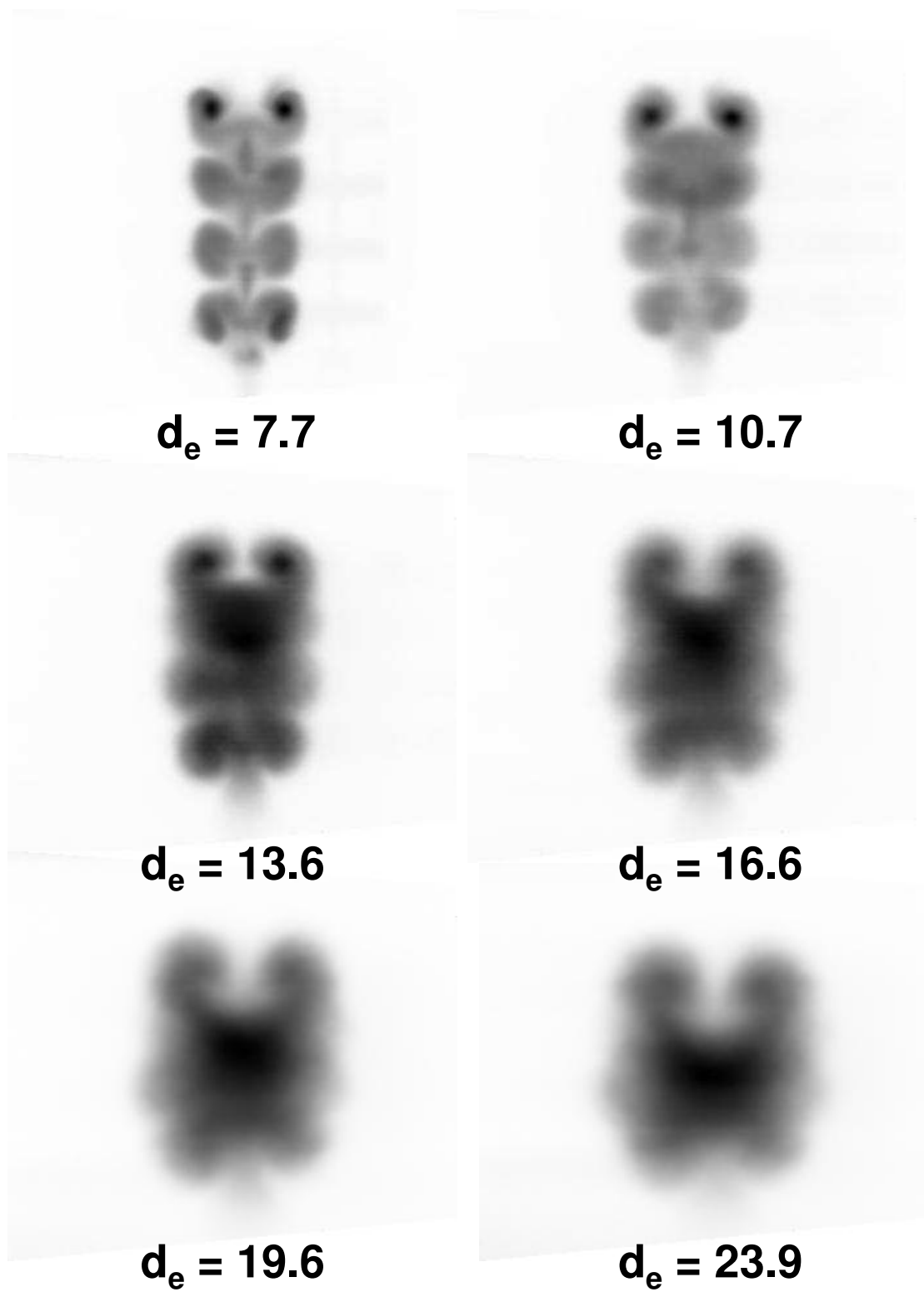


Fig. D.4 Ramp pylon ensemble averaged plume images.

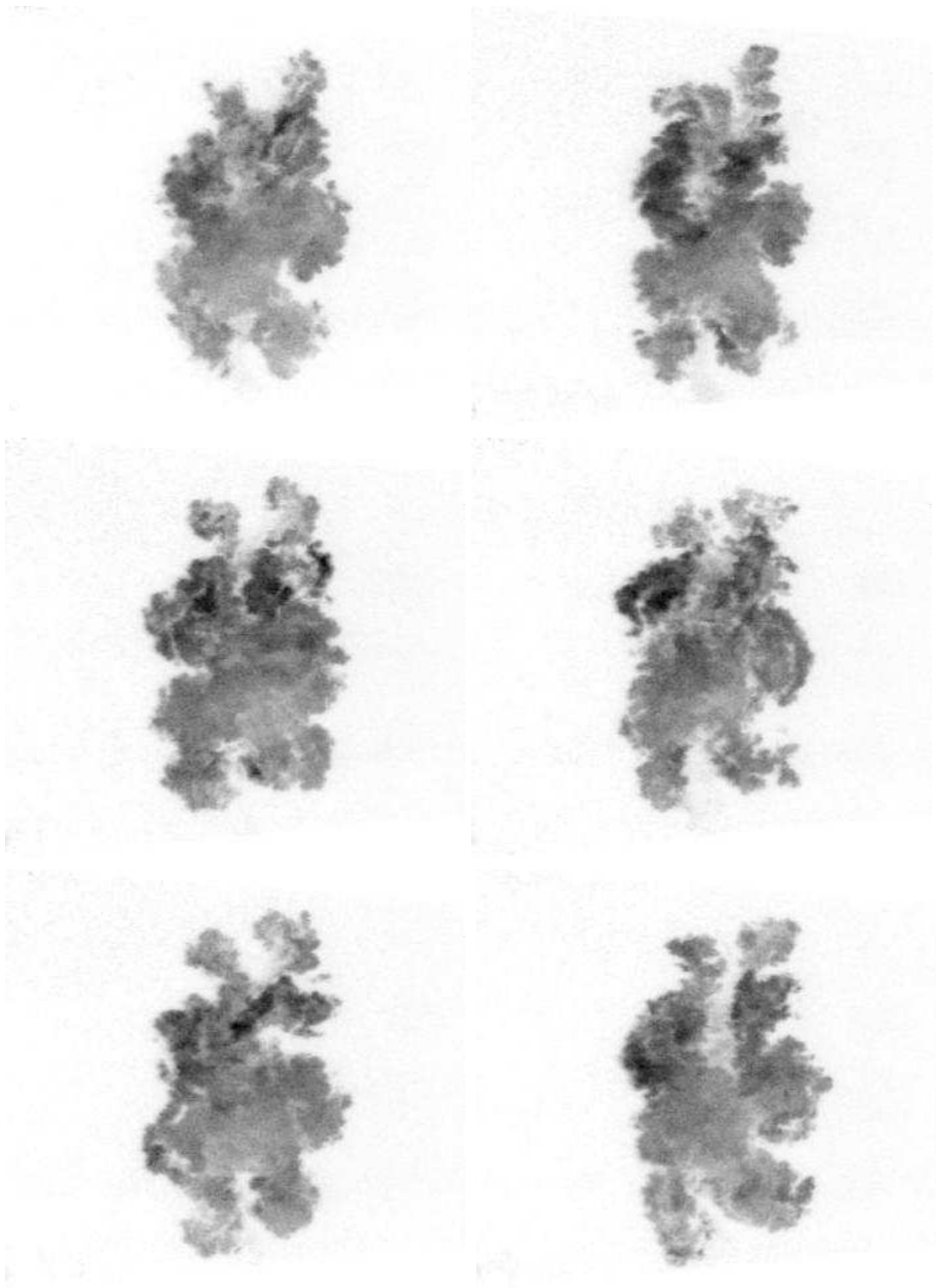


Fig. D.5 Alternating wedge pylon instantaneous plume images at $13.6 d_e$.

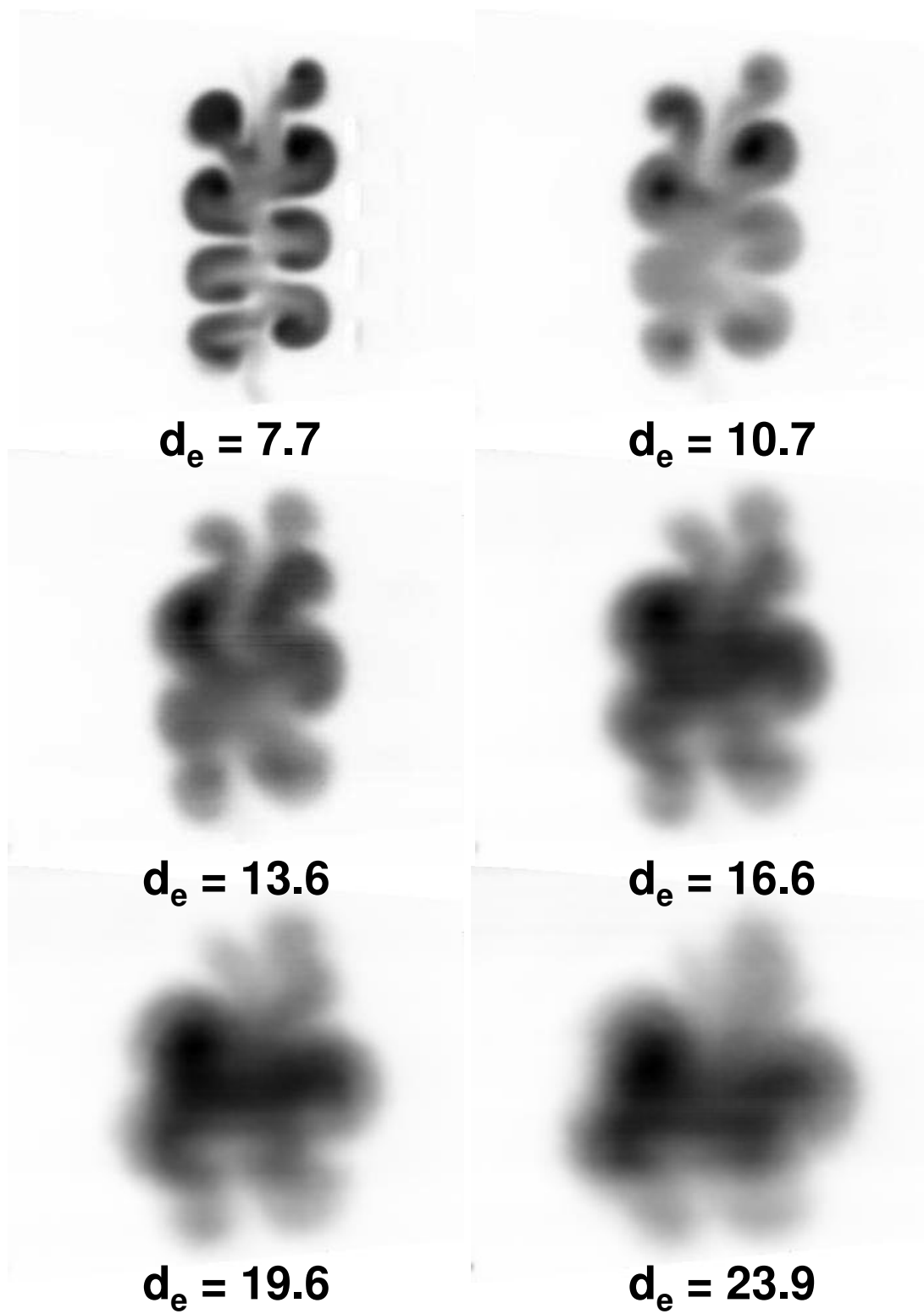


Fig. D.6 Alternating wedge pylon ensemble averaged plume images.

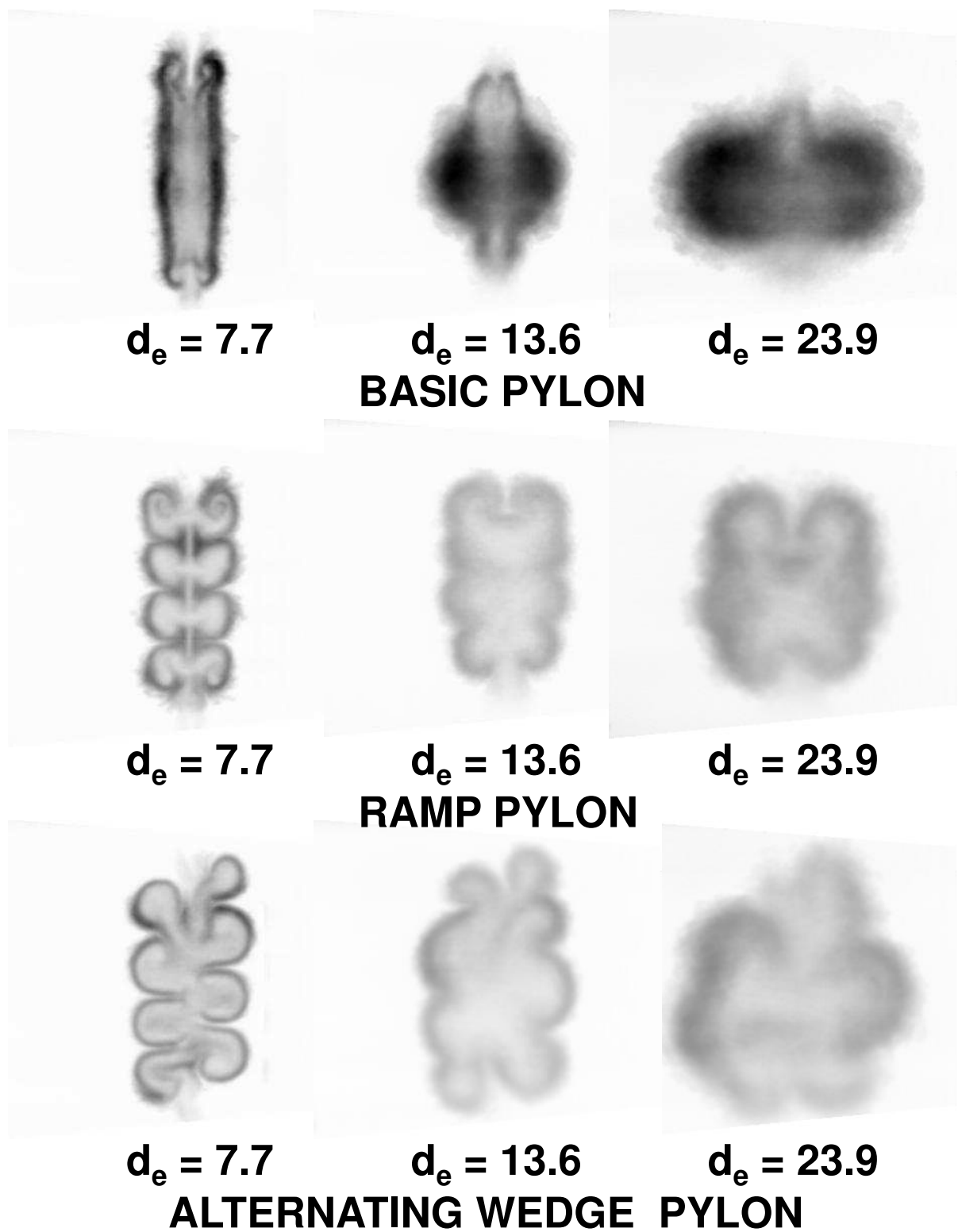


Fig. D.7 Standard deviation plume images.

Bibliography

- ¹Murthy, S. and Curran, E., *High-Speed Flight Propulsion Systems*, Vol. 137 of *Progress in Astronautics and Aeronautics*, American Institute for Aeronautics and Astronautics, 1991.
- ²Gruber, M., Nejad, A., Chen, T., and Dutton, J., "Mixing and Penetration Studies of Sonic Jets in a Mach 2 Freestream," *Journal of Propulsion and Power*, Vol. 11, No. 2, Mar.-Apr. 1995, pp. 315–323.
- ³Northam, G., Greenberg, I., and Byington, C., "Evaluation of Parallel Injector Configurations for Supersonic Combustion," AIAA Paper 89-2525, Jul. 1989.
- ⁴Waitz, I., Marble, F., and Zukoski, E., "Vorticity Generation by Contoured Wall Injectors," AIAA Paper 92-3550, Jul. 1992.
- ⁵Seiner, J., Dash, S., and Kenzakowski, D., "Historical Survey on Enhanced Mixing in Scramjet Engines," *Journal of Propulsion and Power*, Vol. 17, No. 6, Nov.-Dec. 2001, pp. 1273–1286.
- ⁶Sunami, T. and Scheel, F., "Analysis of Mixing Enhancement Using Streamwise Vortices in a Supersonic Combustor by Application of Laser Diagnostics," AIAA Paper 2002-5203, Oct. 2002.
- ⁷Tam, C., Lin, K., and Raffoul, C., "Review of Jet-in-Crossflow Studies for Scramjet Application," Tech. rep., ARFL/PRAT, Wright Patterson Air Force Base, OH 45433, 2007.
- ⁸Vargaftik, N., *Tables on the Thermophysical Properties of Liquids and Gases*, John Wiley and Sons, 2nd ed., 1975.
- ⁹Curran, E. and Murthy, S., *Scramjet Propulsion*, Vol. 189 of *Progress in Astronautics and Aeronautics*, American Institute of Aeronautics and Astronautics, 2000.
- ¹⁰Waltrup, P., "Upper Bounds on the Flight Speed of Hydrocarbon-Fueled Scramjet-Powered Vehicles," *Journal of Propulsion and Power*, Vol. 17, No. 6, Nov.-Dec. 2001, pp. 1199–1204.
- ¹¹Curran, E., "Scramjet Engines: The First Forty Years," *Journal of Propulsion and Power*, Vol. 17, No. 6, Nov.-Dec. 2001, pp. 1138–1148.
- ¹²Townend, L., "Domain of the Scramjet," *Journal of Propulsion and Power*, Vol. 17, No. 6, Nov.-Dec. 2001, pp. 1205–1213.
- ¹³Powell, O., Edwards, J., Norris, R., Numbers, K., and Pearce, J., "Development of Hydrocarbon-Fueled Scramjet Engines: The Hypersonic Technology (HyTech) Program," *Journal of Propulsion and Power*, Vol. 17, No. 6, Nov.-Dec. 2001, pp. 1170–1176.
- ¹⁴Boudreau, A., "Status of the U.S. Air Force HYTECH Program," AIAA Paper 2003-6947, Dec. 2003.
- ¹⁵Heiser, W. and Pratt, D., *Hypersonic Airbreathing Propulsion*, Education Series, American Institute of Aeronautics and Astronautics, 1994.
- ¹⁶Papamoschou, D., "Structure of the Compressible Turbulent Shear Layer," AIAA Paper 89-0126, Jan. 1989.
- ¹⁷Samimy, M., Erwin, D., and Elliott, G., "Compressibility and Shock Wave Interaction Effects on Free Shear Layers," AIAA Paper 89-2460, Jul. 1989.
- ¹⁸Bogdanoff, D., "Advanced Injection and Mixing Techniques for Scramjet Combustors," *Journal of Propulsion and Power*, Vol. 10, No. 2, Mar.-Apr. 1994, pp. 183–190.
- ¹⁹Hollo, S., McDaniel, J., and Hartfield, R., "Characterization of Supersonic Mixing in a Nonreacting Mach 2 Combustor," AIAA Paper 92-0093, Jan. 1992.
- ²⁰VanLerberghe, W., Santiago, J., Dutton, J., and Lucht, R., "Mixing of a Sonic Transverse Jet Injected into a Supersonic Flow," *AIAA Journal*, Vol. 38, No. 3, Mar. 2000, pp. 470–479.
- ²¹Gruber, M., Nejad, A., Chen, T., and Dutton, J., "Transverse Injection from Circular and Elliptical Nozzles into a Supersonic Crossflow," *Journal of Propulsion and Power*, Vol. 16, No. 3, May-Jun. 2000, pp. 449–457.

- ²²Murugappan, S., Gutmark, E., Carter, C., Donbar, J., Gruber, M., and Hsu, K., "Transverse Supersonic Controlled Swirling Jet in a Supersonic Cross Stream," *AIAA Journal*, Vol. 44, No. 2, Feb. 2006, pp. 290–300.
- ²³Gutmark, E., Schadow, K., and Wilson, K., "Mixing Enhancement in Coaxial Supersonic Jets," AIAA Paper 89-1812, Jun. 1989.
- ²⁴Zaman, K., "Spreading Characteristics and Thrust of Jets from Asymmetric Nozzles," AIAA Paper 96-0200, Jan. 1996.
- ²⁵Haimovitch, Y., Gartenberg, E., Roberts, A., and Northam, G., "Effects of Internal Nozzle Geometry on Compression-Ramp Mixing in Supersonic Flow," *AIAA Journal*, Vol. 35, No. 4, Apr. 1997, pp. 663–670.
- ²⁶Zaman, K., Reeder, M., and Samimy, M., "Control of an Axisymmetric Jet Using Vortex Generators," *Physics of Fluids*, Vol. 6, No. 2, Feb. 1994, pp. 778–793.
- ²⁷Riggins, D., Mekkes, G., McClinton, C., and Drummond, J., "A Numerical Study of Mixing Enhancement in a Supersonic Combustor," AIAA Paper 90-0203, Jan. 1990.
- ²⁸Riggins, D., McClinton, C., Rogers, R., and Bittner, R., "A Comparative Study of Scramjet Injection Strategies for High Mach Number Flows," AIAA Paper 92-3287, Jul. 1992.
- ²⁹Walther, R., Sabelnikov, V., Korontsvit, Y., Voloschenko, O., Ostras, V., and Sermanov, V., "Progress in the Joint German-Russian Scramjet Technology Programme," ISABE Paper 95-7121, Sep. 1995.
- ³⁰Walther, R., Koschel, W., Sabelnikov, V., Korontsvit, Y., and Ivanov, V., "Investigations into the Aerothermodynamic Characteristics of Scramjet Components," ISABE Paper 97-7085, Sep. 1997.
- ³¹Manoharan, S., Chandra, B., Chakravarthy, S., Ramakrishnan, S., and Subramanyam, J., "Experimental Studies of Supersonic Cold Flow Mixing with Ramp Mixers," *Journal of Aerospace Engineering*, Vol. 18, No. 4, Oct. 2005, pp. 197–205.
- ³²Abdel-Salam, T., Tiwari, S., Chaturvedi, S., and Mohieldin, T., "Mixing and Combustion in Scramjet Combustor with Raised and Relieved Ramp," AIAA Paper 2000-3709, Jul. 2000.
- ³³Owens, M., Segal, C., and Auslender, A., "Effects of Mixing Schemes on Kerosene Combustion in a Supersonic Airstream," *Journal of Propulsion and Power*, Vol. 13, No. 4, Jul.-Aug. 1997, pp. 525–531.
- ³⁴Aria, T., Sakaue, S., Morisaki, T., Kondo, A., Hiejima, T., and Nishioka, M., "Supersonic Streamwise Vortices Breakdown in a Scramjet Combustor," AIAA Paper 2006-8025, Nov. 2006.
- ³⁵Desikan, S. and Kurian, J., "Mixing Studies in Supersonic Flow Employing Strut Based Hypermixers," AIAA Paper 2005-3643, Jul. 2005.
- ³⁶Desikan, S. and Kurian, J., "Strut-Based Gaseous Injection into a Supersonic Stream," *Journal of Propulsion and Power*, Vol. 22, No. 2, Mar.-Apr. 2006, pp. 474–477.
- ³⁷Sislian, J. and Schumacher, J., "A Comparative Study of Hypersonic Fuel/Air Mixing Enhancement by Ramp and Cantilevered Ramp Injectors," AIAA Paper 99-4873, Nov. 1999.
- ³⁸Sislian, J. and Parent, B., "Hypervelocity Fuel/Air Mixing in a Scramjet Inlet," *Journal of Propulsion and Power*, Vol. 20, No. 2, Mar.-Apr. 2004, pp. 263–272.
- ³⁹Sislian, J., Martens, R., Schwartzentruber, T., and Parent, B., "Numerical Simulation of a Real Scramjet Flowfield," *Journal of Propulsion and Power*, Vol. 22, No. 5, Sep.-Oct. 2006, pp. 1039–1048.
- ⁴⁰Fuller, R., Wu, P., Nejad, A., and Schetz, J., "Comparison of Physical and Aerodynamic Ramps as Fuel Injectors in Supersonic Flow," *Journal of Propulsion and Power*, Vol. 14, No. 2, Mar.-Apr. 1998, pp. 135–145.
- ⁴¹Jacobsen, L., Gallimore, S., Schetz, J., O'Brian, W., and Goss, L., "Improved Aerodynamic-Ramp Injector in Supersonic Flow," *Journal of Propulsion and Power*, Vol. 19, No. 4, Jul.-Aug. 2003, pp. 663–673.

- ⁴²Sunami, T., Wendt, M., and Nishioka, M., "Supersonic Mixing and Combustion Control Using Streamwise Vortices," AIAA Paper 1998-3271, Jul. 1998.
- ⁴³Sunami, T., Magre, P., Bresson, A., Grisch, F., Orain, M., and Kodera, M., "Experimental Study of Strut Injectors in a Supersonic Combustor Using OH-PLIF," AIAA Paper 2005-3304, May 2005.
- ⁴⁴Scherrer, D., Dessornes, O., Montmayeur, N., and Ferrandon, O., "Injection Studies in the French Hypersonic Technologies Program," AIAA Paper 95-6096, Apr. 1995.
- ⁴⁵Campbell, B., Siebenhaar, A., and Nguyen, T., "Strutjet Engine Performance," *Journal of Propulsion and Power*, Vol. 17, No. 6, Nov.-Dec. 2001, pp. 1227-1232.
- ⁴⁶Shreenivasan, O., Kumar, R., Kumar, T., Sujith, R., and Chakravarthy, S., "Mixing in Confined Supersonic Flow Past Strut Based Cavity and Ramps," AIAA Paper 2004-4194, Jul. 2004.
- ⁴⁷Rocci-Denis, S., Maier, D., Erhard, W., and Kau, H., "Free Stream Investigations on Methane Combustion in a Supersonic Air Flow," AIAA Paper 2005-3314, May 2005.
- ⁴⁸Gilinsky, M., Khaikine, V., Akyurtlu, A., Akyurtlu, J., Trexler, C., Baurle, R., Emami, S., and Blankson, I., "Numerical and Experimental Tests of a Supersonic Inlet Utilizing a Pylon Set for Mixing, Combustion and Thrust Enhancement," AIAA Paper 2005-3290, May 2005.
- ⁴⁹Sunami, T., Itoh, K., Sato, K., and Komuro, T., "Mach 8 Ground Tests of the Hypermixer Scramjet for HyShot-IV Flight Experiment," AIAA Paper 2006-8062, Nov. 2006.
- ⁵⁰Akyurtlu, A., Akyurtlu, J., Gonor, A., Khaikine, V., Cutler, A., and Blankson, I., "Numerical and Experimental Tests of a Supersonic Inlet with Pylon Set and Fuel Injection through Pylons," AIAA Paper 2006-1032, Jan. 2006.
- ⁵¹Avrashkov, V., Baranovsky, S., and Levin, V., "Gasdynamic Features of Supersonic Kerosene Combustion in a Model Combustion Chamber," AIAA Paper 90-5268, Oct. 1990.
- ⁵²Naughton, J. and Settles, G., "Experiments on the Enhancement of Compressible Mixing via Streamwise Vorticity, Part I - Optical Measurements," AIAA Paper 92-3549, Jul. 1992.
- ⁵³Rose, S. and Hartfield, R., "Experimental and Analytical Investigation of Injection Behind a Pylon in a Compressible Flow," AIAA Paper 96-0918, Jan. 1996.
- ⁵⁴Sato, S., Izumikawa, M., Tomioka, S., and Mitani, T., "Scramjet Engine Test at the Mach 6 Flight Condition," AIAA Paper 97-3021, Jul. 1997.
- ⁵⁵Semenov, V. and Romankov, O., "The Investigation of Operation Domain of Strut Fuel Feed System for Model Scramjet Combustor," AIAA Paper 98-1514, Apr. 1998.
- ⁵⁶Gruenig, C. and Mayinger, F., "Supersonic Combustion of Kerosene/H₂-Mixtures in a Model Scramjet Combustor," Tech. Rep. D-85747, Institute A for Thermodynamics, Technical University Munich, Garching, Germany, 1999.
- ⁵⁷Gouskov, O., Kopchenov, V., Vinogradov, V., and Waltrup, P., "Numerical Researches of Gaseous Fuel Pre-Injection in Hypersonic 3-D Inlet," AIAA Paper 2000-3599, Jul. 2000.
- ⁵⁸Livingston, T., Segal, C., Schindler, M., and Vinogradov, V., "Penetration and Spreading of Liquid Jets in an External-Internal Compression Inlet," *AIAA Journal*, Vol. 38, No. 6, Jun. 2000, pp. 989-994.
- ⁵⁹Gruenig, C., Avrashkov, V., and Mayinger, F., "Fuel Injection into a Supersonic Airflow by Means of Pylons," *Journal of Propulsion and Power*, Vol. 16, No. 1, Jan.-Feb. 2000, pp. 29-34.
- ⁶⁰Gruenig, C. and Mayinger, F., "Experimental Investigation of Supersonic Flame Stabilization based on Fuel Self-Ignition," *Chemical Engineering Technology*, Vol. 23, No. 10, Oct. 2000, pp. 909-918.
- ⁶¹Owens, M., Mullagiri, S., Segal, C., and Vinogradov, V., "Effects of Fuel Preinjection on Mixing in Mach 1.6 Airflow," *Journal of Propulsion and Power*, Vol. 17, No. 3, May-Jun. 2001, pp. 605-610.

- ⁶²Shikhman, Y., Vinogradov, V., Yanovski, L., Stepanov, V., Shlyakotin, V., and Pen'kov, S., "The Demonstrator of Technologies - Dual Mode Scramjet on Hydrocarbon Endothermic Fuel," AIAA Paper 2001-1787, Apr. 2001.
- ⁶³Vinogradov, V., Shikhman, Y., Albegov, R., and Vedeshkin, G., "Experimental Research of Pre-Injected Methane Combustion in High Speed Supersonic Airflow," AIAA Paper 2003-6940, Dec. 2003.
- ⁶⁴Montes, D., King, P., Gruber, M., Carter, C., and Hsu, K., "Mixing Effects of Pylon-Aided Fuel Injection Located Upstream of a Flameholding Cavity in Supersonic Flow," AIAA Paper 2005-3913, Jul. 2005.
- ⁶⁵Haubelt, L., King, P., Gruber, M., Carter, C., and Hsu, K., "Performance of Pylons Upstream of a Cavity-based Flameholder in Non-reacting Supersonic Flow," AIAA Paper 2006-4679, Jul. 2006.
- ⁶⁶Vinogradov, V., Shikhman, Y., and Segal, C., "Review of Fuel Pre-Injection Studies in a High Speed Airflow," AIAA Paper 2006-1030, Jan. 2006.
- ⁶⁷Kawano, S., Aso, S., and Orino, M., "A Study of a New Injector for Improvement of Supersonic Mixing," AIAA Paper 2000-0089, Jan. 2000.
- ⁶⁸Doster, J., King, P., Gruber, M., and Maple, R., "Pylon Fuel Injector Design for a Scramjet Combustor," AIAA Paper 2007-5404, 2007.
- ⁶⁹Doster, J., King, P., Gruber, M., and Maple, R., "Numerical Simulation of Ethylene Injection from In-stream Fueling Pylons," AIAA Paper 2008-2518, 2008.
- ⁷⁰Doster, J., King, P., Gruber, M., Carter, C., Ryan, M., and Hsu, K.-Y., "Experimental Investigation of Air and Methane Injection from In-Stream Fueling Pylons," AIAA Paper 2008-4501, 2008.
- ⁷¹Wylen, G., Sonntag, R., and Borgnakke, C., *Fundamentals of Classical Thermodynamics*, John Wiley and Sons, 4th ed., 1994.
- ⁷²Glassman, I., *Combustion*, Academic Press, 1996.
- ⁷³Fan, X., Yu, G., Li, J., Zhang, X., and Sung, C., "Combustion and Ignition of Thermally Cracked Kerosene in Supersonic Model Combustors," *Journal of Propulsion and Power*, Vol. 23, No. 2, Mar.-Apr. 2007, pp. 317-324.
- ⁷⁴Nagley, E., *Fuel Composition Analysis of Endothermically Heated JP-8 for Use in a Pulse Detonation Engine*, Master's thesis, Graduate School of Engineering and Management, Wright Patterson AFB, OH, June 2008.
- ⁷⁵Fan, X., Yu, G., Li, J., Zhang, X., and Sung, C., "Investigation of Vaporized Kerosene Injection and Combustion in a Supersonic Model Combustor," *Journal of Propulsion and Power*, Vol. 22, No. 1, Jan.-Feb. 2006, pp. 103-110.
- ⁷⁶"Aviation Fuel Properties," Tech. Rep. 530, Coordinating Research Council, 219 Perimeter Center Parkway, Atlanta, GA 30346, May 1988.
- ⁷⁷Schlichting, H. and Gersten, K., *Boundary Layer Theory*, Springer, eighth ed., 2000.
- ⁷⁸Mao, M., Riggins, D., and McClinton, C., "Numerical Simulation of Transverse Fuel Injection," Tech. Rep. N91-21097, NASA Langley Research Center, Hampton, VA 23665.
- ⁷⁹Gruber, M. and Nejad, A., "New Supersonic Combustion Research Facility," *Journal of Propulsion and Power*, Vol. 11, No. 5, 1995, pp. 1080-1083.
- ⁸⁰Gruber, M., Carter, C., Montes, D., Haubelt, L., King, P., and Hsu, K., "Experimental Studies of Pylon-Aided Fuel Injection into a Supersonic Crossflow," *Journal of Propulsion and Power*, Vol. 24, No. 3, May-Jun. 2008, pp. 460-470.
- ⁸¹Sims, J., "Tables for Supersonic Flow Around Right Circular Cones at Zero Angle of Attack," Tech. Rep. SP-3004, NASA, George C. Marshall Space Flight Center, 1964.
- ⁸²Jacobsen, L., Shetz, J., and Ng, W., "Flowfield near a Multiport Injector Array in a Supersonic Flow," *Journal of Propulsion and Power*, Vol. 16, No. 2, Mar.-Apr. 2000, pp. 216-226.

- ⁸³Tomioka, S., Jacobsen, L., and Schetz, J., “Modified Mixing Analogy for Studies of Mixing in Supersonic Flows,” *Journal of Propulsion and Power*, Vol. 19, No. 1, Jan.-Feb. 2003, pp. 151–154.
- ⁸⁴Tomioka, S., Jacobsen, L., and Schetz, J., “Sonic Injection from Diamond-Shaped Orifices into a Supersonic Crossflow,” *Journal of Propulsion and Power*, Vol. 19, No. 1, Jan.-Feb. 2003, pp. 104–114.
- ⁸⁵Gonor, A., Gilinsky, M., and Khaikine, V., “Development of a Mixing Analogy for Investigation of Injectant Mixing in Supersonic Flow,” AIAA Paper 2005-3234.
- ⁸⁶Hirano, K., Matsuo, A., and Tomioka, S., “Validation of Modified Mixing Analogy by Numerical Analysis,” AIAA Paper 2006-4616.
- ⁸⁷Eckbreth, A., *Laser Diagnostics for Combustion Temperature and Species*, Abacus Press, 1988.
- ⁸⁸Dembroder, W., *Laser Spectroscopy*, Springer, 2003.
- ⁸⁹Hsu, K., Carter, C., Crafton, J., Gruber, M., Donbar, J., and Mathur, T., “Fuel Distribution About a Cavity Flameholder in Supersonic Flow,” AIAA Paper 2000-3585, 2000.
- ⁹⁰Gruber, M., Donbar, J., Carter, C., and Hsu, K., “Mixing and Combustion Studies Using Cavity-Based Flameholders in a Supersonic Flow,” *Journal of Propulsion and Power*, Vol. 20, No. 5, Sep.-Oct. 2004, pp. 769–778.
- ⁹¹Herzberg, G., *Spectra of Diatomic Molecules*, D. Van Nostrand Company, 1945.
- ⁹²Herzberg, G., *Infrared and Raman Spectra*, D. Van Nostrand Company, 1945.
- ⁹³Kobayashi, K., Bowersox, R., Srinivasan, R., Carter, C., and Hsu, K., “Flowfield Studies of a Diamond-Shaped Fuel Injector in a Supersonic Flow,” *Journal of Propulsion and Power*, Vol. 23, No. 6, Nov.-Dec. 2007, pp. 1168–1176.
- ⁹⁴Vincenti, W. and Kruger, C., *Physical Gas Dynamics*, Krieger Publishing Company, 1965.
- ⁹⁵Kinney, J., *Statistics for Science and Engineering*, Addison Wesley, 2002.

REPORT DOCUMENTATION PAGE					Form Approved OMB No. 0704-0188	
<p>The public reporting burden for this collection of information is estimated to average 1 hour per response, including the time for reviewing instructions, searching existing data sources, gathering and maintaining the data needed, and completing and reviewing the collection of information. Send comments regarding this burden estimate or any other aspect of this collection of information, including suggestions for reducing this burden to Department of Defense, Washington Headquarters Services, Directorate for Information Operations and Reports (0704-0188), 1215 Jefferson Davis Highway, Suite 1204, Arlington, VA 22202-4302. Respondents should be aware that notwithstanding any other provision of law, no person shall be subject to any penalty for failing to comply with a collection of information if it does not display a currently valid OMB control number. PLEASE DO NOT RETURN YOUR FORM TO THE ABOVE ADDRESS.</p>						
1. REPORT DATE (DD-MM-YYYY)		2. REPORT TYPE		3. DATES COVERED (From — To)		
11-09-2008		Doctoral Dissertation		Sept 2005 — Sept 2008		
4. TITLE AND SUBTITLE Hypermixer Pylon Fuel Injection for Scramjet Combustors				5a. CONTRACT NUMBER		
				5b. GRANT NUMBER		
				5c. PROGRAM ELEMENT NUMBER		
6. AUTHOR(S) Jason C. Doster, Major, USAF				5d. PROJECT NUMBER		
				5e. TASK NUMBER		
				5f. WORK UNIT NUMBER		
7. PERFORMING ORGANIZATION NAME(S) AND ADDRESS(ES) Air Force Institute of Technology Graduate School of Engineering and Management 2950 Hobson Way WPAFB OH 45433-7765				8. PERFORMING ORGANIZATION REPORT NUMBER AFIT/DS/ENY/08-02		
9. SPONSORING / MONITORING AGENCY NAME(S) AND ADDRESS(ES) Dr. Mark R. Gruber, AFRL/RZAS 1950 Fifth Street Bldg 18, Rm D228 Wright Patterson Air Force Base, OH 45433				10. SPONSOR/MONITOR'S ACRONYM(S)		
				11. SPONSOR/MONITOR'S REPORT NUMBER(S)		
12. DISTRIBUTION / AVAILABILITY STATEMENT Approval for public release; distribution is unlimited.						
13. SUPPLEMENTARY NOTES						
14. ABSTRACT Fueling the core airflow of a circular or elliptical scramjet combustor cross-section often requires intrusive geometries. Intrusive geometries can distribute the fuel evenly across the combustor cross-section and act as a flameholder for the fuel/air mixture. Compared to conventional transverse or angled wall injection, intrusive geometries allow easier penetration into the core combustor airflow and reduced fuel injection pressures. The design and testing of an intrusive pylon geometry for scramjet combustor fueling is the subject of this research. Three pylon configurations are compared: a basic pylon, a ramp pylon, and an alternating wedge pylon. All three pylon configurations exhibit the same frontal area and inject fuel parallel to the combustor airflow with long, thin rectangular injection ports (thin film fueling). However, the three pylon configurations incorporate different aft shapes to facilitate fuel/air mixing. A cold flow fuel injection study is accomplished to compare mixing capabilities and total pressure losses of the three pylon configurations. The ramp and alternating wedge pylons show decisive increases in mixing capability compared to the basic pylon. They also exhibit a slight increase in total pressure loss compared to the basic pylon.						
15. SUBJECT TERMS scramjet, hypermixer, supersonic combustion, fuel mixing, fuel injector, pylon						
16. SECURITY CLASSIFICATION OF:			17. LIMITATION OF ABSTRACT	18. NUMBER OF PAGES	19a. NAME OF RESPONSIBLE PERSON	
a. REPORT	b. ABSTRACT	c. THIS PAGE			Dr. Paul I. King	
U	U	U	UU	188	19b. TELEPHONE NUMBER (include area code) (937) 255-3636, ext 4628	